ISBN 978-2-87355-032-5

Proceedings of the International Meteor Conference

Pezinok-Modra, Slovakia, 2018

August 30 – September 2

IMC 2018
Aug 30 - Sep 2
Pezinok - Modra
SLOVAKIA

Published by the International Meteor Organization

Edited by Regina Rudawska, Jürgen Rendtel,
Charles Powell, Robert Lunsford, Cis Verbeeck, André Knöfel

Editing and printing:

Front cover picture: Logo of the IMC 2018, by Tomas Paulech.
Publisher: The International Meteor Organization
Printed: The International Meteor Organization
Editors: Regina Rudawska, Jürgen Rendtel, Charles Powell, Robert Lunsford, Cis Verbeeck, André Knöfel
Bibliographic records: all papers are listed with the SAO/NASA Astrophysics Data System (ADS)
`http://adsabs.harvard.edu with publication code 2018pimo.conf`.

Distribution:

Further copies of this publication may be ordered from the International Meteor Organization, through the IMO website (`http://www.imo.net`). Legal address: International Meteor Organization, Mattheessensstraat 60, 2540 Hove, Belgium.

ISBN 978-2-87355-032-5

Proceedings of the International Meteor Conference

Pezinok-Modra, Slovakia, 2018

August 30 – September 2

Published by the International Meteor Organization

Edited by Regina Rudawska, Jürgen Rendtel, Charles Powell, Robert Lunsford, Cis Verbeeck, André Knöfel

Table of contents

Table of contents (contd.)

Table of contents (contd.)

Poster contributions

Preface

The IMC 2018 in Pezinok-Modra was the 37th of the conference series, and the 4th in Slovakia. 127 participants from 28 countries used this opportunity to meet, to present results, to discuss and to prepare new projects. The location was close to the Modra observatory which is a well-known meteor astronomy site and which is famous for the 1998 Leonid fireball storm image. This image found its way into the IMC logo. Additional to the IMC, two workshops (on visual and spectroscopic work) took place immediately before the conference. All together, the program and the friendly and the helpful work of our hosts – as usual, a lot happening behind the scenery – made the 2018 event another memorable IMC.

Comparing the IMCs over decades, it is obvious that the topics have changed a lot. In the early years we spent much of our time to establish observing and analysing procedures for visual meteor work - starting more or less from scratch and this way being very creative. Similar processes happened subsequently for other observing techniques as well. This initialising process has reached a kind of saturation now. It may seem that currently all procedures are fixed and defined so that new observers have just to follow guidelines and fill in forms – which may be a less exciting situation as compared to the inventive phase. Newcomers may feel they are just adding tiny bits to an already existing large data archive, not doing anything new. However, I think we are meanwhile in an amazing harvesting phase. With the developed and tested procedures basically everyone is able to perform analyses of shower activity, in numerous cases over decades – not fighting with basic assumptions etc.

Preparing a talk for an IMC requires quite some effort; an idea, tests, observations or analyses and so on, finding a result to share, preparing the presentation, giving the talk – and getting feedback. It seems there is only a small further step to have this all ready as a publication for the Proceedings. Leaving out this final step may mean that all of it gets lost, may be forgotten and perhaps followed by an apparent re-discovery later on. Indeed, several IMC Proceedings volumes were published with long delays. Experience shows that the papers are best prepared at the time of the conference: the thoughts are fresh, the images are done, and some text is there (at least in your mind). As time passes by, the enthusiasm for writing a manuscript dwindles. Combined with the unforeseen very limited availability of the IMO editors during the critical phase right after the 2018 conference, we have arrived at the present situation: incomplete Proceedings.

Generally, the IMO needs your cooperation and help because the IMO is exactly the mirror of what we all are doing. We encourage you to take the opportunities to use the available data and procedures to “play” (in a creative sense) and discover things, and to present your ideas and results – preliminary as well as conclusive – at IMCs (and in the subsequent Proceedings) or in the IMO Journal WGN. Do not assume that everything has been solved in meteor science! The opposite is true. Apply the established methods but do not hesitate to try alternative approaches! Combine data from different sources, check the reliability of previously found results.

This IMC Proceedings is a joint work with very valuable contributions of Francisco Ocaña Gonzalez (compiling the initial manuscript spreadsheet), Regina Rudawska (editing and typesetting most papers), Jürgen Rendtel (editing, preparing the covers and tables, checking and compiling the final version), Charles Powell (editing and proofreading), Robert Lunsford (editing and proofreading), Cis Verbeeck (coordinating the editorial process) and André Knöfel (technical arrangements and compilation of the final volume).

We are looking forward to hear about your new results at the IMC 2019 in Bollmansruh, and to read about it in the IMC 2019 Proceedings! Meanwhile, enjoy reading this issue. Perhaps it is inspiring own projects of which we like to hear in the future.

Jürgen Rendtel, Potsdam, August 2019

Organizer's notes

The members of the Local Organizing Committee of the IMC 2018 (from left to right):
Pavol Zigo (head), Juraj Tóth, Roman Nagy, Jiřı Šilha, Pavol Matlovič, Martin Baláž, Danica Žilková, Adriana Pisarčíková, Leonard Kornoš, Tomáš Paulech.

Vladimír Porubčan of Bratislava, who supported the professional-amateur cooperation in meteor astronomy over many years, had his birthday during the IMC.

Program of the IMC 2018

Thursday, 30 August 2018

14:00-18:00	Arrival of participants
18:00-18:45	Welcome reception and opening of the conference
18:45-20:00	Dinner
	SESSION 1 – Introductory Session
20:00-20:30	Detection of bolides from space with the Global Lightning Mapper on GOES. P. Jenniskens
20:30-21:00	Current status of the European Fireball Network – instruments, methods and examples of data. P. Spurný and J. Borovička

Friday, 31 August 2018

	SESSION 2 – Observing techniques
09:00-09:20	The perfect observing direction. S. Molau
09:20-09:40	SCAMPI – Single Camera Measurement of the Population Index. P.C. Slansky
09:40-09:55	Numerical simulation of meteors as a means of debiasing AMOS data. M. Balaz, J. Toth
09:55-10:15	New spectroscopic program of the European Fireball Network. J. Borovička, P. Spurný
	SESSION 3 – Instruments, data pipelines and software
10:15-10:25	Correction for meteor centroids obtained using rolling shutter cameras. P. Kukić, D. Vida, P. Gural, D. Šegon, A. Merlak
10:25-10:45	Which trajectory solver is best for your optical meteor data? Algorithm implications for radiant and orbit accuracy. D. Vida, P. Brown, M. Campbell-Brown, P. Wiegert, P. Gural
10:45-11:00	Truth about video meteor photometry. R. Piffl
11:00-11:30	Coffee break and poster session
11:30-11:45	Improving astrometry and photometry reduction for all-sky cameras. D. Barghini, D. Gardiol, A. Carbognani
11:45-12:00	Spectral sensitivity of photographic emulsions. Ž. Andreić, D. Šegon, P. Gural
12:00-12:15	Adapter to meteor TV camera for observation of shower's weakest meteors. V. Leonov, A. Bagrov
12:15-12:30	Universal Cam Network API. V. Perlerin, M. Hankey
12:45-14:15	Lunch
14:15-14:30	Encontreitor: a new approach to meteor shower research software. L. Scanferla Amaralil, C. Augusto Di Pietro Bella, L. Trindade, C. Fernando Jung

Friday, 31 August 2018 (continued)

	SESSION 4 – Fireballs and meteorite recovery
14:30-14:45	Fireball over Germany and Poland, 6th October 2017. P. Żołądek, A. Olech, M. Wiśniewski, D. Heinlein, A. Margonis, S. Molau, J. Oberst, M. Stolarz
14:45-15:00	Results of Polish Fireball Network 2017. M. Wiśniewski, P. Żołądek, A. Olech, A. Raj, Z. Tyminski, M. Maciejewski, K. Fietkiewicz, M. Myszkiewicz, M. Przemysław Gawroński, T. Suchodolski, M. Stolarz, M. Gozdalski
15:00-15:20	Simulating meteorite impacts – an outdoor field experiment. F. Bettonvil
15:20-15:35	NEMO Vol 2. – Status of the NEar real-time MOnitoring system. E. Drolshagen, T. Ott, D. Koschny, G. Drolshagen, P. Mialle, J. Vaubaillon, B. Poppe
15:35-16:05	Coffee break and poster session
16:05-16:20	Connecting meteors and meteorites: flight track, spectra, finding and laboratory analysis – suggestion for a collaborative action. A. Kereszturi, M. Ferus, K. Sárneczky, A. Berezhnoy, E. Chatzitheodoridis, J. Koukal, L. Lenža, M. Krøus
16:20-16:40	Calculating orbits and finding meteorites with the Desert Fireball Network. E. K. Sansom, H. Devillepoix, P. A. Bland, T. Jansen-Sturgeon, R. M. Howie, B. A. D. Hartig, M. C. Towner, M. Cupák, M. A. Cox
16:40-16:50	The appearances of meteorite streams. Yang I-Ching, Jann-Yenq Liu

	SESSION 5 – Miscellaneous
16:50-17:00	Visual Workshop 2018: analyzing the Perseids 2016. C. Verbeeck, J. Rendtel, K. Veljković, V. Perlerin, M. Hankey
17:00-17:15	Spectroscopy Workshop 2018. R. Rudawska, J. Tóth
17:15-17:25	The MALBEC project. J. Vaubaillon, A. Caillou, C. Colomer, P. Deverchere, A. Christou, D. Baratoux, P. Beck, M. Birlan, B. Carry, S. Bouley, F. Colas, L. Maquet, P. Vernazza
17:25-17:35	Balloon-borne video observations of Geminids 2016. F. Ocaña
17:35-17:45	Using SPADE for radio meteor observations – status update. A. Martínez Picar, C. Marqué
17:45-18:00	Spurious meteoroid orbits. M. Hajdukova, L. Kornoš
20:00-21:00	IMO General Assembly Meeting

Saturday, 1 September 2018

	SESSION 6 – Camera Networks
09:00-09:20	ANDES-FIRE: The Argentina All-sky Video System. P. Gural
09:20-09:40	Croatian Meteor Network – ongoing work 2017–2018. D. Šegon et al.
09:40-09:55	News from the italian PRISMA fireball network. D. Gardiol
09:55-10:05	Mendocino College – Ukiah Latitude Observatory CAMS Project: first light. T.W. Beck, M. Bradley, E. Cannon, J. Glazier, D. Hunchard, J. Ronco, E. Sherwood, C. Upton
10:05-10:25	Towards a Global Fireball Observatory: new fireball observation hardware. H. Devillepoix, R. Howie, B. Hartig, P. Bland, E. Sansom, D. Busan, S. Buchan, M. Towner, M. Cupák, T. Jansen-Sturgeon, P. Shober, J. Paxman
10:25-10:55	Coffee break and poster session

Saturday, 1 September 2018 (continued)

	SESSION 7 – Atmospheric processes and phenomena (part I)
10:55-11:15	Simulation of meteor plasma using terawatt laser. M. Ferus, P. Kubelík, J. Koukal, L. Lenža, M. Krøus, V. Laitl, L. Petera, S. Civiš
11:15-11:30	Yet another result of the spectral and fragmentation study of small meteoroids. V. Vojáček, J. Borovička, P. Koten, P. Spurný, R. Štork
11:30-11:45	On the energy release after meteoroids fragmentation. L. Egorova, V. Lokhin
11:30-12:00	Testing of the new meteoroid fragmentation model applied to the Chelyabinsk event. I. Brykina, M. Bragin
12:00	Lunch
13:30-20:00	Excursion: Red Stone castle and AGO Observatory
20:00	Conference dinner
21:00	Traditional folklore performance

Sunday, 2 September 2018

	SESSION 7 – Atmospheric processes and phenomena (part II)
09:45-10:00	The effect of the solar wind on the evolution of dust grains trapped in the mean motion orbital resonance with Jupiter J. Klačka, R. Nagy, M. Jurči
10:00-10:15	Spectral properties of slow meteors: Na-rich spectra as tracers of Apollo-type meteoroids. P. Matlovič, J. Tóth, L. Kornoš

	SESSION 8 – Ongoing meteor work – Radio technique
10:15-10:30	BRAMS radio observations analyzed: activity of some major meteor showers. C. Verbeeck, H. Lamy, S. Calders, C. Tétard, A. Martínez Picar
10:30-10:45	Sun influence in meteor height. L. Barbieri
10:45-11:05	EARS Geminids 2017 radio observation. G. Tomezzoli
11:05-11:35	Coffee break and poster session

	SESSION 9 – Meteor showers (observations and modelling)
11:35-11:50	Modelling the Geminid meteor shower activity. G. O. Ryabova
11:50-12:10	Geminid rates over a century. J. Rendtel
12:20-12:40	September ε-Perseids observed by the Czech Fireball Network in 2013, 2015, 2016, and 2017. L. Shrbený, P. Spurný, J. Borovička
12:40-12:55	What resonances are manifested in the Quadrantid meteoroid stream and asteroid (196256) 2003 EH1? G. Sambarov, T. Galushina, O. Syusina
13:00-14:00	Lunch
14:00	Closing of the IMC 2018

Poster contributions

Comparative study of the hypothetical strewn fields of a few previous bolides and real historical ones.
T. Hegedüs, Z. Jäger, S. Csizmadia, Z. Zelkó, Z. Kereszty

Meteor observations by optical and acoustical methods.
A.P. Kartashova, G. Bolgova, Y. Rybnov, O.P. Popova, D.O. Glazachev, V. Efremov

Photographic and visual observation of the Perseids in Greece 2018 – Earlier video Observations
V. Tsamis

Optimization of multistation observation.
R. Piffl

The Plasma Radiation Database (PARADE) to simulate meteor ablation species.
J. Zender, R. Rudawska, D. Koschny, S. Loehle, M. Eberhart, F. Zander, A. Meindl

Initial design and results of a fireball network add-on radiometer to collect meteor light curves.
S.R.G. Buchan, R.M. Howie, J. Paxman, H. Devillepoix

Regular and transitory meteor showers of comet C/1979 Y1.
M. Hajduková, L. Neslušan

Comparison of radio meteor detections at 143 MHz and 50 MHz.
P. Dolinský

MT – a software for calculating meteor trajectories and orbits from multiple-stations observations. F. Ďuriš, L. Kornoš, J. Tóth

AMOS cameras status.
J. Tóth , L. Kornoš, P. Zigo, J. Vilagi, J. Simon, D. Kalmancok, J. Silha, P, Matlovič

Towards an autonomous BRAMS network.
S. Calders, H. Lamy, A. Martinez-Picar, C. Verbeeck, M. Anciaux, S. Ranvier

Bolidozor network. Roman Dvořák and Jakub Kákona

NEMETODE meteor network used for citizen science and education at Dunsink Observatory. S. Green, J. Mackey, L. Drury, H. O'Donnell, M. Topinaka, M. O'Connell, W. Stewart, M. Foylan, P. Stewart, G. Reineke, K. Smith, D. Malone and P. Dempsey.

The first confirmed lunar impact flash observed from Brazil. D. Duarte C. Pinto, L. Trindade, M.L. do P. Villarroel Zurita, R.A.A. Caldas and M. Domingues

Hardware optimization for video network station S. Golubović and A. Dokić

Automation of the video network. V. Nikolić

"Starcounters" - A citizen science project for registering the meteor showers. R. Cedazo, E. Gonzalez, M.R. Alarcón, M. Serra-Ricart and S. Lemes

Extending all-sky photography into twilight. F. Bettonvil

CAMS Update on hardware interfaces and software enhancements. P. Gural

AllSky6 meteor camera. M. Hankey and V. Perlerin

Low-cost raspberry pi meteor station - data quality assessment and first results. D. Vida, D. Šegon, M.J. Mazur, A. Merlak and D. Zubović

Search for faint iron meteoroids. P. Koten, V. Vojáček, J. Borovička, P. Spurný, R. Štork and D. Čapek

Building a better shower look-up table. P. Jenniskens

Meteor detecting efficiency of video cameras. P.C. Slansky

Whether any particle in meteor stream has the same chemical composition? V. Leonov and A. Bagrov

Determination of the meteor particles properties V.V. Efremov, O. P. Popova, D.O. Glazachev, A.P. Kartashova

Adapter to meteor TV camera for observation of shower's weakest meteors. (2 POSTERS) V. A. Leonov, A. V. Bagrov

Trail development of the brightest Perseid during the night of August 12 - 13. S. Kaniansky, J. Skvarka.

Meteor section of the Israeli Astronomical Association.

The Italian bolide of May 2017: trajectory, orbit and preliminary fall data. A. Carbognani, D. Barghini, D. Gardiol, M. di Martino, G. B. Valsecchi, P. Triverof, A. Buzzoni, S. Rasetti, D. Selvestrel, C. Knapic, E. Londero, S. Zorba, C. A. Volpicelli, M. Di Carlo, J. Vaubaillon, C. Marmo, F. Colas, D. Valeri, F. Zanotti, M. Morini, P. Demaria, B. Zanda, S. Bouley, P. Vernazza, J. Gattacceca, J.-L. Rault, L. Maquet, M. Birlan

Determination of the meteor particle's properties from observational data. V. V. Efremov, O. P. Popova, D. O. Glasachev, A. P. Kartashova

Impact effects calculator: scaling relations from shockwave and radiation effects applied to Chelyabinsk and Tungunska event. D.O. Glasachev, E.D. Podobnaya, O.P. Popova, A. P. Kartashova, N.A. Artemyeva, V. V. Shuvalov, V.V. Svetsov.

List of participants

Róbert Adam, Zeljko Andreic, David Asher, Alexander Bagrov, Martin Baláž, Lorenzo Barbieri, Dario Barghini, Timothy Beck, Felix Bettonvil, Uroš Bettonvil, Damir Biondic, Jiří Borovička, Gaetano Brando, Irina Brykina, Stuart Buchan, Stijn Calders, Özcan Çalişkan, I-Ching Yang, François Colas, Helen Collins, Chloé Colomer, Kerem Osman Çubuk, Hadrien Devillepoix, Marcelo Domingues, Esther Drolshagen, Roman Dvořák, František Ďuriš, Lidia Egorova, Martin Ferus, Pilar García Vega, Daniele Gardiol, Stevan Golubović, Sam Green, Peter Gural, Marc Gyssens, Mike Hankey, Maria Hajdukova, Tibor Hegedüs, Eli Fugelso Hillestad, Trond Erik Hillestad, Antal Igaz, Elise IJland, Peter Jenniskens, Javor Kac, Stanislav Kaniansky, Jakub Kapus, Anna Kartashova, Akos Kereszturi, Hutch Kinsman, James Kinsman, André Knöfel, Matej Korec, Leonard Kornoš, Jakub Koukal, Patrik Kukić, Anna Levin, Maciej Maciejewski, Mirjana Malaric, Antonio Martínez Picar, Filip Matković, Pavol Matlovič, Peter Mikloš, Sirko Molau, Lorenzo G. Morillas Sánchez, Roman Nagy, Sumio Nakane, Ana Nikolić, Nagatoshi Nogami, Filip Novoselnik, Francisco Ocaña González, Michael O'Connell, Nándor Opitz, Theresa Ott, Tomáš Paulech, Debora Pavela, Lovro Pavletić, Dušan Pavlović, Vincent Perlerin, Nikola Perović, Suyin Perret-Gentil, Roman Piffl, Adriana Pisarčíková, Miruna Popescu, Vladimir Porubčan, Charles Powell, Arkadiusz Raj, Ella (Elena) Ratz, Jürgen Rendtel, Tom Roelandts, Regina Rudawska, Galina Ryabova, Georgy Sambarov, Alejandro Sanchez de Miguel, Eleanor Sansom, Krisztián Sárneczky, Damir Šegon, Fintan Sheerin, Lukáš Shrbený, Alan Shuttleworth, Jiri Šilha, Ivica Skokić, Peter C. Slansky, Pavel Spurny, Peter Stewart, Chris Steyaert, Tamara Tchenak, Yakov Tchenak, István Tepliczky, Giancarlo Tomezzoli, Juraj Tóth, Lauriston Trindade, Vagelis Tsamis, Arnold Tukkers, Jeremie Vaubaillon, Kristina Veljković, Cis Verbeeck, Denis Vida, Jozef Világi, Vlastimil Vojáček, Maria Vukić, Thomas Weiland, Mariusz Wiśniewski, Pavel Zigo, Danica Žilková, Peter Zimnikoval, Przemysław Żołądek

The perfect observing direction (for video meteor cameras)

Sirko Molau[1]

[1] **Abenstalstr. 13b, 84072 Seysdorf, Germany**
sirko@molau.de

This paper analyses the impact of properties of the observing site, observing direction, and meteor shower on the effective collection area of a video meteor camera. It determines the best observing direction, i.e. in which the camera records most meteors. The perfect observing direction depends on the actual circumstances, but a field of view at 30° altitude in north-eastern to south-eastern direction is well suited for many cameras and meteor showers.

1 Introduction

The effective collection area of a video camera is the basis for the determination of the flux density and population index of meteor showers. The calculation starts from the size of the meteor layer that is covered by the camera and incorporates different boundary conditions thereafter which may increase or reduce the detection efficiency of the camera. The actual model used to calculate the effective collection area is still being improved (e.g. Molau et al., 2017).

A by-product of the calculation is that we know the sensitivity of the camera in different observing directions, i.e. in which direction the camera will record most shower meteors. We used the latest model to calculate and visualize the effective collection area of a video camera and to analyse the impact of the observing site, observing direction and meteor shower properties.

2 Prior Work

In 1993, M. Nitschke derived from a detailed camera model that the best observing direction would be above the radiant (Nitschke, 1993). He examined in particular the dependency on the radiant altitude.

For the analysis of video records from the 1999 airborne Leonid observations, P. Gural used a high-fidelity model and found the highest counts below the radiant close to the horizon (with the altitude depending on the atmospheric extinction). He noted that with higher population indices, the best field of view would be at somewhat higher elevations (Gural and Jenniskens, 1998).

The analysis of Gural and the one described here consider the same boundary conditions, but use different approaches:

- Gural carried out a Monte Carlo simulation of millions of meteors whose number and brightness distribution correspond to a given flux density and population index. For each meteor he calculated the magnitude loss due to the boundary conditions, and then checked if the meteor would cross the field of view. So he obtained the detection efficiency of the camera under the given conditions.
- Molau calculates analytically the collection area and loss of limiting magnitude for each camera pixel, and accumulates over all pixels to get the detection efficiency of the camera.

Under identical boundary conditions, both approaches should yield the same result.

3 Boundary conditions

Base model

Figure 1 depicts the base model with all factors that influence the effective collection area of a camera: Observer, collection area, radiant, zenith, horizon, and meteor layer. Note that the meteor layer is assumed to be very thin (two-dimensional), whereas in reality there is typically a certain height range where meteors are observed. However, meteor light curves are typically not flat but show a distinct maximum. So it is one particular height where a meteor has the highest detection probability.

Boundary conditions

The following boundary conditions affect the effective collection area:

- Collection area per camera pixel: This parameter depends on the altitude of the field of view. Pixels closer to the horizon cover a larger atmospheric layer and have a larger collection area.
- Distance to meteor layer and atmospheric extinction: This parameter depends on the altitude of the field of view and the observing site (height, extinction). Pixels close to the horizon monitor a more distant atmospheric layer. The magnitude loss increases with distance and the longer path through the atmosphere (extinction).

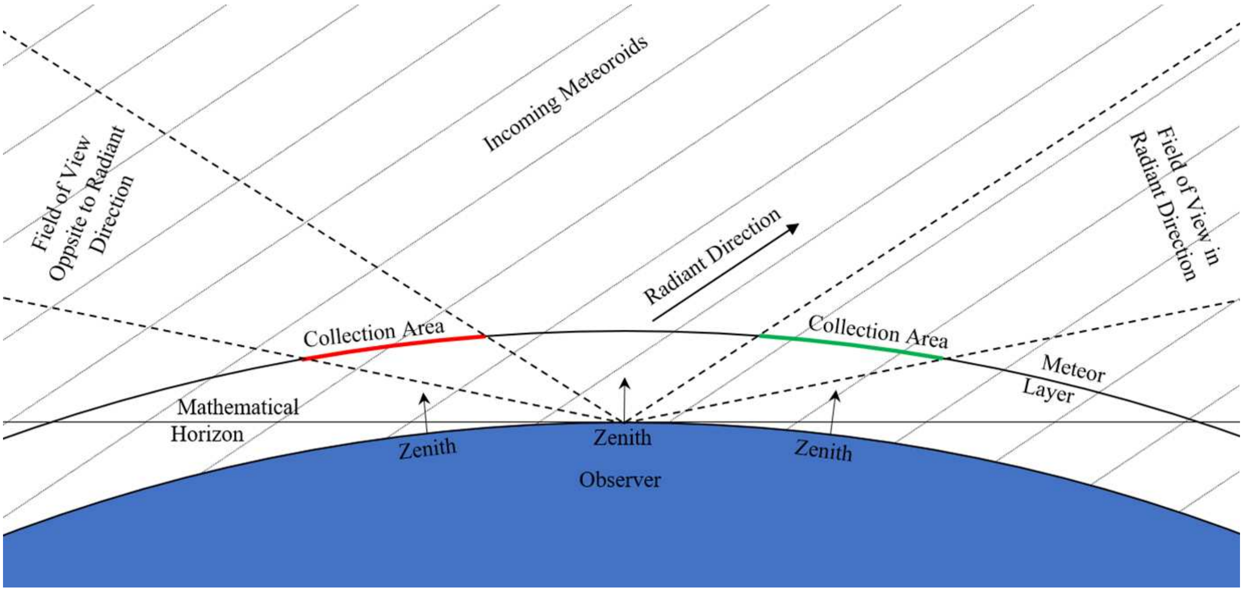

Figure 1 – Base model with different factors that influence the effective collection area.

- Height of meteor layer: The height increases with larger meteor shower velocities and radiant altitudes. The higher the meteor layer, the larger the collection area.
- Angular meteor velocity: This parameter depends on the observing direction and meteor shower velocity. Meteors at larger radiant distances have longer trails and higher angular velocities, which increases the magnitude loss.
- Radiant altitude: This parameter depends on the radiant position, observing site, and time. A larger radiant altitude causes more meteors to cross the same atmospheric layer.
- Limiting magnitude and population index: These parameters depend on the meteor shower and camera. A sensitive camera records more meteors, and a low population index yields brighter meteors which are easier to detect.

Note that boundary conditions may interfere constructively (e.g. distance of meteor layer and atmospheric extinction) or destructively (e.g. distance of meteor layer and size of covered atmospheric layer) with one another. However, even if they have a different sign, they do not simply cancel each other out, because they may have a different functional type (e.g. quadratic distance law vs. exponential population index).

The described boundary conditions are defined by the following model parameters:

- Observing direction (altitude, radiant distance).
- Meteor shower properties (radiant altitude, meteor shower velocity, population index).
- Observing site properties (altitude, extinction).

The limiting magnitude of the camera is a constant offset that has no impact on the perfect observing direction.

There is a complex dependency between these parameters and the effective collection area, because one parameter may influence different boundary conditions at the same time. So the impact of each parameter cannot be estimated easily – it needs to be simulated.

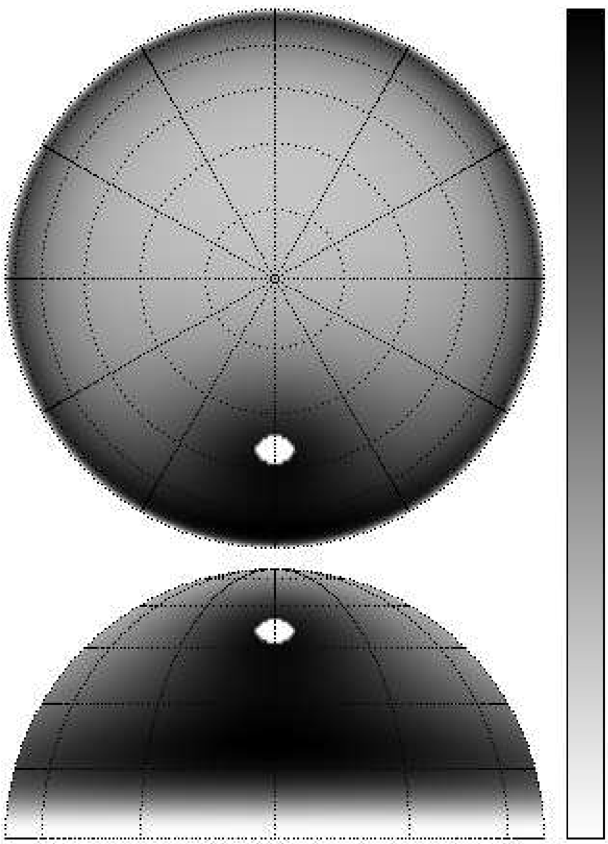

Figure 2 – Effective collection area of the base model.

4 Simulations

Base model

We start to calculate the effective collection area for an "average" meteor shower:

- Declination $\delta = 10°$.
- Velocity $v_{\mathrm{inf}} = 50$ km/s.
- Population index $r = 2.5$.
- Aerosol optical depth aod = 0.25.
- Radiant at culmination.

Figure 2 depicts the effective collection area under these conditions. White represents zero and black the maximum effective collection area. The upper graph shows the whole hemisphere from above (north up, east right), the lower part is a view from the horizon in the direction of highest collection area (here: south).

We see that there are two regions with increased collection area: At about 20° altitude above the horizon and around the radiant. The white spot at the radiant results from the meteor detection software which does not detect meteors slower than 2°/s to avoid false alarms from satellites.

Next we will modify single parameters of this base model to see what effect they have on the effective collection area.

Dependency on the meteor shower velocity.

Figure 3 depicts the effective collection area for a minimum meteor shower velocity of $v_{\mathrm{inf}} = 12$ km/s and for a maximum velocity of $v_{\mathrm{inf}} = 71$ km/s. At low velocities we find the largest effective collection area near the horizon (independent of the azimuth). At high velocities the best direction is at the radiant and at the horizon below the radiant.

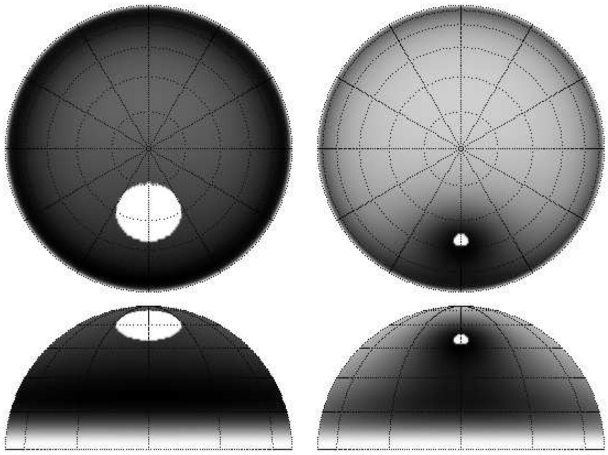

Figure 3 – Effective collection area for low (left) and high (right) meteor shower velocities.

Dependency on the population index.

Figure 4 depicts the effective collection area for a small population index of $r = 1.7$ and for a large population index of $r = 3.3$. At very low population indices the best observing direction is very low towards in the horizon at 10° altitude, independent of the azimuth. At high population indices, the best direction is directly at the radiant.

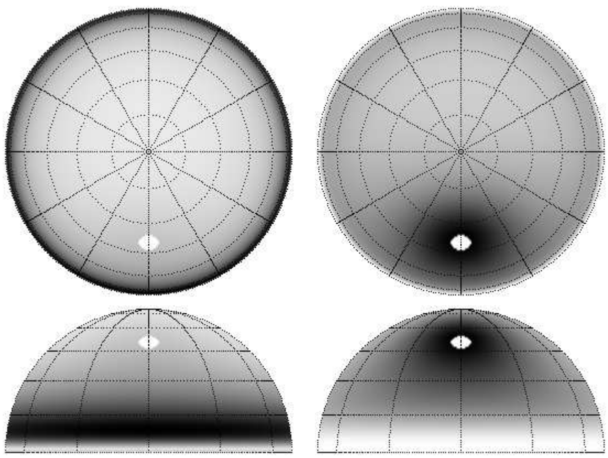

Figure 4 – Effective collection area for small (left) and large (right) population indices.

Dependency on the atmospheric extinction.

Figure 5 depicts the effective collection area for a good observing site with low atmospheric extinction (aod = 0.10) and for a poor site with high extinction (aod = 0.40). The effect is similar to the meteor shower velocity and population index: In the case of low extinction a field of view at the horizon is favorable, at higher extinction values a field of view at the radiant.

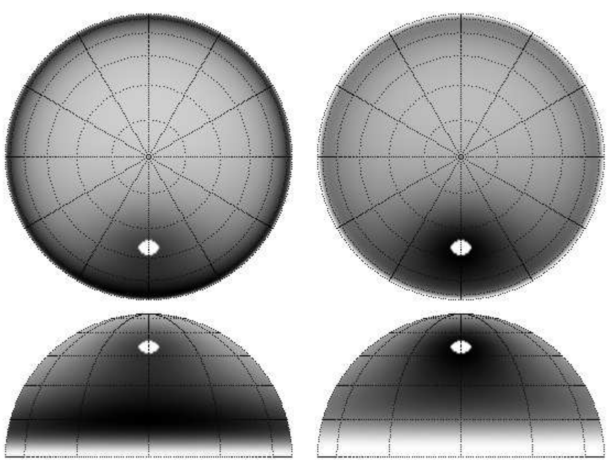

Figure 5 – Effective collection area for low (left) and high (right) atmospheric extinction.

Observing time and size of field of view.

So far, we simulated the effective collection area for one point in time and a camera with a punctual field of view. Both parameters have an integrating effect, i.e. they smear out the detection probability for meteors.

Figure 6 shows on the left side the cumulative collection area of the base model, when the radiant is moving from east to south with six hours of observing time. The "blind spot" at the radiant has become a gray stripe.

On the right side we see the base model for a camera with a circular field of view with 50° diameter. Note that the best observing direction shifts towards higher altitudes because the field of view is cut at the horizon.

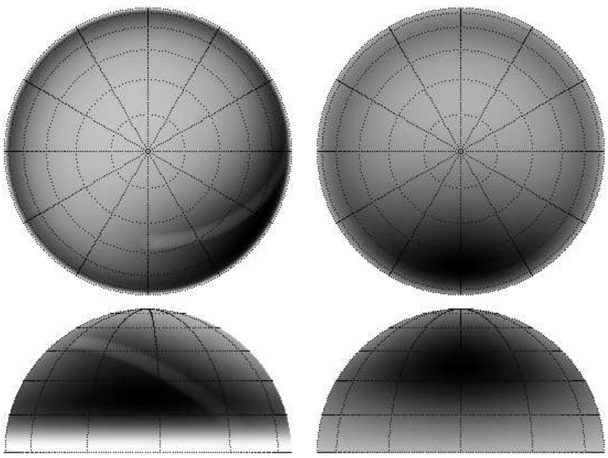

Figure 6 – Effective collection area for an observing session of six hours duration (left), and for a camera with a 50° diameter field of view (right).

Figure 7 shows the net result of both effects. Under these more realistic conditions, the highest collection area can be found in the south-eastern direction at about 30° altitude.

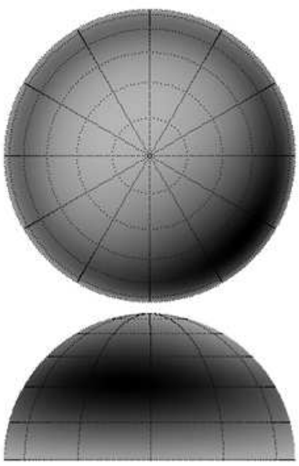

Figure 7 – Effective collection area for an observing session of six hours duration and with a camera with a 50° diameter field of view.

Real meteor showers

Finally, we want to calculate the effective collection area with the parameters of well-known major meteor showers. Figure 8 shows the collection area accumulated over the full night for a camera at a mid-northern observing site (50° N) and a 50° circular field of view.

- Quadrantids: due to the high declination, most of the time the radiant is located in northern directions. Hence, the largest effective collection area is found north-east at about 30° altitude.
- Lyrids: the radiant of the Lyrids rises significantly in the morning, so the best viewing direction is east at the same altitude.
- eta-Aquariids: the radiant rises shortly before dawn and the shower is quite fast, so the camera should be pointed low in the eastern sky.
- Perseids: the Perseids also have a high northern declination, which is why the shower can be observed best in the north-eastern direction at about 30° altitude.
- Orionids: contrary to the Perseids, this low declination shower is viewed best in the south-eastern direction at the same altitude.
- Geminids: in the long December nights the Geminid radiant rises in the eastern, culminates in the southern, and sets in the western direction. The effective collection area is almost independent of the azimuth (with slightly higher values at east and west) and the best altitude is about 30°.

5 Conclusions

There is not a single best observing direction because the effective collection area depends on the parameters of the meteor shower, the camera, and the observing site. However, the difference in detection efficiency between a good and bad observing direction may be as large as a factor of three to four.

In the case of slow meteor showers, small population indices and low atmospheric extinction the camera should be pointed low to the horizon (15° . . . 30° altitude) as is shown in Figure 9, left.

For fast meteor showers, large population indices and high atmospheric extinction the camera should observe close to the radiant as is shown in Figure 9, right.

As a rule of thumb, a field of view at **30° altitude in north-eastern to south-eastern direction** is a good choice for many meteor showers and video meteor cameras.

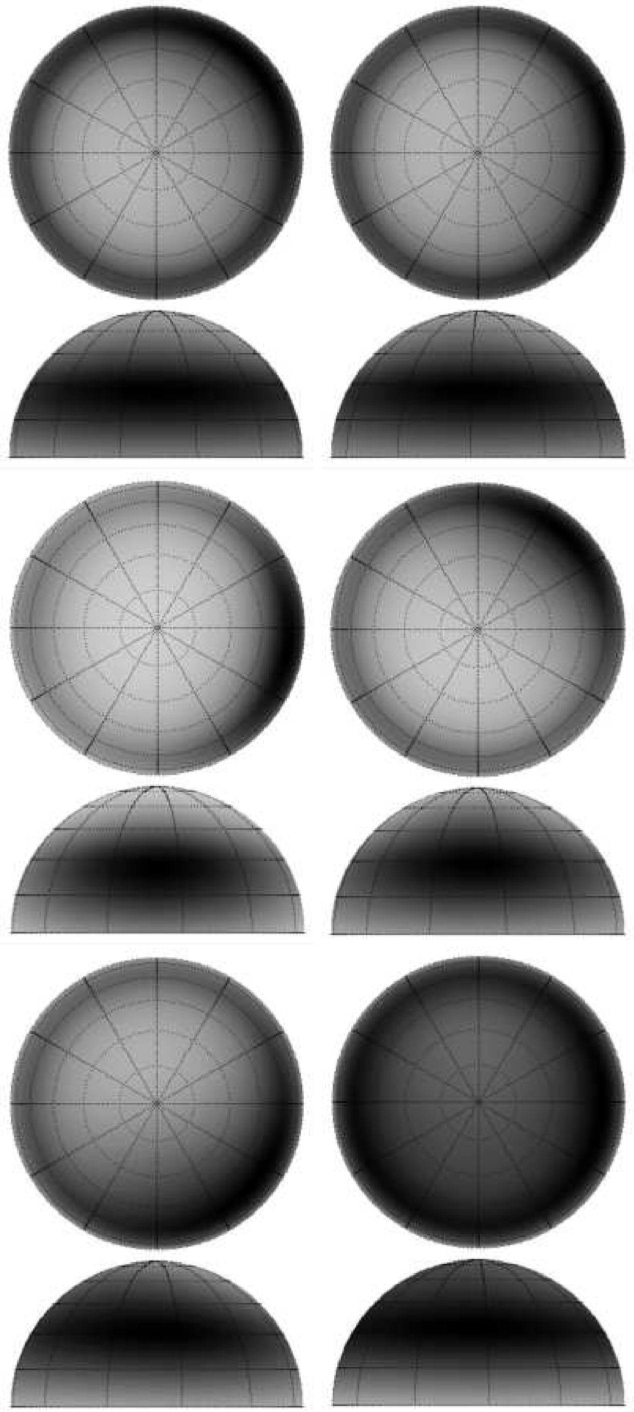

Figure 8 – Effective collection area for the Quadrantids (up left), Lyrids (up right), Eta-Aquariids (middle left), Perseids (middle right), Orionids (bottom left), and Geminids (bottom right).

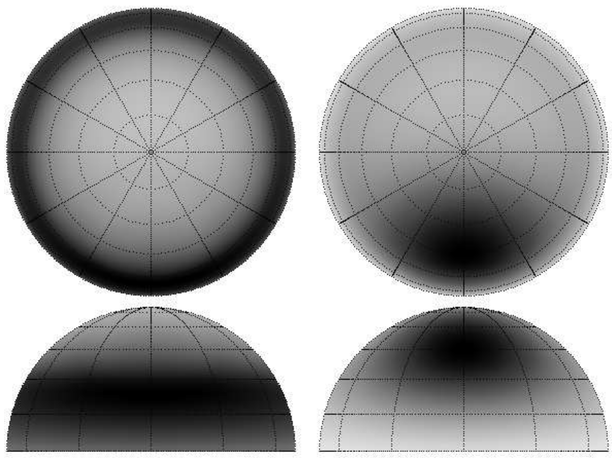

Figure 9 – Effective collection area of a slow meteor shower with small population index and low atmospheric extinction (left) and of a fast meteor shower with large population index and high atmospheric extinction (right).

References

Gural P.S. and Jenniskens P. (1998), "Leonid storm flux analysis from one Leonid MAC video AL50R." *Earth, Moon, and Planets*, **82**, 221–247.

Molau S., Crivello S., Goncalves R., Saraiva C., Stomeo E., Kac J. (2017), "Results of the IMO Video Meteor Network-May 2017, and flux density calculation." *WGN, Journal of the IMO*, **45**, 144–148.

Nitschke M. (1993), "Videoaufzeichnung von Meteoren II: Ausrichtung der Kamera." *Sternschnuppe*, **5**, 38–41.

SCAMPI - Single Camera Measurement of the Population Index

Peter C. Slansky[1]

[1] **HFF München, Bernd-Eichinger-Platz 1, 80333 München**
slansky@mnet-online.de

SCAMPI is the family name of a sequence of projects:

4CAMPI: 4-Camera Measurement of the Population Index (Perseids 2016)

SCAMPI 1.0: Single Camera Measurement of the Population Index (Perseids 2016)

3CAMPI: 3-Camera Measurement of the Population Index (Perseids 2018)

SCAMPI 2.0: Single Camera Measurement of the Population Index (targeted for the Geminids 2018).

The population index r is a very important quantity for meteor science. It describes the brightness distribution of a meteor shower (see e.g. Rendtel & Arlt (2017)). The ideal brightness distribution for $r = 2{,}5$ is shown in Figure 1.

The idea of a constant population index has been criticized by some authors, for example by Richter (2018), because an exponential function would result in an infinite number of faint meteors. On the other side of the magnitude axis the small numbers of very bright meteors inside one observation interval makes their statistics very difficult. Due to both reasons, a "population index" can only be constant in a certain magnitude range.

Two practical problems arise if the PI shall be calculated from video observations: Meteor photometry and meteor detection. Faint meteors tend to "drown" in the image noise. This makes the detection threshold statistically weak instead of sharp. The basic idea of 4CAMPI, 3CAMPI and SCAMPI 2.0 is to generate three or four identical detection thresholds by steps in the meteor detection sensitivity of the camera(s). So, the shortcomings of the unknown character of the detections threshold(s) can be overcome and it can (at least) be investigated if the PI is constant between the detection thresholds.

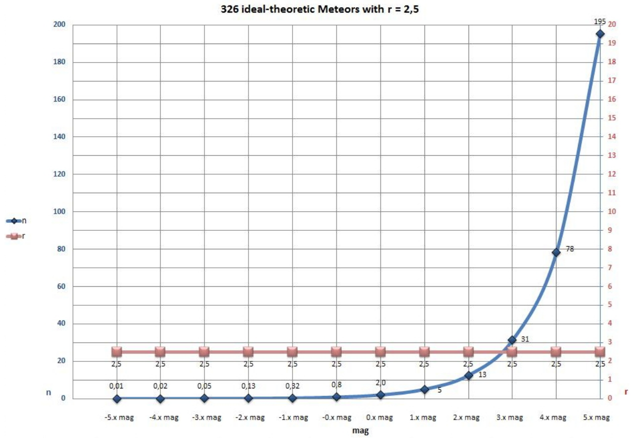

Figure 1 – The number of meteors of a certain magnitude is following an exponential function with r as a constant.

Figure 2 shows the setup of the 4CAMPI-project: The Perseids 2016 were observed with two ultra-high sensitive cameras Canon ME 20F-SH (max. ISO 4.000.000) and two Sony α7S (max. ISO 409.000) with an identical field of view (Slansky, 2016, 2018).

- Camera 1: Canon ME20S-FH at ISO 1.400.000 and F = 2.0 (reference sensitivity)
- Camera 2: Canon ME20S-FH at ISO 175.000 and F = 2.0 (-3 stops)
- Camera 3: Sony α7S at ISO 160.000 and F = 5.6 (-6 stops)
- Camera 4: Sony α7S at ISO 20.000 and F = 5.6 (-9 stops).

Camera 1 recorded more than 900 meteors in six and a half hours. But 4CAMPI failed: The differences in the two camera types, the three lens types and the different F-stop and ISO settings led to irregular stellar limiting magnitudes as well as irregular meteor detection thresholds. Also, the differences in the image noise led to irregular differences in meteor detection.

To make use of the data 4CAMPI was converted to SCAMPI 1.0: The video recordings of camera 1 were analyzed with MetRec by Sirko Molau. In 6:25 hours camera 1 had recorded 906 meteors overall, among them 549 Perseids and 287 Sporadics and Antihelions.

The results of the numeric and photometric analysis are shown in Figure 3. They do not follow the function of Figure 1: The number of Perseids has a maximum at 1.0-1.9 mag. After this, the numbers of fainter meteors decrease nearly constantly. The resulting population index varies strongly. A similar result was determined

Figure 2 – 4CAMPI, Perseids 2016 at Emberger Alm, Austria; Peter C. Slansky (left) with Bernd Gährken.

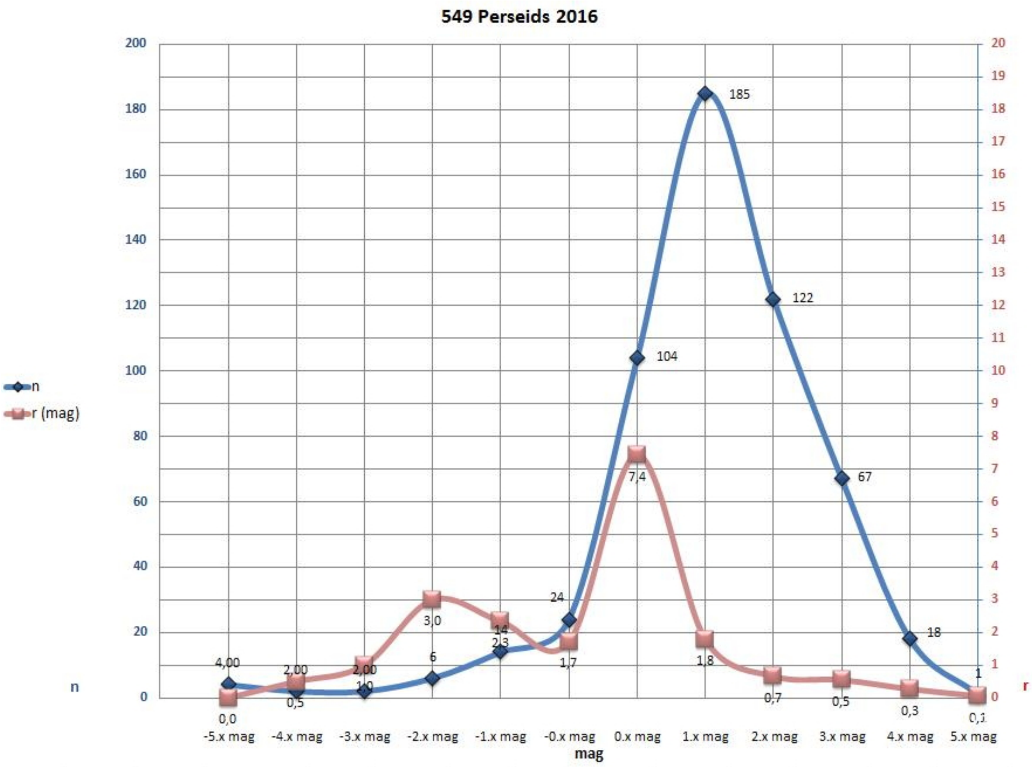

Figure 3 – Perseids 2016 recorded by camera 1.

for the Sporadics and Antihelions in the same time scale (Figure 4).

The results of 4CAMPI/SCAMPI 1.0 allow the following interpretations:

1a: The results go back to errors from the meteor photometry.

1b: The results go back to errors from the meteor detection.

2a: The results are real; the Perseids 2016 were extraordinary.

2b: The results are real; there was no constant PI.

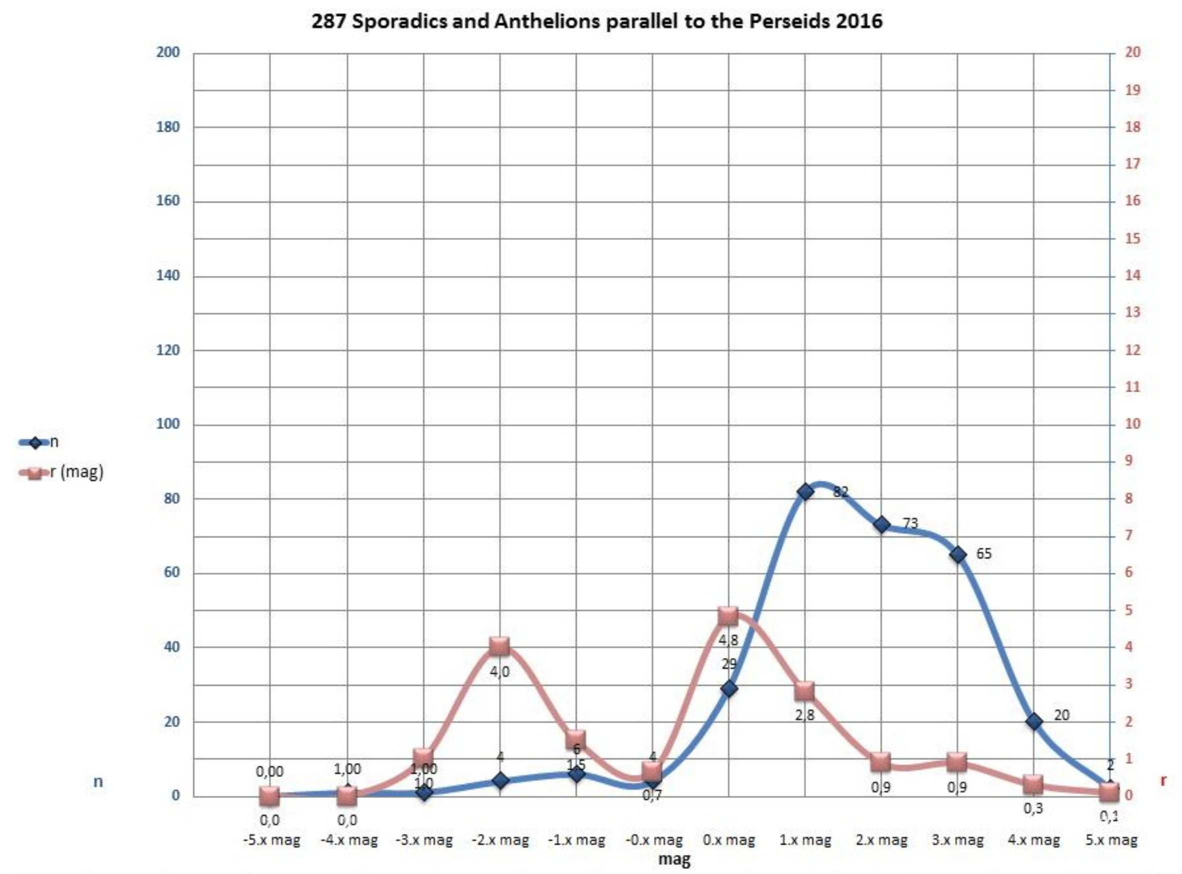

Figure 4 – Sporadics and Antihelions recorded by camera 1 parallel to the Perseids 2016.

Of course, all possible combinations of these interpretations must also be considered.

To overcome the failures of 4CAMPI the Perseids 2018 were observed by 3CAMPI (Figure 5). Three identical cameras Sony α7S were equipped with identical lenses Canon FD 1.4/50mm. The settings for ISO and F-stop were identical: ISO 409.000 at F = 1.4. The three detecting thresholds were realized with neutral density filters: no filter at camera 1, a ND filter of -2 stops for camera 2 and -4 stops for camera 3.

During the nights 11./12. and 12./13.8.2018 eight hours of parallel videos were recorded. For the presentation on the IMC 2018 only a first draft analysis was possible: 1:03 hours were examined "manually" (by eye) as well as the stellar limiting magnitude of each camera compared to a star chart. The resulting inaccuracy in meteor detection should be the same for all three cameras, so that the result for the PI should still be reliable. Figure 6 and 7 show the first draft result. Note, that the axis are different to Figures 1, 3 and 4: horizontally there is the stellar limiting magnitude and vertically there are cumulative numbers of meteors (the numbers of meteors caught by that very camera). Neither the Perseids nor the other meteors follow a constant PI.

In the next step all the data of 3CAMPI shall be analyzed with a meteor detection software.

In the future project SCAMPI shall be reloaded to version 2.0 (Figure 8). The idea is to use a fast liquid crystal element in the camera lens mount that is triggered by the sensor, so that it changes its optical density synchronized with the exposure. The result is a video with three or four sequentially detection thresholds. This shall be done in cooperation with ARRI, Munich, manufacturer of the ARRI Alexa Mini.

First target of SCAMPI 2.0 shall be the Geminids 2018.

Conclusions of the projects 4CAMPI, SCAMPI 1.0 and 3CAMPI:

- For the PI circular observatory effects should be considered.

Figure 5 – 3CAMPI for the Perseids 2018. Three cameras Sony a7S with identical lenses Canon FD 1.4/50mm with different ND filters.

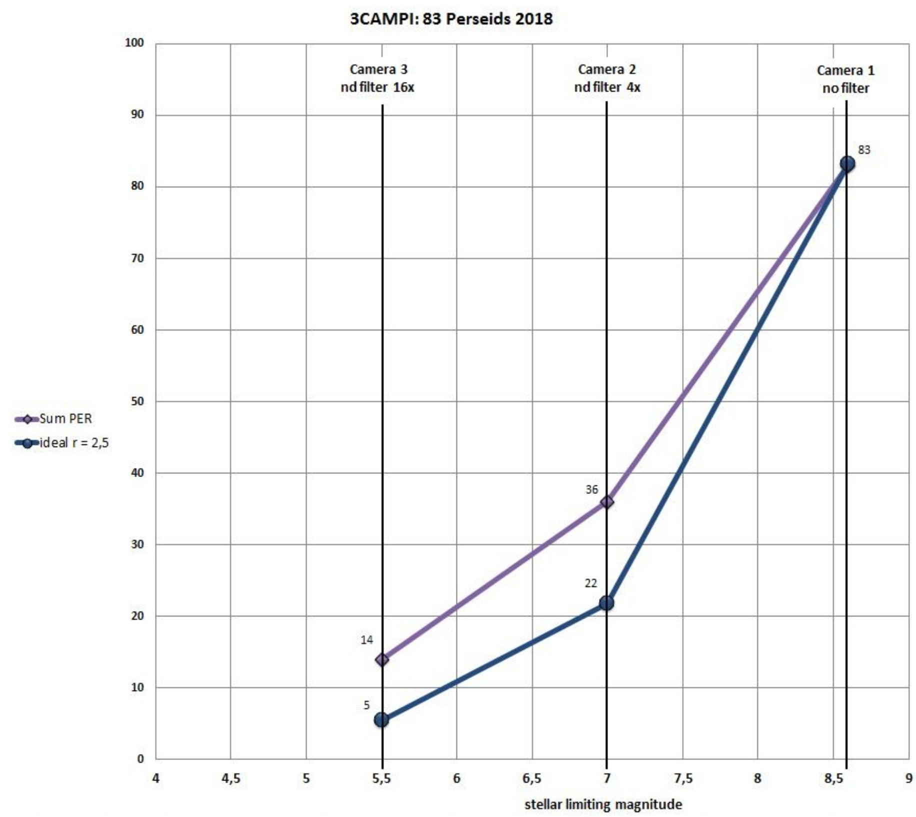

Figure 6 – First draft result of 3CAMPI for the Perseids 2018.

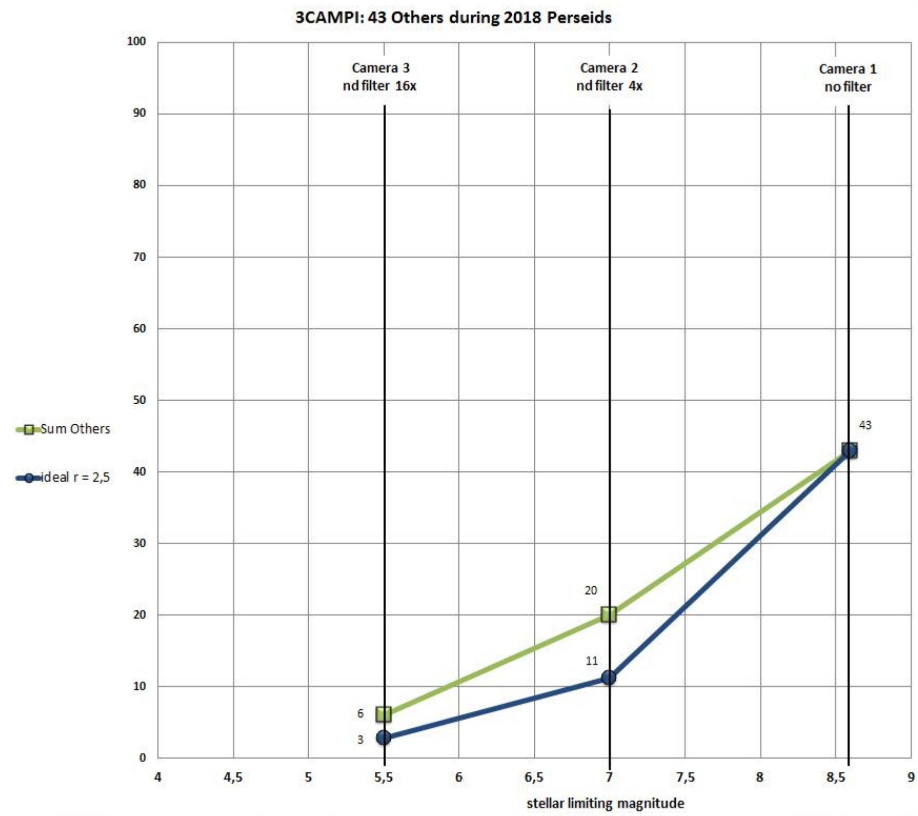

Figure 7 – First draft result of 3CAMPI for other meteors parallel to the Perseids 2018.

- Instead of a constant Population Index the definition of a variable "Brightness Distribution Function" x = f (mag) seems to be appropriate.

- Especially faint meteors should be investigated.

- Therefore meteor video observations with high sensitivity, high resolution and wide field camera-lens-systems are required.

- Parallel or sequential multi- or single-camera observations with different ND filters can avoid the detection threshold problem.

Figure 8 – Project SCAMPI 2.0: Professional digital film camera ARRI Alexa Mini with high speed film lens Zeiss Superspeed 1.3/18mm and a fast liquid crystal element in the lens mount synchronized with the sensor output.

Acknowledgements

- Bernd Gährken for his support with the 4CAMPI and 3CAMPI observations.
- Sirko Molau for his support with the data analysis and his ideas for SCAMPI.
- Felix Bettonville for his valuable input.

References

Rendtel J. and Arlt R. (2017). “Handbook for visual meteor observers”. *IMO*.

Richter J. (2018). “About the mass and magnitude distributions of meteor showers”. *WGN, Journal of the International Meteor Organization*, **46**, 34–38.

Slansky P. C. (2016). “Meteor film recording with digital film cameras with large cmos sensors”. *WGN, Journal of the International Meteor Organization*, **44**, 190–197.

Slansky P. C. (2018). “The efficiency of cameras for video meteor observation-a theoretical contribution and a practical comparison between the watec 120n+ and the sony alpha7s”. *WGN, Journal of the International Meteor Organization*, **46**, 24–29.

Numerical simulation of meteors as a means of debiasing AMOS data

Martin Baláž[1], Juraj Tóth[1]

[1] Comenius University in Bratislava, Mlynská dolina, 84248 Bratislava, Slovakia
martin.balaz@fmph.uniba.sk and toth@fmph.uniba.sk

Deployment of multi-station video meteor networks presents a unique opportunity to measure the total mass flux of meteoroids impinging on the surface of the Earth. However, direct measurement of particle flux is not possible as the data from Earth-based camera are invariably distorted by selection bias. We present a method for debiasing the data using a simulation of meteoroid particles entering the atmosphere. The trajectory of each virtual meteoroid is tracked and after application of bias sources the resulting meteor observation is recorded. Once a sufficiently large dataset is obtained, statistical tests are performed and the distributions are compared to observational data from the AMOS camera network. The entire procedure is repeated and the parameters of the simulation are gradually adjusted until the best possible agreement with observational data is found. Meteoroid flux is then determined directly from the simulation with the determined optimal values of parameters.

Introduction

This submission is a comprehensible summary of the methods used and results obtained in the master's thesis, "Determination of Total Meteoroid Flux in Millimetre to Metre Size Range" (Balaz, 2018). The primary purpose of the thesis was the determination of total number and density of meteoroid particles in the 2016 Perseid meteor shower, using data from the AMOS all-sky camera network in Slovakia. We outlined two possible approaches to the problem: a sequential approach, based on application of correction procedures to the observational dataset; and a numerical simulation of the entire meteoroid population and its comparison to observational data. Tests showed that the second approach was more effective, and was thus investigated in more detail.

The entire virtual population of meteoroids is created and their atmospheric entry is simulated. All considered sources of selection bias are applied to the dataset. Projections of the meteors are then calculated as they would be observed by a virtual ground station of the AMOS camera network, located at the exact same position as the real camera. The resulting dataset is evaluated and tested statistically. The same statistics are calculated for the data obtained from real-world AMOS observations and compared. Simulation parameters are then adjusted and the whole dataset is re-generated repeatedly until the best possible agreement with observational data is found.

Numerical simulations have been used regularly in meteor research, such as tools developed by Gural (2002) and Hill, Rogers & Hawkes (2005). However, to date, we have no knowledge of statistical processing of large virtual datasets or about attempts to estimate the true distribution and count of meteoroid particles using simulations.

Motivation

While data collected by AMOS are not particularly precise when compared to those recorded by high-resolution photographic cameras, high sensitivity of the system and the long-term nature of its operation result in a large database of meteor records that can be used for statistical analyses. Such extensive datasets are well suited for a multitude of tasks, such as identification of less prominent meteor showers or the determination of the total flux of meteoroid particles impinging on the surface of the Earth. These tasks are often much more difficult to accomplish using traditional methods.

The system is able to detect meteors with apparent magnitude down to 5^{m}, although detection efficiency at these magnitudes is quite low. While there is no practical upper limit on brightness, very bright meteors are observed infrequently and thus are not suitable for statistical analyses.

1 Theoretical foundations

Development of a numerical simulation requires understanding of the physics of meteor flight in the upper atmosphere. In the simulation we use the standard single-body model of meteor atmospheric flight conceived by Whipple (1938) and Öpik (1958).

The version used in the simulation is one of the simplest suitable models and should not be used for high-precision calculations, such as simulation of the dark flight of meteorites or for precise determination of heliocentric orbits. Effects of fragmentation, heterogeneity of particles, and variations in chemical composition and physical properties are also not taken into account.

1.1 Equations of motion

The motion of the meteoroid particle in the atmosphere is described by the following *equations of motion*. This set of interdependent differential equations must be solved numerically. We assume that each meteoroid particle always moves in a straight line and is only subject to deceleration caused by aerodynamic drag. We may express a small change in velocity as

$$\mathrm{d}v = -\frac{\Gamma A \rho_{\mathrm{air}} v^2}{m^{1/3} \rho^{2/3}} \mathrm{d}t, \tag{1}$$

where

- m is the mass of the meteoroid particle (kg),
- ρ is the density of the particle ($\mathrm{kg\,m^{-2}}$),
- A is the coefficient of shape (dimensionless),
- S is the cross-sectional area of the particle in the plane perpendicular to its velocity vector ($\mathrm{m^2}$),
- v is its speed relative to the air ($\mathrm{m\,s^{-1}}$).

In the model we assume that all available kinetic energy is converted to thermal energy and used to evaporate the material of the particle. This approximation is justified as long as the heat of vaporisation of meteoroid material is much greater than the thermal capacity of surrounding air. Again, for the numerical simulation we need to isolate the change of mass dm in a small time interval dt:

$$\mathrm{d}m = -\frac{\Lambda}{2Q} \frac{A m^{2/3}}{\rho^{2/3}} \rho_{\mathrm{air}} v^3 \mathrm{d}t, \tag{2}$$

where

- Λ is the heat transfer coefficient (dimensionless);
- Q is the specific enthalpy of vaporisation of meteoroid material ($\mathrm{J\,kg^{-1}} \equiv \mathrm{m^2\,s^{-2}}$).

To determine the apparent brightness of a simulated meteor, its absolute luminous power F_0 must be calculated first. For the sake of simplicity we assume a constant fraction of the total released energy is emitted as visible light. From equation 2 we obtain

$$F_0 = \tau(v) \frac{\Lambda}{4Q} \frac{A m^{2/3}}{\rho^{2/3}} \rho_{\mathrm{air}} v^5. \tag{3}$$

where

$$\tau = \frac{2\epsilon\zeta}{\mu v^2} \tag{4}$$

is the *luminous efficiency factor*. Jones and Halliday (2001) defined the excitation coefficient ζ, which represents the sum of all excitation probabilities over collisions. For estimation of ζ we used a slightly improved version of the model compiled by Hill (2005). ϵ here represents the mean excitation energy and μ is the mean atomic mass.

2 Algorithm

Next, we describe the initialisation and the used algorithm in detail.

2.1 Generating the meteoroids

The first step of the simulation is to create the initial population of meteoroid particles entering the atmosphere. At this point, we pretend we know anything about observers and are only concerned with physical representations of virtual meteoroid objects.

The particles are generated in an area centered on the camera, whose dimensions are large enough that the entire observable portion of the sky is covered. For our purposes, we defined the observable area to include all points with altitudes above 15°, and only evaluated this area in both simulation outputs and observational data. The number of entering meteoroids is also modulated by the so-called *radiant discriminator*. Each generated particle is accepted for further stages of the chain with probability $p = \sin\theta$, where θ denotes the altitude of the radiant at the time of entry.

Next, each particle is assigned its initial velocity. For a meteor shower, this is represented by a constant vector with respect to the non-rotating frame, moving with the Earth, represented by declination δ, right ascension α, and speed v_0. For the 2016 Perseids, we used constant values $\delta = 56°$, $\alpha = 43°$, and $v_0 = 59\,\mathrm{km\,s^{-1}}$. This vector is then transformed to the ECEF[1] reference frame.

2.2 Atmospheric entry

Once the initial position and velocity are set, atmospheric entry may be simulated and recorded. We obtain the position of the particle by numerically solving the equations 1 and 2 and express its apparent magnitude from equation 3, taking distance and atmospheric attenuation into account. Since long-term stability and conservation of energy are not as important as short computation times here, a fast custom-written Runge-Kutta solver was chosen to solve the equations.

The entire state of the meteoroid is captured multiple times per second. The frequency of snapshots was chosen to match the frame rate of real AMOS cameras, which is 15 frames per second. This does not necessarily equal the time step taken by the integrators, as multiple small steps may be taken between two successive frames. In practice, we found that precision of the RK4 integrator does not improve noticeably for time steps less than 1/150 of a second and hence we used this value.

2.3 Processing the observations

In the next step, each meteoroid is *observed* – its projection on the sky is computed for each of the observing

[1]Earth-centered, Earth-fixed

stations, along with its apparent luminosity and other important properties as observed in each frame. Only the brightest frame of each meteor is considered in the evaluation step.

Natural effects, such as distance or atmospheric extinction, are applied first. Then apparent position and magnitude are computed, and finally we need to simulate the instrumental effects, introduced by the detection apparatus. So far, we only considered two physical quantities that may affect the detection ability, the *apparent magnitude* of the meteor and its *altitude* above the local horizon. Each bias source is described by a single *detection probability function* (DPF), representing the probability of a successful detection.

We assumed a sigmoid profile of the magnitude DPF

$$D(m; m_0, \omega, f) = \frac{f}{1 + e^{\frac{m - m_0}{\omega}}}, \tag{5}$$

where

- m_0 is the limiting magnitude, defined as brightness where detection efficiency is equal to one half of its maximum.
- ω denotes the width of the distribution. Small values correspond to a sharp detection efficiency falloff near the limiting magnitude.
- f is the *fill factor*: the upper limit of the system's detection ability. Random occurrences, such as software bugs or power outages may prevent successful detection even with very bright meteors. Based on an analysis of photographic data collected at the same location as one of the AMOS cameras, we used a value of 0.93.

For the altitudinal DPF we considered a class of functions in the form

$$A(\theta; \alpha) = (\sin\theta)^{\alpha} \tag{6}$$

with a single parameter $\alpha > 0$, where higher values represent a steeper detection efficiency loss at lower altitudes. We assumed the functions to be independent, in which case the probability of detection is determined by the product of partial probabilities.

2.4 Simulation run

A population of 100 000 Perseids was generated, with masses sampled from a modified Pareto distribution, effectively yielding a constant mass index $s = 1.8$ and a lower particle mass limit of 5×10^{-6} kg, corresponding to an absolute magnitude of about $+5^{\mathrm{m}}$. After applying the radiant-altitude discriminator (see section 2), approximately 65000 particles were allowed to enter the atmosphere. After calculating magnitude data, we obtained a virtual composite image, such as that displayed in Figure 1. The same dataset, but with only the brightest frame of each meteor shown, is displayed in Figure 2.

Figure 1 – A sample dataset of 2016 Perseids. Darker colors denote higher apparent angular speeds. Apparent magnitude is represented by dot size.

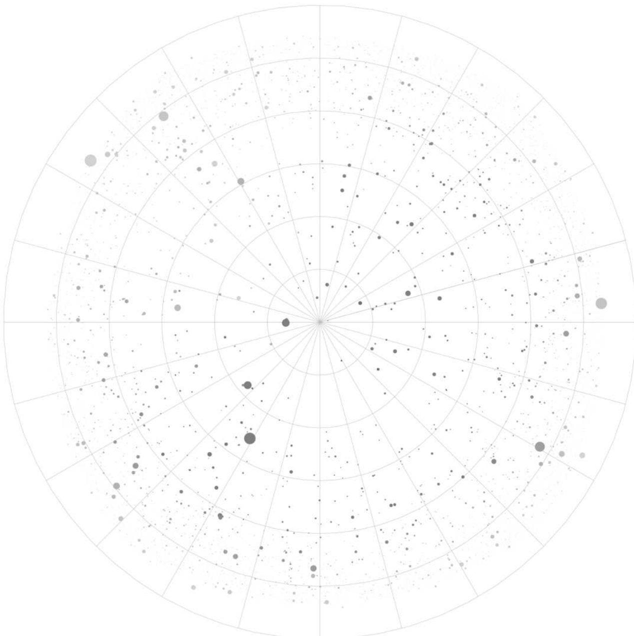

Figure 2 – The same dataset with only the brightest frame of each meteor displayed.

2.5 Determination of parameters

Next, an exhaustive search of the parameter space for m_0, ω and α was performed and optimal values were found. Each time, a new DPF was applied to the dataset in order to determine which meteors were visible to the camera. Then a normalized histogram of data was constructed for both magnitudes and altitudes and compared to a similar histogram, constructed from observational data, using a simple χ^2-test (Press et al., 1992). The χ^2 value is always between 0 and 2, with 0 indicating equal distributions and 2 signaling a perfect disagreement, i.e. no bin having non-zero values in both distributions.

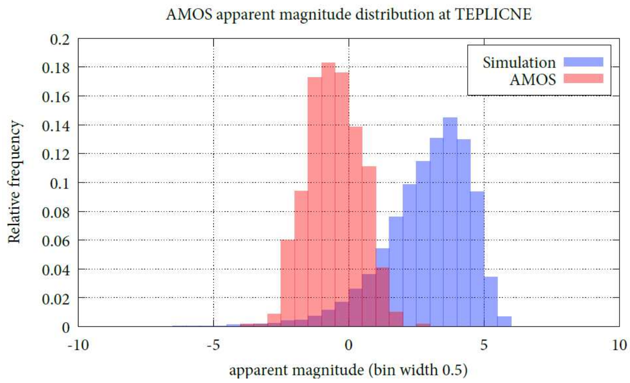

Figure 3 – A comparison of magnitude histograms for simulation and AMOS data with no observational bias applied, i.e. a perfect observer. Most dim meteors would not be seen by a real camera. The match is visibly bad ($\chi^2 \approx 1.6$).

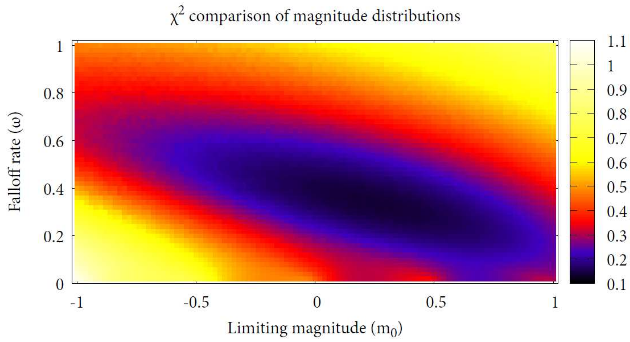

Figure 4 – A goodness-of-fit heatmap for parameter m_0 and ω. Darker values indicate a better fit. Using the centroid method,we determined the optimal values of the parameters to be $m_0 = +0.4, \omega = 0.35$.

A perfect observer, not subject to any selection bias ($m_0 \to +\infty$), would necessarily observe much dimmer meteors than AMOS, as seen in Figure 3. In reality, the number of particles would continue to grow for higher magnitudes. However, none of the meteors dimmer than about 5^{m} can be observed, so they were not included in the simulation. The χ^2 value for this pair of histograms is approximately 1.6, indicating a very poor fit.

After evaluating each combination of parameters ($-1 \leq m_0 \leq 1$, $0 < \omega \leq 1$, both varied with step 0.02) we may plot the results in a heatmap (see Figure 4). Since the method used is inherently stochastic and subject to random noise, the optimum cannot be determined by taking the single lowest value. The centroid method was used to determine the optimal combination of parameters, $m_0 = +0.4$ and $\omega = 0.35$. The corresponding histogram is shown in Figure 5.

We repeated the procedure for the altitudinal DPF and its parameter α and found the optimal value to be $\alpha \approx 0.4$. The optimal detection probability function is thus

$$P(m, \theta) = \frac{0.93}{1 + e^{\frac{m-0.4}{0.35}}} \cdot (\sin\theta)^{0.4}. \tag{7}$$

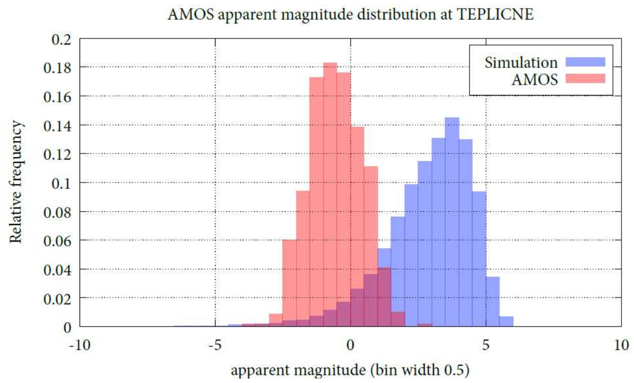

Figure 5 – The comparison histogram with $s = 1.8$ and optimal DPF parameters applied. The agreement between observation and simulation is significantly better ($\chi^2 \approx 0.18$).

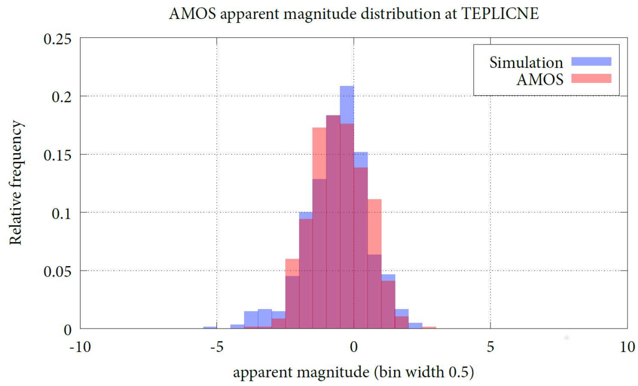

Figure 6 – The comparison histogram for $s = 2.15$, with optimal DPF parameters applied. From the heatmap (not displayed)we deduced the optimal values to be $m_0 = -0.17$ and $\omega = 0.36$, yielding $\chi^2 \approx 0.053$.

2.6 Mass index

Even the best combination of parameters is unable to reproduce the distribution well. In Figure 5 we see there are too many meteors brighter than -4^{m}. The natural reaction to this is to increase the assumed mass index. After running the entire simulation repeatedly with various values of s and performing the exhaustive search procedure in each dataset, we concluded that mass index $s = 1.8$ is indeed too low and it is not possible to reproduce the observations with this value. After retrying with various values of s, the best agreement with observational data was found with $s = 2.15$, as is shown in Figure 6. The corresponding search of parameter space showed that for $s = 2.15$ the values of parameters m_0, ω and α should be adjusted slightly, to $m_0 = -0.17$, $\omega = 0.36$ and $\alpha = 0.25$.

3 Results and future work

Having established the values of the parameters, we may calculate the total flux by simply counting the number of meteors in the simulation and reducing the value to a million square kilometres per hour. For the mass flux, we multiply this value by the average mass of a particle. When all particles with mass larger than 3.25×10^{-7} kg – which corresponds to a diameter of at least 1 mm –

were included, we arrived at a value of about 135 000 particles per million square kilometres per hour, with a total mass of 0.338 kg. The number density of meteoroid particles in free space equals 1.58×10^{-3} kg per every 10^9 km^3.

These findings are roughly consistent with values provided by other researchers, although our methods at this time do not allow for direct comparison. Our best estimate for particles observable by AMOS, 5830 per 1 000 000 km^2 per hour, is roughly consistent with value of 4215 reported by Blaauw, Campbell-Brown & Kingery (2016). Values published by `MeteorFlux.io` range from about 28 000 to 47 000 per 1 000 000 km^2 h, compared to our result of 135 000. Again, the discrepancy can be mostly explained by the fact we also included meteors whose absolute magnitude would be above +6.5. A method that would enable us to compare the data directly is currently under development.

3.1 Mass index

The most prominent issue is the disagreement in mass index. The output of the simulation was not consistent with the observational dataset for any value of $s < 2$, with best match obtained for $s = 2.15$. This finding is not consistent with data provided by other researchers. Both Hughes (1995) and Krisciunas (1980) give values close to 1.85, while Belkovich and Ishmukhametova (2006) lowered this number even further to about 1.7. There are two possible explanations:

- There is a problem with the simulation. While we are convinced the simulation and its evaluation are working as expected, uncertainties in the values of material constants, luminous efficiency factor τ and other variables in the model are currently too large. However, preliminary model validation by simulation of well-measured Perseid meteors Spurný (2014) shows that the simulation is able to reproduce observed data with high accuracy.
- The commonly reported values of mass index for Perseids may actually be understated. Most visual observations treat the limiting magnitude as a threshold and consider all meteors brighter than this threshold to be reliably detected. If such data were used to determine the mass index without further corrections, the number of dim meteors would invariably be underestimated, which would lead to a lower value of s.

4 Conclusion and future plans

While the final values of flux and density are not conclusive, we believe the presented method has a great potential to improve the precision of calibration of camera systems and evaluation of meteor observations and as such is worth further investigation. The simulation can be easily adapted to any all-sky or narrow-field camera with little modification. The source code of the reference implementation will be released on GitHub.

Acknowledgments

This work has been supported by the special stipendium provided by FMPH CU (October 2017). Special thanks belong to RNDr. Peter Vereš, PhD., for suggesting the simulation as an effective means of debiasing observational data. We gratefully acknowledge the support of NVIDIA Corporation with the donation of the Titan Xp GPU used for this research.

References

Baláž M. (2018), "Determination of total meteoroid flux in millimetre to metre size range." Master Thesis, Comenius University in Bratislava.

Bel'kovich O.I. and Ishmukhametova M.G. (2006), "Mass distribution of Perseid meteoroids". *Solar System Research*, **40**, 208–213, doi = 10.1134/S003809460603004X.

Blaauw R.C., Campbell-Brown M. and Kingery A. (2016), "Optical meteor fluxes and application to the 2015 Perseids". *Monthly Notices of the Royal Astronomical Society*, **463**, 441–448

Gural P. (2002), " Meteor observation simulation tool". *Proceedings of the International Meteor Conference 2001, Cerkno, Slovenia*, 29–35.

Hill K.A., Rogers L.A. and Hawkes R.L. (2005), "High geocentric velocity meteor ablation". *Astronomy & Astrophysics*, **444**, 615–624, doi = 10.1051/0004-6361:20053053.

Hughes D.W. (1995), "The Perseid meteor shower". *Earth, Moon and Planets*, **68**, 31–70, doi = 10.1007/BF00671498.

Jones W. and Halliday I. (2001), "Effects of excitation and ionization in meteor trains". *Monthly Notices of the Royal Astronomical Society*, **320**, 417–423.

Krisciunas K. (1980), "The luminosity functions of the 1969 Perseid and Orionid meteor showers". *Icarus*, **43**, 381–384, doi = 10.1016/0019-1035(80)90182-7.

Molau S. and Barentsen G. (2018), `http://meteorflux.io/`.

Öpik E.J. (1958), "Physics of meteor flight in the atmosphere". `https://doi.org/10.1002/qj.49708536526`, Interscience Publishers.

Press W.H., Flannery B.P., Teukolsky S.A. and Vetterling W.T. (1992), "Numerical Recipes in C: The Art of Scientific Computing". Cambridge University Press, New York, NY, USA, ISBN 0-521-43108-5.

Spurný P. et al. (2014), "Bright Perseid fireball with exceptional beginning height of 170 km observed by different techniques". *Astronomy & Astrophysics*, **563**, A64.

Whipple F.L. (1938), "Photographic meteor studies I". *Proceedings of the American Philosophical Society*, **79**, 499–548.

New spectroscopic program of the European Fireball Network

Jiří Borovička[1], Pavel Spurný[1], and Lukáš Shrbený[1]

[1] **Astronomical Institute of the Czech Academy of Sciences, 25165 Ondřejov, Czech Republic**
jiri.borovicka/pavel.spurny/lukas.shrbeny@asu.cas.cz

Spectroscopic observation within the European Fireball Network has recently been extended by constructing the Spectral Digital Autonomous Fireball Observatory (SDAFO). This device contains two Canon EOS 6D DSLR cameras equipped with Sigma 15mm lenses and holographic transmission gratings with 1000 grooves/mm. SDAFOs are currently installed at six stations and provide spectra of fireballs brighter than magnitude −7 in the wavelength range 380–900 nm with dispersion 0.4 nm/pixel. Thanks to 14 bit depth and the linear response of the detector, precise spectral measurements are possible, especially for fireballs brighter than −10 mag. Additional survey spectra of distant fireballs seen low above the horizon are provided by Supplementary Video Arrays installed at two stations.

1 Introduction

In 1960, a program of high resolution photographic spectroscopy of fireballs was started at the Ondřejov Observatory in Czech Republic (then Czechoslovakia). Six Tessar cameras with focal ratio 1:4.5 and focal length 360 mm were used. A nice spectrum of a fireball flare was captured in high spectral orders during the first night of observation on September 13, 1960 (Ceplecha and Rajchl 1963). At the beginning, two cameras were equipped with transmission objective gratings and four with prisms. Photographic plates of size 18 × 24 cm were used as a recording medium. Single rotating shutter producing 15 breaks per second covered all cameras.

This program is still ongoing and has therefore been run uninterrupted for 58 years. Only minor changes to the cameras were made, most notably all prisms were replaced by gratings. Glass plates, which became unavailable in the 1990's, had to be replaced by sheet films. The cameras were also moved to a new location and reconfigured in 2006. They are the only remaining manually operated fireball cameras at the Ondřejov Observatory and in the whole European Fireball Network. Figure 1 shows the current configuration. Over the years, a number of unique spectra were obtained and analysed – e.g. (Ceplecha 1967; Ceplecha 1971; Borovička 1993) – including the extremely rich spectrum of the Benešov superbolide and meteorite fall (Borovička and Spurný 1996).

Although film cameras are capable of recording excellent spectra with unprecedented resolution, their efficiency is generally low. The cameras are located at only one station and all together cover only part of the sky between elevations $\sim 35 - 60^\circ$ above horizon. Although very bright fireballs can produce high order spectra if they are closer to the horizon and thus farther from the station, in general spectra of fireballs in distances 30 – 70 km from Ondřejov can be captured (the range, of course, depends on fireball height; the given range is for

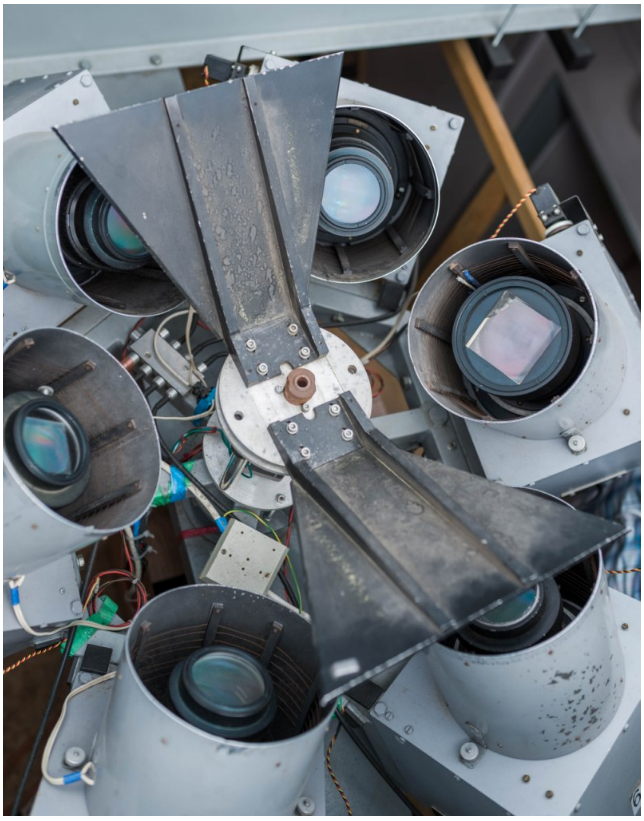

Figure 1 – Battery of six large format photographic film spectral cameras in Ondřejov.

a medium height of 50 km). The cameras are operated on moonless nights with no or little clouds. As a result, only few spectra are obtained in a typical year. It takes several years to capture a really nice spectrum.

Several years ago a new Digital Autonomous Fireball Observatory (DAFO) was developed and started to be deployed on the stations of the European Fireball Network (Spurný et al. 2017). These all-sky systems based on digital still cameras are now used on 14 stations in the Czech Republic, three in Slovakia, and one in Aus-

Figure 2 – Spectral Digital Autonomous Fireball Observatory (SDAFO) and Digital Autonomous Fireball Observatory (DAFO) with lens covers open at the Ondřejov Observatory. Several cameras of the Supplementary Video Array can be seen to the right of DAFO.

tria. They provide trajectories, velocities, orbits, and light curves of fireballs over a large area of central Europe. Since the Ondřejov spectral cameras provide spectra for only a minuscule fraction of fireballs observed by the network, it was decided to develop a spectral version of the cameras (SDAFO), which could be installed at selected stations of the network. In this contribution we describe the SDAFO and its performance. In addition we provide information about the cameras of the Supplementary Video Arrays installed at two stations, which were also equipped with spectral gratings.

2 Spectral Digital Autonomous Fireball Observatory (SDAFO)

SDAFO is a modification of DAFO designed for spectral observations of bright fireballs. Both observatories are shown in Figure 2. In both cases the imaging part consists of two DSLR cameras: the Canon EOS 6D. These commercial cameras contain full frame (35.8×23.9 mm) CMOS sensors with 5472×3648 pixels and a dynamic range of 14 bits per color. For SDAFO the IR cut filters were removed from inside the camera in order to exploit full spectral sensitivity range of the sensors. SDAFO uses Sigma 15mm F2.8 EX DG Diagonal Fisheye lenses. They provide almost two times higher spectral resolution than the Sigma 8mm F3.5 Fisheye used by DAFO. On the other hand, the field of view is smaller.

Figure 3 shows schematically the field of views of both SDAFO cameras. One camera is oriented in the east-west direction and one in the north-south direction. The sky around the zenith, up to zenith distances of about 45°, is covered by both cameras. Most of the sky

Figure 3 – DAFO all-sky image from station Polom containing a fireball and the Moon. Field of views of two SDAFO cameras are shown schematically as black rectangles. North is on the top, east is on the left.

up to zenith distances of about 70° is covered by at least one of the cameras. Plastic holographic gratings with 1000 grooves per mm are mounted in front of the lenses. The gratings are oriented in such a way that spectral dispersion is parallel with the longer side of the image.

Figure 4 shows the spectrum of the fireball from Figure 3 as captured with the SDAFO east-west oriented camera. Here the direction of dispersion was perpendicular to the direction of flight of the fireball (which

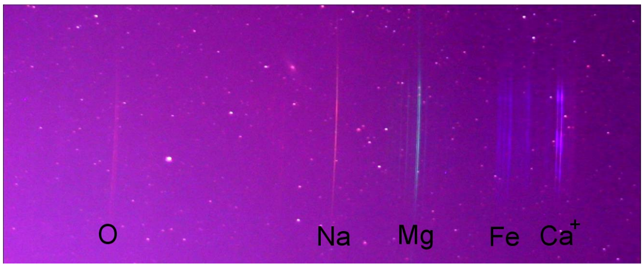

Figure 4 – Spectrum of the fireball from Figure 3 obtained with the SDAFO east-west camera. Atoms and ions responsible for the most important spectral lines are identified. Wavelengths increase from right to left. North is on the top, east is on the left. The brightest star in the background is β Andromedae. The fireball (code EN040818_014525) was a Southern δ Aquariid with maximum absolute magnitude -9.6.

moved from south to north). This was the ideal situation when the best spectral resolution is achieved. The dispersion is 0.4 nm/pixel and lines $\sim$1.5 nm apart can be resolved in the green part of the spectrum where the focus is best. On the other hand, the dispersion was parallel with the direction of the fireball flight in the north-south oriented camera, all lines overlapped, and the spectrum was not usable.

The parallel run of both cameras ensures that for fireballs high above the horizon at least one camera captures the spectrum with a sufficiently large angle between the fireball path and the direction of dispersion. The only exception is the readout time period of one of the cameras. The cameras take images every 30 seconds. The exposure length is 28.3 s and 1.7 s is the readout time. The readout periods alternate between cameras as shown in Figure 5, so that at any time at least one camera is working (provided the weather is good).

Relatively low ISO speeds, from 100 to 500, depending on Moon phase and twilight conditions, are used to keep the background sky signal low and leave enough dynamic range for the spectra. In contrast to DAFO, no LCD shutter is used in SDAFO. The transmittance of the LCD shutter in the open phase is only 30%, so it would consume a lot of light. The disadvantage is that the spectrum of the meteor wake cannot be separated from the head spectrum. The holographic grating has low efficiency in comparison with blazed gratings used in classical film cameras. However, blazed gratings larger than 50 mm are difficult to get and SDAFOs are primarily intended for spectroscopy of bright fireballs, brighter than -10 mag. Such fireballs are saturated in existing video surveys such as SMART (Madiedo 2017) or AMOS (Rudawska et al. 2016), which have higher sensitivity and low dynamic range. The advantage of holographic grating is their symmetry. The quality of the spectrum does not depend on which side of the field the fireball appears.

The sensitivity of SDAFO depends on the wavelength and on the position of the fireball in the sky. Roughly speaking, at least one spectral line can be expected to be captured for fireballs of magnitude -7 and brighter appearing 45° above the horizon or more. Figure 6 shows relative spectral sensitivities of SDAFO, film cameras, and cameras of the Supplementary Video Array (SVA). By comparing commonly detected spectra, it was found that film cameras (thanks to their large aperture and efficient grating) are markedly more sensitive in the blue part of the spectrum than SDAFO. In the green region around the Mg line, SDAFO is more sensitive. Film has better sensitivity again in the yellow part around the Na line but is not sensitive at all in the infrared. The red sensitivity around the Hα line depends on the particular emulsion. The SDAFO with IR cut filter removed has reasonable sensitivity in red and infrared up to 880 nm. The cameras of the SVA have higher sensitivity than SDAFO in the infrared and slightly higher in green but their sensitivity drops rapidly below 480 nm. Note that the sensitivity in the infrared part is modulated by atmospheric absorptions by O_2 and H_2O.

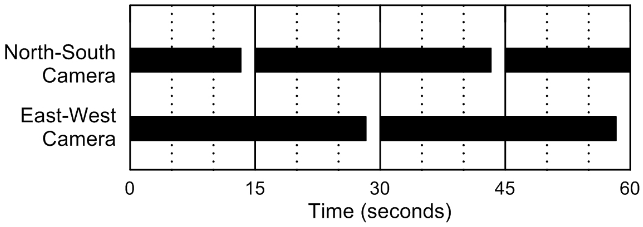

Figure 5 – Exposure pattern of SDAFO during a typical minute. Each exposure (black band) is followed by a brief readout period (blank), which is shifted by 15 seconds between cameras.

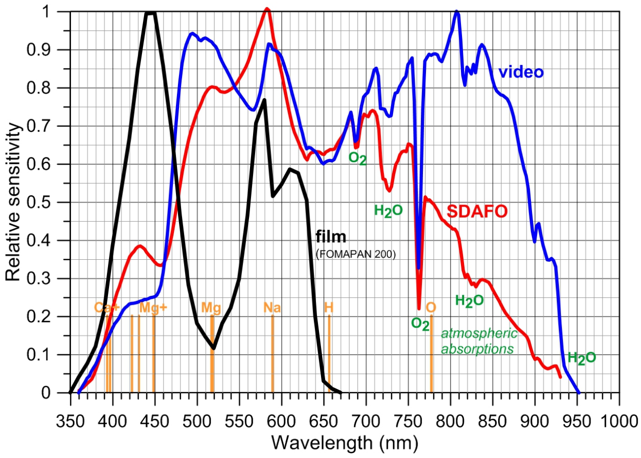

Figure 6 – Estimated relative sensitivities of SDAFO, SVA cameras, and classical film cameras, normalized to unity at maximum. The functions were obtained by measuring spectra of the Moon and stars. They include the influence of the sensor, camera lenses, grating, and atmospheric absorptions. The positions of atmospheric absorption bands and important meteor spectral lines are indicated.

The vignetting of the Sigma 15mm lens was measured at room conditions without a grating. As shown in Figure 7, the signal at the edge of the field (18 mm from the center of the sensor) is only about 30% of that in the center Nevertheless, thanks to the grating, spectra can be obtained for very bright fireballs (magnitude about -15) even if they are outside the field of view close to the horizon.

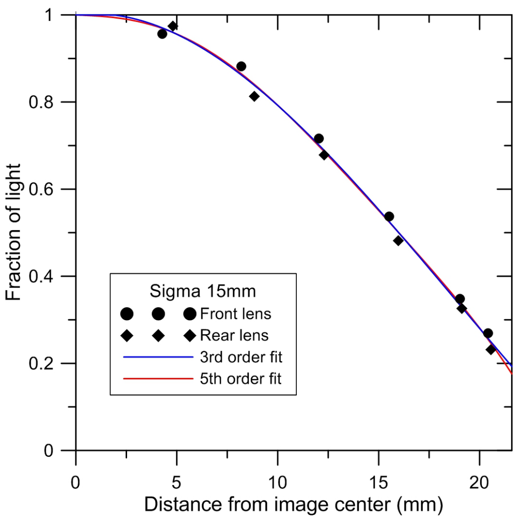

Figure 7 – Measured vignettation of the Sigma 15mm F2.8 EX DG Diagonal Fisheye lens.

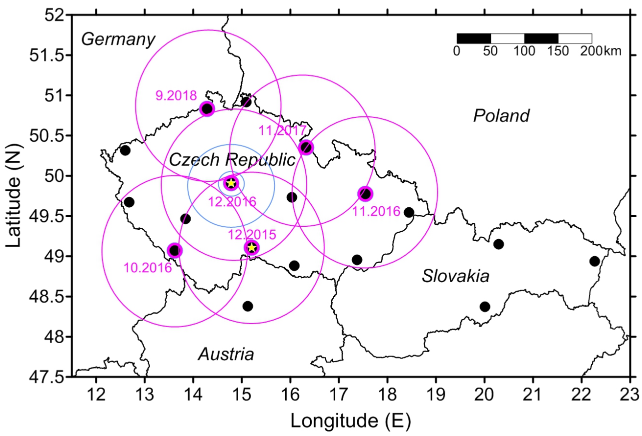

Figure 8 – Geographic coverage of spectral observations. Black dots are the locations of DAFOs and larger magenta dots are locations of SDAFOs. The labels show the month and year of SDAFO installation. Yellow stars mark the stations where SVAs are installed. Magenta circles show schematically the geographical coverage of each SDAFO. The geographical coverage of classical film cameras is between the two blue circles. Situation in September 2018.

Stations without local lights are preferred for SDAFO installation since any bright artificial light on the horizon will produce a spectrum in the field of view. The first SDAFO was permanently installed (after being tested in Ondřejov) at the Kunžak station in December 2015. Currently, SDAFOs are deployed at six stations and cover almost the whole territory of the Czech Republic plus some neighbouring regions (Figure 8). Very bright fireballs can produce spectra even if they are farther away. In any case the coverage is much larger than for film cameras.

As for DAFO, SDAFO have an internal computer with a prescribed observation schedule. The computer clock is controlled by a GPS receiver. Observations are planned when the Sun is more than 8 degrees below the horizon. Cloudiness and precipitation are continuously monitored by the Aurora Cloud Sensor by Aurora Eurotech. Observations are not started or are suspended in the case of mostly cloudy sky or rain. All images are written to a local hard disk in Large Fine JPEG and RAW formats. When a fireball is found in DAFO images, corresponding SDAFO images are downloaded to a central server in Ondřejov.

3 Supplementary Video Arrays (SVA)

The first cameras of the Supplementary Video Arrays were installed in Ondřejov in Summer 2016. The camera type is Dahua IPC-HFW4421E, which provides 20 frames per second in resolution 2688×1520 pixels. Lenses with 6 mm focal length are used providing a field of view of 56×32 degrees. Seven cameras cover the sky around the local horizon. In June 2017, another 6 cameras were added to cover the sky up to an elevation of $\sim 60°$. In November 2017, seven cameras were installed in Kunžak.

The primary aim of SVA is to image individual fireball fragments, which cannot be seen in long exposure all-sky DAFO images. Video cameras also enable velocity measurements for fireballs with an angular speed too low to produce shutter breaks in DAFO images – typically very distant slow fireballs. To gain even more information from them, the cameras were equipped with the same holographic gratings with 1000 grooves/mm as SDAFO. Since the gratings consume only negligible amount of direct light, fragmentation and velocity measurements are not hindered. Spectra can be obtained for bright fireballs. The sensitivity (except the blue part) is somewhat better than for SDAFO located at the same station. The dispersion is also slightly higher (0.34 nm/pixel). On the other hand, video cameras have a dynamic range of only 8 bits and have a non-linear response. They are therefore good to reveal major differences between fireball spectra but a SDAFO spectrum is needed for precise work.

SVAs are working independently on weather and also during daytime. The whole system is based on a commercial security camera system. Video data are continuously recorded using MJPEG codec by a common recorder and are being overwritten after about 8 days. Fireball data must therefore be downloaded and stored manually within this period. There is no automatic fireball search. Fireballs observed by DAFOs or known from other sources (e.g. visual reports) are searched manually.

4 Summary and future work

Spectral Digital Autonomous Fireball Observatories are now successfully providing medium resolution spectroscopic data for bright fireballs observed by the European Fireball Network above the Czech Republic and surrounding regions. In total, spectra of 140 fireballs containing at least one spectral line have been obtained by them as of August 2018. The system is primarily intended for fireballs brighter than magnitude −10, which provide multi-line spectra. Among the most important spectra obtained so far is the spectrum of the Stubenberg meteorite fall of March 6, 2016. Analytical tools for detailed analysis of the spectra are in development. Compared to classical film cameras, the main advantages are much larger temporal and geographical coverage and the sensitivity in infrared. SDAFOs can work during moonlit nights, during partly cloudy nights as well as during twilight. They are currently installed on six stations and further extension is planned. Classical film cameras are still in operation, mainly because they provide nearly ten times higher spectral resolution than SDAFOs.

Supplementary video arrays are now installed at two stations and provide comparable or even a slightly higher number of spectra than SDAFOs. Part of them are common detections with SDAFOs but SVAs also get spectra of distant bright fireballs seen low above the horizon. These spectra can be used to recognize meteoroids with unusual (non-chondritic) composition such as irons, achondrites, or meteoroids depleted in sodium. Higher photometric precision of SDAFO will enable us to reveal finer differences in chemical composition and to study physical processes during meteoroid ablation.

Acknowledgement

This work was supported by project No. 16-00761S from GAČR and by Praemium Academiae of the Czech Academy of Sciences.

References

Borovička J. (1993) A fireball spectrum analysis, *Astronomy and Astrophysics*, 279, 627–645.

Borovička J., and Spurný P. (1996) Radiation study of two very bright terrestrial bolides and an application to the comet S-L 9 collision with Jupiter, *Icarus*, 121, 484–510.

Ceplecha Z., and Rajchl J. (1963) The meteor spectrum with dispersion from 11 to 38 Å/mm, *Bulletin of the Astronomical Institutes of Czechoslovakia*, 14, 29–48.

Ceplecha Z. (1967) Spectroscopic analysis of iron meteoroid radiation, *Bulletin of the Astronomical Institutes of Czechoslovakia*, 18, 303–310.

Ceplecha Z. (1971) Spectral data on terminal flare and wake of double-station meteor No. 38421 (Ondřejov, April 21, 1963), *Bulletin of the Astronomical Institutes of Czechoslovakia*, 22, 219–304.

Madiedo J. M. (2017) Automated systems for the analysis of meteor spectra: The SMART Project, *Planetary and Space Science*, 143, 238–244.

Rudawska R., Tóth J., Kalmančok D., Zigo P., and Matlovič P. (2016) Meteor spectra from AMOS video system, *Planetary and Space Science*, 123, 25–32.

Spurný P., Borovička J., Mucke H., and Svoreň J. (2017) Discovery of a new branch of the Taurid meteoroid stream as a real source of potentially hazardous bodies, *Astronomy and Astrophysics*, 605, A68.

Which trajectory solver is best for your optical meteor data? Algorithm implications for radiant and orbit accuracy

Denis Vida[1], Peter Gural[2], Peter Brown[3], Margaret Campbell-Brown[3], Paul Wiegert[3]

[1] **Department of Earth Sciences, University of Western Ontario, London, Ontario, N6A 5B7, Canada**
`dvida@uwo.ca`

[2] **Gural Software and Analysis LLC, Sterling, Virginia, 20164 USA**
`pgural@gmail.com`

[3] **Department of Physics and Astronomy, University of Western Ontario, London, Ontario, N6A 3K7, Canada**
`pbrown@uwo.ca` and `margaret.campbell@uwo.ca` and `pwiegert@uwo.ca`

The Canadian Automated Meteor Observatory (CAMO) is an electro-optical meteor observation system which uses a wide-field high speed camera to cue a pair of mirrors to track meteors in real time. The mirrors redirect the meteor light through a telescope which gives a very detailed view of the morphology of the meteor, as well as high precision position measurements. It was recently demonstrated that existing methods of meteor trajectory estimation are inaccurate when high-precision data like these are used. In this work we seek to find the optimal method by simulating three types of optical meteor observation systems and investigating how known values of meteor radiant and speed used in simulations compare to estimated values. We also develop a novel method of meteor trajectory estimation and demonstrate that it is superior to all other currently known methods when applied to CAMO data. This paper only gives a high-level overview of the methods, while a more thorough description will be published in a future paper.

1 Introduction

Schiaparelli & von Boguslawski (1871) were the first to demonstrate the connection between meteor showers and comets by computing meteor orbits from multi-station observations. Their method consisted of drawing meteor trails on a globe or a map in gnomonic projection, and searching for the point that fits the best to all backward extended trails. Later, the intersecting planes method was developed (see Gural (2012)) for a historic overview) and was described in detail by Ceplecha (1987). In this classical approach, a set of meteor measurements projected on the plane of the sky from the position of a single observer describes a fan of rays in three-dimensional Cartesian coordinates, such that a plane can be fit through the measurements. The intersection of two planes from two stations produces a line which approximates the trajectory of a meteor. With more than two stations, an *ad hoc* weighting can be applied to estimate this three-dimensional line. Borovicka (1990) introduced a new trajectory solution method which assumes that individual meteor measurements can be treated as lines of sight (LoS) emanating from individual observers. The meteor trajectory is then simply that 3D line which minimizes the distance to all lines of sight. The advantage of this method is that the effects of Earth's rotation on the trajectory can be directly included without need for any additional corrections after trajectory estimation. This approach naturally accounts for multiple stations contributing measurements. Figure 1 shows the visualization of the two methods described above.

These methods only consider the geometry of the meteor's path in the atmosphere for trajectory estimation but do not take meteor dynamics into account. This is largely because high precision timing for individual positional meteor measurements was not available for photographic data – shutter breaks on a photograph had excellent relative timing but poor absolute timing. For these methods, if the geometry of the observations is bad (i.e. the convergence angle between the planes is small), unphysical results may occur – e.g. solutions show different speeds from different stations, a significant shortcoming.

Gural (2012) introduced the multi-parameter fit (MPF) method where meteor dynamics are considered as formulated models. Meteor velocity and optionally deceleration can be modeled using analytic expressions, such that fitting of the lines of sight is done to the model-predicted positions. This allows estimation of the trajectory's radiant orientation, the initial velocity, deceleration terms, and timing offsets between stations, all at the same time. The simultaneity of parameter estimation adds an additional degree of freedom that permitted smaller convergence angles to be processed. Several empirical meteor dynamical models were postulated for the MPF:

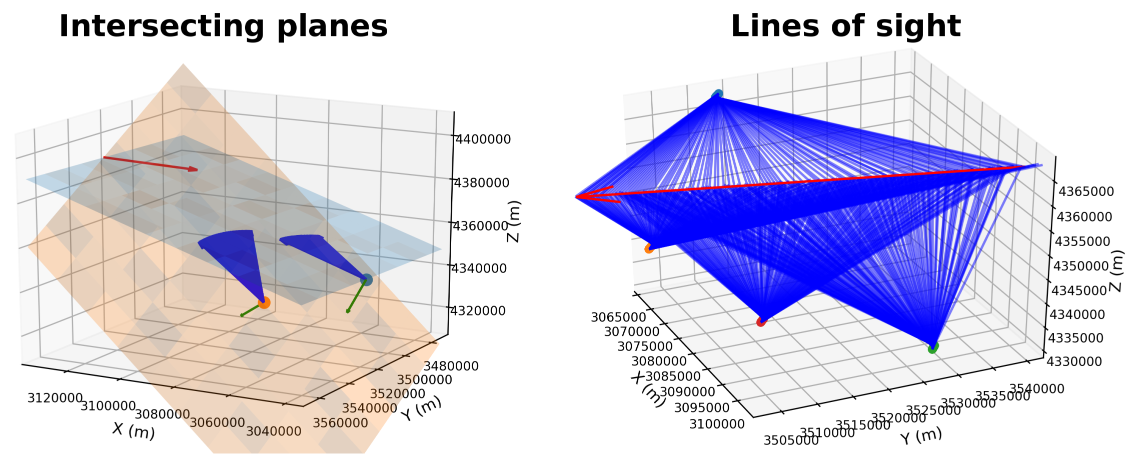

Figure 1 – FLeft: Intersecting planes method - the planes are fitted to observations (blue arrows) and the intersection of these planes is the trajectory (red arrow); Right: Lines of sight method - the trajectory in 3D (red arrow) is fitted to the lines of sight (blue lines).

- Constant velocity model – meteor moves with a constant velocity and does not decelerate.
- Linear deceleration model – meteor decelerates with a constant deceleration after a certain time t_0 since some reference time.
- Exponential deceleration model where the meteor decelerates with an exponential term, as originally proposed by Whipple & Jacchia (1957)

The exponential deceleration model with MPF was adopted as the operational method for the Cameras for Allsky Meteor Surveillance (CAMS) project (Jenniskens et al., 2016), as it is the only one with a physical basis. According to the classical meteor ablation equations (Ceplecha et al., 1998), a meteor's velocity is dependent on the mass density of the atmosphere, which increases exponentially as the meteor descends into the atmosphere. Recently, Egal et al. (2017) have shown that the model is mathematically ill-conditioned and that it is difficult in some cases to obtain a good fit of the model to the data. They have also shown that this leads to questionable radiant and velocity accuracy, especially for high-precision data.

The main motivation behind this work lies in understanding the trajectory and orbit accuracy that can be achieved using high resolution meteor observations obtained using the Canadian Meteor Observatory's meteor tracking system (Weryk et al., 2013). The system observes and tracks meteors using a set of fast steering mirrors and an 80 mm f/11 telescope. The telescopic view employs 1K × 1K cameras operated at 100 FPS and provide an effective angular measurement precision of 1 arc second, or on the order of 1 meter at 100 km range. To understand how this measurement precision influences the accuracy of the radiant and the initial velocity, we built a complex meteor trajectory simulator which allows us to quantitatively assess the performance of individual meteor trajectory solvers on simulated trajectory data for various observation systems, meteoroid types, and shower parameters.

It is important to mention that the accuracy of the meteor orbit is influenced by deceleration that can occur before the luminous phase. That is, before the meteor is detected where measurements cannot be made. We use the term "initial velocity" for the velocity of the meteor at the moment of first detection, and "pre-atmospheric velocity" for the velocity before any significant deceleration (we assume this to be at a height of 180 km). The dependence of the difference between the initial velocity and the pre-atmosphere velocity on meteoroid types and observations systems was analyzed in Vida et al. (2018). It was found that low-velocity meteors significantly decelerate (up to 750 m/s for moderate and narrow field of view systems) prior to detection when their peak magnitude is near the limiting sensitivity of a given observation system. The proposed correction should be used to reconstruct the real pre-atmosphere velocity from the measured initial velocity.

2 Methods

Meteor trajectory simulator

To assess the true precision of CAMO trajectories, the estimated radiant and the velocity must be compared to known values. As the true values for observed meteors are essentially unknown, validation via a meteor trajectory simulator is needed. Gural (2012) and Egal et al. (2017) performed earlier meteor trajectory simulations using limited geometries, simple dynamics and empirical models. Egal et al. (2017) investigated only one trajectory simulation using a full meteor ablation model and concluded that none of the existing trajectory solvers produce good results for high precision measurements. In their work the simulated meteor system had a pixel scale of about 25 arc seconds, an order of magnitude less precise than the higher precision CAMO tracking system.

To address the precision of CAMO, we have built a simulator capable of simulating meteor shower radiants and velocities, propagating meteors in the atmosphere using the ablation model of Campbell-Brown & Koschny (2004) and generating synthetic observations as they would be measured by CAMO stations on the ground. Physical properties of meteoroids, shower mass index and the activity profile are defined as inputs of the simulation. Measurement precision is simulated by adding Gaussian noise on the order of the precision of the system to the simulated positions of meteors.

As an initial test, we have simulated three meteor showers in different years: the 2011 Draconid outburst, 2012 Ursids and 2012 Perseids. These three showers cover the range of possible meteor velocities: the velocity of Draconids is 21 km/s, for Ursids 33 km/s, and Perseids 59 km/s. The true radiant dispersion and velocities of the 2011 Draconid outburst were obtained by numerical modelling of the dust ejection from the comet 21P/Giacobini-Zinner – the results (LaSun = 198.07°, RA_G = 263.39° ± 0.29°, Dec_G = 55.92° ± 0.16°, VG = 20.93 ± 0.04 km/s) corresponded well to the predictions of Vaubaillon et al. (2011) and Maslov (2011). Our simulations also reproduced the double peak of activity observed by Koten et al. (2014). The 2011 Draconids were chosen because the streamlet encountered that year was very young (<100 years old), meaning that the shower radiant was not dispersed due to gravitational perturbations, and it was well observed. The Ursids and Perseids were simulated using observationally estimated parameters from Jenniskens (1994) and Jenniskens et al. (2016).

Two other meteor observation systems were modelled as well - a moderate field of view CAMS-like system (Jenniskens et al., 2011) and an all-sky system based on the Southern Ontario Meteor Network (SOMN) (Brown et al., 2010). The simulated meteor networks were situated in Southern Ontario (around latitude 44° N) and set up in an equilateral triangle configuration where the sides were 100 km long and the camera pointing orientations resulted in maximum volume overlap at 100 km.

3 Monte Carlo meteor trajectory solver

After investigating trajectory solutions of 100 simulated meteors from each shower using all currently known trajectory estimation methods, we decided that none produced satisfactory results (see next section for details). We have noticed that due to the very high precision of CAMO measurements the deceleration of meteors is always present and can be very precisely determined. Furthermore, we have noticed that bad trajectory solutions result in inconsistent deceleration profiles when seen from different stations, while deceleration profiles of good solutions were consistent across multiple stations (Figure 2). As all stations observed the same meteor, we expect that all observers should observe the same dynamics (the full motion characteristics of the meteor: position, velocity, acceleration) and that all discrepancies are caused because the orientation of the trajectory was not well determined due to a simple perspective effect. Thus, we decided to develop our own trajectory estimation method which relies on matching observed dynamics across all stations, but without assuming the meteor must follow any particular analytical propagation model.

Our newly developed method of trajectory estimation uses the method of Borovicka (1990) for obtaining a first guess of the trajectory solution, after which the angular residuals between the measurements and the fitted trajectory are computed. Monte Carlo runs are then performed by adding Gaussian noise to the observations using the standard deviation of the angular residuals and refitting the trajectory using noise-added data. This procedure gives a set of trajectories which are geometrically possible to fit within the measurement uncertainty. The lines of sight from individual stations are then projected on the trajectory line and the dynamics of the meteor as seen from every station is computed. Finally, the best solution is chosen by comparing the observed dynamics between the stations and choosing the one which is the most consistent across all stations. This procedure is performed in several steps:

(a) The radiant and the reference position are estimated using the method of Borovicka (1990).

(b) The lines of sight are projected on the estimated trajectory, and time vs. distance from the beginning of the meteor (TvD) for every observer is computed.

(c) Due to the clock drift, the time when each system observed a meteor at a certain distance from the beginning may differ. Thus, timing offsets can be computed by adjusting the time on a per-station basis by minimizing the mean difference in time between all stations on TvD data. One station is chosen as the station with the reference time ($\Delta t = 0$), and the mean time residual is computed for all pairs of stations. The time separation for measurements that are not taken at the same along-track distance is computed as the difference between the data point from one station and the linearly interpolated curve from the other station. Figure 3 shows the comparison between TvDs before and after timing estimation.

(d) After time estimation, the timing is updated and the trajectory is fit anew. The timing offset estimation is repeated as well, and a final value for the average timing offset is obtained.

(e) The root-mean-square deviation (RMSD) of angular distances between all lines of sight and the trajectory line is computed for every observer. We use this value as an estimate of the measurement accuracy achieved by a given observer.

(f) Random Gaussian noise is added to every line of sight such that the standard deviation of the noise corresponds to the measured RMSD.

(g) Steps from a) to d) are repeated for every noise-added set of observations (hundreds of runs are performed).

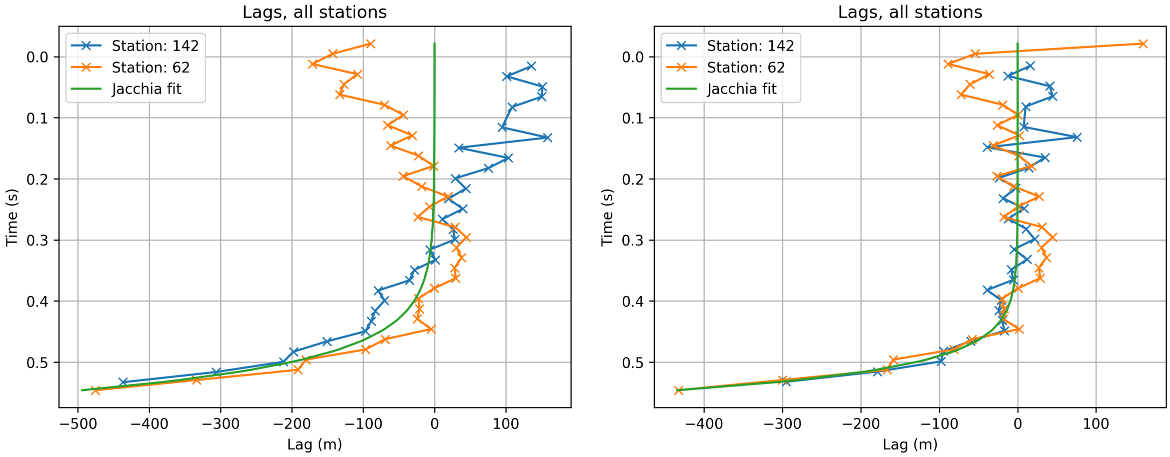

Figure 2 – Left: Deceleration profile of a bad trajectory solution from CAMS data. Right: Deceleration profile of a good trajectory solution. The x-axis lag corresponds to the apparent length a constant speed meteoroid would have as a function of time. Negative lags correspond to deceleration. The difference in the radiants was several degrees. The Jacchia fit is the fit of the empirical exponential deceleration, but with an independent estimate of the initial velocity which made the fit stable.

(h) A solution with the smallest mean time separation between interpolated time-versus-position tracks computed for each station is chosen as the final solution.

Figure 3 Comparison of TvDs before (left) and after (right) timing offset estimation. The procedure is fully automated but produces many graphs to help manually assess the quality of a solution if needed. This procedure constrains the trajectory solution both geometrically and dynamically without forcing use of a propagation/ablation model while keeping the solution within the measurement uncertainty. We note that the procedure described above cannot be performed if the observations have no track overlap (we require at least 4 points of overlap). In that case the trajectory can only be estimated by assuming a propagation model, thus the MPF method must be used.

The initial velocity was estimated by progressively fitting a line through TvD data, starting at the beginning to the first 25% of the trajectory, and repeating the fits by including points up to 80% of the trajectory. The fit with the smallest standard deviation (i.e. the velocity estimated on the part of the trajectory before significant deceleration) is chosen as the final solution.

4 Results

Detailed results for simulated Ursids observed by CAMO

Figures 4 to 7 show a representative selection of 2D histograms which show errors between the simulated values of the geocentric radiant and geocentric velocity, and the values estimated using various trajectory solvers. 100 Ursid meteors have been simulated and a precision for a CAMO-type system has been used. The angular distance between the real and the estimated geocentric radiant is shown on the X axis, while the error in the geocentric velocity is shown on the Y axis. All solutions which were more than 0.5° off in the radiant, and 0.5 km/s in velocity, are counted as failures. The gray vertical line shows the position of 3 standard deviations of the radiant error, while the horizontal line showing the 3 standard deviations in the velocity error is outside the bounds of the graphs (> 0.5 km/s).

Figure 4 shows the results obtained using the Borovicka (1990) lines of sight method where the initial velocity was computed by taking the average of the velocity during the first half of the trajectory, where the deceleration is not very significant. Only 1 out of 100 solutions failed (a trajectory with a convergence angle <1°). The geocentric velocities are underestimated due to deceleration prior to detection. The average underestimation is around 200 m/s for this meteoroid type and system (see Vida et al. (2018) for a complete analysis), while the measurement precision of the initial velocity is much better, around 50 m/s. The accuracy of radiant estimation is approximately 0.02°.

Figure 5 shows the results obtained using the MPF method with the constant velocity model. The geocentric velocity was underestimated even more as the initial velocity estimate was heavily influenced by deceleration, the average difference was around 400 m/s. This difference also drove the error in the radiant, which was up to 0.04°.

Next, Figure 6 shows results obtained using the MPF solver with the exponential deceleration model. This solver had a large failure rate, nearly 50%. The failure was mostly driven by the overestimation of the initial velocity, while the estimation of the radiant position was fairly robust.

Finally, Figure 7 shows the results obtained using the Monte Carlo solver. This solver performed the best on CAMO data. It has a very low failure rate; the radiant accuracy was around 0.01° and the geocentric velocity

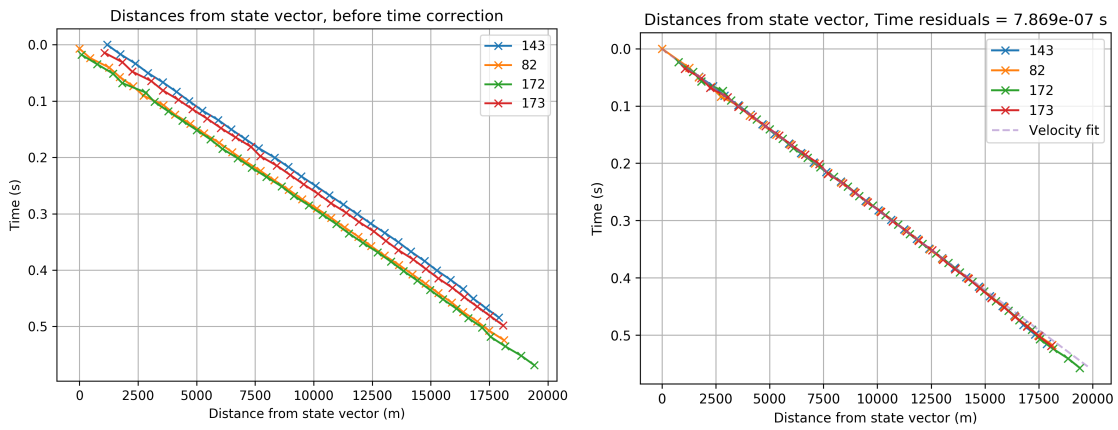

Figure 3 – Comparison of TvDs before (left) and after (right) timing offset estimation.

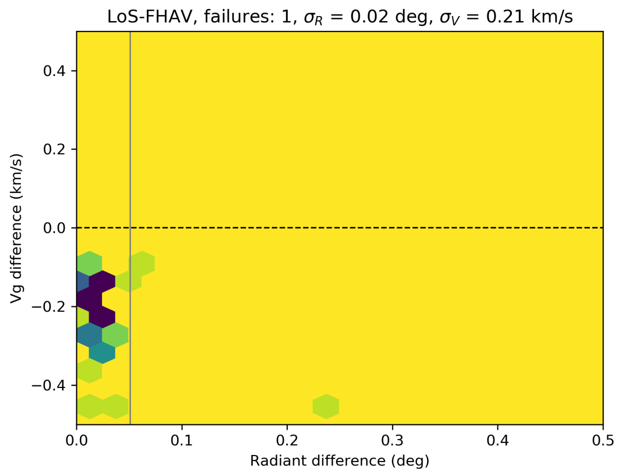

Figure 4 – Line of sight solution for Ursids. Only 1/100 solutions failed.

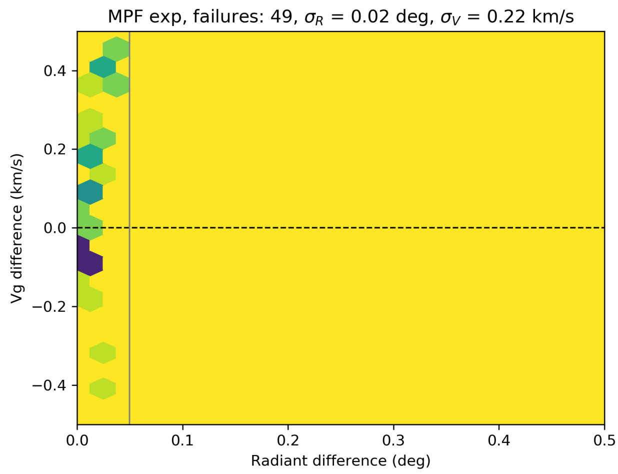

Figure 6 – Multi parameter fit with an exponential deceleration model. Almost half of the solutions failed.

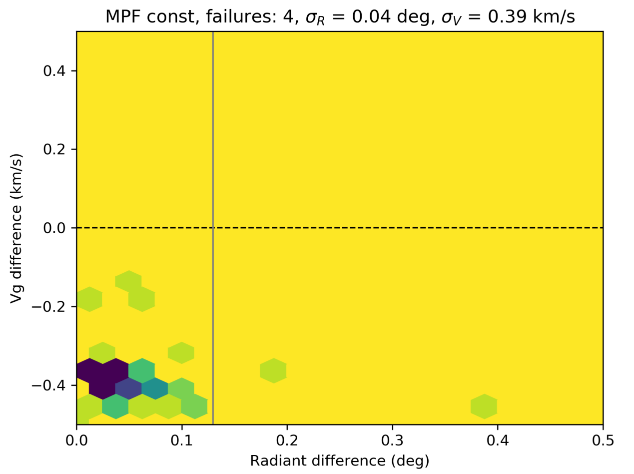

Figure 5 – Multi-parameter fit with a constant velocity model. 4/100 solutions failed.

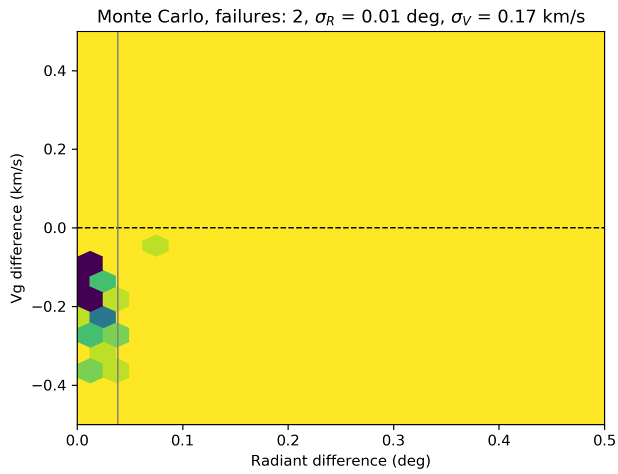

Figure 7 – Monte Carlo solution. Only 2/100 solutions failed.

accuracy around 170 m/s. The geocentric velocity was underestimated due to the deceleration prior to detection, which can be corrected for by applying the correction given in Vida et al. (2018).

5 Results for all solvers, showers, and systems

Below we present graphs which compare the accuracy between various solvers across all simulated systems and showers. The abbreviations on the graphs are the following:

- IP – intersecting planes method, initial velocity estimated as the average velocity of the first half of the trajectory.
- LoS – lines of sight method with the initial velocity estimated by the progressive method used in the Monte Carlo solver.
- LoS-FHAV – lines of sight method with the initial velocity estimated as the average velocity of the first half of the trajectory.
- Monte Carlo – the novel Monte Carlo trajectory solver.
- MPF const – multi-parameter fit method with the constant velocity model.
- MPF const-FHAV – the radiant solution from the MPF const method is taken, the lines of sight are re-projected on the trajectory, and the initial velocity is estimated as the slope of the line fitted through time vs. length along the track (effectively, the average velocity) of the first half of the trajectory.
- MPF linear – multi-parameter fit method with the linear deceleration model.
- MPF exp – multi-parameter fit method with the exponential deceleration model.

The width of individual boxes represents the geocentric velocity error, and the height of the box represents the geocentric radiant error. The numbers above the boxes for the appropriate solver represent the failure rate (out of 100) for the Draconids, the Ursids and the Perseids (in that order). Figure 7 compares the performance of trajectory solvers on simulated CAMO data. All solutions with an error larger than 0.5° and 0.5 km/s were considered to be failures. As can be seen, the Monte Carlo solver performs the best for all three simulated showers. The expected measurement error in the radiant is around 0.01° (around half an arc minute) and the error in the velocity is around 200 m/s assuming no deceleration correction. If the deceleration correction is applied, the error drops to about 50 m/s (see Figure 6).

Figure 8 shows the performance comparison on simulated CAMS data. All solutions with an error larger than 1° and 1 km/s were considered to be failures. The situation is more complex here and it seems the best results are produced by the classical intersecting planes and the lines of sight solvers, while the solvers which include the dynamics perform either marginally worse in the case of the Monte Carlo solver, or significantly worse in the case of the multi-parameter fit methods. The best case expected radiant error is around 0.1°, and the velocity error is around 200 m/s (around 100 m/s after deceleration correction). We emphasize that the MPF methods sometimes do produce better estimates of the radiant, which is consistent with Gural (2012) who only investigated the precision of the radiant position for various solvers. On the other hand, the velocity

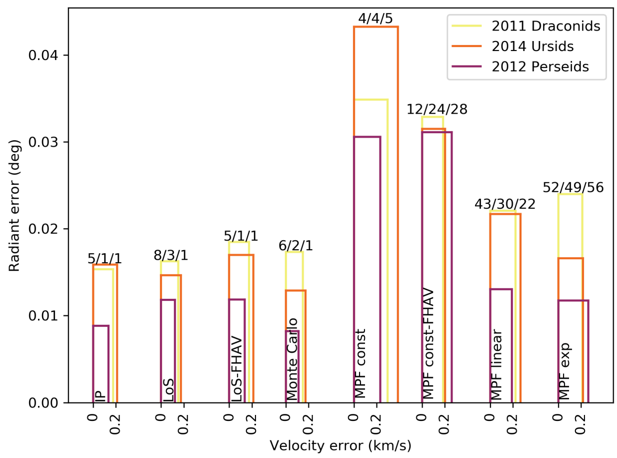

Figure 8 – Comparison of geocentric radiant and velocity accuracy for a simulated CAMO system for the 3 showers and the various trajectory solvers.

estimates are consistently worse by a factor of 2 or more when compared to other methods. The MPF method with the constant velocity model does produce robust solutions, but the correct way of either correcting for the deceleration or an alternate way of computing the initial velocity remain elusive. Computing the initial velocity as the average of the first half (MPF const-FHAV on figure 8) does not result in an improvement but causes an even larger spread in the estimated velocities. Furthermore, the MPF method with the exponential deceleration model produces a high failure rate for this type of data as well.

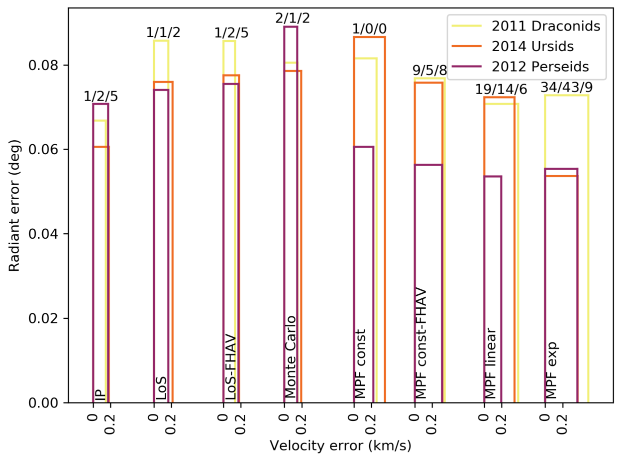

Figure 9 – Comparison of geocentric radiant and velocity accuracy for simulated CAMS systems for the 3 showers and the various trajectory solvers.

Finally, Figure 9 shows the performance comparison on simulated all-sky SOMN data. All solutions with an error larger than 5° and 5 km/s were considered failures. In this case, the MPF method with a constant velocity model produces the most robust solutions, although it consistently underestimates the initial velocity. We have tried to improve on this by computing the initial velocity as the average velocity of the first half of the trajectory, which worked well for the Draconids and the Ursids, but produces a significantly higher error for the

Perseids due to the higher meteor velocity and the lower number of data points on which the velocity can be estimated. We propose that the optimal operational approach for all-sky systems would be to adopt the MPF solver with the constant velocity model, plus a separate deceleration correction. The expected geocentric radiant error with this solver is around 0.25° (0.5° for the Perseids) and around 0.5 km/s in velocity (250 m/s after the deceleration correction).

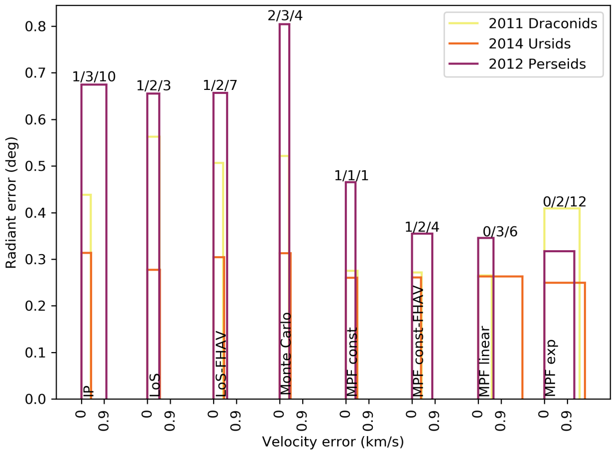

Figure 10 – Comparison of geocentric radiant and velocity accuracy for simulated all-sky SOMN systems for the 3 showers and the various trajectory solvers.

On the other hand, for long lasting or meteorite dropping fireballs observed with all-sky systems which have many data points, we have found that the Monte Carlo approach works the best as it matches the complex dynamics across all stations that these fireballs usually exhibit. Due to the larger inertia of these meteoroids, they do not significantly decelerate before becoming luminous, thus the method provides a reliable estimate of the pre-atmospheric velocity. The precision varies on a case-by-case basis, but assuming a favorable geometry and many data points, the accuracy of the radiant can be below an arc minute and the geocentric velocity can be estimated to within several 10 s of meters per second. Nevertheless, for a true understanding of the accuracy for interesting cases, we propose that they should be individually modeled by using a real station configuration and observation circumstances.

6 Conclusion

We have developed a novel method of meteor trajectory estimation and a complex meteor trajectory simulator. We have tested the performance of all currently known methods of meteor trajectory estimations and have found the following:

- For high precision systems such as CAMO, where the dynamics of a meteor can be well measured, the novel Monte Carlo method should be used.
- For moderate field of view systems such as CAMS, classical methods (intersecting planes and lines of sight) seem to produce the best results overall. MPF methods tend to improve the radiant precision but fail to accurately estimate the velocity.
- For all-sky systems the multi-parameter fit method with the constant velocity model is the most robust, provided a deceleration correction is used. For long duration meteorite-dropping fireballs the Monte Carlo method should be used.

Detailed description of the methods and further elaboration of the results will be published in the near future in a scientific journal.

Acknowledgement

We thank Sirko Molau for providing a translation of relevant sections from Schiaparelli & von Boguslawski (1871).

References

Borovicka J. (1990). “The comparison of two methods of determining meteor trajectories from photographs”. *Bulletin of the Astronomical Institutes of Czechoslovakia*, **41**, 391–396.

Brown P., Weryk R., Kohut S., Edwards W., and Krzeminski Z. (2010). “Development of an all-sky video meteor network in southern ontario, canada the asgard system”. *WGN, Journal of the International Meteor Organization*, **38**, 25–30.

Campbell-Brown M. and Koschny D. (2004). “Model of the ablation of faint meteors”. *Astronomy & Astrophysics*, **418:2**, 751–758.

Ceplecha Z. (1987). “Geometric, dynamic, orbital and photometric data on meteoroids from photographic fireball networks”. *Bulletin of the Astronomical Institutes of Czechoslovakia*, **38**, 222–234.

Ceplecha Z., Borovička J., Elford W. G., ReVelle D. O., Hawkes R. L., Porubčan V., and Šimek M. (1998). “Meteor phenomena and bodies”. *Space Science Reviews*, **84:3-4**, 327–471.

Egal A., Gural P., Vaubaillon J., Colas F., and Thuillot W. (2017). “The challenge associated with the robust computation of meteor velocities from video and photographic records”. *Icarus*, **294**, 43–57.

Gural P. (2012). “A new method of meteor trajectory determination applied to multiple unsynchronized video cameras”. *Meteoritics & Planetary Science*, **47:9**, 1405–1418.

Jenniskens P. (1994). “Meteor stream activity i. the annual streams”. *Astronomy and Astrophysics*, **287**, 990–1013.

Jenniskens P., Gural P., Dynneson L., Grigsby B., Newman K., Borden M., Koop M., and Holman D. (2011). “Cams: Cameras for allsky meteor surveillance to establish minor meteor showers”. *Icarus*, **216:1**, 40–61.

Jenniskens P., Nénon Q., Albers J., Gural P., Haberman B., Holman D., Morales R., Grigsby B., Samuels D., and Johannink C. (2016). “The established meteor showers as observed by cams”. *Icarus*, **266**, 331–354.

Koten P., Vaubaillon J., Tóth J., Margonis A., and Ďuriš F. (2014). “Three peaks of 2011 draconid activity including that connected with pre-1900 material”. *Earth, Moon, and Planets*, **112:1-4**, 15–31.

Maslov M. (2011). “Future draconid outbursts (2011–2100)”. *WGN, Journal of the IMO*, **39**, 3–64.

Schiaparelli G. V. and von Boguslawski G. (1871). *Entwurf einer astronomischen Theorie der Sternschnuppen.* Th. von der Nahmer.

Vaubaillon J., Watanabe J., Sato M., Horii S., and Koten P. (2011). “The coming 2011 draconids meteor shower”. *WGN, Journal of the IMO*, **39**, 3–59.

Vida D., Brown P. G., and Campbell-Brown M. (2018). “Modelling the measurement accuracy of pre-atmosphere velocities of meteoroids”. *Monthly Notices of the Royal Astronomical Society*, **479:4**, 4307–4319.

Weryk R., Campbell-Brown M., Wiegert P., Brown P., Krzeminski Z., and Musci R. (2013). “The canadian automated meteor observatory (camo): system overview”. *Icarus*, **225:1**, 614–622.

Whipple F. L. and Jacchia L. G. (1957). “The orbits of 308 meteors photographed with super-schmidt cameras.”. *The Astronomical Journal*, **62**, 37.

Improving astrometry and photometry reduction for PRISMA all-sky cameras

Dario Barghini[1,2], Daniele Gardiol[1], Albino Carbognani[1,3]

[1] **INAF – Osservatorio Astrofisico di Torino, Torino, Italy**
daniele.gardiol@inaf.it

[2] **Dipartimento di Fisica, Università degli studi di Torino, Italy**
dario.barghini@edu.unito.it

[3] **Osservatorio Astronomico della Regione Autonoma Valle d'Aosta (OAVdA), Italy**
albino.carbognani@inaf.it

The two fundamental steps for the characterization of an all-sky camera are the determination of the astrometric solution and the photometric calibration. In this paper we discuss the methods we developed and implemented for the PRISMA all-sky network: we provide some modifications to the parametric approach to the fish-eye astrometry model by Ceplecha (1987) and Borovicka (1992); Borovicka et al. (1995) and describe the photometric calibration of our instruments, together with discussion of some experimental results and other potential applications in atmosphere systematic monitoring.

1 Introduction

Recovering meteorite samples and track orbits of meteors has proved to be a key task in the study of the solar system's formation and evolution; for this purpose, the PRISMA[1] project (Gardiol et al., 2016) deployed an all-sky cameras network for detecting bright meteors and fireball events. In fact, PRISMA stands for 'Prima Rete Italiana per la Sorveglianza sistematica di Meteore e Atmosfera', i.e. 'First Italian Network for Meteors and Atmosphere systematic Surveillance'. The PRISMA project is closely linked to the French project FRIPON[2] (Fireball Recovery and InterPlanetary Observation Network), started in 2014 and managed by l'Observatoire de Paris, Muséum National d'Histoire Naturelle, Université Paris-Sud, Université Aix Marseille and CNRS (Colas et al., 2014, 2015). The PRISMA network currently uses the same technology as the FRIPON project and each camera is equipped with the FREETURE software (Audureau et al., 2014).

The computation of atmospheric trajectory, the strewn field of the surviving fragments and the orbit elements rely on the capability to translate physical pixel coordinates (pixel on the CCD plate) into celestial coordinates, i.e. the determination of the astrometric solution of the all-sky cameras (section 2); at the same time, the photometric solution is desired to retrieve the magnitude of the meteor along its flight (section 3). We draw our final conclusion in section 4.

2 Astrometry reduction

The determination of the astrometric solution for an all-sky camera device cannot be done by means of the classical CD matrix, following the Flexible Image Transport System (FITS) conventional nomenclature (Pence et al., 2010), because of the presence of heavy distortions effects in both azimuth a and zenith distance z dependencies. A parametric approach to this problem is provided in Ceplecha (1987) and Borovicka (1992); Borovicka et al. (1995). In these works, the parametrization aims to take into account 1) the radial distortion; 2) the mismatching between the optical axis and the zenith direction. The direct transformations from pixel coordinates (x, y) to horizontal celestial coordinates (a, z) can be given in the form of:

$$\begin{aligned} a &= E + \operatorname{atan}\left(\frac{\sin b \, \sin u}{\cos b \, \sin u \, \sin\epsilon + \cos u \, \sin\epsilon}\right) \\ z &= \operatorname{acos}(\cos u \, \cos\epsilon - \cos b \, \sin u \, \sin\epsilon), \end{aligned} \tag{1}$$

where (b, u) are defined as:

$$\begin{aligned} b &= a_0 - E + \operatorname{atan}\left(\frac{y - y_o}{x - x_o}\right) \\ u &= Vr + S(e^{Dr} - 1) \end{aligned} \tag{2}$$

Compared to the original set of equations in Borovicka et al. (1995), we neglected the potential misalignment of the optical plate with respect to the horizontal and the further radial distortions parameters (P, Q), as we did not find experimental evidence to motivate the introduction of these further corrections for our devices. In equations (1-2), (x_o, y_o) is the position of the optical axis direction onto the CCD plate, a_0 is the (anticlockwise) orientation of the camera with respect to the North direction, V, S, D are the lens constants and (E, ϵ) are the azimuth and zenith distance between the zenith direction and the optical axis.

The known issues in the determination of the eight parameters of equations (1-2) are mainly due to their

[1] prisma.inaf.it
[2] fripon.org

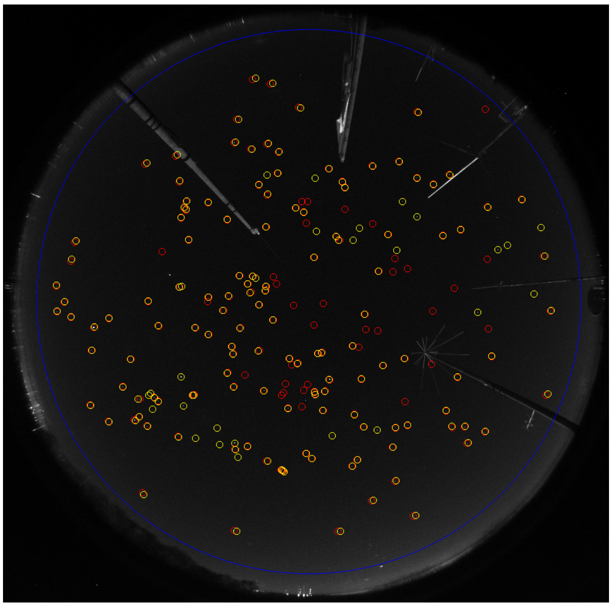

Figure 1 – Example of capture for Pino Torinese camera acquired at 1 January 2017, 00:02:56 UT (5 sec exposure) with the result of the source finding ad association algorithm. Red circles enclose found sources and yellow circles are the catalogue re-projected position in pixel coordinates through the inverse of equation (3).

strongly non-linear mathematical expression and the interdependencies of some of these parameters, reflected in a great sensitivity of the results with respect to the starting point values and a general non-optimal convergence of the optimization algorithm; some examples are reported in Borovicka (1992) and Bannister et al. (2013). To overcome these problems, we implemented a stepwise algorithm; the first operation to be performed is the determination of the associations list with respect to a reference catalogue (e.g. Tycho-2 catalogue, Høog et al. (2000)), and this can be done by using a simplified projection model:

$$a = a_0 + \operatorname{atan}\left(\frac{x - x_c}{y - y_c}\right)$$
$$z = P_1 r + P_2 r^2 \qquad (3)$$

Residuals of equation (3) show a known mean bias of about $\pm 1°$ in both a and z. However, this parametrization is still suitable for the determination of the associations between the identified source onto the CCD and the catalogue, as the star field is not so crowded; in fact, the limiting magnitude for our cameras is $V \simeq +4$ and we can identify about 100-200 stars in each image, resulting in 4000-8000 associations during a photometric night. Calibration data consist of 5 sec exposure images taken every 10 minutes over the night, which are identified as 'captures' following the FREETURE nomenclature; an example of these data and result of the finding algorithm are provided in Figure 1.

The determination of a complete astrometric solution is done with the daily or monthly statistics of these associations, with a modification of the explicit parametrization of equations (1-2):

$$(E, \epsilon) \rightarrow (x_Z, y_Z)$$

where x_Z, y_Z is the position of the zenith direction onto the focal plane. In this way we can provide easier initial estimates, gaining a reduced crosstalk between projection parameters.

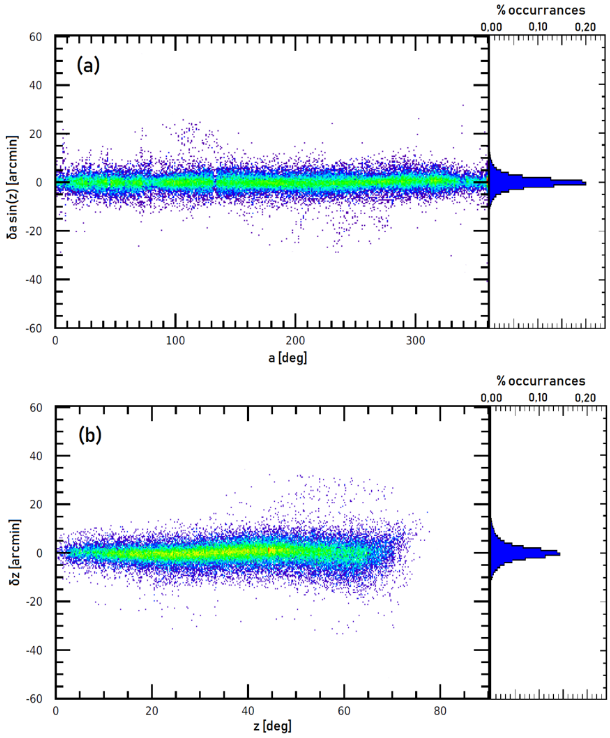

Figure 2 – Mono- and bi-dimensional histograms for azimuth and zenith distance residuals between catalogue and computed sources positions, for January 2017 calibration data of Pino Torinese station.

Figure 2(a-b) show the residuals histograms, for both a and z, between catalogue and computed positions; observed standard deviations are:

$$\sigma_a \simeq 2\,\text{arcmin}$$
$$\sigma_z \simeq 4\,\text{arcmin}$$

as it can be deduced from the 1D residuals histograms, showing a normal distribution around zero. Considering that our plate scale is about 10 arcmin/pixel, we can achieve a sub-pixel precision of about 1/3 pixel in the identification of the sources' positions. A closer look at the zenith distance residuals shows a further bias of the order of some arcmin, which is corrected numerically instead of adding other projections parameters to equations (1-2). The statistical errors affecting the determination of the eight astrometric parameters are reflected in an indetermination of the projection by an order of arcsec, i.e. almost negligible with respect to the error of the PSF center determination (for example, on a frame with a meteor detection).

All the calibration routines are written in IDL[3] (Interactive Data Language) and make extensive use of the IDL Astronomy User's Library[4] (IDL-Astro).

[3] `IDL--InteractiveDataLanguage,HarrisGeospatial`
[4] `dlastro.gsfc.nasa.gov`

3 Photometry reduction

At the same time of the astrometric reduction, a photometric solution is determined as well. As no filter is applied over the camera sensor, we must consider a wideband photometry. Taking into account the quantum efficiency (QE) of the camera with respect to the Jonhson-Cousins UBVRI filters (Figure 3), the corresponding magnitudes are converted into a wideband P ('PRISMA') magnitude by numerical integration; the reference magnitudes are retrieved by a query on the SIMBAD[5] database (Wenger et al., 2000). Another minor but still significant correction is due to the glass dome transmission (not shown), with a minimum in the U band.

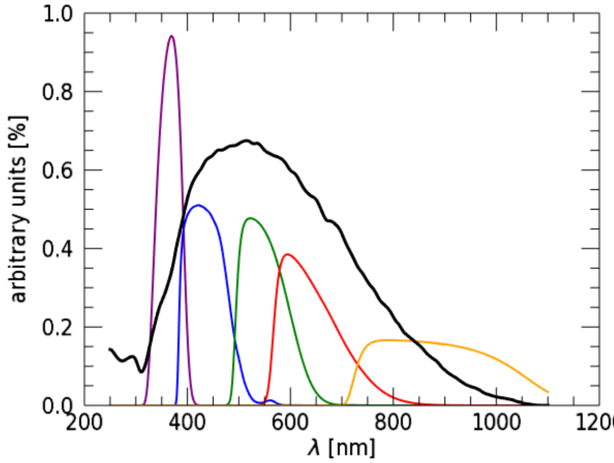

Figure 3 – Wideband photometry for PRISMA cameras. Quantum efficiency of the CCD (black solid line) and Johnson-Cousins filters U (violet line), B (blue line), V (green line), R (red line) and I (orange line) superimposed.

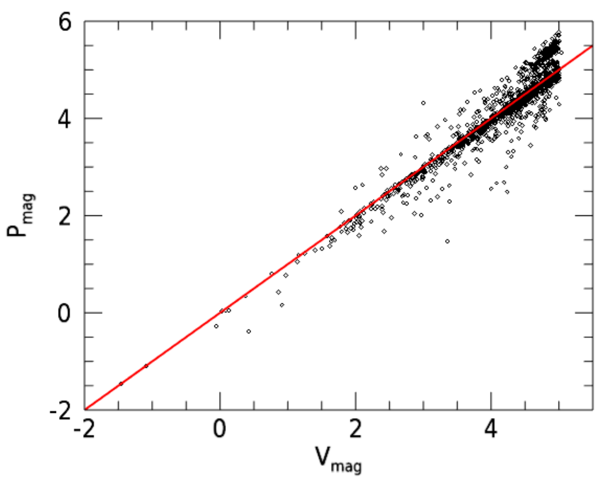

Figure 4 – Correlation between V and computed P magnitude. The V to P conversion is performed for $V < +5$ due to the limiting magnitude (see section 2).

The computed P magnitude shows a strong correlation (Figure 3) with the magnitude ($r = 0.94$), because the QE curve has its maximum in the V filter. Once the list of associations is obtained through the astrometric reduction pipeline, the experimental fluxes F_s of the found sources are computed, by aperture photometry, and the instrumental magnitudes $m_s = -2.5 \cdot \log_{10} F_s$ are retrieved. Then the estimation of the zero-point magnitude C and the atmospheric extinction coefficient k is carried out on each image comparing instrumental and catalogue magnitudes through the relation:

$$\Delta m = m_s - m = C - kx \qquad (4)$$

where x is the airmass, estimated from the Kasten & Young (1989) model; the zero-point C can also be computed with daily or monthly statistics by post-processing the results on each image, to obtain a better accuracy; Figure 5 shows one example of this calibration on a single capture. The uncertainties on the magnitude of zero-point is an important source of indetermination on the calculated magnitude, and we can achieve on the order of 1/10 of the magnitude error for bright sources.

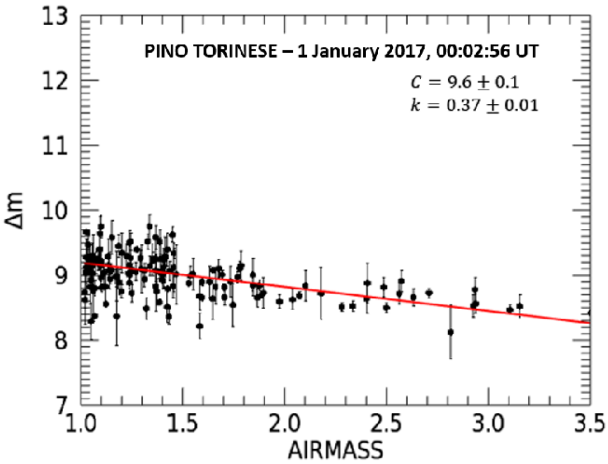

Figure 5 – Calibration of magnitude zero-point and atmospheric extinction coefficient for the Pino Torinese station on the 1 January 2017, 00:02:56 UT capture.

Calibration of the radial dependent sensitivity

A known effect to be estimated for all-sky cameras is the sensitivity loss along the radial direction, i.e. the zenith distance dependencies of measured fluxes not included in the atmospheric extinction, resulting from the whole optical system. To this purpose, we mounted one of our cameras in alt-azimuth configuration to be able to modify the pointing direction and observe different portions of the celestial dome at different apparent elevation on the CCD. The pointing direction is modified at 5° steps and in each configuration a set of images is acquired. Figure 6 shows the results of these measurements from $z = 0°$ to $z = 85°$; the fitted function is in the form of:

$$\eta(z) = B_0 - B_1 z - B_2 \exp\left(\frac{-B_1}{B_2} z\right) \qquad (5)$$

and is specified to fulfill the requirement of null derivative for $z = 0°$, because specular symmetry is expected

[5] simbad.u-strasbg.fr/simbad

around the optical axis. For great zenith distance values, the decreasing slope is nearly constant (about -0.1 each 20°). The sensitivity decreases by about 40% from the centre to the edge of the camera.

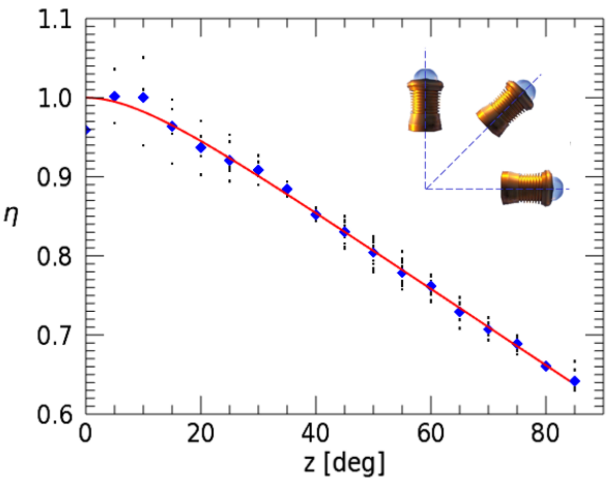

Figure 6 – Radial dependence of the optical system sensitivity (lens, glass dome,...) obtained as described in section 3. Black dots are the single measurements, blue dots are mean values and the red line is the plot of the fitting function of equation (5).

Values obtained for parameters of equation (5) are:
$B_0 = 1.048 \pm 0.005$
$B_1 = (483 \pm 8) \cdot 10^{-5}\text{deg}^{-1}$
$B_2 = (48 \pm 9) \cdot 10^{-3}$

Light pollution monitoring with PRISMA cameras

A possible application for an all-sky network is the automated monitoring of the mean sky brightness during the whole day, from which information about the artificial light pollution (ALAN – Artificial Light At Night) can be deduced (Jechow et al., 2017). During the astrometric and photometric calibration, this data can be easily extracted from the 5 sec exposure images, every 10 minutes, by computing the mean sky background at some points of the sky vault and then deducing magnitudes/arcsec2 using the zero-point value computed from the photometric calibration and the plate scale from the astrometric calibration. Currently, we sample these values for three elevations, i.e. one point at $z = 0°$, eight points at $z = 45°$ (each 45° of azimuth) and twelve point at $z = 70°$ (each 30° of azimuth), for a total of 21 points over the celestial dome. This is an alternative approach to the brightness maps analysis and allows us to create an easily readable time record without the need of storing an excessive amount of data. An example of these results is shown in Figure 7, for the 7 January 2017 night; features caused by the moon transit (first quarter) and cloudiness at the end of the night are also visible, and this shows the potential application of these data for other research fields, e.g. systematic cloud monitoring (Jechow et al., 2017).

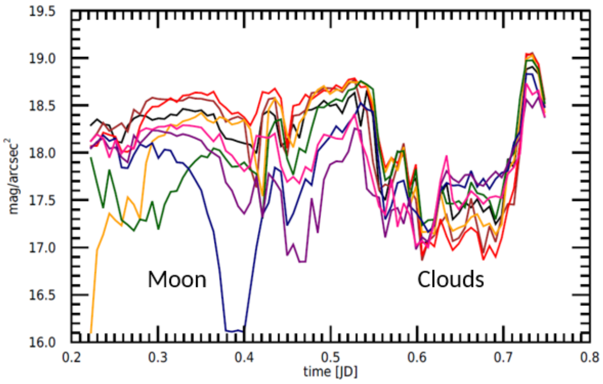

Figure 7 – Mean sky brightness time series from 07/01/2017 night of Pino Torinese station at $z = 45°$ for different azimuth values (0° - black, 45° - brown, 90° - red, 135° - orange, 180° - green, 225° - blue, 270° - violet, 315° - pink). Features caused by moon and clouds are outlined. The time axis lists the Julian Date fractional part of the mid-time exposure for the capture images.

4 Conclusions

The main goal of the PRISMA project is the systematic monitoring of the atmosphere for the detection of bright meteors. We developed reduction routines for astrometric and photometric calibration of our instruments and tested them against almost every station of our current network (27 operative cameras and 18 cameras in the purchasing or installation phase). These calibration procedures are based on the analysis of a set of 5 sec exposure images, acquired every 10 minutes through the night. The astrometric solution allows us to retrieve celestial coordinates from measured positions onto the CCD with sub-pixel precisions, being dominated by the uncertainties in the determination of the PSF center of the observed object, e.g. a detected bolide. The photometric solution provides a wideband P magnitude with uncertainties of about 1/10 mag. We also tested the radial sensitivity dependency for measured fluxes by mounting a camera in alt-azimuth configuration and obtaining a decreasing trend of about 40% from the center to the edge of the camera. From these calibration images it is also possible to deduce the mean sky brightness, with potential applications for the systematic monitoring of light pollution and cloudiness.

Acknowledgement

PRISMA is the Italian Network for Systematic surveillance of Meteors and Atmosphere. It is a collaboration initiated and coordinated by the Italian National Institute for Astrophysics (INAF) that counts members among Research institutes, Associations, Schools. The complete list of PRISMA members is available here: `http://www.prisma.inaf.it`.

PRISMA was partially funded by a 2016 "Research and Education" grant from Fondazione Cassa di Risparmio di Torino and by a 2016 grant from Fondazione De Mari di Savona.

The initial FRIPON hardware and software has been developed by the FRIPON-France core team under a French ANR grant (2014-2018).

References

Audureau Y., Marmo C., Bouley S., Kwon M.-K., Colas F., Vaubaillon J., Birlan M., Zanda B., Vernazza P., Caminade S., et al. (2014). "Freeture: A free software to capture meteors for fripon". In *Proceedings of the International Meteor Conference, Giron, France, 18-21 September 2014*. pages 39–41.

Bannister S. M., Boucheron L. E., and Voelz D. G. (2013). "A numerical analysis of a frame calibration method for video-based all-sky camera systems". *Publications of the Astronomical Society of the Pacific*, **125:931**, 1108.

Borovicka J. (1992). "Astrometry with all-sky cameras.". *Publications of the Astronomical Institute of the Czechoslovak Academy of Sciences*, **79**.

Borovicka J., Spurny P., and Keclikova J. (1995). "A new positional astrometric method for all-sky cameras.". *Astronomy and Astrophysics Supplement Series*, **112**, 173.

Ceplecha Z. (1987). "Geometric, dynamic, orbital and photometric data on meteoroids from photographic fireball networks". *Bulletin of the Astronomical Institutes of Czechoslovakia*, **38**, 222–234.

Colas F., Zanda B., Bouley S., Vaubaillon J., Vernazza P., Gattacceca J., Marmo C., Audureau Y., Kwon M. K., Maquet L., et al. (2014). "The fripon and vigie-ciel networks". In *Proceedings of the 2014 International Meteor Conference, Giron, France*. pages 18–21.

Colas F., Zanda B., Vaubaillon J., Bouley S., Marmo C., Audureau Y., Kwon M. K., Rault J. L., S. C., Vernazza P., Gattecceca J., Birlan M., Maquet L., Egal A., Rotaru M., Birnbaum C., Cochard F., and Thizy O. (2015). "French fireball network fripon". In *Proceedings of the 2015 International Meteor Conference, Mistelbach, Austria*. pages 37–40.

Gardiol D., Cellino A., and Di Martino M. (2016). "Prisma, italian network for meteors and atmospheric studies". In *International Meteor Conference Egmond, the Netherlands, 2-5 June 2016*. pages 76–79.

Høog E., Fabricius C., Makarov V. V., Urban S., Corbin T., Wycoff G., Bastian U., Schwekendiek P., and Wicenec A. (2000). "The tycho-2 catalogue of the 2.5 million brightest stars". Technical report, NAVAL OBSERVATORY WASHINGTON DC.

Jechow A., Kolláth Z., Ribas S. J., Spoelstra H., Hölker F., and Kyba C. C. (2017). "Imaging and mapping the impact of clouds on skyglow with all-sky photometry". *Scientific Reports*, **7:1**, 6741.

Kasten F. and Young A. T. (1989). "Revised optical air mass tables and approximation formula". *Applied optics*, **28:22**, 4735–4738.

Pence W. D., Chiappetti L., Page C. G., Shaw R., and Stobie E. (2010). "Definition of the flexible image transport system (fits), version 3.0". *Astronomy & Astrophysics*, **524**, A42.

Wenger M., Ochsenbein F., Egret D., Dubois P., Bonnarel F., Borde S., Genova F., Jasniewicz G., Laloë S., Lesteven S., et al. (2000). "The simbad astronomical database-the cds reference database for astronomical objects". *Astronomy and Astrophysics Supplement Series*, **143:1**, 9–22.

Spectral sensitivity of photographic emulsions

Željko Andreić[1], Damir Šegon[2] and Peter S. Gural[3]

[1] **Faculty of Mining, Geology, and Petroleum Engineering, University of Zagreb, Pijerottijeva 6, 10000 Zagreb, Croatia**
zandreic@rgn.hr

[2] **Astronomical Society Istra Pula, Park Monte Zaro 2, 52100 Pula, Croatia**
damir@astro.hr

[3] **Gural Software Development, 351 Samantha Drive, Sterling, Virginia, 20164, USA**
pgural@gmail.com

The photographic meteor magnitudes are still in use, and it is important to link them to magnitudes determined with modern detectors. Photographic meteor magnitudes were determined from meteor images registered on photographic film or plates. The spectral sensitivity of various photographic emulsions differs quite a bit, and it is seldom possible to get accurate information on the particular type of emulsion used. The main types of emulsions are analyzed and their average spectral sensitivities recalculated to equal-intensity light, as is usual today. The implications on magnitude determinations are discussed.

1 Introduction

Photographic emulsion was the main detector used in astronomy for the larger part of the 20th century (Walker, 1987). Only in the last 20 years or so it was rather rapidly replaced by the solid-state detectors. The detecting element in photography is called emulsion, although technically it is a solid-state mix of small light sensitive crystals of silver halide embedded in a solid matrix, usually gelatin, that keeps them in place. The average size of silver halide crystals depends on the type of emulsion and ranges from about 0.2 to 2 μm. Larger crystals result in greater sensitivity to light, but also reduced spatial resolution of the emulsion. The emulsion layer itself is between 7-30 μm thick (Junge & Hübner, 1972a). To provide dimensional stability and mechanical strength, the emulsion was coated on a transparent substrate. For professional use thin glass was preferred, resulting in the so called photographic plate. It has excellent durability and stability, but is fragile and difficult to handle. For each image, a new plate had to be used. For may other applications, thin sheet of transparent plastic was preferred, resulting in photographic film that can be cut in any desirable shape, often in long strips containing dozens or more individual images. Films were often put into a light tight box (the camera body) which allowed changing (winding) the images without the need to open the box, allowing capture of several images in a row. Appropriate lenses can be mounted to the camera body, or the body itself can be mounted on a telescope or some other instrument, very similar to modern digital cameras with exchangeable lenses.

Both plates and films were painted on the back side with a paint that absorbed light, to reduce light reflections from the back side of the substrate into the emulsion. This anti-halo coating was dissolved during the development of the film (Junge & Hübner, 1972b).

Exposed emulsion had to be chemically processed to reveal the recorded image (developing) and to make it permanent (fixing). After that the remaining chemicals had to be washed out and the emulsion had to be dried. Only after this procedure was completed, the recorded image was stable and suitable for analysis. A basic property of any emulsion is that the recorded image is a negative, i.e. the areas of the image that received more light energy resulted in a darker tone of the image. Such an image is called a negative. In many scientific applications, the negative is analyzed directly, but if needed, it can be copied to another film, or paper (coated with emulsion of course) and the resulting image is positive.

Most emulsions are black and white emulsions. However, by stacking three different emulsions on top of each other, separated by color filters made of soluble dyes, color images can be recorded. Such emulsions were seldom used in science, although amateurs used them sometimes. In this article, we will limit ourselves to black and white emulsions only.

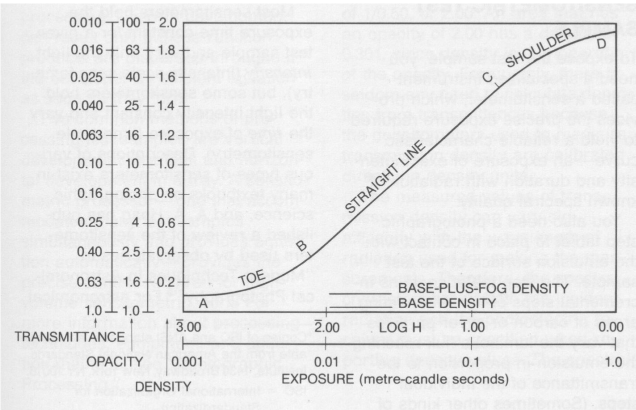

Figure 1 – A typical H-D curve (example from (Kodak,)). Usually only the innermost scales on abscissae and ordinate were used, the others are added here for clarification.

The sensitivity of the emulsion to the light energy is not linear and is usually described by the so-called H-D curve (see Figure 1). The amount of light energy (H) delivered to the emulsion is called exposure and is usually expressed as a product of light intensity and the time during which the light was allowed to fall onto the emulsion. The resulting blackening of the emulsion (once it was processed properly) was measured as opacity (the reciprocal of transparency). Usually, on abscissa of the H-D curve the logarithm of exposure (log H on the Figure 1) was plotted, and on ordinate the density, which is the logarithm of opacity, and was accordingly labeled as D.

2 The spectral sensitivity of photographic emulsion

Today, the spectral sensitivity is defined as response to the incoming light energy of different wavelengths. Uniform spectral distribution of light energy is assumed in this definition, known also under the name "equal energy" or "equal intensity" light. Note that there is no natural source of light with this property, so the measured distribution has to be corrected for the actual distribution of the light source used for calibration. Mostly, the spectral sensitivity curves are given in relative units (relative response) although in some cases absolute units are provided.

However, in the days of photography, different definitions were often used, allowing for simpler and more plausible interpretation of spectral distribution curves (foc, 1976). One standard was sensitivity to daylight (with an approximate color temperature of 5500 K). In the early days of photography actual daylight was used for this purpose, but was soon replaced by artificial source, mostly the tungsten light bulb, the spectral distribution of which being modified by a stack of filters. For the most sensitive emulsions, the spectral sensitivity to the light of the tungsten bulb (with color temperature differing between 2800 and 3200 K) was measured, as it was assumed that such emulsions would be used indoors under artificial light.

The standard instrument for measuring spectral sensitivity was the so called wedge spectrograph. It consisted of a prism spectrograph that produced the spectrum which was allowed to fall onto the emulsion in question through a set of gray filters, or a wedge made out of a gray glass, to provide different light intensities needed for calibration. The resulting image of the spectrum was simply copied onto a graph, with the correction for variable prism dispersion. Spectrograms produced this way (see Figure 2) were only approximate, but adequate for most purposes they were made for.

Some manufacturers, especially in the latter period of emulsion production, used more elaborate spectrophotometers to produce more accurate spectral sensitivity curves (Figure 3).

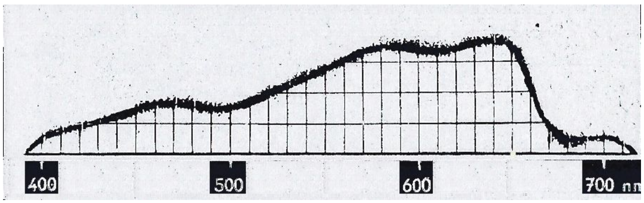

Figure 2 – A wedge spectrogam of Orwo NP-27 emusion, taken with tungsten light of 3200 K (Orwo, 1973). Note that there is no description of the ordinate, either on the graph itself or in the acompanying text, leaving us to guess what it represents.

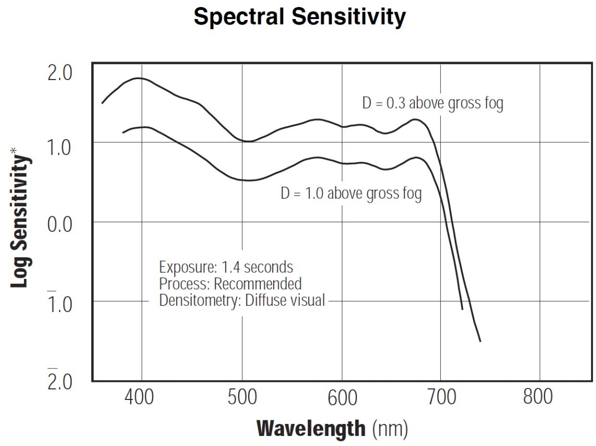

Figure 3 – A modern spectral sensitivity curve (Kodak Plus-X Aerocon II 3404 emulsion) measured with a dedicated spectrophotometer (Kodak, 2005). The sensitivity is given for daylight.

3 Data aquisition and processing

To get more insight into the topics of spectral sensitivity of photographic emulsions we searched the internet, which provided a lot of data for modern emulsions, but almost nothing about emulsions used prior to 1970 or so. For the latter, private archives, old data sheets (if available), and books were consulted. The spectral sensitivity of silver halide alone (sometimes used in slow emulsions called unsensitized emulsions) is well known (Junge & Hübner, 1972c) and is limited to the ultraviolet and blue part of the spectrum. It actually extends far into the ultraviolet, but is usually cut by absorption in optical elements between the emulsion and the light source. Old photographic (and telescope) lenses often cut all wavelengths below about 400 nm, but the modern ones can go to 360 nm or even lower, a fact that should be kept in mind when analyzing old plates. In the early days of photography the spectral sensibilization was discovered. It consists of adding an appropriate organic dye to the emulsion. The dye allows silver halide crystals to respond to light of longer wavelengths. Luckily, just a few dyes were used for the sensibilization, resulting in three additional types of emulsion response to the light: the orthochromatic emulsion, that is sensitive to wavelengths up to about 550 nm, the panchromatic, with sensitivity up to about 680 nm, and infrared, which often reached up to 1300 nm (Junge & Huebner, 1972). Most general purpose emulsions were panchromatic, although for some applications orthochromatic emulsions were used, as they (like unsensitized emulsion) can be processed under dark red light. Panchromatic and infrared emulsions have to be processed in total darkness, although sometimes short glimpses under a very dark green light were used, as all sensitized emulsions have a sensitivity minimum around 520 nm (the so called green hole).

Due to the scarcity of data we were able to find, we decided to create the general equal energy sensibility functions for the three types of emulsions as a first step. Although the emulsions differ in sensitivity between each other, from available data and our experience it can be concluded that these differences are of secondary importance. We settled to relative sensitivity curves as they are enough for most purposes. The absolute response curves are scarce, and more, they are very sensitive to the details of emulsion processing, meaning that to make any sense they had to be measured for the piece of emulsion we intend to analyze Such a process is tedious and cumbersome, and cannot be performed after the emulsion is developed. It was a standard in spectroscopy for instance, but was seldom used in other fields of astronomy. There, a standardized processing was often used, making data reduction easier and faster, but less accurate. However, as most applications (photometry, etc.) relied on comparisons of different image parts recorded on the same piece of emulsion, it was more than sufficient. All data we were able to find are presented in the form of printed graphs, so we digitized them as well as we could and produced digital versions of sensitivity curves that are much more usable in modern calculations. Last but not least, basic data about spectral sensitivity of modern silicon detectors were also gathered for comparison with emulsions.

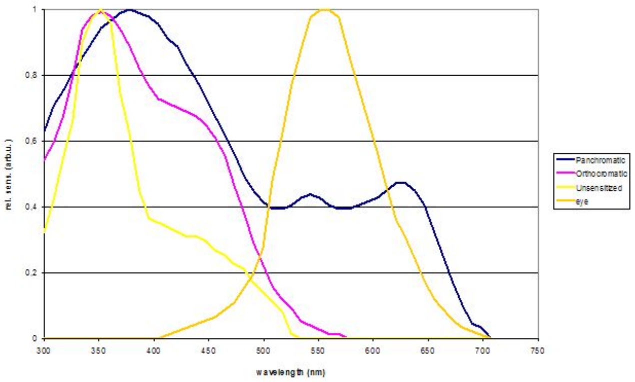

Figure 4 – Relative spectral sensitivity of different photographic emulsions, with the photopic (daylight) sensitivity of the human eye as comparison. The data were taken from (Junge & Hübner, 1972d) and (Fink, 1940) .

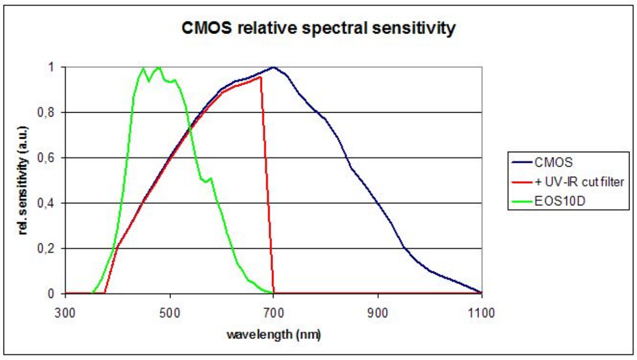

Figure 5 – Relative spectral sensitivity of a CMOS chip. Note that it peaks in the red and extends far into the infrared, up to about 1000 nm. The data are from (Loop Technology Limited, 2018a) for CMOS, (Loop Technology Limited, 2018b) for UV-IR cut filter and (Buil, 2018) for EOS 10D.

4 Results and discussion

The first results of our analysis are presented in Figure 4. The corresponding files can be downloaded from the CMN pages: `http://cmn.rgn.hr/downloads/downloads.html`. A similar procedure was applied to spectral sensitivity curves of modern detectors. The situation here is much easier, as most detectors used today are thick silicon CCD or CMOS chip, which have very similar spectral responses. A few typical examples of such responses are given in Figure 5. Note that the spectral sensitivity of these detectors is quite different from both the photographic emulsion and human eye. Often the infrared part is eliminated by a filter. In addition, the color sensor has three filters in three primary colors (R, G and B) making things more complicated.

However, here we are on easier ground, as the appropriate sensitivity curves for a particular detector/camera are available from manufacturers, and more, they are stable over the lifetime of the detector, so there is no need to make this type of calibration ourselves.

As an illustration of differences that different detectors produce, we calculated magnitudes of a meteor that a particular detector will measure, using the spectrum of the meteor and the sensitivity curves we obtained. In this simple calculation, the influence of the imaging lens was neglected. For this purpose, the meteor spectrum SX726 from (Vojaček et al., 2015) was used, the magnitude given by the original reference taken as the photographic magnitude of the meteor. Here are the results:

pan: $-2^{m}5$ (from Vojaček)
eye: $-2^{m}1$
CMOS (full): $-3^{m}6$
CMOS (VIS): $-2^{m}8$
EOS 10D: $-2^{m}7$

Pan stands for the panchromatic emulsion (such an emulsion was used to record the spectrum in question), the rest is self explanatory. One can see that the unfiltered CMOS produces a very different magnitude, as it is the only detector here that includes the infrared part of the spectrum.

5 Conclusions

The spectral sensitivity of photographic emulsions is important even today in interpreting meteor magnitudes obtained by the means of photography. It is often not known precisely, so we produced the general sensitivity curves for the three most common types of emulsions. These curves can be used in judging the differences in modern and photographic magnitudes, when the data about the particular emulsion type used are not available.

We also applied the obtained spectral sensitivity curves to a spectrum of a normal sporadic meteor, obtaining the meteor magnitude as it would be recorded by a particular detector. The spectral sensitivity of generic silicon solid-state detector was used for comparison. The main conclusion is that the differences in perceived magnitudes can be larger than an order of magnitude, calling for care when mixing old and new data.

Also, when we are comparing different detection systems, the complete sensitivity function has to be determined for all systems in question, including the optical system in front of the detector.

Acknowledgements

Ž. A. was partially supported by the University of Zagreb support "Mathematical research in Geology II" (head T. Malvić) for 2017. and "Mathematical research in Geology III" (head T. Malviić) for 2018.

References

(1976). *The Focal Encyclopedia of Photography, Desk edition.* Focal Press, London and New York, 1429-30 pages.

Buil C. (2018). "Evaluation de la reponse spectrale de l'appareil photo numerique canon eos 10d". `http://astrosurf.com/buil/us/digit/spectra.htm` .

Fink L. (1940). *Photographische Messtechnik.* Verlag von R. Oldenbourg, München and Berlin, 67 pages.

Junge K. W. and Hübner G. (1972a). *Fotografische Chemie.* VEB Fotokinoverlag Leipzig, 56 pages.

Junge K. W. and Hübner G. (1972b). *Fotografische Chemie.* VEB Fotokinoverlag Leipzig, 67 pages.

Junge K. W. and Hübner G. (1972c). *Fotografische Chemie.* VEB Fotokinoverlag Leipzig, 63-66 pages.

Junge K. W. and Hübner G. (1972d). *Fotografische Chemie.* VEB Fotokinoverlag Leipzig, 66 pages.

Junge K. W. and Huebner G. (1972). *Fotografische Chemie.* VEB Fotokinoverlag Leipzig, 64 pages.

Kodak, editor. *Scientific imaging with KODAK films and plates, Kodak manual P315.* Kodak, 7 pages.

Kodak (2005). *Kodak datasheet AS-202 (Kodak Plus-X Aerocon II film 3404).* KODAK, 4 pages.

Loop Technology Limited (2018a). "Cmos sensor cameras for digital vision". `http://www.looptechnology.com/cmos-sensor-cameras.asp` .

Loop Technology Limited (2018b). "Marumi uv-ir filter". `http://www.marumi-filter.co.jp/en/b2b/#band-pass-filter` .

Orwo (1973). *Orwo datasheet Ag 22-33-73 5000 IV-2-23 524 WP-Nr. 20/87/73.* ORWO, 8 pages.

Vojaček V., Borovička J., Koten P., Spurný P., and Štork R. (2015). "Catalogue of representative meteor spectra". *Astronomy and Astrophysics*, **580**, A67, 1–31.

Walker G. (1987). *Astronomical Observations.* Cambridge University Press, 260-261 pages.

Results of Polish Fireball Network in 2017

Mariusz Wiśniewski[1,2], Przemysław Żołądek[1], Arkadiusz Olech[1,3], Arkadiusz Raj[1], Zbigniew Tyminski[1,4], Maciej Maciejewski[1], Karol Fietkiewicz[1], Maciej Myszkiewicz[1], Marcin P. Gawroński[1,5], Tomasz Suchodolski[1,6], Marcin Stolarz[1], Mariusz Gozdalski[1]

[1] **Polish Fireball Network, Comets and Meteors Workshop, ul. Bartycka 18, 00-716 Warsaw, Poland**
brahi@op.pl and mazziek@gmail.com and parmo.pfn@gmail.com and ma.gozdalski@gmail.com and spammer.m@gmail.com and marcin.stolarz@gmail.com and krzysiek-pol20@o2.pl

[2] **Central Office of Measures, ul. Elektoralna 2, 00-139 Warsaw, Poland**
marand.w@gmail.com

[3] **Nicolaus Copernicus Astronomical Center, ul. Bartycka 18, 00-716 Warsaw, Poland**
a.olech@camk.edu.pl

[4] **National Centre of Nuclear Research RC POLATOM, Soltan 7, Otwock-wierk, Poland**
zbyszek.tyminski@gmail.com

[5] **Faculty of Physics, Astronomy and Informatics, Nicolaus Copernicus University, Grudzidzka 5, 87-100 Toru, Poland**
motylek@astro.uni.torun.pl

[6] **Space Research Centre, Polish Academy of Sciences, ul. Bartycka 18A, 00-716 Warszawa, Poland**
tomasz.suchodolski@ptma.pl

The PFN started in March 2004. Most of its observers are amateurs, members of Comets and Meteors Workshop. The network consists of 38 continuously working stations, where nearly 71 sensitive CCTV video and digital cameras operate. In 2016 PFN cameras recorded 100389 single events. Using this data 19087 trajectories and orbits was calculated.

1 Introduction

Since 2004, Polish Fireball Network (PFN) patrolling the skies over Poland. Most of PFN observers are amateurs, members of Comets and Meteors Workshop and perform observations from their homes. Some stations are located in astronomical clubs and schools. In 2017 the network consisted of 38 continuously working stations, with 71 sensitive CCTV video and digital cameras (Olech et al., 2006; Wiśniewski et al., 2017).

2 Cameras of PFN

The cameras of the PFN were able to cover the whole sky above Poland but the south-eastern Poland was particularly well-covered because the majority of cameras are located in that area (see Figure 1). In Most stations we use low cost sensitive CCTV analog video cameras equipped with lenses with 65.6×49.2° field of view. Currently there are 36 cameras of this type. We use MetRec (Molau, 1999) and UFOCapture (SonotaCo, 2005) software for meteor detection. UFOAnnalyzer software are used for astrometric reduction of video recordings.

Part of stations was equipped with 16 high sensitive Mintron 12v6 cameras with fast lenses. This cameras detected up to 4 times more meteors than low cost cameras. Due to higher sensitivity and smaller fields of view we can record large number of fainter meteors.

Setups with digital cameras are based on sensitive DMK 33GX236. These cameras have resolution of 1920x1200 pixels. The new cameras are working with lenses with focal length of 2.4 mm which gives 130x80 deg field of view. New cameras offer image with much better quality compared to analog cameras. Comparison of low cost setup, sensitive setup and new digital HD setup was presented in Table 1.

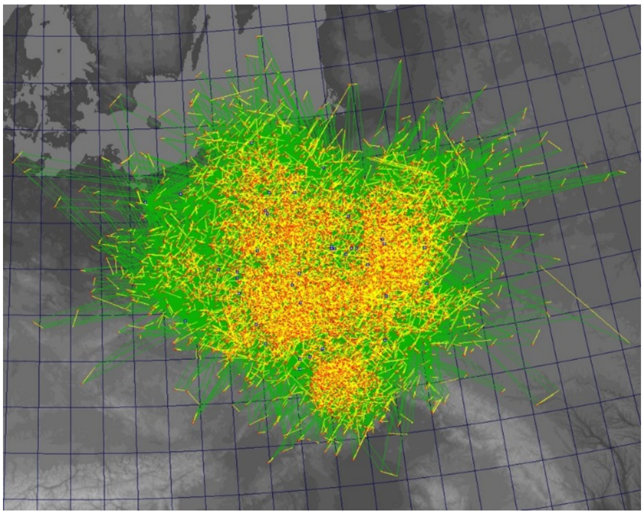

Figure 1 – Calculated trajectories of meteoroids in 2017.

Detections from all PFN cameras are automatically transmitted via internet to central server where double sta-

Table 1 – Types of camera working in PFN.

Parameter	Low cost setup	Sensitive setup	HD digital setup
Camera type	Tayama C3102-01A1	Mintron 12v6	DMK 33GX 236
Image resolution	480×576 pixels Interlaced	768×576 pixels Interlaced	1920×1200 pixels Progressive
Time resolution	25/50 fps 8 bit	25/50 fps 8 bit	50/25 fps 8/12 bit
Lens	1.2/4 mm	0.8/6 mm - 0.8/12 mm	1.2/2.4 mm
FOV	66×50 deg	<66×50 deg	130×80 deg
Pixel size	5'/pixel	<5'/pixel	4'/pixel

tion events are detected, analysed and then trajectory and obit is determined. All calculations are checked by manual inspection.

3 Results of PFN in 2017

In 2017 PFN cameras recorded 83095 single events. The collected data was preliminary analyzed using UFOOrbit software. The calculations were performed in a fully automatic way. The quality of the final results was controlled by UFOOrbit multiple parameter settings. Detailed information about the limiting parameters can be found in the software documentation (SonotaCo, 2005). The results with high uncertainty were rejected and the criterion was based on the set of the limit values.

We create also the PyFN software for trajectory and orbit calculation. PyFN (Żołądek, 2012) utilize the Ceplecha method (Ceplecha, 1987).

Table 2 – Results of PFN in last 6 years.

Year	Detections	Orbits
2011	24099	3430
2012	28471	4186
2013	36347	6114
2014	46936	7351
2015	79083	13528
2016	100389	19087
2017	83095	14586

Using this data 14586 trajectories and orbits was calculated. Detailed numbers of meteors was presented in Table 2. 2017 was the first year since the beginning of the PFN operation in which we recorded a decrease in the number of recorded meteors in relation to the previous year. This happened while maintaining the same number of cameras working in the network. The comparison of the number of recorded phenomena in the last two years showed a significant decrease in registered numbers of meteors after August (see Figure 2). The reason for this decline may be a large number of cloudy nights between August and the end of the year (see Figure 3).

Acknowledgement

We would like to thank to all station owners, operators and observers for long term and precise work for Polish Fireball Network (see Table 3).

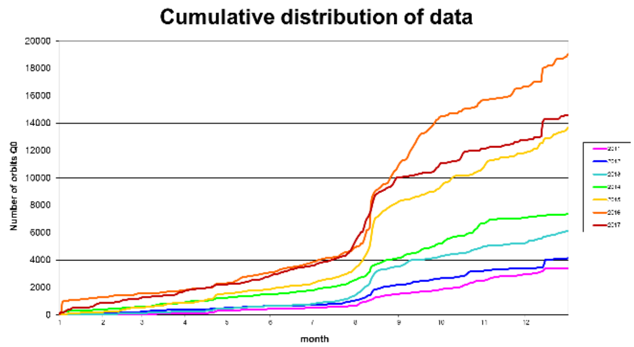

Figure 2 – Cumulative distribution of multistation detections in 2011-2017.

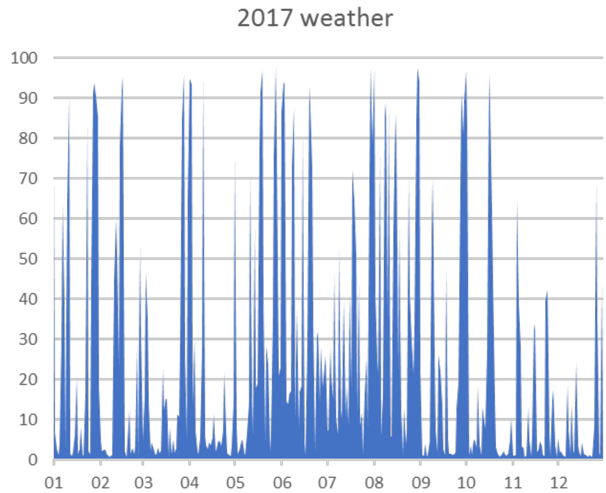

Figure 3 – Cloud coverage for PFN stations in 2017. 100% is for clrear sky.

References

Ceplecha Z. (1987). "Geometric, dynamic, orbital and photometric data on meteoroids from photographic fireball networks". *Bulletin of the Astronomical Institutes of Czechoslovakia*, **38**, 222–234.

Molau S. (1999). "The meteor detection software metrec". In *Proceedings of the International Meteor Conference, 17th IMC, Stara Lesna, Slovakia, 1998*. pages 9–16.

Olech A., Zoladek P., Wisniewski M., Krasnowski M., Kwinta M., Fajfer T., Fietkiewicz K., Dorosz D., Kowalski L., Olejnik J., et al. (2006). "Polish fireball network". In *Proceedings of the International*

Table 3 – Types of camera working in PFN.

ID	Name	Observer	Equipment
PFN01	Ostrowik	Maciej Myszkiewicz	PAVO1
PFN03	Złotokłos	Karol Fietkiewicz	PAVO3
PFN06	Kraków	Maciej Kwinta	PAVO6, PAVO7, PAV79 MDC14
PFN13	Toruń	Tomasz Fajfer	PAV14
PFN19	Kobiernice	Mariusz Szlagor	PAVO8
PFN20	Urzędów	Mariusz Gozdalski	PAV25, PAV26, PAV38, PAV99
PFN24	Gniewowo	Krzysztof Polakowski	PAV40, MDC09
PFN32	Chełm	Maciej Maciejewski	PAV35, PAV36, PAV43, PAV60, MDC09
PFN37	Nowe Miasto Lubawskie	Janusz Laskowski	PAV41
PFN38	Podgórzyn	Tomasz Krzyżanowski	PAV44, PAV49, PAV50, MDC15
PFN39	Rosocha	Andrzej Dobrychłop	PAV42
PFN40	Otwock	Zbigniew Tymiński	PAVO1, PAVO9, PAV52
PFN41	Twardogóra	Henryk Krygiel	PAV45, PAV53
PFN43	Siedlce	Maciej Myszkiewicz	PAV27, PAV61, PAV67, MDC07
PFN45	łańcut	łukasz Woźniak	PAV37
PFN46	Grabniak	Tomasz łojek	PAV57, MDC06
PFN47	Jeziorko	Tomasz Lewandowski	PAV13, PAV62, PAV63, PAV65
PFN48	Rzeszów	Marcin Bęben	PAV59, PAV64, PAV77, MDC03
PFN49	Helenów	Paweł Woźniak	PAV23
PFN51	Zelów	Jarosław Twardowski	PAV22
PFN52	Stary Sielc	Marcin Stolarz	PAV66, PAV75, MDC04, MDC12
PFN53	Belęcin	Michał Kałużny	PAV68
PFN54	Lęgowo	Grzegorz Tisler	PAV69
PFN55	Ursynów	Przemysław Żołdek	MDC01, MDC02
PFN56	Kolbudy	Cezary Wierucki	PAV71
PFN57	Krotoszyn	Tomasz Suchodolski	PAV70
PFN58	Opole	Filip Kucharski	PAV72
PFN59	Drawsko Pomorskie	Mirek Krasnowski	MDC10
PFN60	Bystra	Piotr Nowak	PAV74, PAV80
PFN61	Piwnice	Marcin Gawroński	PAV10
PFN62	Szczecin	Zbyszek Laskowski	MDC05
PFN63	Starowa Góra	Arek Raj	MDC11, MDC20
PFN64	Grudzidz	Sebastian Soberski	MDC18
PFN65	Wadowice	Mariusz Szlagor	MDC13
PFN67	Nieznaszyn	Walburga Węgrzyk	PAV78
PFN69	Lampówko	Jacek Kapcia	PAV69
PFN70	Kodeń	Piotr Onyszczuk	PAV67
PFN71	Radomsko	Hubert Dróżdż	PAVO1
PFN72	Koźmin Wielkopolski	Krzysztof Polak	PAVO1, PAVO2
PFN73	Chrzanów Mały	Paweł Zaręba	PAVO1, PAVO2, PAVO3
PFN74	Brwinów	Paweł Zaręba	PAVO1, PAVO2

Meteor Conference, 24th IMC, Oostmalle, Belgium, 2005. pages 53–62.

SonotaCo (2005). “Ufcapturev2 users manual”. `http://sonotaco.com/soft/UFO2/help/english/index.html`.

Wiśniewski M., Żołądek P., Olech A., Tyminski Z., Maciejewski M., Fietkiewicz K., Rudawska R., Gozdalski M., Gawroński M., Suchodolski T., et al. (2017). “Current status of polish fireball network”. *Planetary and Space Science*, **143**, 12–20.

Żołądek P. (2012). “Pyfn-multipurpose meteor software”. In *Proceedings of the International Meteor Conference, 30th IMC, Sibiu, Romania, 2011*. pages 53–55.

NEMO Vol 2. – Status of the NEar real-time MOnitoring system

Theresa Ott[1*], Esther Drolshagen[1*], Pierrick Mialle[2], Detlef Koschny[3,4], Gerhard Drolshagen[1], Christoph Pilger[5], Jeremie Vaubaillon[6], Björn Poppe[1]

[1] **University of Oldenburg, Germany**

[2] **CTBTO PTS/IDC, Vienna International Center, Austria**

[3] **ESA/ESTEC, Noordwijk, The Netherlands**

[4] **Chair of Astronautics, TU Munich, Germany**

[5] **BGR, Hannover, Germany**

[6] **Observatoire de Paris, France.**

Our near real-time monitoring system for atmospheric impacts from small NEOs (near-Earth objects) has been in test operation mode since autumn 2017 and is still under development. For NEMO (NEar real-time MOnitoring system) various data sources will be, and have already been, combined to archive the largest possible amount of scientific information on large fireball events.

To get very fast information, an alert system is under development, based on social media. Twitter was found to be a good source of information as well as the Google Alert system. After receiving information that there was a fireball event from our NEMO alert system we contact ground-based stations and networks, which monitor meteors and fireballs optically or by radar, and could have detected the event. For this part different co-operations and a more automated information transfer are planned. A collaboration with the FRIPON (Fireball Recovery and InterPlanetary Observation Network) system has already been established and is a fast source of scientific information for objects that entered the Earth atmosphere above Europe. Additionally, for entering asteroids or largest meteoroids, infrasound data may be available. A collaboration with the CTBTO (Comprehensive Nuclear-Test-Ban Treaty Organisation) enables us to obtain infrasound data of events. This system monitors most of the Earth atmosphere and contains worldwide information on atmospheric explosions. Furthermore, debris re-entry data is considered, to know if the impacting object was of natural origin or man-made.

This work will give an overview on the current situation, first results, and next steps of NEMO. For this, the Russian fireball from 21 June 2018 will be presented. This event was found by the NEMO alert system since the daytime fireball caused a lot of public attention. Moreover, it was detected by at least ten infrasound stations, enabling us to determine a source energy of about 2.4 kt TNT and a size estimation of the entering body of about 4 m in diameter.

1 Introduction

NEMO, the NEar real-time MOnitoring system is in test operational mode since autumn 2017. The system is still under development and its status will be presented in the following.

NEMO focusses on bright fireballs that cause a lot of public attention. The goal is to develop a world-wide information system that is able to provide information on bright events in near-real time. To reach this, different data sources have to be combined. On the one hand, there are ground-based networks that exist for meteor and fireball monitoring optically or by radar. These systems include a lot of scientific information but are only locally confined. On the other hand, more unconventional data sources as e.g. infrasound data can provide global information for the larger events. Furthermore, to get very fast information, social media is investigated permanently. The NEMO alert system is currently being built based on this information. A more detailed description of the NEMO system and its goals can be found in Drolshagen et al. (2018).

2 Data Sources

Spectacular Meteors, or bright fireballs, often cause a lot of public attention. One goal of NEMO is to first give very fast information on the event, and following to combine all available information of this event, and to make a summary public available. To do so, as many different data sources as possible will be used.

2.1 Social Media

Since NEMO will give very fast information on a fireball event, we created an alert system mainly based on social media. We found Twitter to be a very fast source of

*These authors contributed equally to this work information and the Google Alert system for further information.

Often, witness reports are also available very early and with growing number of reports the accuracy of the information increases.

The cooperation of NEMO with the AMS/IMO (American Meteor Society / International Meteor Organisation) is growing. On the one hand, it provides us with fast information regarding the time and location of a fireball. On the other hand, we started publishing information on events, collected by NEMO, on the IMO homepage. For information on the AMS/IMO see e.g. Hankey & Perlerin (2014).

2.2 Meteor and Fireball Networks

Spread over the world there are various meteor and fireball monitoring networks. A lot of scientific data is available if a fireball happened in the sky monitored by such a system which might cover only a relatively small part of the sky. The goal of NEMO is to unify the available information to archive all scientific output.

After receiving information that there was a fireball event from the alert system we contact the ground-based stations and networks that could have detected the event. To improve this, there are further co-operations as well as a more automated information transfer planned.

The cooperation of NEMO with FRIPON (Fireball Recovery and InterPlanetary Observation Network) is well established. The network covers the sky of France, and its extension into different countries is in progress. For more information about the FRIPON network see e.g. Colas et al. (2014). Currently, NEMO receives information from FRIPON about all fireballs that were detected by multiple cameras on a regular basis.

One interesting example of a European fireball is the fireball over the Netherlands on 29 June 2018 at about 21:30 UTC.

It was observed by people in the Netherlands, Belgium, Germany, France, England, and Luxembourg. The FRIPON cameras caught this fireball, amongst other cameras, see Figure 1. Furthermore, Langbroek (2018) published the velocity and a trajectory of the entering object. A summary of this fireball was written as part of the NEMO project with all information collected by it and published on the IMO homepage (Ott & Drolshagen, 2018b).

Receiving scientific information from various fireball monitoring systems, and providing summaries for a lot of bright fireballs is one of the aims of NEMO.

2.3 Infrasound Data

As shown by different authors (as e.g. Brown et al. (2013); Pilger et al. (2015); Silber et al. (2011)) it is possible to detect fireballs with infrasound stations. There are infrasound stations all around the world, operated by the CTBTO (Comprehensive Nuclear-Test-Ban Treaty Organization) searching for atmospheric explosions during day and night. One of the German contact institutes is the BGR (Bundesanstalt für Geowissenschaften und Rohstoffe). The cooperation of NEMO with the CTBTO and the BGR is under development and we are already receiving infrasound data of fireballs. If an event was detected with the IMS (International Monitoring System) of the CTBTO it is possible to derive the source energy of the entering object using the signal's relation between time and pressure.

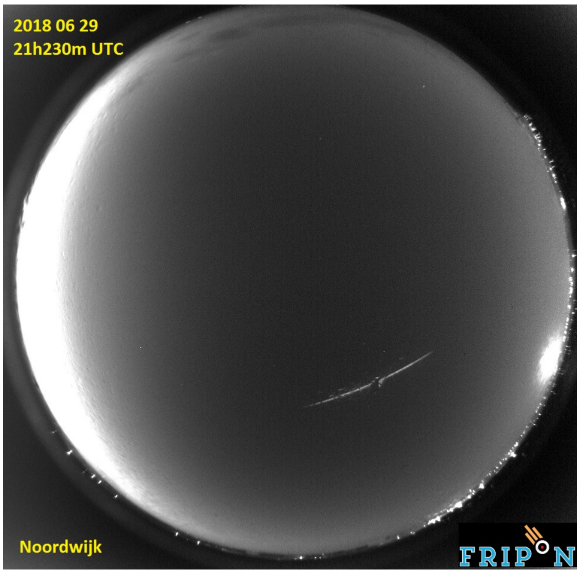

Figure 1 – Fireball over the Netherlands on 20 June 2018 - detection by the FRIPON camera at ESTEC, Noordwijk, NL.

For the infrasound data it is planned to analyse the data in a more automated manner in the future. Moreover, the detection method itself and its limitations have to be investigated further.

2.4 Additional sources

It has been demonstrated that there can be information on fireballs in the most diverse data sources, like in the data of meteorological satellites (see e.g. Borovička & Charvát (2009); Miller et al. (2013)) or in the data of lightning detectors (see e.g. Jenniskens et al. (2018)). Furthermore, meteorite findings that can be related to a fireball event can offer information on the entering object. The CNEOS/JPL (NASA/CNEOS - Center for NEO Studies and JPL - Jet Propulsion Laboratory) US Govt. satellites data is publicly available for some of the larger events giving the date and location of an event as well as a source energy and sometimes even a velocity for the entering object.

Knowing if the event was of natural origin or a re-entry of a man-made object is also of interest for NEMO. For this purpose information from the Aerospace database of upcoming and recent re-entries and ESA's re-entry predictions are used.

3 Russian daytime fireball

On 21 June 2018, around 01:15 UT (04:15 LT) a very bright fireball occurred over Russia, reported from Kursk, Lipetsk, Voronzeh, and Orel. On the same day, the NEMO alert system found this event. First, there were some tweets sent to us, so we knew that there was an event, and soon also its time and rough location, followed by impressive videos. An example of a tweet (The Watchers, 2018) we received as an alert from the system is presented in Figure 2Example of a tweet about the Russian daytime fireball that occurred on 21 June 2018 over Russia that triggered the NEMO alert system (The Watchers, 2018).

Figure 2 – Example of a tweet about the Russian daytime fireball that occurred on 21 June 2018 over Russia that triggered the NEMO alert system (The Watchers, 2018).

The videos we received in addition to reports of a loud boom by some witness reports indicated a large entering object that could have been detected with infrasound. Analysing the data enabled us to find a signal related to the fireball in data of ten IMS infrasound stations. A detailed investigation of the waveform signals yielded a source energy of the entering object of about 2.4 kt TNT. This enabled us to derive the size of the entering asteroid. We derived a diameter of about 4 m. The analysis of the infrasound data is explained in more detail in Ott et al. (2019) and further information on meteor generated infrasound can be found in Silber et al. (2018).

The Google Alert system found some additional information on the fireball, e.g. that it was detected with weather radar (Astro Alert, 2018) on the same day. We received an alert with a video uploaded to YouTube, showing that the fireball was visible in the data of the EUMETSAT satellites.

Some days later the Google Alert system found some further information: meteorites related to the event were found by scientists from the Ural Federal University (Urfu, 2018).

For this event an IMO summary was written, too, see Ott & Drolshagen (2018a).

4 Conclusion

In this work, we gave a status report on NEMO, the NEar real-time MOnitoring system for bright fireballs. It is in test operation mode since autumn 2017 and its goal is to analyse and combine as much available data of bright fireballs as possible in near-real time for world-wide events. This way, the highest amount of knowledge can be achieved.

The near-real time information is collected with the NEMO alert system which is under development and mainly based on Social Media including the witness report database AMS/IMO. It is planned that in the future more NEMO summaries for events will be included in this database.

A huge 'mosaic' of as much combined meteor and fireball networks all around the world could provide scientific information about a large amount of fireballs and the corresponding meteoroid or asteroid. There are further co-operations as well as a more automated information transfer planned and new ones highly welcome.

Furthermore, rather unconventional sources are used as a source of information for NEMO fireball events. Especially, the CTBTO infrasound data turned out to be a very promising source of world-wide information for bright fireballs.

The goal of NEMO is to collect as much knowledge of a fireball event as possible. This can only be achieved by combination of all known information.

Acknowledgements

We thank the European Space Agency and the University of Oldenburg for funding this project. We are also grateful to all networks and projects that have already agreed to cooperate with this endeavour. A special gratitude goes to the CTBTO for the help with this work and for providing us with data and software.

References

Astro Alert (2018). `https://youtu.be/Ww1KGkz7tiA`. [Online; accessed: 22.06.2018].

Borovička J. and Charvát Z. (2009). "Meteosat observation of the atmospheric entry of 2008 TC_3 over Sudan and the associated dust cloud". *Astronomy and Astrophysics*, **507**, 1015–1022.

Brown P. G., Assink J. D., Astiz L., Blaauw R., Boslough M. B., Borovička J., Brachet N., Brown D., Campbell-Brown M., Ceranna L., Cooke W., de Groot-Hedlin C., Drob D. P., Edwards W., Evers

L. G., Garces M., Gill J., Hedlin M., Kingery A., Laske G., Le Pichon A., Mialle P., Moser D. E., Saffer A., Silber E., Smets P., Spalding R. E., Spurný P., Tagliaferri E., Uren D., Weryk R. J., Whitaker R., and Krzeminski Z. (2013). "A 500-kiloton airburst over Chelyabinsk and an enhanced hazard from small impactors". *Nature*, **503**, 238–241.

Colas F., Zanda B., Bouley S., Vaubaillon J., Vernazza P., Gattacceca J., Marmo C., Audureau Y., Kwon M. K., Maquet L., Rault J.-L., Birlan M., Egal A., Rotaru M., Birnbaum C., Cochard F., and Thizy O. (2014). "The FRIPON and Vigie-Ciel networks". In Rault J. L. and Roggemans P., editors, *Proceedings of the International Meteor Conference, Giron, France, 18-21 September 2014*. pages 34–38.

Drolshagen E., Ott T., Koschny D., Drolshagen G., and Poppe B. (2018). "NEMO Near real-time Monitoring system". In Gyssens M. and Rault J.-L., editors, *International Meteor Conference, Petnica, Serbia, 21-24 Sep 2017*. pages 38–41.

Hankey M. and Perlerin V. (2014). "IMO Fireball Reports". In Rault J. L. and Roggemans P., editors, *Proceedings of the International Meteor Conference, Giron, France, 18-21 September 2014*. pages 160–161.

Jenniskens P., Albers J., Tillier C. E., Edgington S. F., Longenbaugh R. S., Goodman S. J., Rudlosky S. D., Hildebrand A. R., Hanton L., Ciceri F., Nowell R., Lyytinen E., Hladiuk D., Free D., Moskovitz N., Bright L., Johnston C. O., and Stern E. (2018). "Detection of meteoroid impacts by the Geostationary Lightning Mapper on the GOES-16 satellite". *Meteoritics and Planetary Science*, **53**, 2445–2469.

Langbroek M. (2018). `https://twitter.com/Marco_Langbroek/status/1014279821206151168`. Online, tweet; accessed: 12.09.2018.

Miller S. D., Straka, William C. I., Bachmeier A. S., Schmit T. J., Partain P. T., and Noh Y.-J. (2013). "Earth-viewing satellite perspectives on the Chelyabinsk meteor event". *Proceedings of the National Academy of Science*, **110**, 18092–18097.

Ott T. and Drolshagen E. (2018a). "Daytime Fireball over Russia on June 21". `https://www.imo.net/daytime-fireball-over-russia-on-june-21`. Online; accessed: 12.09.2018.

Ott T. and Drolshagen E. (2018b). "Fireball over the Netherlands on 29 June 2018". `https://www.imo.net/fireball-over-the-netherlands-on-29-june-2018`. Online; accessed: 12.09.2018.

Ott T., Drolshagen E., Koschny D., Mialle P., Pilger C., Vaubaillon J., Drolshagen G., and Poppe B. (2019). "Combination of infrasound signals and complementary data for the analysis of bright fireballs". *Planetary and Space Science*, page 104715.

Pilger C., Ceranna L., Ross J. O., Le Pichon A., Mialle P., and Garcés M. A. (2015). "CTBT infrasound network performance to detect the 2013 Russian fireball event". *Geophysics Research Letters*, **42**, 2523–2531.

Silber E. A., Boslough M., Hocking W. K., Gritsevich M., and Whitaker R. W. (2018). "Physics of meteor generated shock waves in the Earth's atmosphere - A review". *Advances in Space Research*, **62**, 489–532.

Silber E. A., Le Pichon A., and Brown P. G. (2011). "Infrasonic detection of a near-Earth object impact over Indonesia on 8 October 2009". *Geophysics Research Letters*, **38**, L12201.

The Watchers (2018). `https://twitter.com/TheWatchers_/status/1009766073426563O7`. [Online, tweet; accessed: 13.06.2018].

Urfu (2018). `https://urfu.ru/ru/news/24106/`. [Online, press release; accessed: 20.07.2018].

Tricks of the trade: global analysis of visual meteor observations using VMDB and MetFns — an example

Kristina Veljković[1], Jürgen Rendtel[2], Cis Verbeeck[3], Thomas Weiland[4], and André Knöfel[5]

[1] **Petnica Meteor Group**
mackikac@gmail.com
[2] **Leibniz-Institut für Astrophysik, An der Sternwarte 16, 14480 Potsdam and International Meteor Organization, Eschenweg 16, 14476 Potsdam, Germany**
jrendtel@web.de
[3] **Royal Observatory of Belgium, Ringlaan 3, 1180 Brussels, Belgium**
cis.verbeeck@oma.be
[4] **Ospelgasse 12-14/6/19, 1200 Wien, Austria**
thomas.weiland@aon.at
[5] **Am Observatorium 2, 15848 Lindenberg, Germany**
aknoefel@minorplanets.de

This paper aims at providing its readers practical insight into the process of global analysis of a meteor shower. After a description of the Visual Meteor Data Base and of the online application MetFnsApp and R package MetFns for meteor shower analysis, the algorithms and formulas employed in meteor shower analysis are presented. Section 4 explains the typical steps in a global meteor shower analysis, by the specific example of the Perseids 2018 as they were analyzed at the Visual Meteor Workshop during the IMC 2018 in Pezinok. Readers are strongly encouraged to carry out their own analyses of visual observations of meteor showers.

1 Introduction

The International Meteor Organization (IMO) organized a Visual Meteor Workshop on August 29–30, 2018 at Pezinok, Slovakia, right before the International Meteor Conference 2018. At the Visual Workshop, the authors conducted a joint global analysis of the visual observations of the Perseids 2018 in IMO's Visual Meteor Data Base (VMDB). We employed Kristina Veljković's online application MetFnsApp (Veljković, 2017a) and R package MetFns (Veljković, 2017b) to perform the analysis. MetFns provides an easy access to powerful meteor analysis routines. In this paper, we do not just present the results of the analysis – which are described and discussed in (Rendtel et al., 2019) – but rather focus on our strategies in the trial and error process we followed when analyzing the data (finding optimal binning parameters, filtering the data where needed). We are convinced that the guidelines in the current paper, through the VMDB and MetFns, will enable meteor workers with no prior experience in analysis of visual data, to perform their own population index r and Zenithal Hourly Rate (ZHR) analysis of meteor showers within a short learning period. We strongly invite our readers to carry out their own analyses of visual observations of meteor showers. The data and tools are there for you to use!

2 Description of the VMDB

The Visual Meteor Data Base (VMDB) contains meteor data collected since 1980, from the visual observers around the world. In their visual observations, meteor observers use the set of standardized methods, which are described in the Handbook for Meteor Observers (Rendtel and Arlt, 2017). Data can be submitted to the IMO, using the on-line visual form which is on the IMO web page `https://www.imo.net/members/imo_observation/add_observation`.

Thanks to the integration of the VMDB with the IMO website by Mike Hankey and Vincent Perlerin in 2016, registered users of the IMO site can download meteor rate and magnitude data, first selecting data by year (1980–present) or by date and time range and, then, by selecting one or all showers. The Visual Meteor DataBase (VMDB) can be found on the IMO web page `http://www.imo.net/members/imo_vmdb/download`. Data is saved in csv format (columns are semicolon separated), in three files: session, rate and magnitude. The session file contains data about the observer's session: identifier numbers (session, user), user's first and last name, start date and time, the details about observing location (city, country, elevation, latitude and longitude). The rate data table has columns with identifier numbers (rate, user, session), start and end date and time, coordinates of the center of the field-of-view (right ascension and declination), effective observing time, correction factor F for obstruction of the field-of-view, limiting magnitude, shower code, observing method and number of meteors. Magnitude data consists of columns with identifier numbers (magnitude, user, session), shower code, start and end date and time, magnitude distribution (number of meteors of magnitude ranging from -6 to $+7$).

3 Description of the MetFns package and application

3.1 MetFns

MetFns is a package of functions for selection and analysis of visual meteor data. It is written in the statistical programming language R and it can be freely downloaded from the CRAN webpage `https://cran.r-project.org/web/packages/MetFns/index.html`. Calculations of r and ZHR are based on an optimal bin size algorithm, which will be described, together with other used formulas and algorithms, in the next subsections.

3.2 MetFnsApp

MetFnsApp is an R shiny application which complements the MetFns package. It enables users without the knowledge of the R programming language to perform data selection and analysis. It is divided into five tabs: About, Filter, Population index, ZHR and References. The About tab contains a description of the application. In the Filter tab, the user can choose the rate and magnitude data by year (1984–present) and select data by ranges of: date and time, limiting magnitude, percentage of obstruction of the field-of-view, radiant elevation and by shower code. After selecting the data by shower at least, the user can proceed to r and ZHR analysis, in the third and fourth tab, respectively. Time range in these two tabs is automatically updated after shower selection. Further, for data analysis, the following parameters can be selected: date and time range, minimum and maximum bin size in degrees of solar longitude, number of meteors and zenith exponent. For the ZHR calculation it is possible to apply a constant r or values of r calculated from selected magnitude data. Once the tables of r and ZHR values are calculated, the user can visually represent them by selecting the parameters for the graph: limits and increments on both and axes. Finally, the Reference tab consists of the manual of the package MetFns.

3.3 Formulas and algorithms

3.3.1 Optimal bin size algorithm

For calculation of r and ZHR, magnitude and rate data is divided into blocks of optimal bin sizes, using an optimal bin size algorithm. Parameters of this algorithm are: rate or magnitude data, shower code, date and time range, minimum and maximum bin size and total number of meteors. It searches for an optimal bin, going from minimum to maximum bin size, trying to accumulate at least the specified number of meteors per bin.

Data is selected by shower and date range. Solar longitudes corresponding to the middle of the observing time interval are sorted in increasing order. Only data with observing lengths less or equal to the maximum bin size are considered.

Starting from the top of the sorted data, a block of data of maximum bin size is taken. The cumulative sum of the number of meteors in the block is calculated. Next, the algorithm tries to find a sub-block of smaller bin size, so that the following conditions are fulfilled:

1. The bin size is greater than or equal to the minimum bin size.
2. Only data with interval lengths smaller than or equal to the bin size are used, where first and last solar longitudes of the sub-block represent beginning and end of the bin, respectively.
3. The cumulative sum of meteors is greater than or equal to the specified number of meteors.

It should be noted that the third condition applies to the data which fulfilled the second condition. If there are not enough meteor data in the sub-block, the full block of data of maximum bin size is returned. Then, the algorithm proceeds with applying the described procedure on the next block of data, which continues with the previously found optimal block. As a result, the optimal bin size algorithm will return a list of data blocks, each with its own optimal bin size.

3.3.2 Population index

In the package MetFns, both the method of linear regression and the method of the average distance from the limiting magnitude are implemented in the calculation of the population index. MetFnsApp uses the latter method, which will be described here.

The algorithm first calculates individual average distances from the limiting magnitude, as the differences between the limiting magnitude and the average meteor magnitude, for each observing time interval. The final average distance from the limiting magnitude is calculated as a weighted average of all individual average distances, where the numbers of meteors in each observing interval represent weights. Next, a conversion of the average distance from limiting magnitude to population index is done using natural spline interpolation of table values published in (Arlt, 2003).

The standard error of the population index is calculated using bilinear interpolation of table values (applied on the number of meteors n and population index r). Table values cover the number of meteors between 10 and 9369. If the total number of meteors per bin is smaller than 10, NA values are returned for the population index and its standard error. In the case when the total number of meteors is greater than 9369, polynomial regression of the second degree is used in the calculation of the standard error σ_r

$$\begin{aligned}\sigma_r \;=\;& 0.163r + 0.007r^2 - 0.056\log(n) - 0.019r\log(n) \\ & +0.005(\log(n))^2 + 0.112. \qquad (1)\end{aligned}$$

In the results, we get a table of population index values calculated for blocks of magnitude data of optimal bin sizes. The mean solar longitude is also given for each population index value. It is the mean of observers' solar longitudes, weighted by $\frac{N_{\text{obs}}}{C_{\text{obs}}}$, the number of meteors divided by the total correction factor $C_{obs} = \frac{F_{obs} r^{(6.5-\text{lm}_{\text{obs}})}}{(\sin(h_{\text{obs}}))^{\gamma}}$, where F_{obs} is observer's correction factor for obstruction of field-of-view, lm_{obs} limiting magnitude, h_{obs} radiant elevation and γ zenith exponent (by default, $\gamma = 1$). In other words, advantage is given to the observing intervals with greater number of meteors seen under better observing conditions.

3.3.3 ZHR

The average zenithal hourly rate is calculated for each block of rate data of optimal bin size by the formula

$$\text{ZHR} = \frac{0.5 + \sum_i N_i}{\sum_i \frac{T_{\text{eff},i}}{C_i}}, i = 1, 2, \ldots, k, \tag{2}$$

where k is the number of observing periods, N_i the number of meteors, $T_{\text{eff},i}$ the effective time and C_i the total correction factor in the observing period i .

The standard error of the average zenithal hourly rate is calculated by the formula

$$\sigma = \frac{\sqrt{0.5 + \sum_i N_i}}{\sum_i \frac{T_{\text{eff},i}}{C_i}}, i = 1, 2, \ldots, k. \tag{3}$$

The table of mean solar longitudes and ZHR values for each data block is printed in the results. The given solar longitude is the mean of observers' solar longitudes weighted by $\frac{T_{\text{eff},i}}{C_i}$. Greater weight is given to observing intervals of longer effective time under better observing conditions.

4 Example – Perseid 2018 peak analysis

We will illustrate how to use MetFnsApp on the example of the Perseids 2018 peak population index analysis. We will show how we chose parameters of the optimal bin size algorithm (minimum and maximum bin size and number of meteors) for each block of considered magnitude data.

In our analysis of the 2018 Perseids activity, we selected rate and magnitude data with a limiting magnitude of 5.5 and higher, percentage of obstruction of the field-of-view of 0% to 20% and a radiant elevation of at least 15 degrees. The selection of the filters in MetFnsApp is represented in Figure 1.

In this example, we will calculate values of the population index for the period around the Perseid peak, from August 12, $06^{\text{h}}15^{\text{m}}$ UT to August 13, 12^{h} UT. For the first rough profile, we chose the following bin size parameters: minimum bin size $k_{\text{min}} = 0.01$ ($\sim$ 15 min),

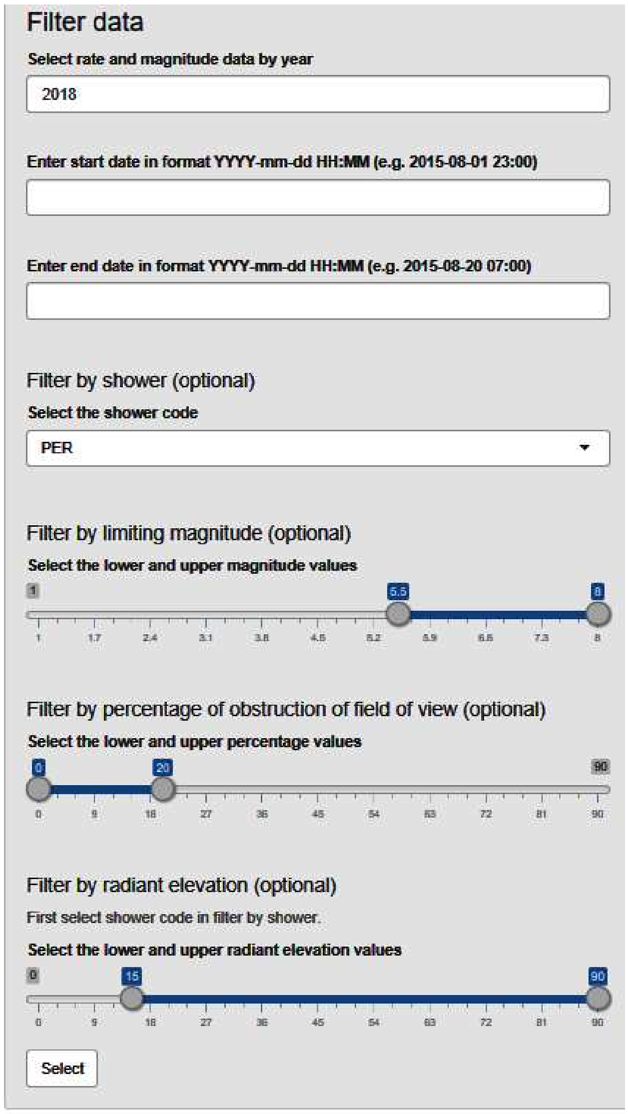

Figure 1 – Filters in MetFnsApp for the selection of the magnitude and rate data.

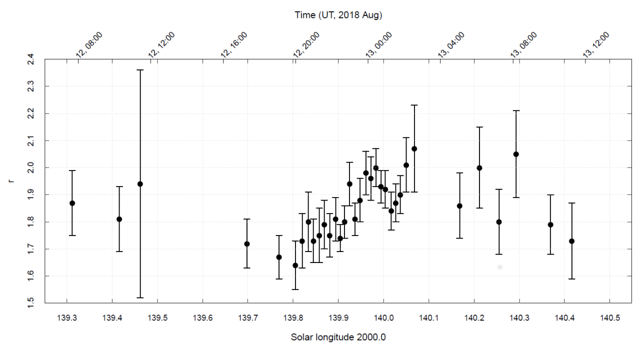

Figure 2 – Rough profile of the population index r in the period from August 12, $06^{\text{h}}15^{\text{m}}$ UT to August 13, 12^{h} UT.

maximum bin size $k_{\text{max}} = 0.16$ ($\approx$ 4 hours), number of meteors num = 100 (Figure 2). The parameters should allow us to see enough details and not too much scatter.

As a result we obtain Figure 2. It shows in total three ups and downs in the population index values, each of them defined with its own coverage with observing intervals. This implies the need to divide the considered period into three sub-periods, each with its own optimal bin size parameters.

We will take the first sub-period from August 12, $06^{\mathrm{h}}15^{\mathrm{m}}$ UT to August 12, 21^{h} UT and choose $k_{min} = 0.02$ (≈ 30 minutes), $k_{\max} = 1$ (≈ 24 hours), num $= 100$. In this sub-period, there is a sparse coverage with observing intervals, so we chose a much larger maximum bin size. The results are presented in Table 1.

Table 1 – Values of the population index r in the period from August 12, $06^{\mathrm{h}}15^{\mathrm{m}}$ UT to August 12, 21^{h} UT.

sollong	date	nINT	nPER	pop.index	r.error
139.312	2018-08-12 07:39:34	11	105	1.87	0.12
139.416	2018-08-12 10:15:33	11	104	1.81	0.12
139.619	2018-08-12 15:20:02	8	112	1.72	0.10
139.759	2018-08-12 18:49:59	7	112	1.74	0.10
139.797	2018-08-12 19:46:58	14	102	1.60	0.08
139.824	2018-08-12 20:27:27	49	256	1.77	0.07
139.840	2018-08-12 20:51:27	40	391	1.71	0.05

Now, we will plot the population index with the error bars. Based on the values in Table 1, we chose the following range of solar longitude values on the x-axis: 139.3 to 139.9, and the following range of population index values on the y-axis: 1.5 to 2. On both axes, we set increment 0.1 for the tick marks. On the secondary x-axes, we chose the range of dates from 2018-08-12 07:00 to 2018-08-12 21:00, with an increment of 2 hours. Selected parameters in MetFnsApp are presented in Figure 3 and the resulting plot of the population index in Figure 4.

We can see in Table 1 that the two last blocks of magnitude data (the lines with mean $\lambda_{\odot} = 139.824$ and $\lambda_{\odot} = 139.840$) do not follow the same pattern as the previous blocks. These two blocks are covered with a larger number of observing intervals, with almost 3-4 times larger number of meteors than the specified number. We will keep the first 5 lines of the table. The last two data blocks will be adjoined to the next sub-period. To determine the end of the 5th block, we should enter the following two commands directly into the R console:

```
pop12<-opt.bin(magper,date.start="2018-08-12
06:15",date.end="2018-08-12 21:00",shw="PER",
kmin=0.02,kmax=1,num=100)
```

```
max(pop12[[5]]$Sollong)
```

[1] 139.811

```
sollong_date(139.811,year=2018)
```

[1] "2018-08-12 20:07:58 UTC"

where *magper* is the filtered magnitude data saved from MetFnsApp and loaded into R. We first apply an optimal bin size algorithm to the selected data, find the maximum value of solar longitude in the 5th block and, finally, determine the date corresponding to this value. The optimal bin size algorithm returns a list of data blocks. Using [[*block number*]], we extract a particular data block and with $*column name*, we approach to the column values.

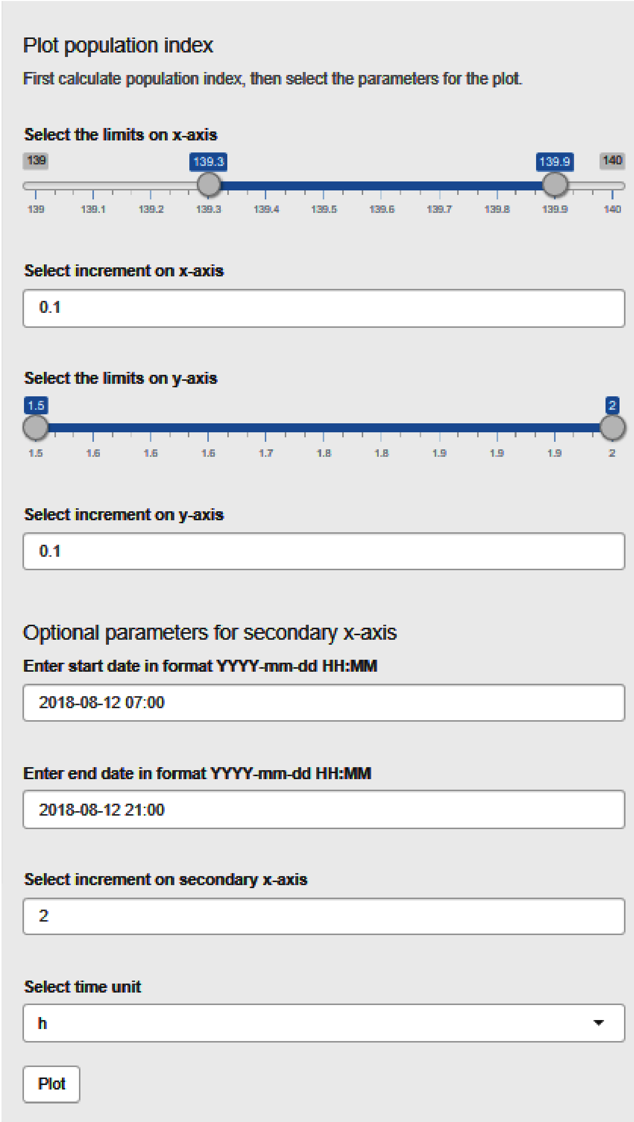

Figure 3 – Selected parameters in MetFnsApp for making a plot of the population index r in the period from August 12, $06^{\mathrm{h}}15^{\mathrm{m}}$ UT to August 12, 21^{h} UT.

Therefore, the next sub-period will start at $\lambda_{\odot} = 139.812$ (August 12, $20^{\mathrm{h}}09^{\mathrm{m}}$) and end on August 13, 05^{h}. We will take $k_{\min} = 0.02$, $k_{\max} = 0.16$, num $= 800$. There are many observing intervals in this sub-period, so we choose a higher value of number of meteors for the optimal bin size algorithm. The results are presented in Table 2.

Table 2 – Values of the population index r in the period from August 12, $20^{\mathrm{h}}09^{\mathrm{m}}$ UT to August 13, 05^{h} UT.

sollong	date	nINT	nPER	pop.index	r.error
139.836	2018-08-12 20:45:27	101	810	1.73	0.03
139.862	2018-08-12 21:24:27	88	848	1.79	0.04
139.886	2018-08-12 22:00:26	80	802	1.76	0.04
139.906	2018-08-12 22:30:26	90	936	1.78	0.03
139.924	2018-08-12 22:57:26	82	869	1.83	0.04
139.945	2018-08-12 23:28:55	69	867	1.84	0.04
139.966	2018-08-13 00:00:25	68	880	1.90	0.04
139.987	2018-08-13 00:31:54	82	894	1.94	0.05
140.007	2018-08-13 01:01:54	83	897	1.91	0.04
140.029	2018-08-13 01:34:53	69	940	1.86	0.04
140.059	2018-08-13 02:19:53	50	546	1.94	0.06

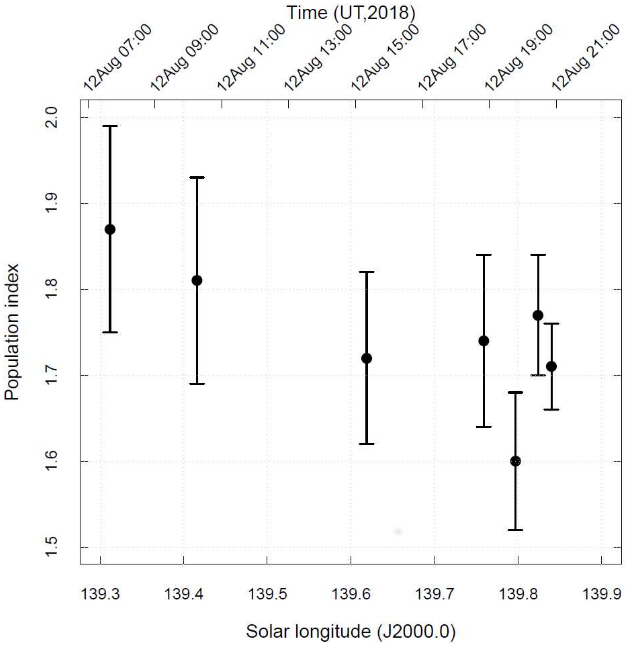

Figure 4 – Profile of the population index r in the period from August 12, $06^{\mathrm{h}}15^{\mathrm{m}}$ UT to August 12, 21^{h} UT.

We should investigate the properties of the observing intervals in the listed 11 magnitude data blocks. It turns out that the last block represents a mixture of European (with Israel) and Canadian intervals. We got the list of countries by typing these two commands into the R console:

```
popmax<-opt.bin(magper, date.start="2018-08-12
20:09", date.end="2018-08-13 05:00", shw="PER",
kmin=0.02, kmax=0.16, num=800)
```

```
popmax[[11]]$Country
```

From the 50 intervals in the 11th block (last line in Table 2), 41 of them belong to observing locations in Europe (with Israel) with radiant elevation ranging from 57.9 to 67.7 degrees and nine of them belong to observing locations in Canada with radiant elevation 26 to 38.5 degrees. As a reminder, observing conditions (measured with correction factors), enter not only into the calculation of the ZHR, but also into the calculation of the weighted mean solar longitude of data blocks for both population index and ZHR tables. In order to get a "purer" block, we will break the 11th block just before the mean solar longitude of the first Canadian interval, which is equal to $\lambda_{\odot} = 140.083$ (2018-08-13 02:55:51 UT). The last block of data ends at $\lambda_{\odot} = 140.082$ (2018-08-13 02:55 UT). The results are presented in Table 3 and in Figure 5.

Next, we will examine the effect of the parameter number of meteors of the optimal bin size algorithm in this sub-period. Figure 6 shows the population index profiles for 600, 800, and 1000 number of meteors. The minimum and maximum number of meteors are the same for all the graphs ($k_{\min} = 0.02$, $k_{\max} = 0.16$).

As we see in Figure 6, the pattern of the points is similar

Table 3 – Values of the population index r in the period from August 12, $20^{\mathrm{h}}09^{\mathrm{m}}$ UT to August 13, $02^{\mathrm{h}}55^{m}$ UT.

sollong	date	nINT	nPER	pop.index	r.error
139.836	2018-08-12 20:45:27	101	810	1.73	0.03
139.862	2018-08-12 21:24:27	88	848	1.79	0.04
139.886	2018-08-12 22:00:26	80	802	1.76	0.04
139.906	2018-08-12 22:30:26	90	936	1.78	0.03
139.924	2018-08-12 22:57:26	82	869	1.83	0.04
139.945	2018-08-12 23:28:55	69	867	1.84	0.04
139.966	2018-08-13 00:00:25	68	880	1.90	0.04
139.987	2018-08-13 00:31:54	82	894	1.94	0.05
140.007	2018-08-13 01:01:54	83	897	1.91	0.04
140.029	2018-08-13 01:34:53	69	940	1.86	0.04
140.049	2018-08-13 02:04:52	41	463	1.93	0.06

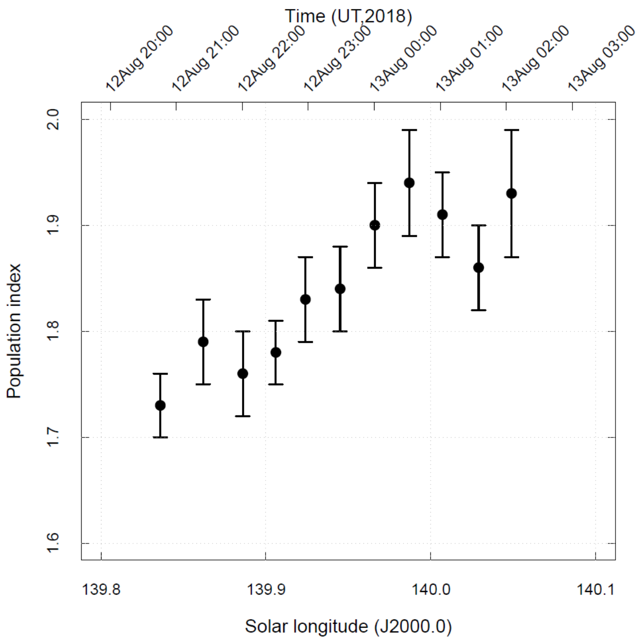

Figure 5 – Profile of population index r in the period from August 12, $20^{\mathrm{h}}09^{\mathrm{m}}$ UT to August 13,$02^{\mathrm{h}}55^{m}$ UT.

in all three graphs. In the last block of data, the standard error of the population index is larger on graphics made with 600 and 1000 meteors. The last block of data for num = 600 is made of 14 observing intervals with 107 Perseids observed in total, for num = 800 of 41 observing intervals with 463 Perseids and for num = 1000 of 29 observing intervals with 313 Perseids. When we take this into the consideration, choice of num = 800 meteors for the optimal bin size algorithm in this sub-period seems the best one.

For the third sub-period on August 13 from $02^{\mathrm{h}}56^{\mathrm{m}}$ to 12^{h}, we set the following optimal bin size algorithm parameters: $k_{\min} = 0.02$, $k_{\max} = 0.16$, num = 200. Results of the calculation are given in Table 4.

Table 4 – Values of the population index r in the period from August 13, $02^{\mathrm{h}}56^{\mathrm{m}}$ UT to August 13, 12^{h} UT.

sollong	date	nINT	nPER	pop.index	r.error
140.180	2018-08-13 05:21:19	18	213	1.96	0.10
140.265	2018-08-13 07:28:46	20	206	1.88	0.09
140.382	2018-08-13 10:24:12	21	184	1.81	0.08

Finally, we will produce a composite population index profile made from the values in three sub-periods: the

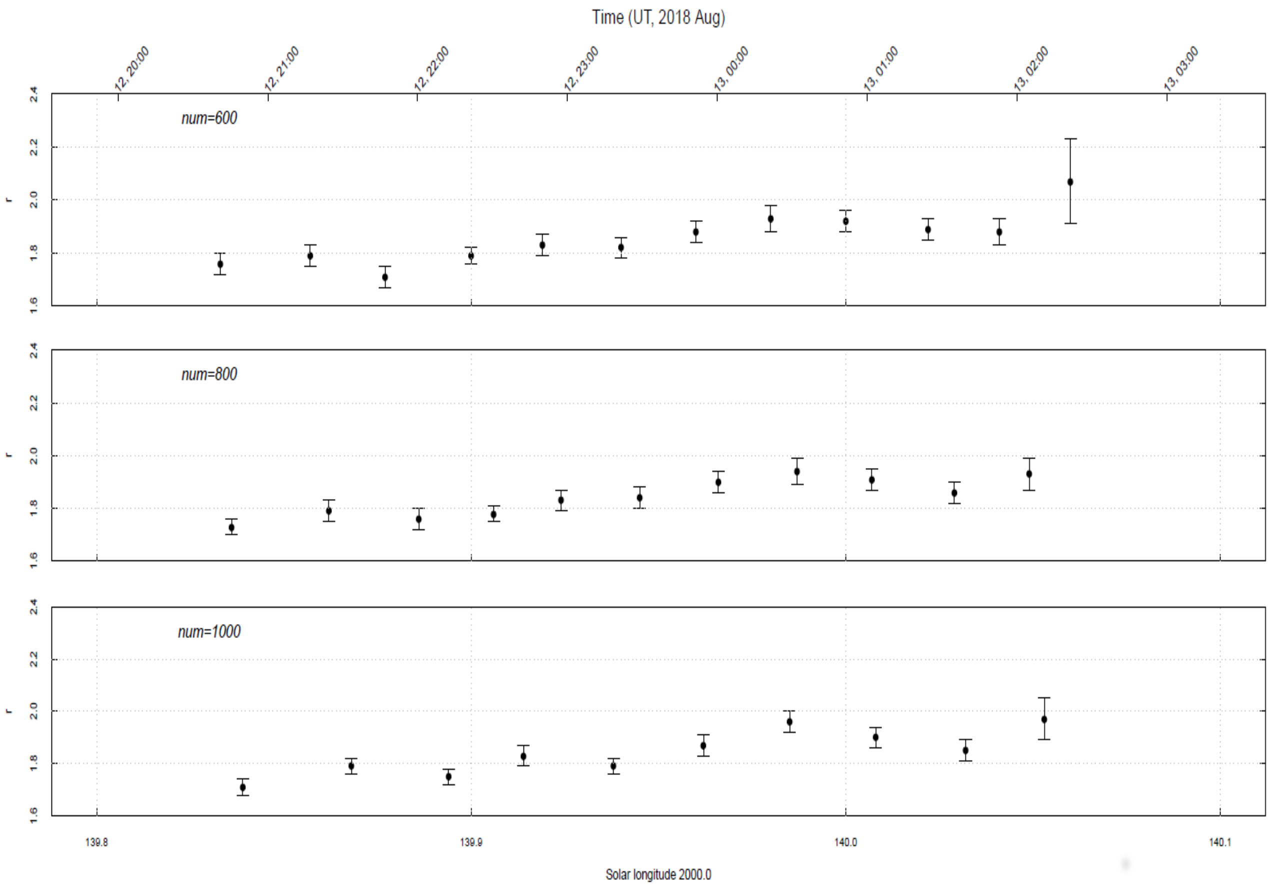

Figure 6 – Profile of the population index r in the period from August 12, $20^{\mathrm{h}}09^{\mathrm{m}}$ UT to August 13,$02^{\mathrm{h}}55^{m}$ UT, for number of meteors 600, 800 and 1000.

first five lines of Table 1 and all lines in Tables 3 and 4. The composite table of values is presented in Table 5 and the plot in Figure 7. The plot is made in R first by loading the *csv* file of the composite table of values and then by using the function *pop.index.plot* from the package MetFns.

Table 5 – Values of the population index r in the period from August 12, $06^{\mathrm{h}}15^{\mathrm{m}}$ UT to August 13, 12^{h} UT.

sollong	date	nINT	nPER	pop.index	r.error
139.312	2018-08-12 07:39:34	11	105	1.87	0.12
139.416	2018-08-12 10:15:33	11	104	1.81	0.12
139.619	2018-08-12 15:20:02	8	112	1.72	0.10
139.759	2018-08-12 18:49:59	7	112	1.74	0.10
139.797	2018-08-12 19:46:58	14	102	1.60	0.08
139.836	2018-08-12 20:45:27	101	810	1.73	0.03
139.862	2018-08-12 21:24:27	88	848	1.79	0.04
139.886	2018-08-12 22:00:26	80	802	1.76	0.04
139.906	2018-08-12 22:30:26	90	936	1.78	0.03
139.924	2018-08-12 22:57:26	82	869	1.83	0.04
139.945	2018-08-12 23:28:55	69	867	1.84	0.04
139.966	2018-08-13 00:00:25	68	880	1.90	0.04
139.987	2018-08-13 00:31:54	82	894	1.94	0.05
140.007	2018-08-13 01:01:54	83	897	1.91	0.04
140.029	2018-08-13 01:34:53	69	940	1.86	0.04
140.049	2018-08-13 02:04:52	41	463	1.93	0.06
140.180	2018-08-13 05:21:19	18	213	1.96	0.10
140.265	2018-08-13 07:28:46	20	206	1.88	0.09
140.382	2018-08-13 10:24:12	21	184	1.81	0.08

5 Conclusions

Thanks to the online Visual Meteor Data Base (VMDB) and the availability of the MetFns package and application, performing a global analysis of the visual observations of a meteor shower is now within reach of every meteor worker. This paper aims to show how these tools can be exploited to conduct high quality global analyses.

After a short introduction to the VMDB, MetFns and MetFnsApp, the basics of global analysis of a meteor shower were explained. The observations are distributed over bins in solar longitude (or, equivalently, time intervals) using a dedicated bin size algorithm which takes into account a minimum and maximum bin size and tries to accumulate at least a specified number of meteors in every bin. For every bin, the population index r and the Zenithal Hourly Rate (ZHR) can be calculated, accompanied by their error bars.

Since we think examples are the best way to learn, the authors described the iterative process that they followed for the analysis of the Perseids 2018 during the Visual Meteor Workshop right before the IMC 2018 in Pezinok. Indeed, an iterative process, since it is unlikely that the initial choice of bins will provide an optimal understanding of the real r or ZHR structure. Step by step and illustrated by figures and tables, the population index profile of the Perseids 2018 was derived for their

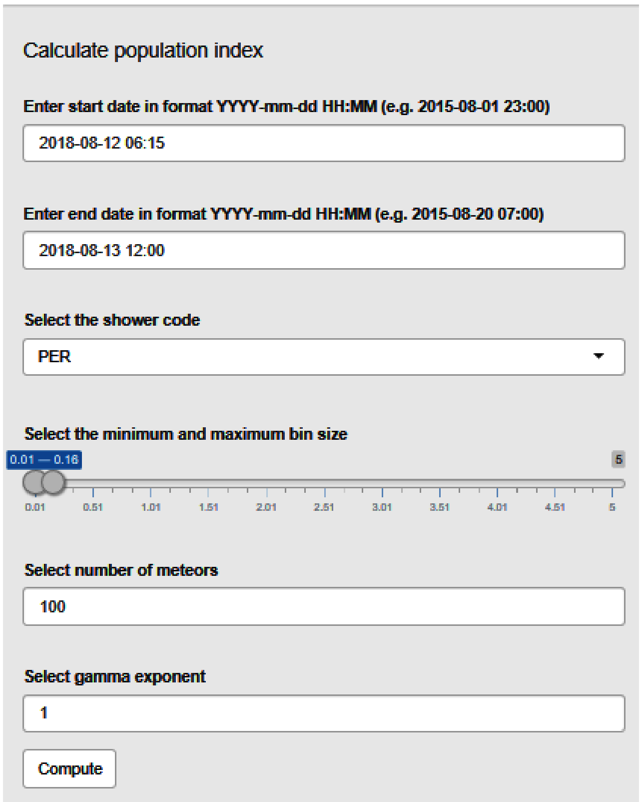

Figure 7 – Composite profile of the population index r in the period August 12, $06^{h}15^{m}$ UT to August 13,12^{h} UT.

peak period from August 12, $06^{h}15^{m}$ UT to August 13, 12^{h} UT.

First, we employed MetFnsApp to select the start and end date and time and the Perseids shower, and to filter the observation sessions by specifying the allowed range of limiting magnitude, percentage of obstructed field of view, and radiant elevation. We also selected a first trial value for the minimum and maximum bin size and the specified number of meteors per bin. Then, MetFnsApp calculated and plotted the resulting r profile.

It is no surprise that the resulting r profile looks a bit noisy, which is due to non-optimal binning. Based on the local minima and maxima ("ups and downs") in the r profile, we then split the period into three subperiods, and varied the minimum and maximum bin size and the specified number of meteors per bin separately for each of the subperiods. This allowed us to take into account the number of observation sessions, which of course was much higher close to the Perseid peak than before or after. We also took advantage of MetFns tools to investigate the influence of different radiant heights within one interval (e.g., the start of American observations with low radiant altitude when the European observations had a high radiant altitude). Trying out several values for the number of meteors per bin, we checked the influence of this parameter on the resulting r profiles and saw that it had little influence.

Finally, we joined the results for the three subperiods and had MetFnsApp plot the resulting profile, which is much more consistent than the original profile at first trial.

The authors hope you get tempted and inspired to try this out for yourself. We will be happy to provide support if needed.

References

Arlt R. (2003), "Bulletin 19 of the International Leonid Watch: Population index study of the 2002 Leonid meteors." *WGN, Journal of the IMO*, **31**, 77–87.

Rendtel J., Arlt R. (2017). "Handbook for Meteor Observers" (3rd edition), IMO.

Rendtel J., Veljković K., Weiland T., Verbeeck C., Knöfel, A. (2019), "Perseids 2018 – Analysis of Global Visual Data" *WGN, Journal of the IMO* **47**, 18–25.

Veljković K. (2017). "Demonstration of R package MetFns for analysis of visual meteor data." In: Gyssens, M. and Rault, J.-L., editors, *Proc. IMC Petnica, 2017*, 43–45.

Balloon-borne video observations of Geminids 2016

Francisco Ocaña[1], Alejandro Sánchez de Miguel[1,2,3], ORISON team, and Daedalus Project.

[1] **Dpto. de Fìsica de la Tierra y Astrofìsica, Facultad de Ciencias Fìsicas, Universidad Complutense de Madrid, E-28040 Madrid, Spain**
focana@sciops.esa.int

[2] **Environment and Sustainability Institute, University of Exeter, Penryn, Cornwall TR10 9FE, UK,**
a.sanchez-de-miguel@exeter.ac.uk

[3] **Instituto de Astrofísica de Andalucía, Glorieta de la Astronomía, s/n, C.P.18008 Granada, Spain**

We investigate the observation of meteors with video cameras in stratospheric balloons, overcoming tropospheric handicaps like weather and extinction. We have studied the practical implementation of the idea, designed and tested instrumentation for balloon-borne missions. We have analysed the data of the Geminids 2016 campaign, determining the meteoroid flux just before the maximum.

1 Introduction

This text is an adaption of the work by the first author for his PhD Thesis: Techniques for near-Earth interplanetary matter detection and characterisation from optical ground-based observatories (Ocaña, 2017). Refer to his thesis for further detail. The lines here are a summary of the presentation given, for the sake of completeness of these proceedings of the IMC 2018 in Pezinok-Modra. The multimedia material shown during the presentation at IMC 2018 can be found in the Zenodo repository for the ORISON Project and Daedalus Project. Zenodo is an open-access repository aimed for datasets, it provides them a Data Object Identifier (DOI) and it is intended for otherwise orphan records, making them easier to cite. All our datasets are licensed under Creative Commons Attribution 4.0 [CC BY 4.0] (i.e., you are free to share, adapt, use or whatever, just give appropriate credit). Moreover the authors encourage you to use the data and contact them for more details.

These are the DOI of the three datasets:

- Geminids 2016 - Part 1 : https://doi.org/10.5281/zenodo.579708 (Sánchez de Miguel & Gomez, 2017a)
- Geminids 2016 - Part 2 : https://doi.org/10.5281/zenodo.801598 (Sánchez de Miguel & Gomez, 2017b)
- Geminids 2016 - Part 3 : https://doi.org/10.5281/zenodo.842269 (Sánchez de Miguel & Gomez, 2017c)

2 Balloon-borne meteoroid flux determination: Geminids 2016 show-case

In order to determine meteoroid fluxes, the area surveyed by a sensor is calculated as the projection of the field of view onto the meteor layer. The method employed here is a generalization of the method defined by Koschack and Rendtel (1990) and later applied for cameras by Bellot Rubio (1994b). The work by the first author (Ocaña, 2017) includes the height of the observer, h_b, as an extension for airborne and balloon-borne observations. Measurements are limited to horizon elevation due to the difficulties to correct for extinction.

To perform the observations of Geminids, we used the balloonborne platform developed by Daedalus project. Since 2011, when we sent a low-light video camera to observe the Draconids 2011 outburst (Ocaña et al., 2013), they carried a meteor detection payload for 8 nighttime missions so far. Since 2016 the payloads have flown onboard the ORISON Pathfinder missions. ORISON is a H2020 project to study feasibility of innovative astronomical research infrastructure based on stratospheric balloons (Ortiz Moreno et al., 2016).

ORISON project provided new hardware, and the B&W low-light 1/2" CCD video camera was replaced by a full-frame colour CMOS videocamera with better sensitivity, a Sony α7S (formally Sony ILCE-A7S). The colour information provides basic spectral information from the objects (Ocaña et al., 2012). The Sony α7S is an EVIL (Electronic Viewfinder with Interchangeable Lens) camera with a backlit CMOS sensor and a self-recording system included. The camera hosts a full-frame format (35.6 mm $\times$ 23.8 mm Exmor$^{\mathrm{TM}}$) CMOS sensor with a total of 12.2 megapixels and a pixel size of 8.4 μm and a sensitivity up to 409600 ISO. The nominal configuration we use for the record of meteors is full-HD-1080p colour frames (1920 x 1980 pixels = 2 Mpix), at 30 fps with $\frac{1}{50}$ s exposure time and sensitivity of 60000 ISO (over that value the noise increases with no apparent increase of sensitivity). The video is stored in clips of 1m44s with a data rate of 50 Mbps, and a total filesize of 650 MB. The format of the video is MPEG-4 Part 14 (international standard ISO/IEC

14496-14:2003), using the Sony proprietary codec for professional videos XAVC S.

The camera has been flown in several missions, some of them during meteor shower peaks. We have selected one as a show-case. For Geminids 2016 the lens we used is a Samyang with a focal length of 24 mm and f/1.5, that produces a slight vignetting in the corners of the full format chip.

We have analysed the astrometry of the image splitting the video in all the frames, and each frame in the R, G, B channels. Using the suite `astrometry.net` (Lang et al., 2010) we calculated the plate constants. The plate scale of the system in video mode is 153 arcsec/pixel. Measured PSF for the stars in the FoV has a FWHM of 460 arcsec on average, in the range of a critical sampling frequency according to the Nyquist theorem. The field of view is $82^\circ \times 46^\circ$ with the centre at $hf = 0^\circ$.

The launch took place at 23h17m UT the 13$^{\text{th}}$ December 2016 and the burst took place at 01h50m UT. In total the mission lasted 276 minutes as the probe landed at 03h55m UT. The first visual inspection of the video shows stable and unstable phases. We have used the date from the 3-axis accelerators to identify these phases using the Lomb method for frequency analysis (Lomb, 1976; Ruf, 1999). During the whole mission we find a constant 1-second vertical tilt and 3 to 8-second roll movement (partial rotation along the optical axis). The other movement present is the rotation around the vertical axis of the probe, that results in a panning movement of the camera along the whole range of azimuth. The period of this movement changes during the different phases, and we define the stable phases when the period is larger than 6 minutes, that corresponds to a movement of 1°/s. This selection yields a useful period of 5 consecutive clips, for a total of 8 minutes and 40 seconds, from 01h40m UT on.

The video is analysed by visual inspection and only the upper half of the frame is considered (elevation$> 0^\circ$), yielding an effective field of view of $82^\circ \times 23^\circ$. For the meteor count we have followed the visual analysis method as described in (Jenniskens, 1999). As Jenniskens states the researcher only detects 70% ± 30% during the first visualisation, and up to 3 viewings were needed for our video clips. Star limiting magnitude was calculated measuring frames in G band with V magnitudes from catalogue, and meteor magnitudes were derived by visual comparison with stars. The star limiting magnitude is 6.0 for the period analysed, and we get the same value for the meteor video limiting magnitude vlm as the magnitude loss due to the meteor speed is < 0.1 magnitudes thanks to slow speed of meteors when pointing to the horizon.

The area monitored was 525729 km^2 and the correction factors yielded an effective area A_{red}=26110 km^2. For the full period we get an average value of $(15 \pm 3) \cdot 10^{-3}$ meteoroids km^{-2}h^{-1} producing meteors brighter than magnitude 6.5 (meteoroid mass > 0.6 mg). There are no published results available for Geminids 2016, but the shower is stable through years and we can compare with other values from literature for solar longitude 261.1°, which range between 15 to 60 meteoroids km^{-2}h^{-1} (Molau et al., 2013; Blaauw et al., 2014; Neslušan, 2015; Blaauw, 2016). Therefore our results for Geminids 2016 from balloon-borne observations are in agreement with the values from previous years.

References

Blaauw R. (2016). “Mass Index and Mass of the Geminid Meteoroid Stream as Found with Radar, Optical, and Lunar Impact Data”. *NASA Technical Reports Server.*

Blaauw R., Campbell-Brown M., and Cooke W. (2014). “Characteristics of the 2012 Geminids”. *NASA Technical Reports Server.*

Jenniskens P. (1999). “Activity of the 1998 Leonid shower from video records”. *Meteoritics & Planetary Science*, **34:6**, 959–968.

Lang D., Hogg D. W., Mierle K., Blanton M., and Roweis S. (2010). “Astrometry. net: Blind astrometric calibration of arbitrary astronomical images”. *The Astronomical Journal*, **139:5**, 1782.

Lomb N. R. (1976). “Least-squares frequency analysis of unequally spaced data”. *Astrophysics and Space Science*, **39:2**, 447–462.

Molau S. et al. (2013). “Monthly Reports of the AKM/IMO Video Meteor Network”. `http://www.imonet.org/reports/` . IMONET website.

Neslušan L. (2015). “A summary of the research of Geminid meteoroid stream”. *Contrib. Astron. Obs. Skalnaté Pleso*, **45**, 60–82.

Ocaña F. (2017). *Techniques For Near-Earth Interplanetary Matter Detection And Characterisation From Optical Ground-Based Observatories.* PhD thesis, Universidad Complutense de Madrid.

Ocaña F., Zamorano J., de Miguel A. S., Izquierdo J., Gallego J., Palos M., Muñoz-Ibáñez B., Rodríguez-Coira G., García R., Santamaría A., and others (2013). “First scientific results of the Fireball Detection Station at UCM Observatory”. In Gyssens M. and Roggemans P., editors, *Proceedings of the International Meteor Conference, 31st IMC, La Palma, Canary Islands, Spain, 2012*, volume 1. pages 178–181.

Ocaña F., Zamorano J., and Gallego J. (2012). “Narrow-band photometry of meteors”. In Gyssens M. and Roggemans P., editors, *Proceedings of the International Meteor Conference, 30th IMC, Sibiu, Romania, 2011.* pages 48–52.

Ortiz Moreno J. L., Mueller T., Duffard R., Juan Lopez-Moreno J., Wolf J., Schindler K., and Graf F. (2016). "ORISON, a stratospheric project". In *41st COSPAR Scientific Assembly*, volume 41. pages PSB.1–31–16.

Ruf T. (1999). "The Lomb-Scargle periodogram in biological rhythm research: analysis of incomplete and unequally spaced time-series". *Biological Rhythm Research*, **30:2**, 178–201.

Sánchez de Miguel A. and Gomez M. Á. (2017a). "Geminids 2016 (part 1)".

Sánchez de Miguel A. and Gomez M. Á. (2017b). "Geminids 2016 (part 2)".

Sánchez de Miguel A. and Gomez M. Á. (2017c). "Geminids 2016 (part 3)".

Using SPADE for radio meteor observations

Antonio Martínez Picar[1] and Christophe Marqué[1]

[1] **Solar-Terrestrial Centre of Excellence – Royal Observatory of Belgium**
Av. Circulaire 3, 1180 Brussels, Belgium
antonio.martinez@observatory.be

The Small Phase Array DEmonstrator is a solar radio instrument being built in the Humain Radio-Astronomy Station by the Royal Observatory of Belgium. Although its main goal is performing solar radio observations in the frequency range of 20 – 80 MHz, observing radio meteors using the Belgian Radio Meteor Stations (BRAMS) beacon based on forward-scatter techniques is possible. In this work we present some preliminary results towards its first light.

1 Introduction

The Royal Observatory of Belgium is currently building the Small Phased Array DEmonstrator (SPADE) in the premises of the Humain Radio-Astronomy Station (HuRAS), which is located about 100 km south-east of Brussels.

The frequency range intended for SPADE is 20–80 MHz and its operation design is based on the *beamforming* principle which allows, using a set of many very simple (and inexpensive) antennas, mimicking of the performance of a single complex (and expensive) steerable dish antenna system.

SPADE's main hardware structure has been almost totally installed at HuRAS but a proof-of-concept was needed in order to test the basic performance of the array elements.

A similar radio-telescope had successfully registered meteor echoes (Helmboldt et al., 2014), and the Perseids (007 PER) major meteor shower of mid-August 2018 offered an excellent opportunity to run such a test.

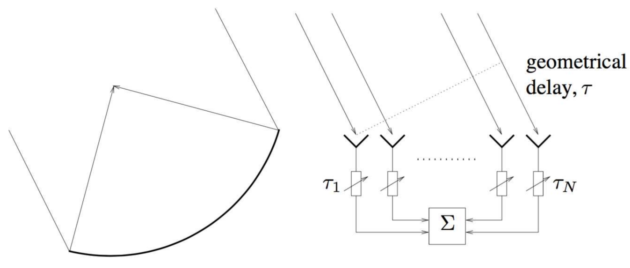

Figure 1 – Comparative diagram of the orientation technique performed with a classical single dish radio-telescope (left) and a phase array telescope (right).

2 SPADE description

Phased array radio telescopes consist of a series of small antennas instead of a single large dish. Those antennas are required to have a large field-of-view (FOV), allowing them to receive signals from all over the sky simultaneously. The radio telescope is then oriented to the direction of interest by combining the signals from each array antenna element after correcting for the geometrical delay (see Fig. 1).

The SPADE array includes a total of eight *tied-fork dipole*[1] fixed antennas that offer a convenient frequency range and a broad antenna pattern (*i.e.,* wide FOV). Each antenna has a built-in Front-End Electronics (FEE) board which includes an active-balun (∼24.5 dB of gain and noise temperature 250 K when terminated in 50 Ω), a local voltage regulator, an integral 5$^{\text{th}}$ order Butterworth filter, transient protection, and an additional Low Noise Amplifier which adds 12 dB of gain to handle cable losses without affecting noise performance (Hicks et al., 2012).

A series of simulations considering different antenna array layouts led us to select an evenly-spaced, 11-m diameter circular distribution around a central antenna due to its satisfactory ratio of combined gain *vs* reduced side lobes levels.

In order to mitigate ground and variable soil conditions losses, a 20 m × 20 m *ground plane* consisting of 15 cm × 15 cm ∅ 6 mm galvanized welded wire mesh material was deployed beneath the antennas after leveling and flattening the terrain, for which more than 500 tons of material was required.

Each antenna FEE is powered through a RG-213 coaxial cable (+600 m in total for the whole system) using a Bias-T device. Figure 2 shows a general view of the SPADE array field at HuRAS.

3 Test setup

During the second week of August 2018, an on-site test of the installed hardware of SPADE was scheduled. Taking into account that the BRAMS beacon operating frequency $f_{\mathrm{T_x}} = 49.97$ MHz (Lamy et al., 2011) lies in SPADE's observational range, it appeared a good opportunity to test the installed hardware by means of receiving radio-echoes from the Perseids (007 PER) major meteor shower employing the *forward-scatter* technique (McKinley, 1961).

[1] Also found as *inverse thick Vee* in some literature.

Figure 2 – General view of the SPADE array field in HuRAS.

Three SPADE antennas (array elements, AE) were selected for the test. The input of an analog receiver *Icom IC-PCR1500* was connected to the AE-3, while the AE-6 was connected to the input of a *FUNcube Dongle Pro+* (FCD) receiver[2]. Additionally, the output of AE-0 was directly connected to an *Agilent CXA N9000A* spectrum analyser (SA). A *Sorensen SRL 20-25* power supply provided the +12 V required by the three AE's FEEs to operate.

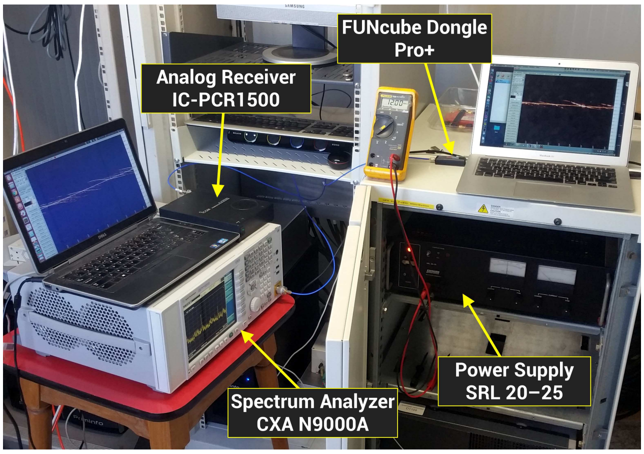

Figure 3 – View of the setup used for testing the hardware of SPADE.

Each receiver (appropriately tuned to 49.969 MHz[3] and working in *upper sideband* reception mode) delivered the signal directly to a laptop equipped with the software *Spectrum Lab*[4] which, running under the typical BRAMS receiving station parameters (*i.e.,* using its standard `config` file), allows registering periodically the received signal in `WAV` format, and storing a spectrogram image in `JPG` file format[5]. The SA was set up as a "narrow-band receiver" through its *zero span* mode, using a resolution bandwidth of 3 kHz and a video bandwidth of 10 Hz. Figure 3 shows a view of the equipment employed during the test.

4 Results

Between 8th and 12th of August 2018 both receivers and the SA were employed to record forward-scattered signals from meteor trails during different observational periods. In particular, the IC-PCR1500 analog receiver accumulated 65.1 hours of observation in which a sum of 7765 radio meteor echoes where registered and, afterwards, counted manually. Similar values were obtained with the FCD.

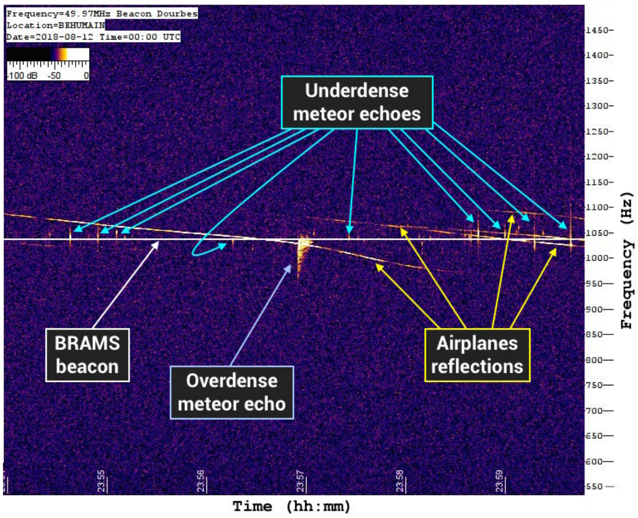

Figure 4 – Spectrogram obtained by SPADE (AE-3 + analog receiver) during the night of 11/12 August 2018.

Figure 4 shows in particular a spectrogram obtained during the night of 11th to 12th of August 2018 containing many of the typical features observed by a standard BRAMS receiving station: The horizontal continuous line corresponds to the beacon signal received directly by the antenna, the long lasting curved lines are reflections of the radio wave by airplanes, the short-lived vertical *spikes* are underdense radio meteor echoes, and

[2]http://www.funcubedongle.com

[3]Corresponding to $f_{\mathrm{Tx}} - 1$ kHz, a common practice to avoid undesirable DC and low frequency noise.

[4]https://www.qsl.net/dl4yhf/spectra1.html

[5]http://brams.aeronomie.be

the *diffuse blob* registered shortly before 23^h57^m(around the centre of the spectrogram) is a long-lasting overdense radio meteor echo (Lamy et al., 2017). Please notice that the frequencies on the vertical axis of the figure are those of the demodulated signal (*i.e.,* audio frequencies).

Figure 5 shows two different examples of power profiles obtained during the observational campaign. Both plots show great similarity with theoretical curves obtained for underdense (*top*), and overdense (*bottom*) radio meteor echoes (*see, e.g.,* Belkovich, 2006).

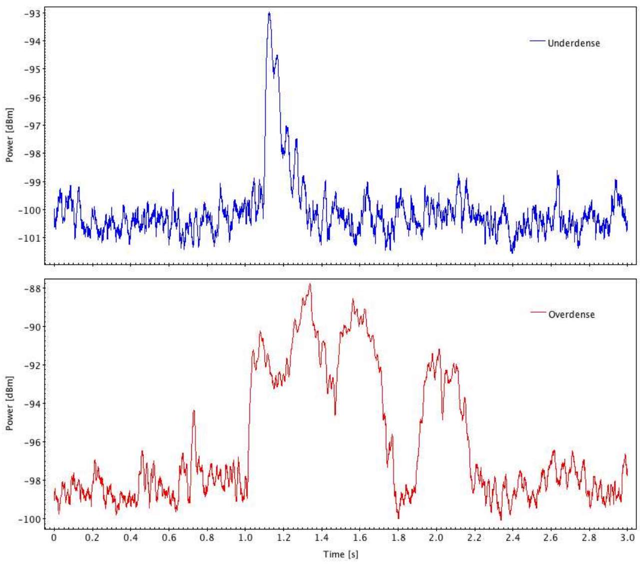

Figure 5 – Power profiles of underdense (*top*) and overdense (*bottom*) meteor echoes registered with the SA. The scale on the x-axis represents the elapsed time, starting on some arbitrary moment.

It is worth mentioning that even the oscillations in the declining part of the underdense meteor profile due to the scattering of the signal over the *Fresnel zones* of the meteor trail (Wislez, 2006) are easily recognizable on the plot.

5 Conclusions

The project is at present in its very last development stage, facing the challenge to be completed before the end of 2018. However, the results showed in this work have proven unmistakably the capability of SPADE to observe radio meteor echoes.

Currently the efforts of the project's team are focused on the *beamformer* development. Once the beamforming scheme is implemented, the tied-array beam will have a higher combined gain, allowing detection of even fainter radio meteor echoes. Additionally, the functionality of steering the beam allows pointing the beam towards a convenient area of the *potential reflection zone* in the sky (Verbeeck, 1995), increasing the probability of receiving radio echoes from specific meteor showers.

There is still work to be done, however the results obtained during this test and the promising capability of the fully operational instrument encourage the team to finalize the project in the forthcoming months.

Acknowledgements

The authors wish to thank Marc De Knijf, Aydin Ergen, Vincent Honet, Phillipe Motte, and the rest of the ROB's Technical Services department for their prompt and effective implementation of all necessary tasks to successfully complete this mission.

References

Belkovich O. I. (2006). "The physics of backscattering of radio waves from ionized meteor trails". In Verbeeck C. and Wislez J.-M., editors, *Proceedings of the Radio Meteor School*. pages 27–33.

Helmboldt J. F., Ellingson S. W., Hartman J. M., Lazio T. J. W., Taylor G. B., Wilson T. L., and Wolfe C. N. (2014). "All-sky imaging of meteor trails at 55.25 MHz with the first station of the Long Wavelength Array". *Radio Sci.*, **49**, 157–180.

Hicks B. C., Paravastu-Dalal N., Stewart K. P., Erickson W. C., Ray P. S., Kassim N. E., Burns S., Clarke T., Schmitt H., Craig J., Hartman J., and Weiler K. W. (2012). "A wide-band, active antenna system for long wavelength radio astronomy". *Publications of the Astronomical Society of the Pacific*, **124**, 1090–1104.

Lamy H., Calders S., Tétard C., Verbeeck C., Martinez Picar A., and Gamby E. (2017). "The Radio Meteor Zoo: searching for meteors in BRAMS radio observations". In *European Planetary Science Congress*. pages EPSC2017–714.

Lamy H., Ranvier S., de Keyser J., Calders S., Gamby E., and Verbeeck C. (2011). "BRAMS: the Belgian RAdio Meteor Stations". In Cooke W. J., Moser D. E., Hardin B. F., and Janches D., editors, *Meteoroids: The Smallest Solar System Bodies*. pages 351–356.

McKinley D. W. R. (1961). *Meteor science and engineering*. New York, McGraw-Hill.

Verbeeck C. (1995). "The Spatial Distribution of Potential Forward Scatter Reflection Points". *WGN, Journal of the International Meteor Organization*, **23**, 236–243.

Wislez J.-M. (2006). "Meteor astronomy using a forward scatter set-up". In Verbeeck C. and Wislez J.-M., editors, *Proceedings of the Radio Meteor School*. pages 84–106.

Spurious meteoroid orbits from video observations

Maria Hajdukova[1] and Leonard Kornos[2]

[1] **Astronomical Institute of the Slovak Academy of Science, Bratislava, Slovakia**
astromia@savba.sk

[2] **Faculty of Mathematics, Physics and Informatics, Comenius University, Bratislava, Slovakia**
kornos@fmph.uniba.sk

The present study demonstrates how strong the influence of measurement errors on the resulting meteoroid orbit is. The semi-major axis a, which defines the type of the orbit, depends considerably upon the derived heliocentric velocity and, thus, speed measurements and their precision are of the greatest importance. The range of heliocentric velocities at $r=$ 1 AU is relatively narrow, which indicates the high sensitivity of this influence. We concentrate on the regions where the occurrence of meteoroid orbits is exceptionally rare. Here belong hyperbolic orbits that might indicate an interstellar origin but which can easily be caused by measurement errors transferring near-parabolic orbits over the parabolic limit. The error required for this change need not be large; the higher the heliocentric velocity of the meteoroid, the smaller the error needed. Another region which deserves particular attention is the intermediate part of the bimodal entry or geocentric velocity distribution (v_{inf} between 45 and 55 kms^{-1}) which corresponds to nearly perpendicular encounters. In this case, measurement errors can produce an enhancement of particles of small perihelion distances.

1 Introduction

Rapidly-developed video techniques which produce a massive number of meteoroid orbits has become extremely important for statistical evidence on the nature of the meteoroid population. The use of the orbits on an individual basis, however, requires high accuracy data to ensure that the resulting analyses are not biased by the effects of measurement and determination errors. Discriminating between orbits of different natures for individual meteoroids is demanding, even for the most accurate photographic meteors (Hajdukova & Wiegert, 2019; Hughes & Williams, 2000; Kresák & Kresákova, 1976). For fainter meteors obtained by video techniques, this discrimination is for some kinds of orbits almost critical. The difficulty arrives from the methods used for both the measurement of meteor position and speed. Most of the orbits determined from video meteors are systematically biased due to underestimation of their initial velocities, subsequently shifting determined semi-major axes towards lower values (Hajduková et al., 2017). Improving accuracy involves also numerical ablation modelling and additional assumptions about the composition of each meteoroid (Vida et al., 2018). For our analysis, we use 251805 video meteors from the European Video Meteor Network Database (EDMOND, Kornoš et al. (2014)).

2 Hyperbolic orbits

The influence of inaccurate velocity measurements (considering different observational techniques) on the resulting orbit was examined by several authors (Egal et al. (2014); Moorhead et al. (2017); Skokic et al. (2016); Štohl (1970) and others). Based on Kresák & Kresákova (1976), we demonstrate the effect of measurement errors in both the radiant position and the velocity, with a diagram showing the correlation between the non-atmospheric velocity v_{inf} (or geocentric velocity v_G) and the angular elongation of the apparent radiant from the apex, ϵ_A (Figure 1). Resolutions needed to distinguish between different kinds of orbits can be deduced from the graph. To discriminate between a long-period orbit and a hyperbolic orbit needs a resolution about ±1 kms^{-1} in speed and ±1-2 deg in radiant coordinates. This requires higher accuracy measurements than the above-mentioned values, which by video observations is rarely fulfilled. The result, seen on the graph in Figure 1, is a huge amount of orbits that fall behind the parabolic limit (red crosses). This clearly demonstrate that distinguishing a real hyperbolic orbit from an apparent one is a significant challenge.

3 Low-perihelion distance orbits

The distribution of meteoroid orbits around the sun (the concentration of short-period orbits in the ecliptic plane and the random distribution of long-periodic orbits' planes) more or less reflects their various origins (short-period comets, asteroids, long-period high-inclined or retrograde comets, etc.). When observing meteors from the Earth, apex and antapex effects, stressed by the distribution of the planes of meteoroid orbits, result in a bimodal distribution of the velocities with respect to the Earth (Jenniskens, 2006; McKinley, 1961; Millman & McKinley, 1963). The behavior of the velocity distribution curve also depends on the technique of observation and method used for the velocity determination (Brown et al., 2005; Koseki, 2015).

Concerning measurement errors, the intermediate part between the two maxima of the distribution can be used as another example which may reveal their influence. Based on Kresák & Kresákova (1976), we con-

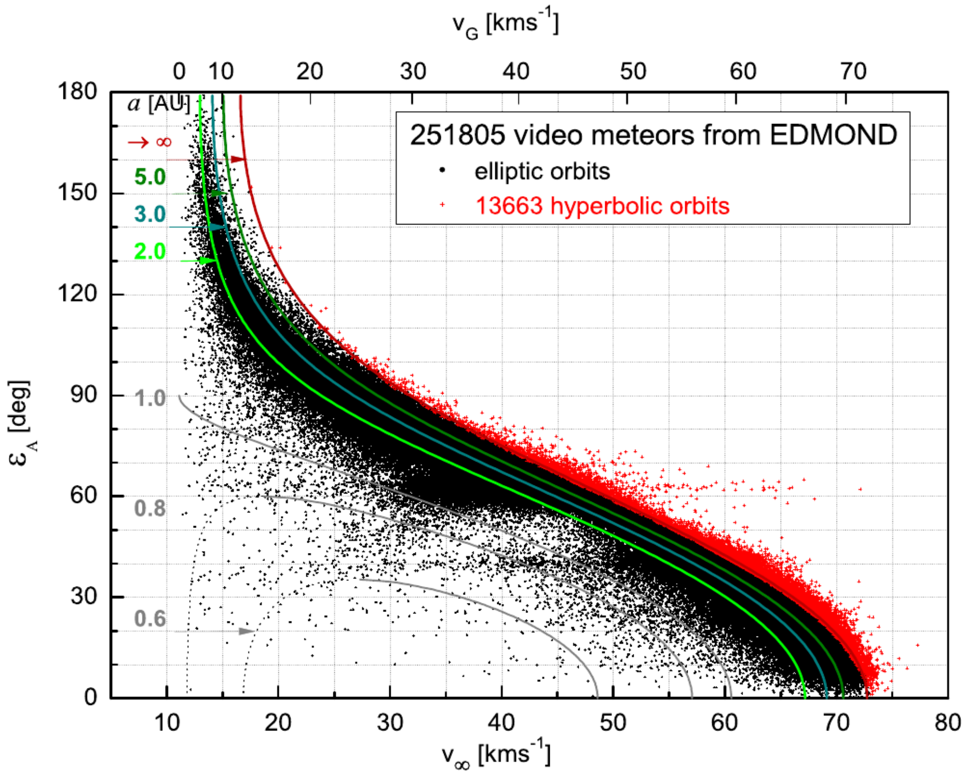

Figure 1 – The angular elongation of the apparent radiant from the apex is plotted against the non-atmospheric velocity of meteors from the EDMOND data in which 5.4% orbits were determined as hyperbolic (red crosses). The curves represent orbits with different values of semi-major axes a.

structed graphs showing the relation between the perihelion distance and the encounter velocity (Figure 2). Meteors are distributed into two zones, corresponding to the two maxima of the velocity distribution. Entry-velocities about 50 kms^{-1} correspond to nearly perpendicular crossings of orbits. This requires either a 90 deg inclination or low-perihelion distance orbits. Both kinds of orbits are rather rare.

The low number of low-perihelion orbits is emphasized by the fact that many objects on these orbits vaporize when passing too close to the sun. But, many of these orbits can easily result from the dispersion of the measured velocity (Figure 2). All the medium velocity meteors from the ecliptic plane will be attributed to orbits with small perihelions (Kresák & Kresáková, 1976). Thus, a random dispersion of velocity errors is able to produce a strong non-random bias towards small perihelion distances. Measurement errors, in this case, create another population of spurious orbits, or at least, an enhancement of low-perihelion orbits.

4 Conclusions

In the present study, we showed the influence of measurement errors on the resulting meteoroid orbit using video meteors from the EDMOND data. We concentrated on orbits which are exceptionally rare and can easily be caused by measurement errors. Here belong (1) hyperbolic orbits and (2) orbits with low-perihelion distances and velocities around the gap of the bimodal velocity distribution (v_{inf} between 45 and 55 kms^{-1}). In both cases, large dispersion of the measurement errors, can produce an enhancement of these kinds of orbits. Therefore, high accuracy is as important for the observations and measurements as for the meteor trajectory determination and meteoroid orbit calculation. Moreover, each analysis that uses the rough velocity data without a proper error examination will be seriously affected by measurement errors.

Acknowledgement

The work is supported by Slovak grants APVV-16-0148 and VEGA 2/0037/18

References

Brown P., Jones J., Weryk R., and Campbell-Brown M. (2005). “The velocity distribution of meteoroids at the earth as measured by the canadian meteor orbit radar (cmor)”. In *Modern Meteor Science An Interdisciplinary View*, pages 617–626. Springer.

Egal A., Vaubaillon J., Colas F., and Atreya P. (2014). “Low dispersion meteor velocity measurements with cabernet”. In *Proceedings of the International Meteor Conference, Giron, France, 18-21 September 2014*. pages 49–51.

Hajduková M. J., Koten P., Kornoš L., and Tóth J. (2017). “Meteoroid orbits from video meteors. the case of the geminid stream”. *Planetary and Space Science*, **143**, 89–98.

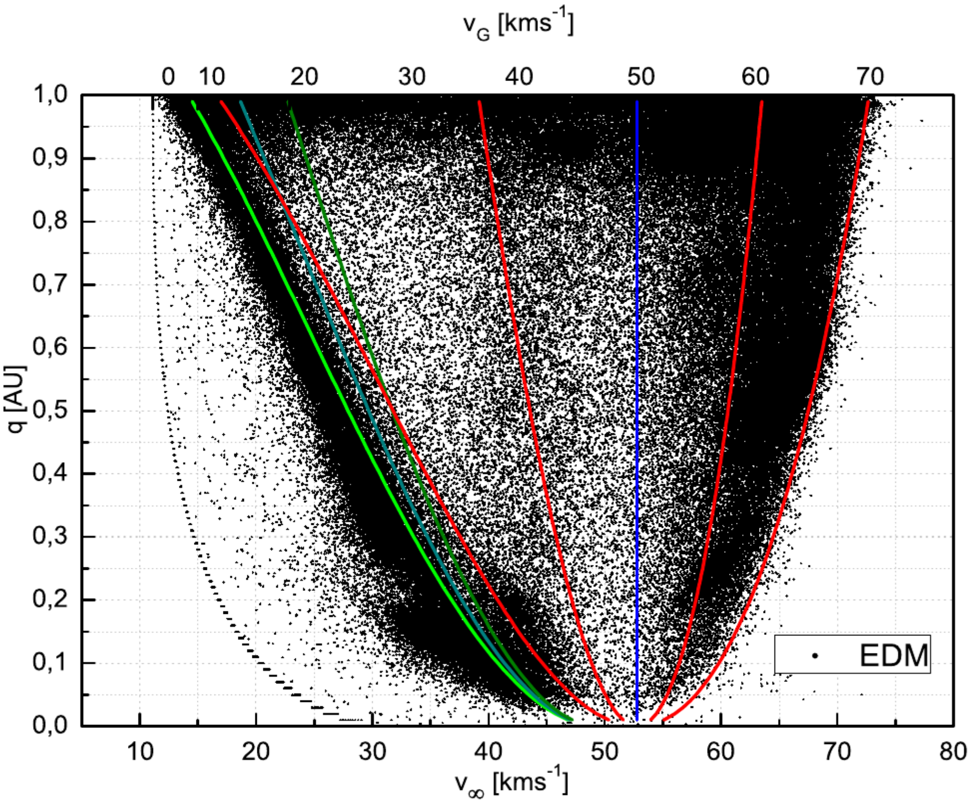

Figure 2 – The perihelion distance q of the meteoroid orbit is plotted as a function of the non-atmospheric velocity v_{inf} or geocentric velocity v_G of meteors from the EDMOND database. The curves represent different types of orbits: elliptical orbits with aphelia at the orbit of Jupiter for the inclination of 0 deg (light green), 20 deg (dark cyan) and 30 deg (olive green), respectively; and parabolic orbits for inclinations 0, 60, 120, 180 deg (red) and 90 deg (blue).

Hajdukova, M. S. V. and Wiegert P. (2019). "". In Ryabova, G. O., Asher, D. J., Campbell-Brown, M., editor, *Interstellar Meteoroids. Meteoroids: Sources of Meteors on Earth and Beyond*, page . Cambridge University Press (submitted).

Hughes D. W. and Williams I. P. (2000). "The velocity distributions of periodic comets and stream meteoroids". *Monthly Notices of the Royal Astronomical Society*, **315:3**, 629–634.

Jenniskens P. (2006). *Meteor showers and their parent comets*. Cambridge University Press.

Kornoš L., Koukal J., Piffl R., and Tóth J. (2014). "EDMOND Meteor Database". In Gyssens M., Roggemans P., and Zoladek P., editors, *Proceedings of the International Meteor Conference, Poznan, Poland, 22-25 August 2013*. pages 23–25.

Koseki M. (2015). "What do we see as ant, apex and toroidal sources?-what meteors are, where meteors came from, where meteoroids are going". *WGN, Journal of the International Meteor Organization*, **43**, 127–146.

Kresák L. and Kresákova M. (1976). "A note on meteor and micrometeoroid orbits determined from rough velocity data". *Bulletin of the Astronomical Institutes of Czechoslovakia*, **27**, 106–109.

McKinley D. (1961). "Meteor science and engineering.". *New York, McGraw-Hill, 1961.*

Millman P. M. and McKinley D. W. R. (1963). "Meteors". In Kuiper G. P. and Middlehurst B. M., editors, *The Moon Meteorites and Comets*, page 674.

Moorhead A., Blaauw R., Moser D., Campbell-Brown M., Brown P., and Cooke W. (2017). "A two-population sporadic meteoroid bulk density distribution and its implications for environment models". *Monthly Notices of the Royal Astronomical Society*, **472:4**, 3833–3841.

Skokic I., Segon D., and Kurtovic G. (2016). "On the accuracy of orbits from video meteor observations". In *International Meteor Conference Egmond, the Netherlands, 2-5 June 2016*. pages 280–283.

Štohl J. (1970). "On the problem of hyperbolic meteors". *Bulletin of the Astronomical Institutes of Czechoslovakia*, **21**, 10.

Vida D., Brown P., and Campbell-Brown M. (2018). "Modelling the measurement accuracy of pre-atmosphere velocities of meteoroids". *Monthly Notices of the Royal Astronomical Society*, **479:4**, 4307–4319.

ANDES-FIRE: The Argentina All-sky Video System

Peter S. Gural[1], Diego Janches[2], Juan Sebastian Bruzzone[3], Jose Luis Hormaechea[4], Fernando Gigi[5]

[1] **Gural Software and Analysis LLC, Sterling VA, USA**
pgural@gmail.com

[2] **ITM Laboratory, Heliophysics Division, GSFC, Greenbelt MD, USA**

[3] **Dept. of Physics, Catholic University of America, Washington DC, USA**

[4] **Estacion Astronomica Rio Grande, Rio Grande, Tierra del Fuego, Argentina**

[5] **Centro Austral de Investigaciones Cientificas, CONICET, Ushuaia, Tierra del Fuego, Argentina**

A quartet of GigE all-sky video cameras has been deployed to the southern tip of Argentina for the purpose of simultaneous visual and radar observations of bright meteors. The development of the software modules for GigE capture, all-sky astrometric calibration, and CAMS detection module interface will be discussed along with image processing considerations.

1 Introduction

The All-sky Network and Detection Software for FIREballs (ANDES-FIRE) is a recent equipment deployment by Dr. Diego Janches of NASA Goddard, to place three all-sky cameras in the southern hemisphere and attempt to capture bright meteor fireballs in both the visual electro-optical and radar wavelengths. By capturing a fireball in video and radar, the hope is to obtain better mass estimation through cross-calibration between the two collection modalities. To achieve this, all-sky cameras were deployed at the southernmost tip of Argentina, in a region named Tierra del Fuego around the SAAMER radar (Janches et al., 2015, 2014). The video cameras were located in the towns of Rio Grande, Ushuaia, Tolhuin, and Despedida with baselines ranging from 80 to 120 km between stations. The camera views overlap the meteor cap layer of the SAAMER radar located just a few kilometers northwest of Rio Grande. Dr. Janches has been operating the SAAMER radar for several years to collect both very wide field (specular trail) and narrow beam-formed (head echo) meteor signatures.

A major issue arose two years previously when this project was first setup in Argentina. The cameras used were the FRIPON GigE systems and were tied to the "Freeture" software for capture and detection of meteors. However, Freeture could never be made to operate reliably on the deployed systems in Argentina. Also, there was no automated astrometry capability nor trajectory estimation available at the time for FRIPON. To mitigate the processing shortfalls, NASA Goddard through support from NASA's Solar System Observations program, decided to develop the necessary processing software as a risk reduction effort and get the system online by the summer of 2018. To do so, it was decided to integrate three new modules into the existing CAMS processing pipeline (Jenniskens et al., 2011) to leverage currently mature software capabilities. This required the implementation of a GigE camera interface module, development of an all-sky astrometric fitting capability for CAMS, and to build a customized CAMS pre-processing and detection application. CAMS already had a detection module based on fast clustering and tracking, whose track output was already integrated into a "coincidence" application that aggregates multiple site measurements into atmospheric trajectories and Solar System orbits. So the only upgrades needed were image capture, all-sky astrometry, and detection pre-processing.

2 GigE Camera Interface

The FRIPON system design utilizes a Basler GigE camera (model number acA1300-30gm) that is capable of 12-bits grayscale dynamic range with 1296 × 966 pixels. With the included Rainbow 1.25mm f/2 lens, the angular resolution per pixel is nearly 10 arc-minutes at the zenith and 13 arc-minutes for five degrees above the horizon. Fortunately, Basler also provides a software development kit (SDK) named Pylon 5.0 to build C applications that interface and control the camera. An interface module was quickly implemented that could adjust gain, frames per second, exposure time, area of interest (subset of the full image), and bit depth of the Basler camera. This allowed for switching between daylight, night, and astrometry modes of collection. Since the Pylon SDK is GigE standards compliant, the C interface module developed will function on other GigE compliant cameras sold by other manufacturers.

Pylon also includes two compiled apps for configuration setup of the camera, as well as a live viewer. These were very useful for initial testing of the camera and setting up the network interface card (NIC) optimally. It was found that for the default NIC settings the "jumbo" frames option was disabled, and thus to avoid transmission packet losses, jumbo frames needed to be enabled. Also the inter-packet delay required optimization using the Pylon Viewer after a system level reboot. In addition, for long cable runs, it was found that it was best to use CAT6 cables. Once these network related issues were resolved, the interface module with a simple capture loop, ran for several days without a dropped frame.

3 Astrometric Capability

Once imagery could be captured, an experiment was run to determine if the nominal night time frame rate of 25 fps could be used to also collect a summed multi-frame astrometry image. This was desirable to avoid any meteor detection dead time during a separate astrometry collection that would be necessary periodically. Examining the 40 millisecond exposures, only minus-one magnitude stars could be easily identified in the image. By summing 750 frames over 30 seconds, it was hoped the SNR would increase and one could pull out many more stars. However, the Basler camera chosen for FRIPON has a high read noise component on a per frame basis, which swamped the stars in the multi-frame sum. Thus, astrometry collections with long exposure times were needed to minimize the read noise. The maximum exposure for the camera was ten seconds, so three sequential exposures were collected and summed into an astrometry image. This meant that no fireballs could be detected during the 30 second astrometry collection mode, which was nominally done once per hour. The limiting stellar magnitude achieved was +4.5 and provided a sufficient number of stars spread across the FOV to perform the astrometric fit.

Given the astrometry collection, the image was enhanced with a spatial median background removal of size 15 $\times$ 15 pixels and then log histogram equalized. A star locator and centroid estimation is run across the image to obtain stellar positions. Both a manual and semi-automatic application was developed to point-and-click on visually associated stars between a catalog based star field and the ANDES-FIRE star image centroids. Once sufficient stars were associated, especially those at a large zenith angle, a fit was performed on the paired star lists with the option to add additional stars if available. Thus, one can bootstrap up from say a 20 star fit to get an approximate fit solution, and use that as an initial starting guess as more stars are added.

Note that the CAMS astrometric calibration was only designed for moderate to narrow FOVs and not all-sky. Thus, the existing warp functions only included affine, quadratic and cubic polynomials. The latter being the most commonly used but fails to adequately handle barrel distortion of an all-sky lens. To address this shortcoming in the CAMS pipeline, four all-sky astrometry formulations were implemented as a single C function, as they all had similar functional forms but with various radial dependencies (Bannister et al., 2013; Borovicka, 1992; Borovicka et al., 1995; Howell, 2018). The most successful warping function found was Borovicka's 1995 radial formulation with two exponential terms in the radial component and non-axisymmetric azimuth dependency. Since these formulations are all non-linear, a particle swarm optimization module was used to find the cost function minimum (O-C residuals). The resultant fit super-imposed on the Rio Grande star image is shown in Figure 1 with mean O-C residuals of 2.9 arcminutes or about 1/3 of a pixel. The residuals dependency with zenith angle is shown in Figure 2, showing a flat error for all distances from the image center.

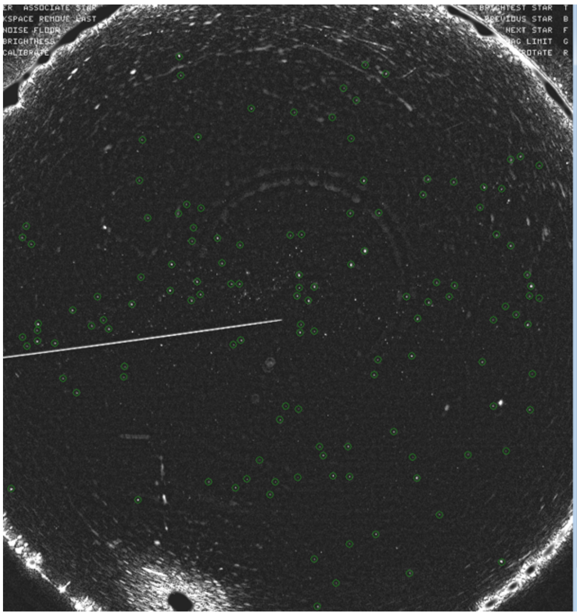

Figure 1: Astrometry image collect with the stars fit as overlapping green circles on the stellar positions of white spots.

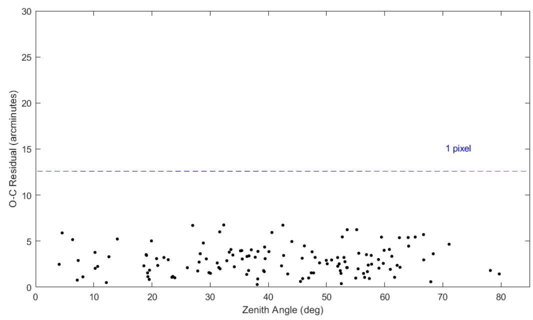

Figure 2: O-C residuals as a function of zenith angle.

During the 2018 IMC, the PRISMA team from Italy discussed an alternative fitting formulation for FRIPON all-sky cameras, which is to be published in the near future. The FRIPON team themselves also has looked into higher odd orders of radial dependency up to ninth order. And lastly, the Croatian Meteor Network team uses a simple first order radial term scaled by x and y standard coordinates for very wide field astrometry. Once details of these methods become publicly available and implemented, an evaluation will be made comparing these various approaches side-by-side on the same all-sky imagery, to identify the best solution for FRIPON type cameras. For now, the Borovicka 1995 formulation is used in ANDES-FIRE.

4 Detection Processing

As indicated above, the live real-time video frame capture was setup and configured successfully. The next step was to integrate the CAMS clustering and tracking detection software into the video processing pipeline. See Figure 3 for the image processing flow diagram for ANDES-FIRE. The goal was to process imagery in real-time on a dual-core Intel i3 processor. This was easily achieved for all processing stages except the archival step which is indicated in Figure 3 as the block labeled "Save Frame in H.264 File" to be discussed in the next section. The remaining steps operate on the 1K × 1K imagery in about 4 milliseconds out of the 40 milliseconds available at the 25 fps frame rate.

The flow proceeds on each frame by first testing if it is time to switch to an astrometry collection or flip-flop between day versus night collections and adjust the associated gain and exposure settings. The next fully exposed frame from the camera is captured to a circular buffer in memory. The circular buffer is used to allow a running mean and standard deviation to use frames sufficiently back in time to avoid any potential contamination in a pixel from a slow-moving fireball near the horizon. For the angular resolution of the imaging system, eight frames back in time was determined to be sufficient look back, but is user configurable. The mean and standard deviation is tracked on a per pixel basis independently using a first order response filter. This defines a threshold per pixel of the mean plus k times the standard deviation, with k user selectable to control false alarm rates. Exceedances from the threshold operation are passed to the fast clustering algorithm of CAMS, followed by a multi-frame tracker to establish "firm" linearly propagating tracks (Gural, 2016). A "no detection" loops back to process the next frame in the buffer.

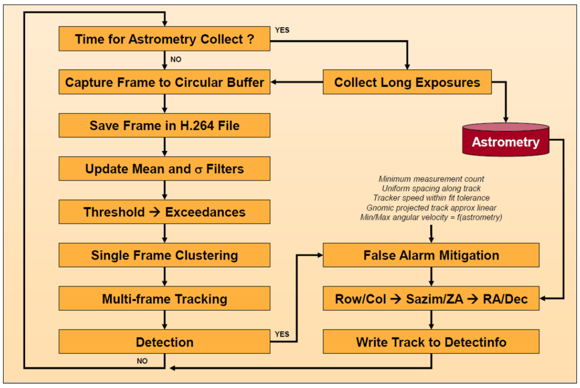

Figure 3: Imaging processing flow diagram for ANDES-FIRE

A potential detection meeting the FIRM track criteria is passed to a false alarm mitigation screener. This includes tests for minimum measurement count, nearly uniform spacing along track, tracker speed within a fit tolerance, the gnomic projection appears linear, and the minimum/maximum angular velocity is within astrometric geometry bounds, all with settings that are user configurable. Once obvious false alarms are removed, the detected track is converted to both equatorial and azimuth/zenith angle coordinates and written to the standard format of a CAMS "Detectinfo" file. This allows the track result to be aggregated with other stations and post-processed with the CAMS coincidence application to obtain trajectories and orbits.

5 Archiving the Imagery

It was realized that the potential exists for only one or two of the three stations to actually detect and record the meteor track, and that it may be necessary to examine and process the collected imagery from the missed detection cameras. The FRIPON system in France expects to handle this by having live internet communications between stations that inform neighbor stations to save imagery when another station has a detection. Since the internet is not 100% reliable at the Argentina deployments sites and the FRIPON notification system was yet to be implemented, it was decided for ANDES-FIRE to archive the entire night's imagery from each station independently.

Saving the raw imagery would have required 4.6 Terabytes of storage per day per camera. So instead, the imagery was compressed using FFMPEG (`https://www.ffmpeg.org`) into a format playable on virtually any PC. The selection was to use a MPEG4 video container file and H.264 compression on a user selectable number of frames per file (nominally 250 frames or 10 seconds of video). Since the H.264 compressor only works on 8-bit imagery, the top 8 bits of the 12 bit raw imagery were actually saved since the desire for this system is bright fireball processing. It has been found that H.264 provides good compression characteristics for high contrast night sky imagery in terms of astrometry and photometry (Weryk R., private communication). The result is that a single night of collection occupies only 3 Gigabytes of hard drive storage. To avoid filling up the hard drive over time, a daily imagery purge was implemented that allows for retaining approximately seven days' worth of collection.

6 Next Steps

All the components are in place now for the ANDES-FIRE processing pipeline and it has been running continuously for several months at the Rio Grande station. Ushuaia, Tolhuin and Despedida have just come online so the first triangulations and orbits should be out soon. Next steps in the project include the following:

- Optimize detection processing parameters and algorithms based on FRIPON collected meteor imagery provided by Jeremie Vaubaillon and Francois Colas of the IMCCE.
- Test multi-site coincidence and trajectory/orbit estimation.

- Perform daily monitoring of weather conditions and potential detections in Argentina.
- Deploy a triad of narrow FOV cameras systems in addition to the all-sky systems in Argentina, the former of which will be used for head-echo studies with the radar. This new narrow FOV system is expected to be online in December 2018, which will employ 17mm f/0.95 lenses on Watec 902H2 Ultimate cameras and processed using the CAMS software pipeline.

Acknowledgements

The authors would like to thank the NASA Solar System Observations (SSO) program for supporting the ANDES-FIRE software enhancement project and all-sky FOV deployment in Tierra del Fuego, Argentina. Special thanks goes out to the personnel of EARG (Estacion Astronomica Rio Grande) in Argentina for their invaluable and constant support during the equipment deployment, on-site testing, and continued daily operation of the systems.

References

Bannister S., Boucheron L. E., and Voelz D. G. (2013). "A numerical analysis of a frame calibration method for video-based all-sky camera systems". *Publications of the Astronomical Society of the Pacific*, **125:931**, 1108.

Borovicka J. (1992). "Astrometry with all-sky cameras.". *Publications of the Astronomical Institute of the Czechoslovak Academy of Sciences*, **79**.

Borovicka J., Spurny P., and Keclikova J. (1995). "A new positional astrometric method for all-sky cameras.". *Astronomy and Astrophysics Supplement Series*, **112**, 173.

Gural P. (2016). "A fast meteor detection algorithm". In *International Meteor Conference Egmond, the Netherlands, 2-5 June 2016*. pages 96–104.

Howell A. (2018). Private communication.

Janches D., Close S., Hormaechea J. L., Swarnalingam N., Murphy A., OConnor D., Vandepeer B., Fuller B., Fritts D., and Brunini C. (2015). "The southern argentina agile meteor radar orbital system (saameros): an initial sporadic meteoroid orbital survey in the southern sky". *The Astrophysical Journal*, **809:1**, 36.

Janches D., Hocking W., Pifko S., Hormaechea J. L., Fritts D., Brunini C., Michell R., and Samara M. (2014). "Interferometric meteor head echo observations using the southern argentina agile meteor radar". *Journal of Geophysical Research: Space Physics*, **119:3**, 2269–2287.

Jenniskens P., Gural P., Dynneson L., Grigsby B., Newman K., Borden M., Koop M., and Holman D. (2011). "Cams: Cameras for allsky meteor surveillance to establish minor meteor showers". *Icarus*, **216:1**, 40–61.

Croatian Meteor Network: ongoing work 2017-2018

Damir Šegon[1,4], Denis Vida[2], Željko Andreić[3], Korado Korlević[4], Aleksandar Merlak[5], Patrik Kukić[6], Matej Butković[7], Renato Turčinov[8]

[1] **Astronomical Society Istra Pula, Park Monte Zaro 2, 52100 Pula, Croatia**
damir.segon@pu.htnet.hr

[2] **Department of Earth Sciences, University of Western Ontario, London, Ontario, N6A 5B7, Canada**

[2] **Department of Physics and Astronomy, University ofWestern Ontario, London, Ontario, N6A 3K7, Canada.**
dvida@uwo.ca

[3] **University of Zagreb, Faculty of Mining, Geology and Petroleum Engineering, Pierottijeva 6, 10000 Zagreb**
zeljko.andreic@oblak.rgn.hr

[4] **Vinjan Science and Education Center, Istarska 5, 51463 Višnjan, Croatia**
korado@astro.hr

[5] **Istrastream d.o.o., Hum, Croatia**
info@istrastream.com

[6] **XV Gymnasium, Jordanovac 8, HR-10000 Zagreb, Croatia**

[7] **Grammar school "Gimnaza Pula", Trierska 8, HR-52100 Pula, Croatia**

[8] **Uljanik TESU elektronika d.o.o., Flaciusova 1, 52100 Pula, Croatia**

Ongoing work of the Croatian Meteor Network (CMN) between 2017 and 2018 International Meteor Conferences is presented. The overview of ongoing activities covering the developments in RaspberryPi based meteor camera solution, low cost radiometer, initial low cost infrasound sensor results as well as notes on other activities has been given.

1 Introduction

In this paper we present the ongoing work of the Croatian Meteor Network (CMN) between the 2017 and 2019 IMCs. Topics covered by this paper contain information on the current status of Raspberry Pi meteor station (RMS) solution, low cost radiometer, initial results from testing a low cost infrasound detector and notes on some important work which has been described in detail in separate papers.

2 RMS

Since the start of the Croatian Meteor Network project, it has been using two softwares for meteor work: SkyPatrol and CAMS (Jenniskens et al., 2011). Some of older CMN stations use the SkyPatrol software even at the moment (reason for that being lack of computer processing power or lack of capture card drivers supported by CAMS), but majority of stations has been migrated to CAMS package. Both solutions, SkyPatrol and CAMS are covered by a single data processing pipeline - ADAPT - as described in Vida et al. (2014).

The development of a cheap RaspberryPi based solution for video meteor capture and detection has been initiated by Zubović during 2014, first presented by Zubović et al. at the IMC 2015 at Mistelbach (Zubović et al., 2015). The following developments (Vida et al., 2018b, 2016) led to the solution which we at the CMN consider the way to go in the future of our video meteor astronomy: it has been named Raspberry Pi Meteor Station (RMS), it is open source and detailed description as well as the code itself is available for free (GitHub_CMN). First scientific result of the RMS project has been recently published in WGN (Vida et al., 2018a), moreover, latest tests done on a Linux based PC had shown that the RMS works with older BT878 chipset based capture cards, allowing existing stations to migrate to this new solution. All mentioned above allows us to migrate the CMN to a completely new, unique video meteor astronomy platform.

The CMN is not the only one applying the RMS solution. At the moment, as far as for author's knowledge, besides Croatia there are operative stations operative in Canada, France and Brazil. We encourage all amateur astronomers worldwide to adopt this solution, either by building their cameras on their own (as stated, complete details are available online for free) or by purchasing a complete solution (see Figure 1) for about 300€ in which case please contact authors for details.

As a part of the result of ongoing tests, we have not only standard 4mm lenses adopted but wider angle 2.8 mm ones as well as 16mm ones. Astrometry and resulting trajectories show that the RMS solution is the correct choice for migration from current one, and due to its simplicity will be very soon deployed to a number of astronomical societies and schools interested in astronomy and software projects.

Figure 1 – The RMS camera

3 Low cost radiometer

The CMN low-cost radiometer project has first been presented by Vida et al. at the IMC 2015 at Mistelbach (Vida et al., 2015). Basic idea is to use low-cost BTW34 photodiodes, connected as a current source to a set of operational amplifiers. First version consisted of a single BPW34 diode, followed by an improved system of 9 diodes presented at the IMC 2016 at Egmond (Šegon et al., 2016) which suppresses photodiode's and operational amplifier's natural (dark current) noise by a factor of three. The results of simultaneous radiometer and all-sky camera fireball observations were published recently in WGN (Šegon et al., 2018), showing that the second radiometer sensor version provides very useful data on fireball light curves. Recent case of a Perseid fireball is presented on Figure 2, showing consistent radiometric light curve compared to a DSLR camera data.

Main obstacle in radiometer work we found consists in the signal noise. Spectrograms shown the reason being at the power supply frequency (almost stable 50 Hz), so the digital filters are applied in order to remove this noise we presumed mainly comes out from light pollution. One detail we missed was the fact that the light sources working on 50 Hz main supply frequency produce light which varies on twice of that frequency! So the reason for high noise level at 50 Hz is not due the light pollution but mainly due to electromagnetic field around the sensor. Luckily, this may be suppressed down to an almost negligible level by caging the sensor in a Faraday cage, a solution we are currently working at.

Up to the IMC 2018, dozens of fireballs were simultaneously observed by the radiometer and by nearby all-sky camera, but also captured by the rest of CMN cameras which allows us to have complete trajectory and light curve data combined. Two examples provided below show the light curves of a bright fireball, and a very bright meteor (yet not quite a fireball). It is interesting to see that the radiometer light curve provides much more detailed information than data coming in by video camera. This is of course an expected behavior, but we had the feeling that the level of camera's data would still be of higher value. The reason for such deviations from radiometer light curve lies mostly in the video compression and saturation issues, but in the fact that the sample rate ratio between the radiometer sensor and the camera is of 10:1. One of very interesting information that can be extracted from the light curve and trajectory data is the dynamic pressure meteoroid survived until its fragmentation, if any. One of results we obtained for the 20181231 01:15:58 fireball is presented here as well.

Despite all issues with electromagnetic field and light pollution noise, we are very satisfied with current results we obtain with this simple and cheap radiometer solution. A new version of the sensor is currently under development: the plan is to have a 2 kHz sample rate 24-bit data acquisition solution which the new sensor should be able to feed accordingly. Among other hardware signal conditioning details a very low frequencies dynamical suppressing filter is taken into consideration, in order to allow wider dynamical range.

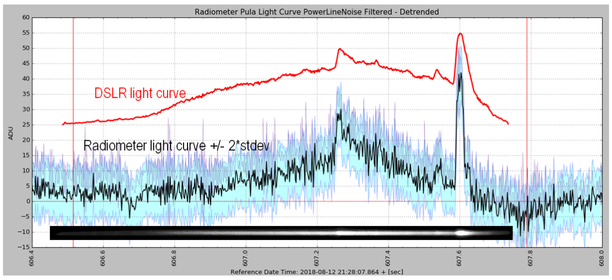

Figure 2 – Perseid meteor lightcurve as obtained by DSLR camera and the radiometer

4 Low cost infrasound sensor

In order to cover the volume of the sky over Croatia, we would like to cover it in any known sense it can be done. Since from obvious reason of being amateurs radar observations are out of our reach, we decided to cover another aspect of fireball observations, that one being the infrasound and its effects produced in case of very bright events. Such an event may occur during the daytime as well, or during a cloudy night – and this make us think a network of infrasound sensors may be the way to obtain data on it. First infrasound observations of a meteor event date more than 100 years ago, the Tunguska event being the first one recorded. Today, the infrasound observations of big events are certainly covered by the Comprehensive Nuclear-Test-Ban Treaty (CTBT) sensors, among other seismograph data. However, besides of the fact that those sensors are not available for public queries, limitation of such sensors is their sensitivity and coverage.

What we found important to point out is the fact it is possible to estimate the fireball trajectory from arrival time data of event associated seismic wave (for example, Kalenda et al. (2014) where examples of infrasound and seismic data are presented). In case we would be able to build up a sensor which would record infrasound and seismic data continuously through the year, we would be able to detect big meteor events, and by having a network of such sensors we would be able to calculate event's trajectory. To have a network of infrasound sensors, that would be our goal. In order to build such a network, we have to keep the price of the sensor/station low - so we started with development of a cheap infrasound sensor.

We decided to build the sensor based on piezo microphone, coupled with appropriate amplifier. After initial considerations we picked the 35mm piezo element as our choice, mostly driven by experiences by DeWolf (2006). As always when more than one man works on the project, there are different opinions on the way we should go. And we decided to go both ways - the first one being an trivial solution which has been found on the web (Nawrath, 2012), the second one being the development of an infrasound - citing the words from one of the authors: "as it should be build".

The very cheap solution we found on the internet has been corrected in the way we may use the LMC6464 operational amplifier we already used in case of the radiometer sensor, and the prototype build on a piece of experimental printed circuit board. In order to protect the PCB from external electromagnetic noise, the PCB has been inserted into an iron box, which once grounded represents the Faraday cage. We do not have any intention of working on any improvements of this sensor, and as will be presented further on, it works. How well, that will be a part of further investigations and we will certainly let interested amateurs know about our results. The second solution represents serious development of a sensor which would still be reasonably cheap (below 50€), but would be more reliable. At the moment, this version has been adjusted to filter frequencies over 30 Hz and has a flat response over the range from 0.033 Hz (30 seconds) to 33 Hz, which we consider enough for meteor work purposes.

In order to acquire data from the sensor, we applied an USB digital oscilloscope and data logger from iCircuit Tchnologies (2018, 1 mV sensitivity version) able to convert analog to digital signal at various sample rates up to 1 kHz, having most of the tests done using the 100 Hz sample rate.

One may ask himself about testing: how on the Earth to test if the sensor is working – not that meteors producing infrasound are something that happens every day, nor is the setup for producing infrasound something I may build easily. Well, mother Nature came to help us here, by providing an infrasound source which occur moreless on regular basis in Croatia: a thunder! Thunderstorms are something common in Croatia, having most of thunders retraceable by checking lightning data coming from the Blitzortung project (LightningMaps, 2018). So we arranged our tests for announced thunderstorms, and check out for data on lightning which occurred in sensor's "neighborhood" ranging up to 20km.

The graph on Figure 3 shows some of thunders we associated with signals recorded by the test setup. Since the testing setup has been deployed on author's balcony, we found out that the direction of the incoming infrasound is of great importance (you can hardly hear something behind a house-sized fence unless it is really LOUD), wind direction being the of the main importance, but we also found that air humidity (clouds) plays important role as well due to sound attenuation in the media.

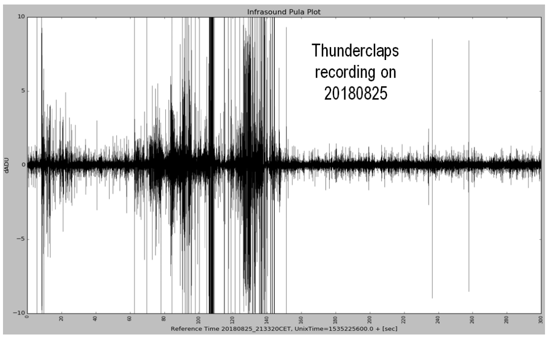

Figure 3 – Thunderclaps recording on 20180825

Since there are two kind of infrasound data we would like to obtain, meaning pressure changes and seismic waves caused by infrasound, we should work on calibration for both cases. We find pressure calibration to be the main issue, while the seismic one would be a very interesting project for some of our young CMN members.

Of course, we are only at the beginning of this project, and there are some "missing parts" - this primary goes to a stable and continuous data acquisition. We are considering different approaches, all of them Raspberry Pi based but with different versions of analog to digital convertors. Moreover, further tests will be done using different piezo elements as well as more piezo elements attached with different configurations (unipolar/bipolar).

5 Other

Among important things that we would like to point out happened between two IMCs, the most exciting one for sure is the meteorite dropping fireball case from April the 8th 2018. The IMO fireball event 2018/1336 has been noted by many visual observers and covered very well by European Network cameras (IMO Fireball Report, 2018), so we were immediately alerted on the possibility we have meteorites on the Croatian soil again after 7 years. Unfortunately, the search did not produce any positive findings, for various reasons: one of them all the rocks in the area are black, the other one the strewn field is extremely difficult to go through... on one occasion, there were issue finding part of the expedition members, rather to do the search for the meteorite itself! More efforts on this case will be taken until the complete strewn field would be thoroughly searched for.

Sensitive CMOS based cameras digital were present on the market for quite a time, but up to the moment those cameras were avoided by video meteor astronomers due to the fact that most of them use rolling shutter technique as for image readout. The solution for correction of side effects of the rolling shutter has been presented at this IMC by Kukić, as well as in a separate paper which should be published in the WGN.

Work on meteor spectra and its impact on meteor magnitudes is going on. In order to completely cover the issue we find to exist regarding meteor photometry, we made a step back and collected all data on emulsions used for meteor photography we were able to find. It is important to have this introduction step in order to see where would be the very probable differences in resulting masses coming from. This work will be presented in a separate talk(Andreić et al., 2019).

Educational part of our work goes on as well, for another year we had one of our young members receiving the award for the best practical work on national level. More efforts however need to be done in organizational sense, involving more professors and raising up their knowledge on meteor astronomy. In this sense, we would point out that there's no book on the market covering current meteor astronomy status, techniques and knowledge we gained during last decade(s), and this should be one of tasks IMO may look after.

Acknowledgements

Our acknowledgments go to all members of the Croatian Meteor Network, for their devoted work on this project. This work was partially supported by the Faculty of Mining, Geology and Petroleum Engineering, University of Zagreb, Višnjan Science and Education Center, the Istrian County and by private funds of CMN members.

References

Andreić Ž., Šegon D., and Gural P. (2019). "Spectral sensitivity of photographic emulsions". In Eds.: Rudawska R., Rendtel J., Powell C., Lunsford R., Verbeeck C., and Knöfel A., editors, *International Meteor Conference Pezinok, Slovakia, 30 August – 2 September 2018*. pages 46–49.

DeWolf S. (2006). "Characterizing the Mechanical Sensitivity of Three Piezo-Based Infrasound Sensors". In *Infrasound Technology Workshop, Fairbanks, Alaska, USA*.

iCircuit Tchnologies (2018). `http://www.piccircuit.com/shop/pic-dev-board/119-icp12-usbstick-pic18f2550-io-board.html`.

IMO Fireball Report (2018). `http://fireball.imo.net/members/imo_view/event/2018/1336`.

Jenniskens P., Gural P. S., Dynneson L., Grigsby B. J., Newman K. E., Borden M., Koop M., and Holman D. (2011). "CAMS: Cameras for Allsky Meteor Surveillance to establish minor meteor showers". *Icarus*, **216**, 40–61.

Kalenda P., Borovička J., and Spurný P. (2014). "The localization of fireball trajectories with the help of seismic networks". *Studia Geophysica et Geodaetica*, **58**, 84–99.

LightningMaps (2018). `https://www.lightningmaps.org/blitzortung/europe/index.php?bo_page=map&lang=en`.

Nawrath M. (2012). "Laboratory for Experimental Computer Science at the Academy of Media Arts Cologne". `http://interface.khm.de/index.php/lab-log/piezo-disk-preamplifier/`.

Šegon D., Vida D., Butković M., Malarić M., and Turcinov R. (2018). "First simultaneous radiometric and video observations of fireballs using a low-cost radiometer". *WGN, Journal of the International Meteor Organization*, **46**, 62–70.

Šegon D., Vida D., Korlević K., and Andreić Ž. (2016). "Croatian Meteor Network: Ongoing work 2015 - 2016". In Roggemans A. and Roggemans P., editors, *International Meteor Conference Egmond, the Netherlands, 2-5 June 2016*. pages 270–274.

Vida D., Mazur M. J., Šegon D., Kukić P., and Merlak A. (2018a). "Compressive strength of a skirting Daytime Arietid first science results from low-cost Raspberry Pi-based meteor stations". *WGN, Journal of the International Meteor Organization*, **46**, 113–118.

Vida D., Mazur M. J., Šegon D., Zubović D., Kukić P., Parag F., and Macan A. (2018b). "First results of a Raspberry Pi based meteor camera system". *WGN, Journal of the International Meteor Organization*, **46**, 71–78.

Vida D., Turčinov, Šegon D., and Silai E. (2015). "Low-cost meteor radiometer". In Rault J.-L. and Roggemans P., editors, *Proceedings of the International Meteor Conference, Mistelbach, Austria, 27-30 August 2015*. pages 180–184.

Vida D., Šegon D., Gural P. S., Martinović G., and Skokić I. (2014). "CMN_ADAPT and CMN_binViewer software". In Rault J.-L. and Roggemans P., editors, *Proceedings of the International Meteor Conference, Giron, France, 18-21 September 2014*. pages 59–63.

Vida D., Zubović D., Šegon D., Gural P., and Cupec R. (2016). "Open-source meteor detection software for low-cost single-board computers". In Roggemans A. and Roggemans P., editors, *International Meteor Conference Egmond, the Netherlands, 2-5 June 2016*. pages 307–318.

Zubović D., Vida D., Gural P., and Šegon D. (2015). "Advances in the development of a low-cost video meteor station". In Rault J.-L. and Roggemans P., editors, *International Meteor Conference Mistelbach, Austria*. pages 94–97.

News from the Italian PRISMA fireball network

PRISMA Team: Daniele Gardiol[1], Fausto Affaticati[2], Marzia Albani[2], Alberto Andreis[3], Giovanni Ascione[4], Paolo Bacci[5], Roberto Baldini[6], Andrea Balestrero[7], Sandro Bardelli[8], Dario Barghini[1,9], Stefano Basso[10], Ester Battistini[11], Roberto Bellitto[11], Massimiliano Belluso[12], Carlo Benna[1], Fabrizio Bernardi[13], Gianfranco Bernucci[14], Mario Bertaina[9], Walter Biamino[15], Sergio Billotta[12], Raffaella Bonino[9], Kristijan Boros[16], Alberto Buzzoni[8], Fabrizio Capaccioni[17], Giulio Capasso[18], Albino Carbognani[1,19], Tullia Carriero[1], Enrico Cascone[18], Cristiana Cattaneo[20], Giampiero Cellini[21], Alberto Cellino[1], Emanuela Colombi[22], Marina Costa[7], Gabriele Cremonese[23], Giuseppe D'Agostino[24], Marcella D'Elia[25], Paolo Demaria[3], Matteo Di Carlo[26], Andrea Di Dato[18], Roberto Di Luca[8], Mario Di Martino[1], Fortunata Farina[27], Umberto Fornasari[21], Filippo Frontera[28], Vincenzo Gagliarducci[29], Antonio Gerardi29, Gabriele Giuli[30], Roberto Guarino[31], Adriano Guerriero[32], Daria Guidetti[33], Marina Incerti[34], Giorgio Interrante[35], Roberto Jarre[3], Cristina Knapic[36], Monica Lazzarin[37], Domenico Licchelli[38], Fabio Lippolis[39], Elisa Londero[36], Davide Loreggia[1], Giuseppe Maccaferri[33], Francesco Manca[40], Salvatore Mancuso[1], Filippo Mannucci[41], Salvo Massaro[42], Paola Mercogliano[43], Angela Misiano[24], Pino Mogavero[42], Vanni Moggi Cecchi[44], Jader Monari[43], Eleonora Monge[45], Matteo Montemaggi[11], Giuliano Monti[46], Roberta Morosin[1], Emanuele Pace[47], Roberto Pardini[22], Michele Pavone[48], Aldo Pegoraro[49], Stefano Pietronave[46], Giovanni Pratesi[50], Nicola Pugno[31], Giuseppe Pupillo[33], Stefania Rasetti[1], Umberto Repetti[32], Walter Riva[7], Nicola Rizzi[39], Simona Romaniello[45], Claudio Romeni[51], Pasquale Russo[4], Francesco Salvati[1], Danilo Selvestrel[23], Romano Serra[52], Riccardo Smareglia[36], Matteo Soldi[20], Antonio Stasi53, Giovanna M. Stirpe[8], Francesco Strafella[25], Gianni Talami[34], Carla Taricco[9], Maura Tombelli[35], Damiano Trisciani[47], Paolo Trivero[15], Gabriele Umbriaco[37], Rino Vairetti[54],, Gianpaolo Valente[55], Giovanni B. Valsecchi[17], Antonio C. Volpicelli[1], Roberto Zagarella[56], Alessandra Zollo[43], Sonia Zorba[36]
FRIPON Team: Franois Colas[57], JeremieVaubaillon[57], Pierre Vernazza[58], Sylvain Bouley[59], Brigitte Zanda[60], Mirel Birlan[57], Jerome Gattacceca[61], Cyril Blanpain[62], Julien Lecubin[62], Adrien Malgoyre[62]

[1] **INAF – Osservatorio Astrofisico di Torino, Pino Torinese (TO), Italia**
`daniele.gardiol@inaf.it`

[2] **La Torre del Sole, Brembate di Sopra (BG), Italia**

[3] **Associazione Astrofili Bisalta, Chiusa di Pesio (CN), Italia**

[4] **Associazione Sky Sentinel, San Nicola la Strada (CE), Italia**

[5] **Gruppo Astrofili Montagna Pistoiese, San Marcello Pistoiese (PT), Italia**

[6] **Gruppo Astrofili Antares, Brisighella (RA), Italia**

[7] **Osservatorio Astronomico del Righi, Genova, Italia**

[8] **INAF – Osservatorio di Astrofisica e Scienza dello Spazio, Bologna, Italia**

[9] **Dipartimento di Fisica, Università degli Studi di Torino, Torino, Italia**

[10] **INAF – Osservatorio Astronomico di Brera-Merate, San Rocco (LC), Italia**

[11] **Associazione Astronomica del Rubicone, Savignano sul Rubicone (FC), Italia**

[12] **INAF – Osservatorio Astrofisico di Catania, Catania, Italia**

[13] **Space Dynamics Systems, Navacchio di Cascina (PI), Italia**

[14] **Istituto Statale d'Istruzione Superiore "Marie Curie", Savignano sul Rubicone (FC), Italia**

[15] **Dipartimento di Scienze e Innovazione Tecnologica, Università degli Studi del Piemonte Orientale, Alessandria, Italia**

[16] **Associazione Astrofili Urania, Luserna San Giovanni (TO), Italia**

[17] **INAF – Istituto di Astrofisica e Planetologia Spaziali, Roma, Italia**
[18] **INAF – Osservatorio Astronomico di Capodimonte, Napoli, Italia**
[19] **Osservatorio Astronomico della Regione Autonoma Valle d'Aosta, Lignan (AO), Italia**
[20] **Osservatorio e Planetario di Ca' del Monte, Cecima (PV), Italia**
[21] **Collegio Alberoni, Piacenza, Italia**
[22] **Planetario di Bedonia, Bedonia (PR), Italia**
[23] **INAF – Osservatorio Astronomico di Padova, Padova, Italia**
[24] **Planetario Pythagoras – Parco Nazionale dell'Aspromonte, Reggio di Calabria, Italia**
[25] **Dipartimento di Matematica e Fisica, Università del Salento, Lecce, Italia**
[26] **INAF – Osservatorio Astronomico d'Abruzzo, Teramo, Italia**
[27] **Liceo Statale Alessandro Manzoni, Caserta, Italia**
[28] **Parco Astronomico Lilio, Savelli (KR), Italia**
[29] **Osservatorio Astronomico e Planetario di Gorga, Gorga (RM), Italia**
[30] **Università degli Studi di Camerino, Camerino (MC), Italia**
[31] **Department of Civil, Environmental and Mechanical Engineering, Università degli Studi di Trento, Trento, Italia**
[32] **Associazione Meteoriti Italia, Feltre (BL), Italia**
[33] **INAF – Istituto di Radio Astronomia, Medicina (BO), Italia**
[34] **Associazione Scandianese Fisica Astronomica, Scandiano (RE), Italia**
[35] **Gruppo Astrofili Montelupo Fiorentino, Montelupo Fiorentino (FI), Italia**
[36] **INAF – Osservatorio Astronomico di Trieste, Trieste, Italia**
[37] **Dipartimento di Fisica e Astronomia, Università degli Studi di Padova, Padova, Italia**
[38] **Osservatorio Astrofisico R.P.Feynman, Gagliano del Capo (LC), Italia**
[39] **Osservatorio Astronomico Sirio, Castellana Grotte (BA), Italia**
[40] **Osservatorio Astronomico di Sormano, Sormano (CO), Italia**
[41] **INAF – Osservatorio Astronomico di Arcetri, Firenze, Italia**
[42] **Parco Astronomico Gal Hassin, Isnello (PA), Italia**
[43] **Centro Italiano Ricerche Aerospaziali, Capua (CE), Italia**
[44] **Museo di Storia Naturale dell'Università degli Studi di Firenze, Firenze, Italia**
[45] **Infini.to Planetario di Torino, Pino Torinese (TO), Italia**
[46] **Astrobioparco l'Oasi di Felizzano, Felizzano (AL), Italia**
[47] **Osservatorio Polifunzionale del Chianti, Barberino val d'Elsa (FI), Italia**
[48] **Istituto d'Istruzione Superiore "Enrico Fermi", Montesarchio (BN), Italia**
[49] **Liceo Scientifico "G.B.Quadri", Vicenza, Italia**
[50] **Dipartimento di Scienza della Terra, Università degli Studi di Firenze, Firenze, Italia**
[51] **Liceo Statale "Arturo Issel", Finale Ligure (SV), Italia**
[52] **Gruppo Astrofili Persicetani, San Giovanni in Persiceto (BO), Italia**
[53] **Liceo "G.Stampacchia", Tricase (LC), Italia**
[54] **Osservatorio Astronomico "Giuseppe Piazzi", Ponte in Valtellina (SO), Italia**
[55] **Liceo Scientifico "Pietro Paleocapa", Rovigo, Italia**
[56] **Osservatorio Astronomico Amatoriale Bob House, Palermo, Italia**
[57] **IMCCE, Observatoire de Paris, PSL Research University, CNRS, Sorbonne Universités, UPMC, France**
[58] **LAM, Institut Pytheas, Marseille, France**
[59] **GEOPS, Univ. Paris-Sud, CNRS, Univ. Paris-Saclay Orsay, France**
[60] **IMPMC, Muséum National d'Histoire Naturelle, Paris, France**
[61] **CNRS, Aix Marseille Univ, IRD, Coll France, INRA, CEREGE, Aix en Provence, France**

Since 2017 we are deploying a network of all-sky cameras in Italy to monitor fireballs and bolides. Currently more than 40 cameras are operational or in installation phase.The PRISMA (Prima Rete Italiana per la Sorveglianza sistematica di Meteore e Atmosfera) network is connected to the french project FRIPON. We present the status of the network and the most recent developments made on data analysis as well as in the field of outreach and educational activities.

1 Introduction

PRISMA is the first attempt to establish a national fireball network in Italy. Scientific motivations and description of the project are described in Gardiol et al. (2016). In this paper we provide an update of the status of the project.

2 The Network

PRISMA and FRIPON

Since the very beginning the PRISMA project has been closely linked with the twin FRIPON network (Colas et al., 2015). The reason is twofold: on one hand we had no funding enabling us to perform research and development on hardware and software solutions. On the other hand the lack of funds suggested us to start with a small step, i.e. the extension of an existing neighboring network. Being the proposing institution (INAF – Osservatorio Astrofisico di Torino) located in North-Western Italy, it was a natural choice to go for the FRIPON solution. Since then PRISMA has spread further over Italy, becoming a real national network, but it is still connected to FRIPON for the purpose of management of the nodes and collection of data, that are then transferred on the INAF IA2 archive facility located in Trieste to be processed.

Figure 1 – Map of the PRISMA network. Red: operational cameras; orange and yellow: in installation phase. Blu: FRIPON

Network structure

PRISMA is a collaboration among professional and amateur astronomers, university researchers, school teachers, people working in museums and planetaria. The collaboration counts currently nearly sixty institutions, both public and private, and more than one hundred people involved at different levels. There is one National Coordinator and a Project Office managing the network and several Working Group dealing with the various aspects of the project. A geographical distribution of the PRISMA stations is shown in Figure 1.

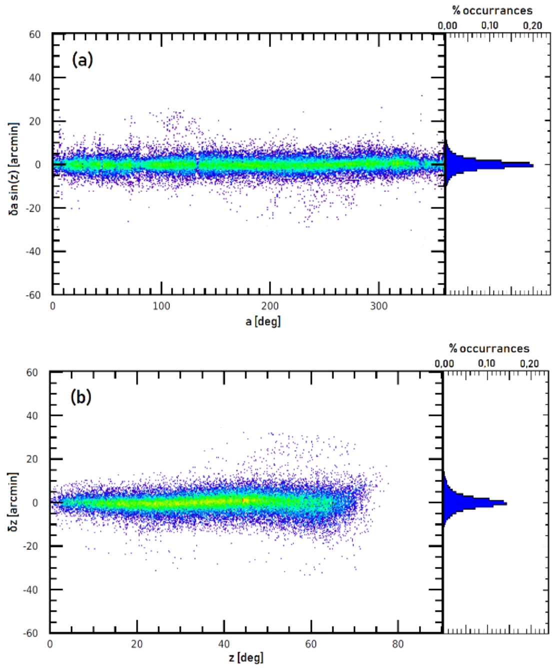

Figure 2 – Mono- and bi-dimensional histograms for azimuth and zenith distance residuals between catalogue and computed sources positions, for January 2017 calibration data of Pino Torinese station.

3 Data processing and analysis

Astrometry

One fundamental step for the characterization of an all-sky camera is the determination of the astrometric solution in order to be able to convert the observed coordinates (x,y) on the detector frame into horizontal celestial coordinates (Azimuth and Zenith distance). For PRISMA we implemented the parametric approach described in Ceplecha (1987) and Borovicka et al. (1995); Borovicka (1992) with some modifications. The two main effects that are taken into account are 1) the radial distortion and 2) the mismatch between the optical axis and the zenith direction, for a total of 8 parameters to be estimated for each camera. Our implementation is fully described in Barghini et al. (2018). The results so far show (see Figure 2) a dispersion of the residuals between measured and computed star positions of about $\sigma_a \simeq 2\,\mathrm{arcmin}$ and $\sigma_z \simeq 4\,\mathrm{arcmin}$.

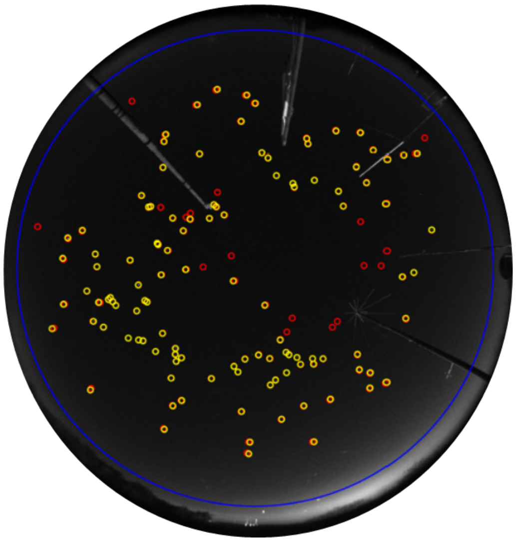

Figure 3 – Sample image from the astrometric routine. Red circles are real stars identified by the procedure onto the CCD, yellow circles represent projected catalogue sources.

The estimated statistical error associated to the astrometric projection using one month of data is of few arcsecs, negligible with respect to the error on a single measure of one bright bolide track (of the order of 1 arcmin). A residual systematic contribution of few arcmins at low elevations is taken into account by numerical correction.

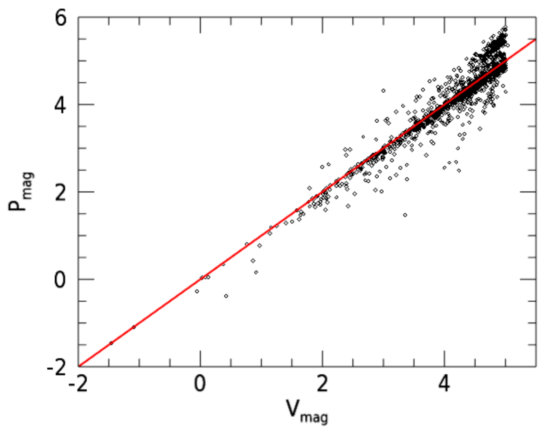

Figure 4 – Correlation between V and computed P magnitude.

Photometry

Photometric calibration is performed assuming to be dominated by the measured quantum efficiency of the camera with respect to the standard Johnson-Cousins astronomical system. A wideband P ('PRISMA') magnitude is defined and computed by numerical integration. Results show a quite strong correlation with the V band magnitude (see Figure 4). Other effects that are considered in the magnitude zero point determination are the dimming at increasing zenith distance given by both the airmass value combined with the atmospheric extinction and the radial dependent sensitivity of the optical system. Figure 5 shows a typical calibration curve on a random image taken with the Pino Torinese camera. Besides the application to meteor light curves, the photometry calibration can be applied to systematic monitoring of artificial light pollution enabling the possibility to create frequent maps of sky brightness. For further details on photometric calibration see again Barghini et al. (2018).

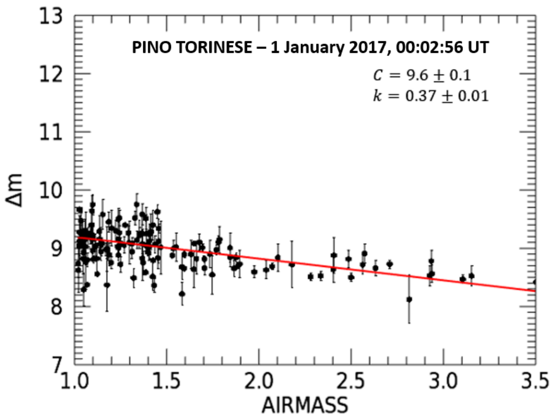

Figure 5 – Calibration of magnitude zero-point and atmospheric extinction coefficient for the Pino Torinese station on the 1 January 2017, 00:02:56 UT capture.

Trajectory and Dynamic model

To compute the atmospheric trajectory of observed fireballs we have implemented up to now two procedures. The simpler one is based on geometric intersection of the best planes containing two stations and the unit vectors of the fireball's observed points (Ceplecha, 1987). A second procedure is also available for simultaneous triangulation from more than two stations by Least-Square minimization (Borovicka, 1990). We also implemented a single body dynamical model following (Ceplecha et al., 1998) to be able to estimate the fireball main physical parameters (i.e. drag and ablation coefficients, pre-atmospheric velocity, mass/section ratio) assuming that no fragmentation has occurred, as well as the height, velocity and acceleration in the terminal point of the luminous path to be used as a starting solution for the potential computation of dark flight and strewn field.

Dark Flight, Strewn Field and Orbital parameters

If the previous step tells us that some fragment may have survived the fireball phase, then computation of the dark flight and strewn field is performed. Our implementation follows the Newton's Resistance law in turbulent regime (Ceplecha, 1987) and takes into account when available the wind profile (both intensity and direction) and the atmospheric conditions (Density, Pressure and Temperature vs. height). The heliocentric orbital elements of the progenitor body are also computed.

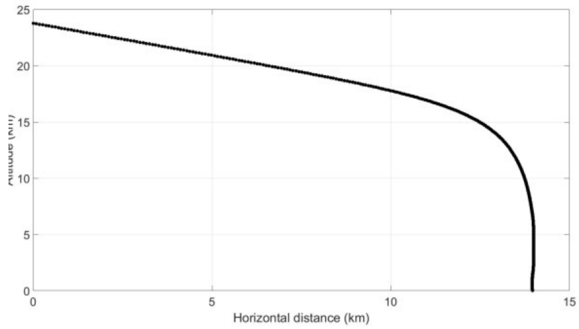

Figure 6 – Dark flight for IT20170530 (height vs. horizontal distance). It may be noticed the effect of the wind in the last part of the fall.

Further details on trajectory, dark flight, strewn field, dynamic model and orbital parameter computation are available in Carbognani et al. (2018).

Figure 7 – A negative image showing the full path of IT20170530 from PRISMA-Rovigo (ITVE02). North is down, south is up. The bright object on the left is the Moon near the western horizon. The fireball moved from top-left to bottom-right.

4 Some observed bolide

The data processing pipeline has been successfully tested on several very bright bolides. We mention here the one occurred on May 30th, 2017 at 21:09 UTC (labelled IT20170530) in North-Eastern Italy, that was seen also by many visual observers. A detailed study of this event is available in Carbognani et al. (2018). At that time only few cameras where operative, and therefore we used also data from the IMTN (Italian Meteor and TLE network) to perform triangulation. Figure 7 shows the cumulative image captured by the PRISMA camera in Rovigo. Figure 8 shows the computed trajectory, while in Figure 6 we report the estimated dark flight path. We think very likely that a residual of the original meteoroid survived, with an estimated mass of about 2 kg and a dimension of 10 cm. Unfortunately the strewn field area is densely populated and a place of intensive agricultural activity, so besides a short search campaign public appeals have been made to the population on newspapers and radio as well as social networks.

Following these appeals, over 10 suspected meteorites have been collected by local inhabitants, all identified as common ground stones. More recently, in summer 2018, there were a couple of bright bolides over Italy (Sardinia and Adriatic Sea), very popular because witnessed by many people. Unfortunately both locations were poorly covered by our cameras. We cite instead the event of August 22nd, 2018 at 21:37 UTC (labelled IT20180822), occurred in Valtellina (Lombardia) and recorded by six PRISMA cameras, that allowed us to perform reliable computations (see the results in Figure 9). The inclination of the trajectory was very high (72 degrees) with a probable survivor of quite small size (5 cm). Again the area is difficult to search because it is situated in the mountains at 1500 meters a.s.l., a very steep terrain covered with woods and some pastures (see Figure 10). However, we are now ready to deploy an automatic data reduction pipeline.

Figure 8 – Trajectory for IT20170530 bolide.

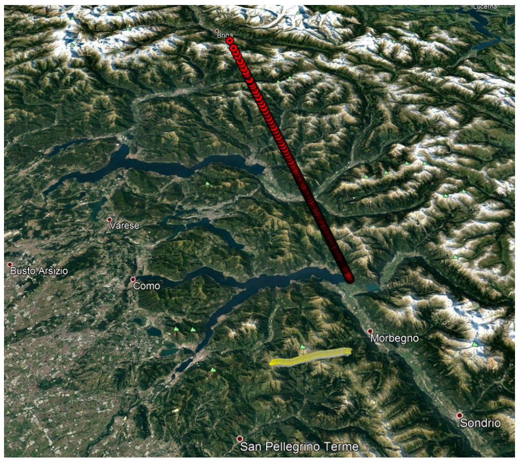

Figure 9 – Computed trajectory (red) and on-ground projection (yellow) for IT20180822 bolide. Lakes Maggiore, d'Iseo and di Como are visible in between the two trails.

5 Outreach and educational activities

While growing in size PRISMA has also increased its presence in the Italian society in general and in the meteor community in particular. Whenever possible we participate to local public events organized by amateurs or science festivals of national relevance, where we propose conferences and activities, like a meteorite treasure hunt that was very popular (see Figure 11). PRISMA researchers are more and more frequently asked to participate to TV and Radio emissions or give interviews

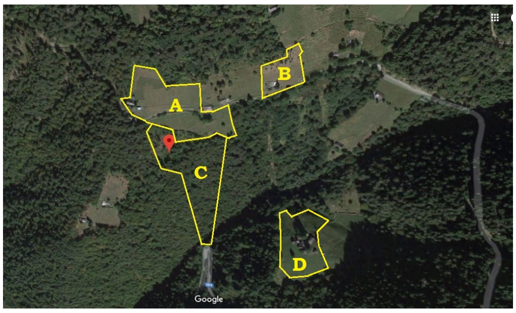

Figure 10 – Strewn field for IT20180822 bolide, with estimated impact point and areas already covered by search campaign.

to local and national newspapers, as well as specialist press, each time some bright bolide is reported by visual observers. Thanks to a collaboration with IMO it is now possible for everyone to report a bolide through the PRISMA website (`www.prisma.inaf.it`). A dedicated working group produces educational material in Italian language for students, in collaboration with their teachers. This material has been used to carry out hands-on laboratories on the subject of meteor and meteorites in several schools, in particular those that installed a PRISMA camera on their roof.

Figure 11 – One of the meteorite treasure hunt events organized by PRISMA during the Genova Science Festival in 2017.

6 Conclusion

Two years after its first steps PRISMA is a well-established fireball network in Italy. Data are collected via the FRIPON system and transferred at the INAF IA2 archiving facilities in Trieste. The data analysis pipeline is ready to be implemented in an automatic way, performing astrometry and photometry calibration and computation of the main characteristics of the observed bolide (triangulation, dark flight, dynamics, strewn field, orbit). An intense educational and outreach activity is taking place and media attention for this project is constantly growing.

Acknowledgement

PRISMA is the Italian Network for Systematic surveillance of Meteors and Atmosphere. It is a collaboration initiated and coordinated by the Italian National Institute for Astrophysics (INAF) that counts members among Research institutes, Associations, Schools. The complete list of PRISMA members is available here: `http://www.prisma.inaf.it` PRISMA was partially funded by a 2016 "Research and Education" grant from Fondazione Cassa di Risparmio di Torino and by a 2016 grant from Fondazione De Mari di Savona. The initial FRIPON hardware and software has been developed by the FRIPON-France core team under a French ANR grant (2014-2018).

References

Barghini D., Gardiol D., and Carbognani A. (2018). "Improving astrometry and photometry reduction for PRISMA all-sky cameras". In *International Meteor Conference Pezinok, Slovakia, 30 August – 2 September 2018*.

Borovicka J., Spurny P., and Keclikova J. (1995). "A new positional astrometric method for all-sky cameras.". *Astronomy and Astrophysics Supplement*, **112**, 173.

Borovicka J. (1990). "The comparison of two methods of determining meteor trajectories from photographs". *Bulletin of the Astronomical Institutes of Czechoslovakia*, **41**, 391–396.

Borovicka J. (1992). "Astrometry with all-sky cameras.". *Publications of the Astronomical Institute of the Czechoslovak Academy of Sciences*, **79**.

Carbognani A., Barghini D., Gardiol D., Di Martino M., Valsecchi G., Trivero P., Buzzoni A., Rasetti S., Selvestrel D., Knapic C., Londero E., Zorba S., Volpicelli C., Di Carlo M., Vaubaillon J., Marmo C., Colas F., Valeri D., Zanotti F., Morini M., Demaria P., Zanda B., Bouley S., Vernazza P., Gattacceca J., Rault J., Maquet L., and Birlan M. (2018). "The italian bolide of May 2017: trajectory, orbit and preliminary fall data". In *International Meteor Conference Pezinok, Slovakia, 30 August – 2 September 2018*.

Ceplecha Z. (1987). "Geometric, dynamic, orbital and photometric data on meteoroids from photographic fireball networks". *Bulletin of the Astronomical Institutes of Czechoslovakia*, **38**, 222–234.

Ceplecha Z., Borovička J., Elford W., ReVelle D., Hawkes R., Porubčan V., and Šimek M. (1998). "Meteor phenomena and bodies". *Space Science Reviews*, **84:3-4**, 327–471.

Colas F., Zanda B., Bouley S., Vaubaillon J., Marmo C., Audureau Y., Kwon M., Rault J., Caminade S., Vernazza P., et al. (2015). "Fripon, the french fireball network". In *European Planetary Science Congress*, volume 10.

Gardiol D., Cellino A., and Di Martino M. (2016). "Prisma, italian network for meteors and atmospheric studies". In *International Meteor Conference Egmond, the Netherlands, 2-5 June 2016*. pages 76–79.

Mendocino College-Ukiah Latitude Observatory CAMS Project: First Light

Beck, Timothy William[1], Bradley, Martin[2], Edward, Cannon[1], Jesse Glazier[1], Hunchard, Daniel[1], Ronco, Jeremy[1], Emerald Sherwood[1] Upton, Chatnaree[1]

[1] **Mendocino Community College, Ukiah CA 95482 USA 2**

[2] **Ukiah International Latitude Observatory, Ukiah CA 95482 USA**

In the spring of 2018 both camera stations of the Mendocino College-Ukiah Latitude Observatory Project became operational and began recording coincident meteor events and calculating trajectories and orbits. This success followed numerous natural and human caused disasters some of which required acquisition of replacement apparatus and remodeling of laboratory space. This Northern California extension of the CAMS network is currently being synced to the CAMS network of the San Francisco Bay Area. We present preliminary data from June and August of 2018 and outline imminent expansion of the network to include greater sky coverage and the possible installation of a third camera station at the Mendocino College Point Arena Field Station.

1 Location of Instruments

Our original camera site remains at the Ukiah Latitude Observatory adjacent to its historic office. After determining that the Mendocino College North County campus is too close to measure trajectories, the second camera site was installed at a private residence in Sonoma County approximately 75 km away (see Figure 1). This second location is also preferable for being within reasonable distance of existing California CAMS sites (Jenniskens, 2011).

Figure 1 – Location of camera sites in Northern California.

2 Specifications

Each location of our prototype setup was to be equipped with 2 1/3" Color SONY 960H CCD Effio-E DSP cameras manufactured without an IR cut filter. However, it became clear during testing of our first site that one of the cameras was defective so each site uses a single camera with an additional redundant camera in Sonoma County. Our initial camera placement was constrained by a desire for ready access as well as privacy hence the sky coverage and overlap is not optimal (see Figure 2). This will be corrected in the expanded project this autumn.

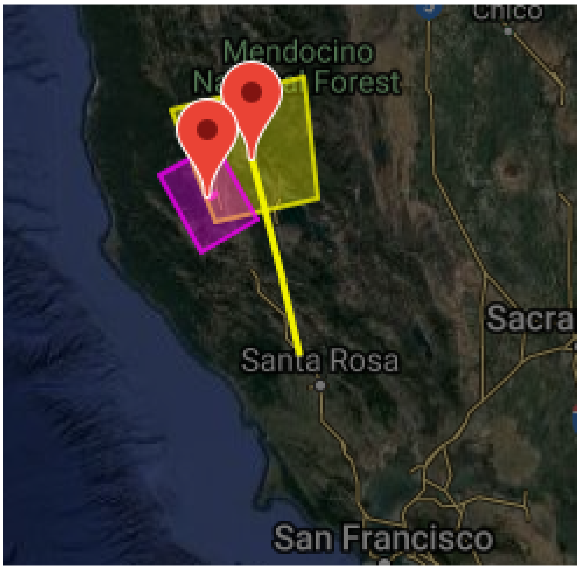

Figure 2 – Not optimized overlap of prototype setup.

3 First light

Following a seemingly endless succession of natural and human caused disasters, we recorded our first coincident meteor event on April 30th (see Figure 3). A few more equipment moves relating to the remodel of the historic office resulted in intermittent data collection throughout the summer with both sites permanently coming online on August 1st, 2018. Figure 4 is a gnomonic projection of single camera detections during the night of August 13th. The limited sky coverage is apparent as is the Perseid radiant.

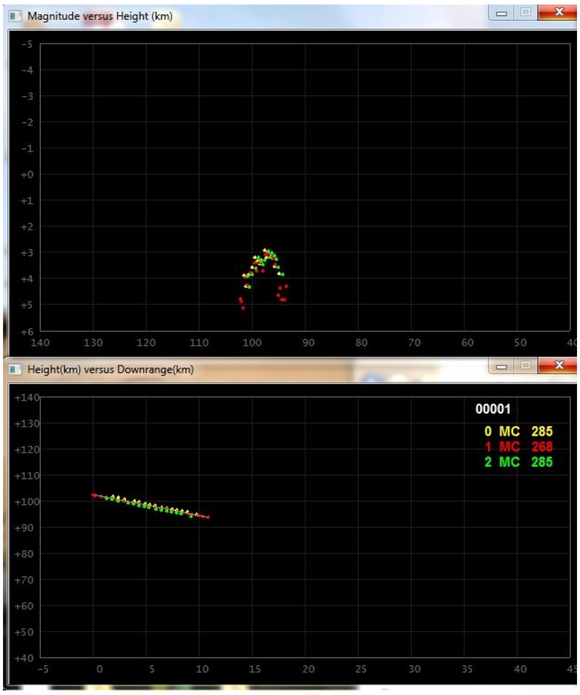

Figure 3 – First coincident event recorded by CAMS Northern California.

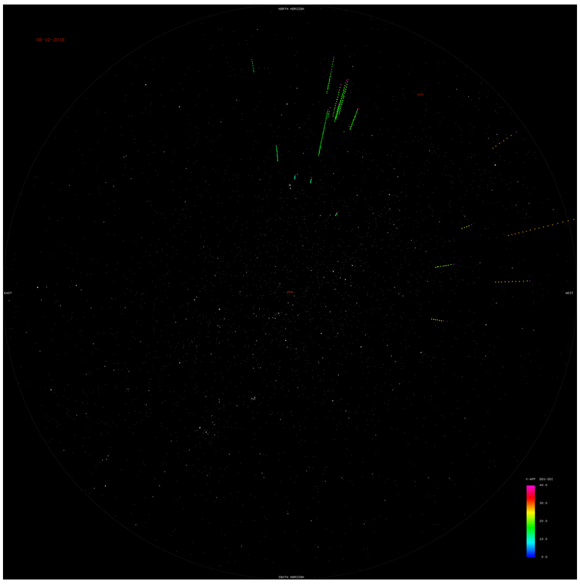

Figure 4 – Single camera Perseid events from August 13th, 2018.

4 Future work

Our limited data is currently being uploaded to the CAMS database. As of writing, our project has acquired 5 new cameras the installation of which will increase our sky coverage and overlap manifold. We are also exploring the installation of a 3rd camera site with all-sky coverage at the Mendocino College Point Arena Field Station (see Figure 5). This will further increase our coverage as well as refine our orbit calculations.

Figure 5 – Proposed 3rd camera sites and distances from existing NorCal locations.

Acknowledgements

We would like to thank the Mendocino College Foundation for providing primary funding to acquire our computers, cameras, and other apparatus. We would also like to thank the City of Ukiah for use of the historic Latitude Observatory office space. In addition we thank Damir Šegon and Pete Gural for remote assistance in constructing our project, and Peter Jenniskens and Dave Samuels for helping to integrate us into the CAMS network.

References

Jenniskens P., Gural P.S., Dynneson L., Grigsby B.J., Newman K.E., Borden M., Koop M., Holman D. (2011). "CAMS: Cameras for Allsky Meteor Surveillance to establish minor meteor showers." *Icarus*, **216**, 40–61.

On the energy release after meteoroid fragmentation

Lidia Egorova[1] and †Valeriy Lokhin[1]

[1] **Institute of Mechanics, Lomonosov Moscow State Univercity, Moscow, Russia**
egorova@imec.msu.ru

†Died September 05, 2018

The instantaneous fragmentation of large meteoroids (fireballs) moving in Earth's atmosphere is considered. The simulation of energy release is proposed assuming that the kinetic energy of meteoroid particles turns into heat energy of the gas cloud. The distribution of the particles by mass after fragmentation is discussed.

1 Introduction

A number of factors determine the nature of meteoric body fragmentation in the atmosphere. Some of them are the magnitude of the load, the structure of the body and its internal properties (composition, density, strength with respect to various loads). The complicated phenomena turned the scientists to choose and to develop new models. Popova (2004) and Brykina (2018) did the review.

We concern with a class of phenomena when the energy of a fragmented meteoroid reaches the Earth surface. We assumed that the body breaks up into separate fragments of different sizes moving independently. The explosive nature of the observed effects suggests that the aerodynamic drag is several times greater than the strength of the body or fragments of the pre-destroyed body. An important property of this type of fragmentation is the distribution of the produced particles by mass. We choose the particle distribution developed for a body suddenly destroyed by high-speed impact. The high velocity of the meteoroid and the exponential growth of the air density as the altitude decreases makes this proposal reasonable.

2 Mass distribution of destroyed body fragments

A number of theoretical and experimental works provide the distribution of destroyed particles by mass.

Experiments show that catastrophic destruction depending on the projectile velocity could be longitude (with rather small velocity), cone (bigger velocity) and core (high velocity) types. The details can be found in the work of Fujiwara (1986). Experiments carried out by Pilyugin (2008) show big particles in this distribution have isometric form and we could assume they are spheres.

Experimental work on destruction by high-speed impact of gypsum spheres by Okamoto & Arakawa (2009) shows that the higher velocity (or higher energy) impact produces smaller particles. The lower energy impact produces a cone type of fragmentation, the more energetic and the more catastrophic one. Figure 1 shows

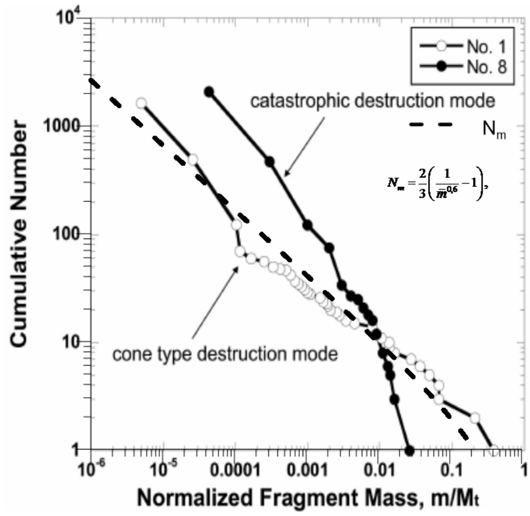

Figure 1 – Number of fragments via their mass.

the experimental results of Okamoto & Arakawa (2009). Black and white circles represent the number of fragments via their mass for cone and catastrophic fragmentation consequently. The dashed line shows the theoretical model of Fujiwara et al. (1989). This model is also used by Nemtchinov with colleagues (Nemchinov et al., 1999).

$$\frac{\mathrm{d}N_m}{\mathrm{d}m} = C\, m^{\frac{k}{3}-2}, \;\; k = 1.2 \tag{1}$$

Solving this equation, we get

$$N_m = \frac{2}{3}\left(\frac{1}{\overline{m}^{0.6}} - 1\right),$$

where $\overline{m} = m/M$ is a normalized fragment mass. We could see at Figure 1, that theoretical distribution relate to the cone type of fragmentation. This distribution of particles for meteoroid fragmentation was used in our previous work (Egorova & Lokhin, 2016) and is used in present research.

3 Transition of kinetic energy of particles into heat energy of a gas

Nowadays researchers simulate the entry and destruction of meteoric bodies in the atmosphere to evaluate

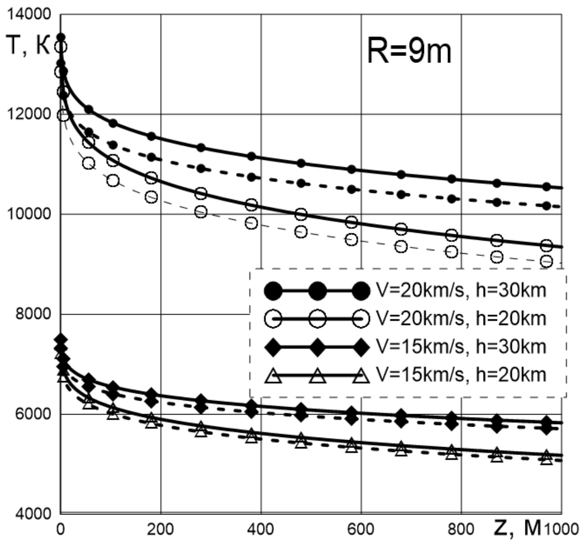

Figure 2 – The temperature in a cloud of gas and vapor for a meteor body of radius 9 m.

the released energy. Numerical simulations developed by Shuvalov and colleagues (Popova et al., 2013; Shuvalov et al., 2013). For a quick approximation of damage at the Earth's surface, it is reasonable to use a cylindrical explosion or a point explosion analogy. We decide to prove the validity of this analogy. The goal of present study is to get conditions of cylindrical explosion solving the problem of fragmentation. The first stage of the work is to find the temperature in a gas cloud after meteoroid destruction.

We assumed the destruction of the meteoroid is into many fragments. The kinetic energy of the moving particles passes into the thermal energy of the gas volume in which their motions take place.

According to our model the size and number of fragments of meteoroids in the cloud corresponds to that of suddenly destroyed by explosion.

The energy transferred to heat in a gas cloud is the initial kinetic energy of a parent body with mass M_0 and velocity V0 minus kinetic energy of the ensemble of particles at the given point

$$\Delta E = M_0 \frac{V_0^2}{2} - M_0 V_0^2 \int_0^1 \left[N(\overline{r}_0 \frac{\mathrm{d}}{\mathrm{d}\overline{r}_0} \left(\overline{m}(\overline{r}_0) \frac{\overline{V}^2(\overline{r}_0, z)}{2} \right) \right] \mathrm{d}\overline{r}_0 \quad (2)$$

where $\overline{r}_0 = r_0/R_0$ is the initial relative radius, relative mass $\overline{m}(\overline{r}_0) = m_0/M_0$ and relative velocity $\overline{V}(\overline{r}_0, z) = V/V_0$, R_0 is parent body radius and z is the vertical coordinate, measured from the altitude of fragmentation.

For each particle, we used meteor physics equations. We estimate the parameter of ablation and find that it is small. We assume that the final velocity of particle is a small quantity compared to body velocity before the fragmentation. Under these assumptions we expand the exponent into series and get the approximate solution for physical theory of meteor equation. We find the analytical relation for the integral in 2, using distribution 1 and the approximate solution for physical theory of meteor equation. We do not cite the calculations because of its awkwardness. One could see the details in our work (Egorova & Lokhin, 2018).

The temperature in the longitude gas cloud is equal differential of energy divided by heat capacity of gas C_V and gas volume

$$T = \frac{\frac{\mathrm{d}E}{\mathrm{d}z}\mathrm{d}z}{C_V \rho \pi R_*^2 \mathrm{d}z}$$

The final formula for the gas temperature is

$$T = \frac{3R^2 V_0^2 C_D}{C_V R_*^2}(1+\kappa V_0^2) \times \left[1 - \left(\frac{3}{4}\frac{\rho C_D}{\delta} \right)^{1/5} (1+\kappa V_0^2)^{1/5} \, \Gamma\left(\frac{4}{5}\right) \left(\frac{z}{R}\right)^{1/5} \right],$$

$$\kappa = \frac{C_H}{6 C_D Q},$$

where Q is enthalpy of mass loss for meteoroid substance due to aerodynamic forces and heat transfer, C_D and C_H are the drag and heat transfer coefficients (constants), ρ is atmosphere density and δ is the meteoroid density.

4 Results

Figure 2 show the temperature in a gas cloud calculated for body of radius 9 m. The velocity at the moment of fragmentation is 20 km/s (red and purple lines) and 15 km/s (green and blue lines). Circles related to distraction at altitude of 30 km. Triangles and rhombs related to 20 km. Solid line referred to model taking to account ablation and dashed ones to model without ablation of particles. Taking into account the ablation of particles in the cloud gives rise to temperature, since the decrease in particle size leads to their faster braking and, consequently, the kinetic energy of the particles transferred to the gas faster. The smaller height of fragmentation gives a sharper drop in temperature in the cloud.

We also calculated the temperature for fragmentation into the equal particles but resulting temperature overestimated the real value. Therefore equal particles fragmentation is not valuable under condition specified.

5 Conclusion

Assuming a known distribution of meteoroid fragments by mass, a change in the temperature in the cloud of gas after meteoroid destruction by the explosive mechanism obtained. The high temperature of the gas in such a cloud allows us to talk about the phenomenon of a "thermal explosion". Calculating the temperature of a gas cloud is a first step in a problem of estimation of energy release by fragmenting meteoroid in Earth atmosphere.

Acknowledgement

This work was done under Government contract and partially supported by RFBR according to the research project No. 18-01-00740 a.

†Valeriy Lokhin was born 10.04.1932 and devoted his life to research in various fields of mechanics and mathematics, some of them are theory of nonlinear tensor functions, hypersonic flows of dusty gas, theory of heterogeneous elastic media and motion and destruction of meteor bodies in the atmosphere. At the start of his career after graduation in Moscow University he worked with Sergey Korolev and in University he study from academicians Aleksandrov, Kolmogorov and Sedov. He was kind and respondent person but rigorous in science work. He died on September 05, 2018.

References

Brown W. K. and Wohletz K. H. (1995). "Derivation of the weibull distribution based on physical principles and its connection to the rosin–rammler and lognormal distributions". *Journal of Applied Physics*, **78:4**, 2758–2763.

Brykina I. G. (2018). "Large meteoroid fragmentation: Modeling the interaction of the chelyabinsk meteoroid with the atmosphere". *Solar System Research*, **52:5**, 426–434. In english.

Egorova L. and Lokhin V. (2018). "Modeling of energy release at the final stage of the meteoroid movement". *Open Astronomy (in print)*, **27**.

Egorova L. A. and Lokhin V. V. (2016). "Two-stage destruction of a meteoroid with a final burst". *Moscow University Mechanics Bulletin*, **71:4**, 82–86.

Fujiwara A. (1986). "Results obtained by laboratory simulations of catastrophic impact". *Memorie della Societa Astronomica Italiana*, **57**, 47–64.

Fujiwara A., Cerroni P., Davis D., Ryan E., Di Martino M., Holsapple K., and Housen K. (1989). "Experiments and scaling laws for catastrophic collisions". In *Asteroids Ii*. pages 240–265.

Nemchinov I., Popova O., and Teterev A. (1999). "Penetration of large meteoroids into the atmosphere: Theory and observations". *Journal of Engineering Physics and Thermophysics*, **72:6**, 1194–1223.

Okamoto C. and Arakawa M. (2009). "Experimental study on the collisional disruption of porous gypsum spheres". *Meteoritics & Planetary Science*, **44:12**, 1947–1954.

Pilyugin N. (2008). "Destruction of filled polymer targets by high-velocity impact". *Combustion, Explosion, and Shock Waves*, **44:2**, 239.

Popova O. (2004). "Meteoroid ablation models". *Earth, Moon, and Planets*, **95:1-4**, 303–319.

Popova O., Glazachev D., Podobnaya E., Svetsov V., and Shuvalov V. (2017). "Radiation and ablation of large meteoroids decelerated in the earth's atmosphere". In *European Planetary Science Congress*, volume 11.

Popova O. and Nemchinov I. (2008). "Bolides in the earth atmosphere". In *Catastrophic events caused by cosmic objects*, pages 131–162. Springer.

Popova O. P., Jenniskens P., Emelyanenko V., Kartashova A., Biryukov E., Khaibrakhmanov S., Shuvalov V., Rybnov Y., Dudorov A., Grokhovsky V., et al. (2013). "Chelyabinsk airburst, damage assessment, meteorite recovery, and characterization". *Science*, **342:6162**, 1069–1073.

Shuvalov V., Svettsov V., and Trubetskaya I. (2013). "An estimate for the size of the area of damage on the earths surface after impacts of 10–300-m asteroids". *Solar System Research*, **47:4**, 260–267.

Testing of the new meteoroid fragmentation model applied to the Chelyabinsk event

Irina G. Brykina[1] **and Michael D. Bragin**[2]

[1] **Lomonosov Moscow State University, Moscow, Russia**
shantii@mail.ru

[2] **Moscow Institute of Physics and Technology, Moscow, Russia**
michael@bragin.cc

The problem of modelling the interaction of a large meteoroid with the atmosphereis considered. A new model of meteoroid disruption to the cloud of fragments moving with the common shock wave is proposed. The model takes into account changes of shape and density of this cloud. Comparison with similar models used in the literature is made. The numerical solution of meteor physics equations for the mass loss and energy deposition of the Chelyabinsk meteoroid and its light curve normalized to the maximum brightness has been obtained. Comparison of the solution with the observational data is made.

1 Introduction

Most large meteoroids are disrupted during their passage through the Earth's atmosphere. There exist different approaches to modeling their disruption. In one approach it is assumed that fragments move separately with their own shock waves. These are models of one-stage and progressive fragmentation – discrete or continuous. In another approach it is assumed that a meteoroid is broken up into a cloud of small fragments which move with the common shock wave as a single body. This body possessing properties of plasticity and fluidity is deformed under the action of aerodynamic forces: it is expanding in a lateral direction and reducing in thickness in a flight direction. In recent years, to achieve the agreement between calculations and observation data, combinations of both approaches have been used.

In this study we use the second approach. Grigoryan (1979) was the first who developed the model of the continuous flattening of the large disrupted meteoroid due to the difference in pressures at the frontal and side parts of the body. For such models, the term "pancake" introduced by Melosh (1981) is used. Later similar models of the flattened cloud of fragments were used in many studies and continue to be used until the present time (Grigoryan et al. (2013); Hills & Goda (1993); Register et al. (2017); and other).

In "pancake" models commonly used in the literature, the rate of lateral expansion of the disrupted meteoroid does not depend on the degree of its flattening because of neglecting its shape change in deriving the expression for this rate. This leads to too high values of the meteoroid midsection radius along the trajectory. In our model the equation for the rate of lateral expansion was derived with consideration of a pressure distribution over the body whose shape varies with time. This model differs from other "pancake" models also in that it takes into account the decrease in density of the disrupted meteoroid due to the increase of spacing between fragments.

2 Fragmentation model

We suggest a spherical shape of the meteoroid before the start of breakup, and then the meteoroid continues its flight as a cloud of fragments and vapor, which fill in gaps between fragments. We assume two related processes: flattening – the sphere is transformed to the flattened spheroid with ratio of axes $b/a = k (k \geq 1)$ under the effect of pressure forces, and the decrease of the density of the fragmented meteoroid due to the increase of spacing between fragments (Figure 1). Thus we introduce the parameter $\gamma : \delta = \delta_e/\gamma^3$, ρ is a density of the fragmented meteoroid, δ_e is its initial density.

To obtain the rate of lateral expansion of the cloud of fragments we considered the pressure distribution over spheroid and estimated the force acting in the transverse direction (Brykina, 2018). As a result we obtained an equation for the rate of increase of the midsection radius R_S of the disrupted meteoroid

$$\frac{\mathrm{d}R_S}{\mathrm{d}t} = \frac{1}{k^{1/2}} \left(\frac{\gamma^3 \rho}{\delta_e} \right)^{1/2} V, \; k = \frac{4\pi\delta_e}{3} \frac{R_S^3}{M\gamma^3} \qquad (1)$$

Here t is the time, V is the meteoroid velocity, ρ is the atmospheric density. The radius R_S and the parameter of flattening k are connected by a relation depending on meteoroid mass M at current time t.

We assume that the rate of increase of the parameter γ characterizing the distance between fragments is proportional to $\rho^{1/2}$ (Artemieva & Shuvalov, 2001; Passey & Melosh, 1980). Then we can submit the dependence γ on ρ in a form

$$\gamma = 1 + \frac{\rho^{1/2} - \rho_f^{1/2}}{\rho_m^{1/2} - \rho_f^{1/2}} (\gamma_m - 1) \qquad (2)$$

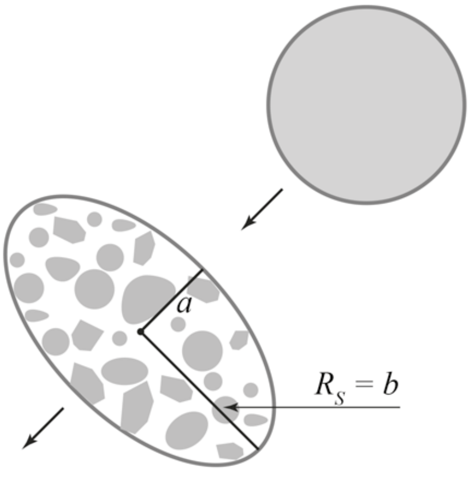

Figure 1 – Meteoroid before and after start of breakup.

Subscript f corresponds to values at the height h_f of fragmentation starting and subscript m corresponds to values at the height h_m of maximum brightness of the bolide. Parameter γ_m is determined by correlation of calculated and observational values of h_m. We assume that the value of γ should not be much more than 2 (Artemieva & Shuvalov, 2001), because at large γ fragments can be separated by a distance sufficient to move independently.

3 Comparison of "pancake" models

In "pancake" models used in previous studies, the rate of increase of the midsection radius R_S of the disrupted meteoroid can be represented in the form

$$\frac{\mathrm{d}R_S}{\mathrm{d}t} = c\left(\frac{\rho}{\delta_e}\right)^{1/2} V, \tag{3}$$

where coefficient c is a constant of the order of unity. For example $c = 1$ in the model of Grigoryan (1979); Grigoryan et al. (2013) and $c = (7/2)^{1/2}$ in the commonly used model of Hills & Goda (1993). Equation (3) has an analytical solution (we used the equality $\frac{\mathrm{d}}{\mathrm{d}t} = \rho V \sin\theta / h^* \cdot \frac{\mathrm{d}}{\mathrm{d}\rho}$, h^* is a height scale)

$$R_S = R_f\left(1 + \frac{2c\,h^*}{\sin\theta\,\delta_e^{1/2} R_f}(\rho^{1/2} - \rho_f^{1/2})\right) \tag{4}$$

From (4) it follows that in commonly used models, the values of midsection radius R_S are completely determined by only initial parameters: the height of fragmentation start h_f, meteoroid radius R_f at this height, entry angle θ (with respect to horizon) and density δ_e, and atmospheric density. There is no influence of ablation on R_S.

The main differences of the proposed fragmentation model from other "pancake" models are the following. First, our model takes into account the decrease of density of the disrupted meteoroid. Secondly, in our model (1) the rate of lateral expansion of the disrupted meteoroid essentially depends on the degree of its flattening, expressed by parameter k, in other words, on the meteoroid shape. Equation (3) does not take into account the change of meteoroid shape. Note that in the case of $\gamma = 1$ and $k = 1$ (sphere) (1) coincides with (3) at $c = 1$. Thirdly, in our model the rate of midsection radius increase depends on the meteoroid mass M which can change due to ablation. Thus to find R_S and M we must solve the joint problem of fragmentation, ablation and deceleration. In other models the fragmentation problem is separated from the problem of ablation and deceleration because R_S is determined only by the initial parameters, and not by the current parameters. The formula (4) merely determines the increase of midsection area in ablation and deceleration equations.

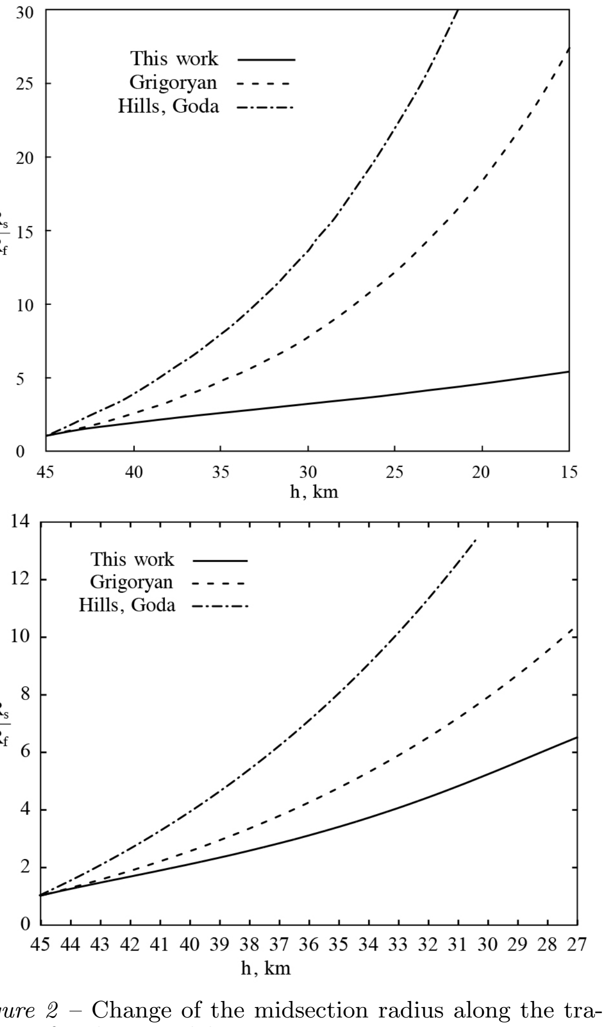

Figure 2 – Change of the midsection radius along the trajectory for three models.

Change of the meteoroid midsection radius along the trajectory obtained using models of this work, Grigoryan, and Hills and Goda is shown in Figure 2. Upper figure corresponds to calculations without taking into account ablation and $\gamma = 1$, lower – with taking into account ablation and using (2) for γ. Calculation parameters correspond to $h_f = 45\,\mathrm{km}$, $R_f = 10\,\mathrm{m}$, $\delta_e = 3.3\,\mathrm{g/cm^3}$, $\theta = 18°$ (characteristic parameters for the Chelyabinsk bolide), ablation coefficient was set equal to $0.01\,\mathrm{s^2/km^2}$. Figure 2 demonstrates the fact that our model predicts considerably lower values of R_S as compared to "pancake" models commonly used.

4 Solution of meteor physics equations

To model the interaction of the meteoroid with the atmosphere we use the equations of meteor physics – the deceleration and mass loss equations and equations of the rectilinear trajectory and the isothermal atmosphere

$$M\frac{\mathrm{d}V}{\mathrm{d}t} = -\frac{\pi}{2}R_S^2 C_D \rho V^2, \quad Q\frac{\mathrm{d}M}{\mathrm{d}t} = -\frac{\pi}{2}C_H \rho V^3$$
$$\frac{\mathrm{d}h}{\mathrm{d}t} = -V\sin\theta, \quad \rho = \rho_0 \exp\left(-\frac{h}{h^*}\right) \tag{5}$$

Here Q is the effective heat of mass loss, C_D is the drag coefficient, C_H is the heat transfer coefficient per unit area of the midsection, $\rho_0 = 1.225 \cdot 10^{-3}\,\mathrm{g/sm^3}$, $h_* = 7\,\mathrm{km}$. Equations (5) must be solved together with (1) and (2).

For the drag coefficient of spheroid we used the simple formula approximating the exact analytical solution obtained for a spheroid when setting the Newtonian pressure distribution (Brykina, 2018): $C_D = 2 - 1/k$. We obtained also the formula approximating results of numerical calculations (Golomazov et al., 2011) for hypersonic flow of dissociated air over spacecrafts with spheroidal front surface: $C_D = 1.78 - 1/k$.

For the radiative heat transfer coefficient for a spheroid, we obtained an approximate expression depending on V, R, k, ρ. The expression is a combination of Suttles et al. (1974) and (Brandis & Johnston, 2014) formulas approximating results of numerical calculations of radiative heat flux, with corrections which we made in accordance with numerical results of Apshtein et al. (1986); Biberman et al. (1978, 1972), and others. We do not cite the expression for C_H because of its awkwardness. The mean value of ablation coefficient was about $0.013\,\mathrm{s^2/km^2}$ on most of the calculated trajectory after the start of break up.

To model the interaction of the Chelyabinsk meteoroid with the atmosphere, we solved the system of equations (1), (2) and (5) using the explicit third-order Runge-Kutta method. We used also an approximate analytical solution (Brykina, 2018). In calculations, we took into account gravitational force, but the difference was small.

5 Application to the Chelyabinsk event

Disruption of the Chelyabinsk meteoroid is a very complex phenomenon and, certainly, the simple fragment cloud model does not provide an accurate account of its fragmentation. Individual fragments separated from the cloud and behaved independently, small fragments were decelerated and fell on the ground. However, considering that the largest observed fragments separated at height of 25 km and below (Borovička et al., 2013), it is an interesting question what can be obtained by using our simple model in modeling the interaction of the Chelyabinsk meteoroid with the atmosphere above this height.

In calculations we used as initial parameters the results of analysis and processing of observational data (Borovička et al., 2013). We set entry velocity to 19 km/s, $\theta = 18°$, $\delta_e = 3.3\,\mathrm{g/sm^3}$, $Q = 6\,\mathrm{km^2/s^2}$; we varied the bulk strength σ from 0.5 to 1.5 MPa. The unknown entry mass M_e of the Chelyabinsk meteoroid was determined by the reproducing of the observational curve of energy deposition per unit height (Brown et al., 2013) and was set to be $M_e = 1.28 \times 10^{10}\,\mathrm{g}$. This value is close to the estimate of Borovička et al. (2013) of $1.2 \times 10^1 0\,\mathrm{g}$. Variation of the ablation parameter within 30% led to a change in M_e by no more than 5%.

Numerical solution for mass loss of the Chelyabinsk meteoroid at $\sigma = 0.7$ MPa is shown in Figure 3 down to a height of 27 km. Comparison of calculated light curves normalized to the maximum brightness I/I_m with observed ones Popova et al. (2014) and Borovička et al. (2013) is presented in Figure 4 and 5. Dots correspond to numerical solution at $\sigma = 0.7$ MPa, dashed and dash-and-dotted lines – to analytical ones at $\sigma = 0.7$ and 0.5 MPa.

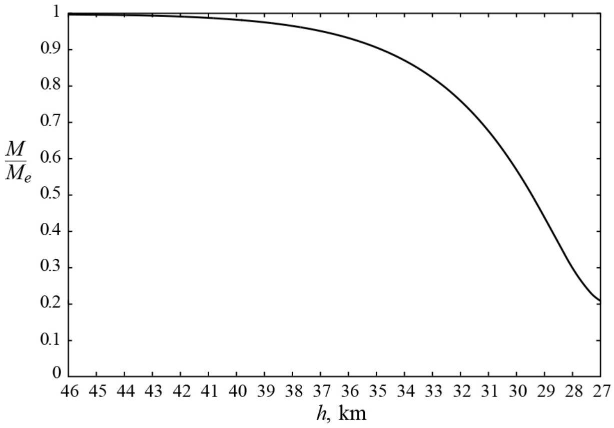

Figure 3 – Meteoroid mass loss along the trajectory.

Comparison of the calculated curves of energy deposition per unit height $\mathrm{d}E/\mathrm{d}h$ with the corresponding observational curve (Brown et al., 2013) is presented in Figure 6. Dots correspond to the numerical solution at $\sigma = 0.7\,\mathrm{MPa}$, dash-and-double dotted, dashed, and dash-and-dotted lines – to analytical ones at $\sigma = 1$, 1.2, and 1.5 MPa. Figures 4-6 demonstrate a satisfactory agreement between calculations and observational data for the Chelyabinsk superbolide.

6 Conclusion

The developed fragment cloud model takes into account the decrease in density of the disintegrated meteoroid

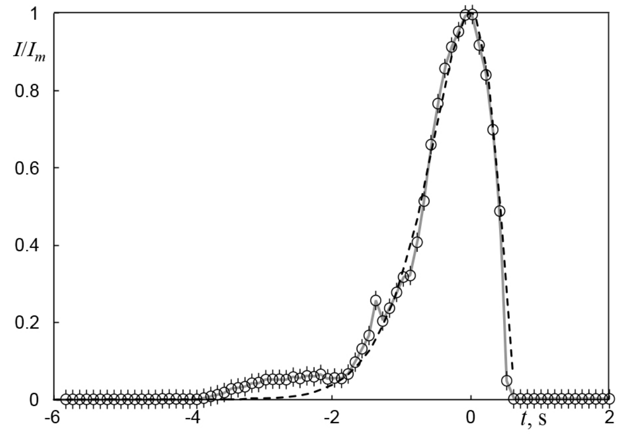

Figure 4 – Calculated and observational (Popova et al., 2014) (circles) light curves, t – time from the peak brightness.

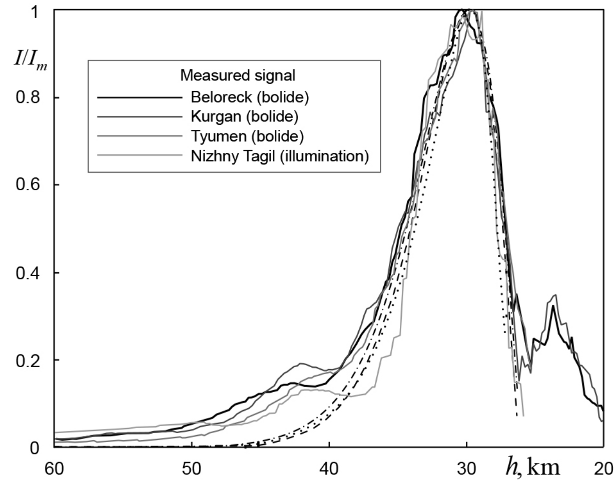

Figure 5 – Calculated and observational (Borovička et al., 2013) (solid lines) light curves.

and dependence of the rate of lateral expansion of this cloud on the degree of its flattening. That leads to considerably smaller values of midsection radius as compared with other "pancake" models. The mass loss, energy deposition and relative light curve of the Chelyabinsk meteoroid have been modeled down to a height of 27 km. Modeling results satisfactorily agree with observational data. At lower heights, one must take into account the motion of independent fragments.

Acknowledgement

This work was partially funded by the Russian Foundation for Basic Research, project No 18-01-00740.

References

Apshtein É. Z., Vartanyan N. V., and Sakharov V. I. (1986). "Distribution of radiant heat fluxes over the surface of three-dimensional and axisymmetric bodies in a supersonic ideal-gas flow". *Fluid Dynamics*, **21**, 78–83.

Artemieva N. A. and Shuvalov V. V. (2001). "Motion of a fragmented meteoroid through the planetary atmo-

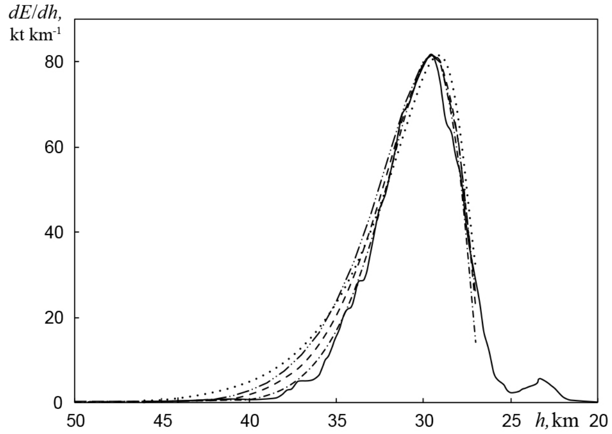

Figure 6 – Comparison of calculated and observational (Brown et al., 2013) (solid line) energy deposition per unit height.

sphere". *Journal of Geophysical Researc*, **106**, 3297–3310.

Biberman L., Bronin S., Brykin M., and Mnatsakanyan A. K. (1978). "Influence of gaseous heat-shield destruction products on the heat transfer in the neighborhood of the stagnation point on a blunt body". *Fluid Dynamics*, **13:3**, 440–447.

Biberman L., Bronin S. Y., and Lagar'kov A. (1972). "Radiative and convective heat transfer in hypersonic flow around a blunt body". *Fluid Dynamics*, **7:5**, 800–809.

Borovička J., Spurný P., Brown P., Wiegert P., Kalenda P., Clark D., and Shrbený L. (2013). "The trajectory, structure and origin of the chelyabinsk asteroidal impactor". *Nature*, **503:7475**, 235.

Brandis A. and Johnston C. (2014). "Characterization of stagnation-point heat flux for earth entry". In *45th AIAA Plasmadynamics and Lasers Conference*. page 2374.

Brown P., Assink J., Astiz L., Blaauw R., Boslough M., Borovička J., Brachet N., Brown D., Campbell-Brown M., Ceranna L., et al. (2013). "A 500-kiloton airburst over chelyabinsk and an enhanced hazard from small impactors". *Nature*, **503:7475**, 238.

Brykina I. G. (2018). "Large meteoroid fragmentation: Modeling the interaction of the chelyabinsk meteoroid with the atmosphere". *Solar System Research*, **52:5**, 426–434. In english.

Golomazov M., Litvinov I., Litvinov L., Ivankov A., and V.S. F. (2011). "Numerical simulation of flow over the reentry vehicles entering into the planet atmosphere". *Vestnik of Bauman Moscow State Technical University. Ser. Mashinostr.*, **4**, 42–53.

Grigoryan S. (1979). "Meteorites motion and destruction in planet atmospheres". *Cosmic Res.*, **17**, 724–740.

Grigoryan S., Ibodov F., and Ibadov S. (2013). “Physical mechanism of chelyabinsk superbolide explosion”. *Solar System Research*, **47:4**, 268–274.

Hills J. and Goda M. (1993). “The fragmentation of small asteroids in the atmosphere”. *The Astronomical Journal*, **105**, 1114–1144.

Melosh H. J. (1981). “Atmospheric breakup of terrestrial impactors”. In Merill R. B. and Schultz P. H., editors, *Multi-ring basins: Formation and Evolution*. pages 29–35.

Passey Q. and Melosh H. (1980). “Effects of atmospheric breakup on crater field formation”. *Icarus*, **42:2**, 211–233.

Popova O., Jenniskens P., and Glazachev D. (2014). “Chelyabinsk meteoroid fragmentation”. In *Collection of Scientific Papers of Institute of Geosphere Dynamics RAS), issue 5: Geophysical Effect Caused by Chelyabinsk Meteoroid Fall. Moscow: GEOS*. pages 59–78.

Register P., Mathias D., and Wheeler L. (2017). “Asteroid fragmentation approaches for modeling atmospheric energy deposition”. *Icarus*, **284**, 157–166.

Suttles J., Sullivan E., and Margolis S. (1974). “Curve fits of predicted inviscid stagnation-point radiative heating rates, cooling factors, and shock standoff distances for hyperbolic earth entry”.

The effect of the solar wind on the evolution of dust grains trapped in the mean motion orbital resonance with Jupiter

Roman Nagy[1], Jozef Klačka[1] and Milan Jurči[2]

[1] **Faculty of Mathematics, Physics and Informatics, Comenius University in Bratislava, Slovakia**
`roman.nagy@fmph.uniba.sk` and `klacka@fmph.uniba.sk`

[2] **Faculty of Civil Engineering, Slovak University of Technology, Bratislava, Slovakia**
`milan.jurci@stuba.sk`

1 Introduction

Evolution of interplanetary dust in the Solar System is governed by the gravitational forces of the Sun and planets, and non-gravitational forces manifested mainly on long-time scales. We consider the solar corpuscular (the solar wind effect) and electromagnetic (Poynting-Robertson, P-R, effect) radiation. The solar wind effect is more significant than the P-R effect, the importance of both of them increases with a decreasing size of the dust grains.

We focus on the orbital evolution of dust grains in the mean motion orbital resonance with the planet Jupiter. The solar wind and P-R effects simultaneously act in the restricted three-body problem; the Sun, the Jupiter and the dust grain. We also investigate the equilibrium solution and its stability. We deal with spherical particles of various sizes, from 1 to 100 microns.

2 The equation of motion

The equation of motion reads:

$$\begin{aligned}
\frac{d\vec{v}}{dt} &= -\frac{G\,M_\odot\,(1-\beta)}{r^2}\,\vec{e}_R \\
&\quad - \beta\,\frac{G\,M_\odot}{r^2}\left(1 + \frac{\eta_1}{\overline{Q}\,'_{pr}}\right)\frac{\vec{v}\cdot\vec{e}_R}{c}\,\vec{e}_R \\
&\quad - \beta\,\frac{G\,M_\odot}{r^2}\left(1 + \frac{\eta_2}{\overline{Q}\,'_{pr}}\right)\frac{\vec{v}}{c} \\
&\quad - G\,m_P\left(\frac{\vec{r}-\vec{r}_P}{|\vec{r}-\vec{r}_P|^3} + \frac{\vec{r}_P}{|\vec{r}_P|^3}\right)\,, \qquad (1)
\end{aligned}$$

where β is the ratio of the electromagnetic radiation force to the force of gravity

$$\begin{aligned}
\beta &= \frac{F_{ng}}{F_g} = 5.760\times 10^2\,\frac{\overline{Q}\,'_{pr}}{R[\mu\mathrm{m}]\;\rho[\mathrm{kg\ m^{-3}}]}\,, \\
\eta_1 &= 1.1\,, \\
\eta_2 &= 1.4\,, \qquad (2)
\end{aligned}$$

G is the gravitational constant, $M_\odot$ it the mass of the Sun and $\overline{Q}\,'_{pr}$ is the dimensionless efficiency factor of the radiation pressure averaged over the solar spectrum. Equation (1) holds for radial solar wind.

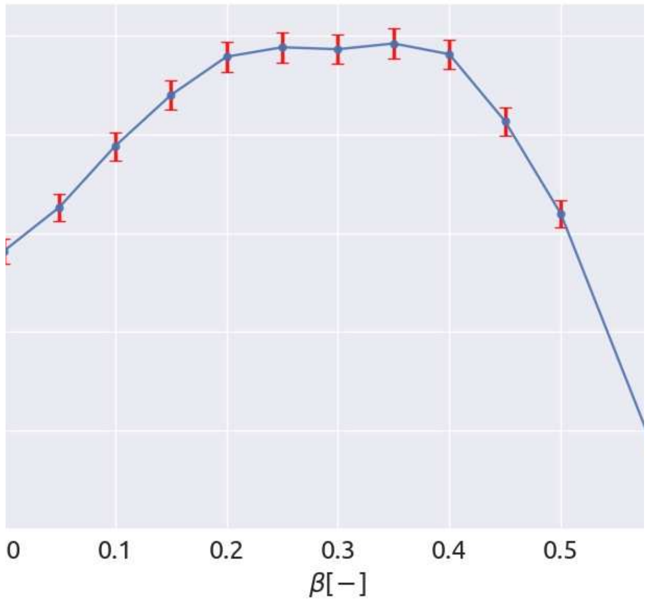

Figure 1 – Number of stable orbits of test particles for various values of β parameter. The total number of test particles was 50 000. All test particles were unstable for $\beta \geq 0.7$

3 Results

We studied the influence of non-gravitational effects on the orbital evolution of dust grains in the Solar System. We found the equilibrium points in the restricted three-body problem. We simulated the motion of 5×10^4 test particles randomly distributed near the equilibrium point L_4 of Jupiter (with maximal distance 1.5 AU) and with various initial tangential velocities (±8km/s in the co-rotating frame).

The number of stable orbits for various values of β parameter are plotted in Figure 1. We conclude that the non-gravitational effects increased the number of stable orbits for $\beta < 0.5$ in comparison with $\beta = 0.0$ (when the influence of the non-gravitational effects is negligible). On the other hand, higher values of the β parameter ($\beta > 0.5$) causes continuous descent of the number of temporary stable orbits. And finally, the number of stable orbits plunged to zero for $\beta \geq 0.7$ and none of the test particles remained in the stable orbit during the integration time.

Acknowledgements

This work was supported by the Scientific Grant Agency VEGA No. 1/0911/17.

Spectral properties of slow meteors: Na-rich spectra as tracers of Apollo-type meteoroids

Pavol Matlovič[1], Juraj Tóth[1], Leonard Kornoš[1]

[1] **Faculty of Mathematics, Physics and Informatics, Comenius University, Bratislava, Slovakia**
matlovic@fmph.uniba.sk

We provide a brief summary of the recent results of the All-sky Meteor Orbit System (AMOS) spectral program. Specifically, the origin of spectral classes enhanced in sodium is discussed with respect to the determined strong speed dependency on Na/Mg ratio.

1 Summary

As of 2018, the spectral program of the AMOS network is based on observations from five spectral systems installed along the standard AMOS cameras at stations in Slovakia (AGO Modra), Canary Islands (Tenerife), Chile (San Pedro de Atacama and Chiu Chiu) and Hawaii (Mauna Kea). The results presented in this work are based on low-resolution spectra observed by the AMOS-Spec system (Matlovič et al., 2017).

Introduced as a useful tool to study meteoroid composition from lower-resolution meteor spectra, the spectral classification of Borovička et al. (2005) defines the spectral types of faint meteors based on varying intensity ratios of Mg I, Na I and Fe I. While most meteors are usually defined by normal type with ratios similar to those found in C-chondritic meteoroids and cometary dust, several distinct classes have been identified suggesting atypical composition. Specifically, Na-depletion in meteors has been linked with space weathering effects, causing the loss of the volatile element. There was also detected enhancement of Na in numerous spectra (Na-enhanced and Na-rich classes), which however has not yet been clearly explained or supported by sufficient orbital and structural data.

It was found that spectral classes enhanced in Na are the dominant type among slow meteors (< 27 km s^{-1}). The only clear deviation from this trend was represented by meteors with spectra rich in Fe emission. In all of these cases, the spectra were strongly affected by occurrence of bright flares causing saturation and optical thickness of the radiating gas. Furthermore, the dependency of detected Na/Mg intensity ratio on meteor speed caused by the difference in excitation energies of the two lines, as already noted by Borovička et al. (2005), needs to be taken into account for correct spectral classification of meteors. Based our data of 200 calibrated spectra of mainly -2 to -7 *mag* meteors, the detected Na enhancement cannot be in any case unambiguously distinguished from the effects of present physical conditions during the atmospheric interaction. The Na-enhanced and Na-rich spectral classes are produced by the preference of the low-excitation Na line at the low achieved temperatures in slow meteors and typically moderate magnitudes of these meteors. The observed spectra therefore do not reflect the composition of these meteoroids, which are in most cases likely of chondritic composition.

Nevertheless, since Na-enhanced and Na-rich meteors form a group of meteors with similar atmospheric behavior, we further focused on determining their orbital source and structural properties. The orbits were determined using the newly developed software *Meteor Trajectory 3.4* (updated from Kornoš et al., 2015). It was found that Na-rich and part of Na-enhanced meteors are produced by stronger stony meteoroids on orbits close to several Apollo-type near-Earth asteroids. The second source contributing to these spectral classes are meteoroids with apparently more fragile structure, originating from short-period comets. As a byproduct of this work, we have discovered significant spectral and structural heterogeneity of Alpha Capricornid meteoroids originating from the inactive comet 169P/NEAT.

Acknowledgements

This work was supported by the Slovak Research and Development Agency under the contract No. APVV-16-0148 and by the Slovak Grant Agency for Science grant VEGA 01/0596/18. Additional support was provided by the Comenius University grant UK/179/2018 and special scholarship of the FMPH, CU in Bratislava.

References

Matlovič P., Tóth J., Rudawska R., Kornoš, L. (2017), "Spectra and physical properties of Taurid meteoroids". *Planetary and Space Science*, **143**, 104–115.

Borovička J., Koten P., Spurný P., Boček J., Štork R. (2005), "A survey of meteor spectra and orbits: evidence for three populations of Na-free meteoroids". *Icarus*, **174**, 15–30.

Kornoš L., Ďuriš F., Tóth J. (2016), "Astrometric precision and orbit determination by AMOS". *Proceedings International Meteor Conference, Mistelbach, Austria, August 2015, Eds. J.-L. Rault, P. Roggemans, IMO, 2016*, 101–104.

BRAMS radio observations analyzed: activity of some major meteor showers

Cis Verbeeck[1], Hervé Lamy[2], Stijn Calders[2], Cédric Tétard[2], Antonio Martínez Picar[1], and Antoine Calegaro[2]

[1] **Royal Observatory of Belgium, Ringlaan 3, 1180 Brussels, Belgium**
cis.verbeeck@oma.be and antonio.martinez@oma.be

[2] **Royal Belgian Institute of Space Aeronomy, Ringlaan 3, 1180 Brussels, Belgium**
herve.lamy@aeronomie.be, stijn.calders@aeronomie.be, cedric.tetard@aeronomie.be and antoine.calegaro@aeronomie.be

We present and discuss activity curves from BRAMS forward scatter observations of the Geminids 2017, the Quadrantids 2018, and the Perseids 2018. The estimated shower component is obtained after subtracting an estimate of the sporadic background. The results are still preliminary, as this study does not include correction for the sensitivity of the setup as a function of the radiant position (the Observability Function).

1 Introduction

BRAMS (Belgian RAdio Meteor Stations) is a radio network located in Belgium using forward scatter measurements to detect and characterize meteoroids. It consists of one dedicated transmitter located in Dourbes in the south of Belgium and approximately 25 receiving stations spread all over the Belgian territory. The transmitter emits a circularly polarized continuous wave (CW) at a frequency of 49.97 MHz and with a power of 150 W. All receiving stations use the same material (including a 3 elements Yagi antenna) and are synchronized using GPS clocks. More details can be found in, e.g., (Lamy et al., 2015).

Each BRAMS receiving station is recording continuously, producing each day 288 WAV files and detecting about 1500–2000 meteors. Though significant advances in automatic detection of meteor reflections in the BRAMS spectrograms has been made, the best detector stays the human eye. In August 2016, the Radio Meteor Zoo[1] was launched. This citizen science project, hosted on the Zooniverse platform (Lintott, 2008), exploits the (trained) human eye of many volunteers for classifying meteor reflections during certain observing campaigns. This enabled the BRAMS team to publish the present shower activity results. More information about the Radio Meteor Zoo can be found in (Calders, 2016) and (Calders, 2017).

In the current paper, we present meteor shower activity profiles from BRAMS observations of the Geminids 2017, the Quadrantids 2018, and the Perseids 2018. All observations pertain to the BRAMS receiving station in Humain. In order to estimate the sporadic background during shower observations, a sine curve is fitted to the average diurnal hourly rates of meteor echoes on a few days well outside the main shower activity. This sine curve is then subtracted from the hourly total number of meteor reflections to yield an estimate of the hourly number of shower meteors. This approach was described in detail in (Verbeeck et al., 2017). The hourly total duration of meteor reflections (i.e., the sum of all durations of the meteor reflections during that hour) is often a more robust measure of meteor activity than the hourly number of reflections. We present both the results for hourly number of reflections and hourly total duration of meteor reflections.

A word of caution is in order. The shower meteor numbers in the present paper have not yet been corrected for the relative sensitivity of the forward scatter setup, which shows a large daily variation as the radiant crosses the sky. This daily variation is clearly seen in the plots presented in this article, meaning it is pointless at this stage to determine at which exact time the shower maximum occurred. Nevertheless a quick comparison with visual and video observations will be provided for completeness. The relative sensitivity of the forward scatter setup is called the Observability Function and was modeled in (Verbeeck, 1997).

Sections 2, 3, and 4 present the BRAMS activity curves near the maximum period of the Perseids 2018, Quadrantids 2018, and Geminids 2017, respectively. Conclusions and future plans are outlined in Section 5.

2 Perseids 2018

The BRAMS station in Humain observed the 2018 Perseids from August 11, 0^{h} UT until August 15, 0^{h} UT. Figure 1 shows an estimate of the Perseids 2018 activity as observed from Humain during this period.

The hourly total number of meteor reflections is shown in the top left plot (red curve). As a proxy for the diurnal variation of the sporadic background, the average hourly number of meteors observed away from the shower maximum is plotted (black circles for the average and black sine curve for its weighted sine fit), as

[1] http://www.radiometeorzoo.org

explained in (Verbeeck et al., 2017). An estimate of the number of Perseid reflections per hour (blue curve) is obtained by subtracting the modeled sporadic background (the black weighted sine fit) from the hourly total number of reflections. The Perseid radiant elevation is featured in the bottom left plot. The plots on the right in Figure 1 show the same curves, but for the total duration of meteor reflections rather than the number of meteor reflections.

It is clear that the number of Perseid reflections is smaller than the large number of underdense sporadic reflections (faint sporadic meteors) observed by Humain (top left plot in Figure 1). Hence, the scatter in the true sporadic rates (the difference between the real and modeled sporadic rates) hides the salient features in the Perseid rates.

In the top right plot in Figure 1 (total duration of meteor reflections), the Perseid contribution is a bit larger than the sporadic component, and there is a hint of peak Perseid activity on August 13. This feature stands out better in Figure 2, which shows the same plots as Figure 1, but only taking into account the larger particles (meteor reflections lasting at least 10 seconds, corresponding to larger particles that are much more abundant in a meteor stream than in the sporadic background).

Rendtel et al. (2019) found a Perseid maximum in the late UT hours of August 12 rather than on August 13. The BRAMS observations are modulated by the (diurnal) Observability Function which is small before 0^{h} UT. Still, the BRAMS estimated Perseid activity is a lot higher in the late UT hours of August 12 than in the late UT hours of August 11, which is in line with the observations in (Rendtel et al., 2019).

3 Quadrantids 2018

The top left plot in Figure 3 shows the hourly number of meteor reflections (total observed, estimated sporadic, and estimated Quadrantids) for the observations by the BRAMS receiving station at Humain, from January 3, 0^{h} UT until January 5, 0^{h} UT, while the top right plot in Figure 3 provides similar information about the hourly total duration of meteor reflections. Figure 4 provides the same information, but only taking into account reflections lasting at least 10 seconds.

Figure 4 clearly shows enhanced Quadrantid activity in the early UT hours of January 4, in line with the video results in (Molau et al., 2018b), though it should be noted that the video observations suffered from poor weather conditions and cover only limited periods during the Quadrantid activity period.

4 Geminids 2017

The top left plot in Figure 5 shows the hourly number of meteor reflections (total observed, estimated sporadic, and estimated Geminids) for the observations by the BRAMS receiving station at Humain, from December 13, 0^{h} UT until December 15, 0^{h} UT, while the top right plot in Figure 5 provides similar information about the hourly total duration of meteor reflections.

While the short observing interval of 48 hours does not allow to clearly identify the shower maximum from these plots, the corresponding plots in Figure 6 (only taking into account reflections lasting at least 10 seconds), clearly show an increased activity in the late UT hours of December 13 and the early UT hours of December 14, in line with the video observations reported by (Molau et al., 2018a).

It should be pointed out that the sine fits for the sporadic background of reflections lasting at least 10 seconds (both for number of reflections and total duration) in Figure 6 is rather poor, with a maximum close to local midnight. However, due to the small amplitude of this sporadic background with respect to the shower component of reflections lasting at least 10 seconds, this does not influence the shower activity interpretations above.

5 Conclusions and future outlook

Employing the Radio Meteor Zoo detections of radio meteor echoes from forward scatter observations at the BRAMS receiving station at Humain, we have estimated the sporadic background and subtracted it from the total radio meteor activity to obtain an estimate of the shower activity for the Perseids 2018, Quadrantids 2018, and Geminids 2017.

It should be stressed that the current results are just the first step in the envisaged procedure to obtain a realistic estimate of shower activity, since the shower activity estimates in the present paper have not yet been corrected for the diurnal sensitivity of the forward scatter setup as the radiant crosses the sky, which modulates the observed rates in a major way. This effect is modeled by the Observability Function (Verbeeck, 1997). The authors will incorporate the Observability Function into the analysis of shower data in a future paper. It is expected that this will enable us to determine the exact time of occurrence of shower maxima.

The current method used by the Radio Meteor Zoo to aggregate the detections of a meteor echo by several citizen scientists into one box in the spectrogram can in some cases produce an artificially large rectangle. We aim to improve this aggregation method and exploit the skill scores of the citizen scientists to further increase the accuracy of the meteor detections.

Acknowledgements

The BRAMS network is a project from the Royal Belgian Institute for Space Aeronomy and funded by the

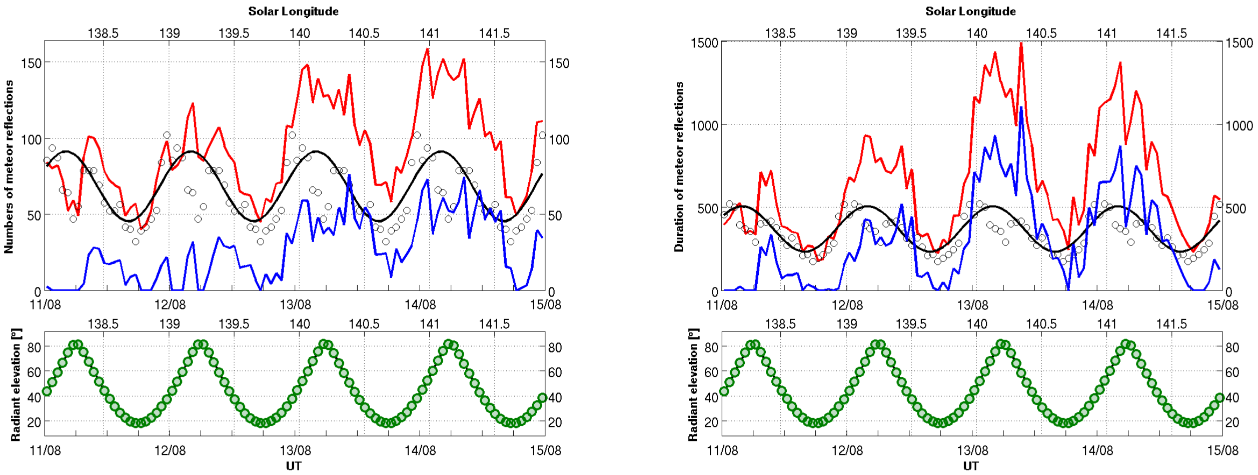

Figure 1 – Estimate of Perseids 2018 activity (BRAMS receiving station: Humain). *Top left:* Hourly number of meteor reflections (upper red curve: total observed; black circles and curve: estimation of diurnal variation of sporadic background and its weighted sine fit; lower blue curve: estimated hourly number of Perseid reflections). *Bottom left:* Radiant elevation. *Top right:* Hourly total duration (s) of meteor reflections (upper red curve: total observed; black circles and curve: estimation of diurnal variation of sporadic background and its weighted sine fit; lower blue curve: estimated hourly total duration of Perseid reflections). *Bottom right:* Radiant elevation. Times are in UT and durations in seconds.

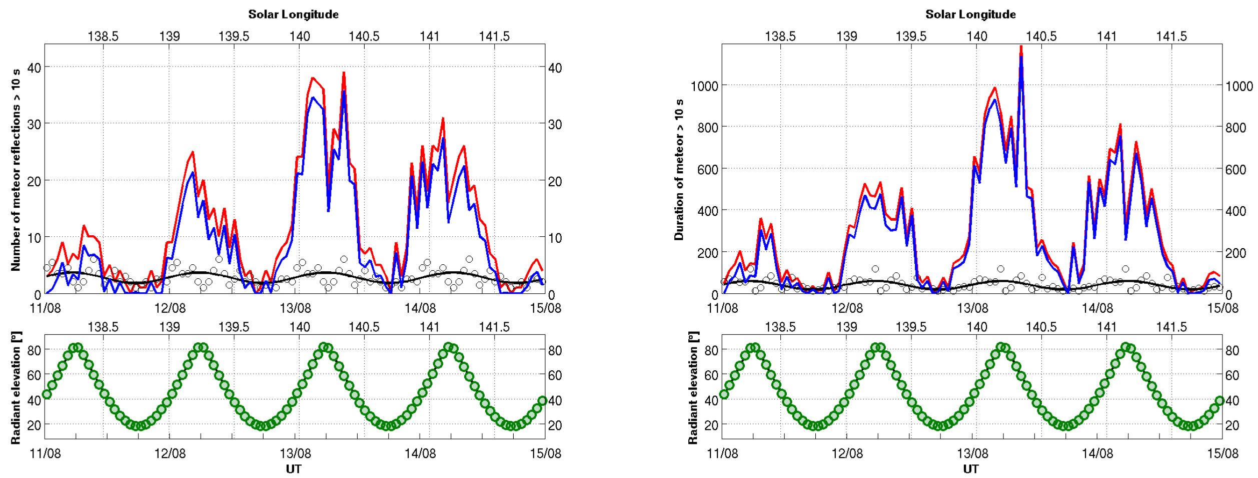

Figure 2 – Estimate of Perseids 2018 activity (BRAMS receiving station: Humain). *Top left:* Hourly number of meteor reflections lasting at least 10 seconds (upper red curve: total observed; black circles and curve: estimation of diurnal variation of sporadic background and its weighted sine fit; lower blue curve: estimated hourly number of Perseid reflections). *Bottom left:* Radiant elevation. *Top right:* Hourly total duration (s) of meteor reflections lasting at least 10 seconds (upper red curve: total observed; black circles and curve: estimation of diurnal variation of sporadic background and its weighted sine fit; lower blue curve: estimated hourly total duration of Perseid reflections). *Bottom right:* Radiant elevation. Times are in UT and durations in seconds.

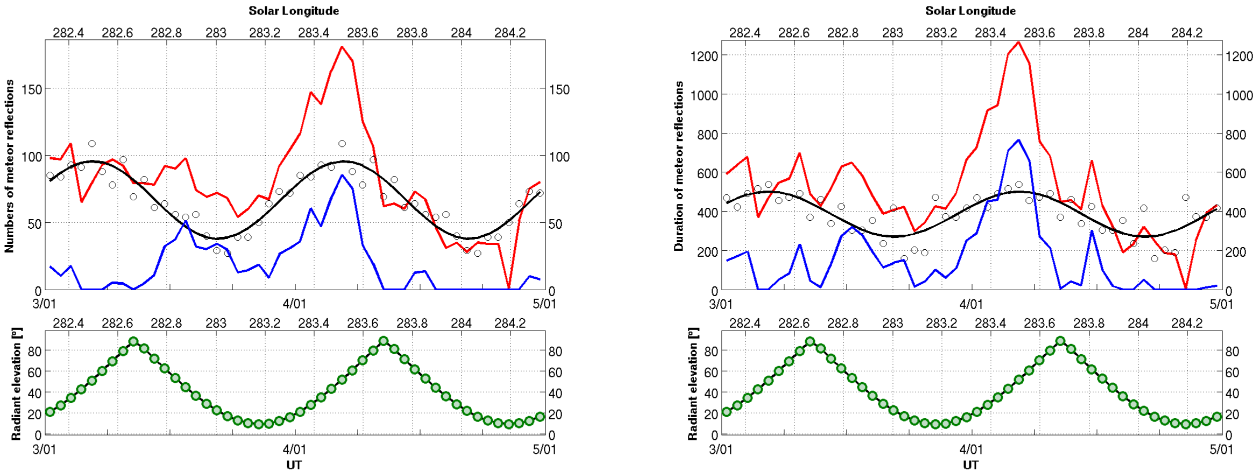

Figure 3 – Estimate of Quadrantids 2018 activity (BRAMS receiving station: Humain). *Top left:* Hourly number of meteor reflections (upper red curve: total observed; black circles and curve: estimation of diurnal variation of sporadic background and its weighted sine fit; lower blue curve: estimated hourly number of Quadrantid reflections). *Bottom left:* Radiant elevation. *Top right:* Hourly total duration (s) of meteor reflections (upper red curve: total observed; black circles and curve: estimation of diurnal variation of sporadic background and its weighted sine fit; lower blue curve: estimated hourly total duration of Quadrantid reflections). *Bottom right:* Radiant elevation. Times are in UT and durations in seconds.

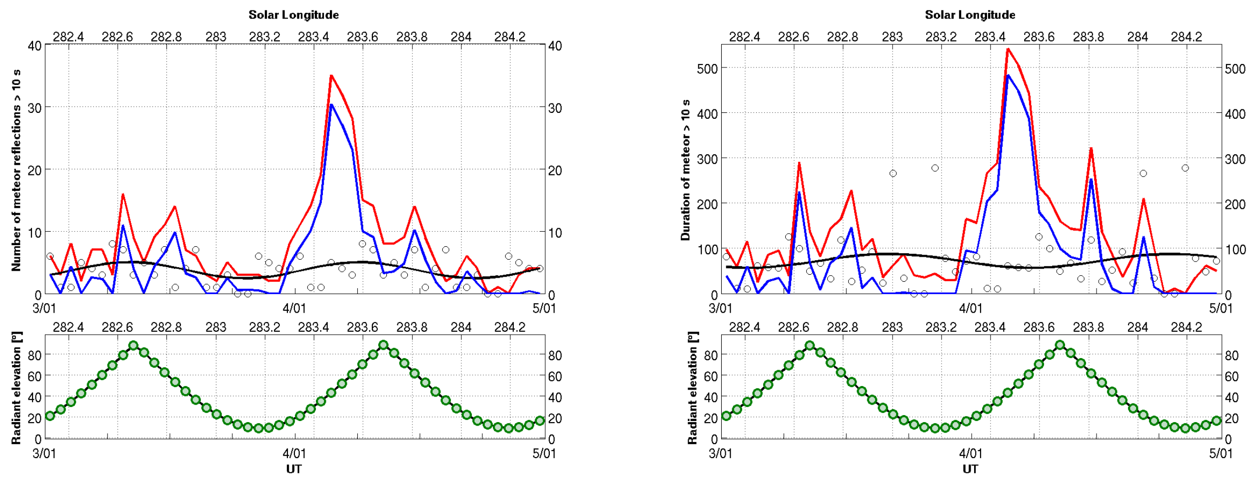

Figure 4 – Estimate of Quadrantids 2018 activity (BRAMS receiving station: Humain). *Top left:* Hourly number of meteor reflections lasting at least 10 seconds (upper red curve: total observed; black circles and curve: estimation of diurnal variation of sporadic background and its weighted sine fit; lower blue curve: estimated hourly number of Quadrantid reflections). *Bottom left:* Radiant elevation. *Top right:* Hourly total duration (s) of meteor reflections lasting at least 10 seconds (upper red curve: total observed; black circles and curve: estimation of diurnal variation of sporadic background and its weighted sine fit; lower blue curve: estimated hourly total duration of Quadrantid reflections). *Bottom right:* Radiant elevation. Times are in UT and durations in seconds.

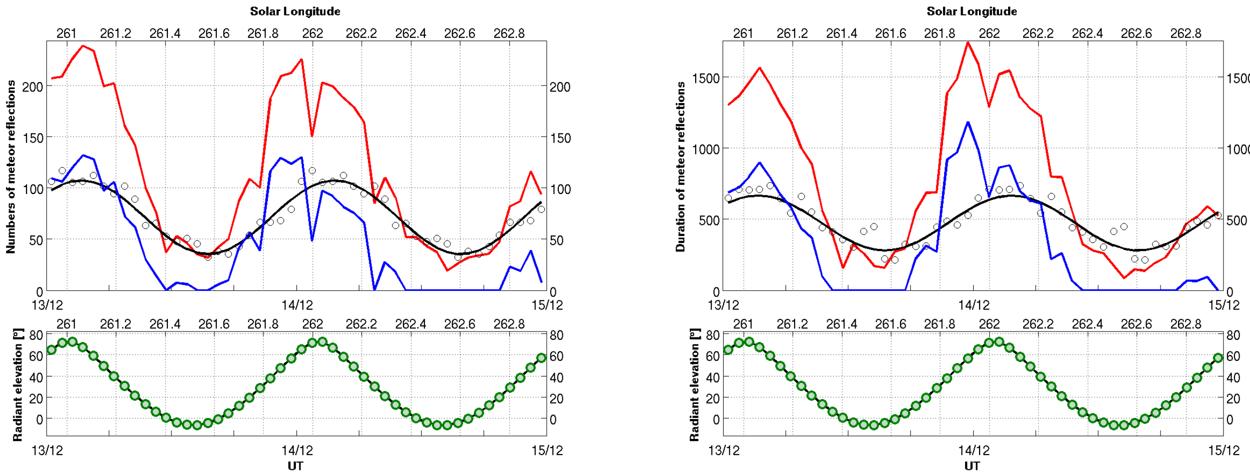

Figure 5 – Estimate of Geminids 2017 activity (BRAMS receiving station: Humain). *Top left:* Hourly number of meteor reflections (upper red curve: total observed; black circles and curve: estimation of diurnal variation of sporadic background and its weighted sine fit; lower blue curve: estimated hourly number of Geminid reflections). *Bottom left:* Radiant elevation. *Top right:* Hourly total duration (s) of meteor reflections (upper red curve: total observed; black circles and curve: estimation of diurnal variation of sporadic background and its weighted sine fit; lower blue curve: estimated hourly total duration of Geminid reflections). *Bottom right:* Radiant elevation. Times are in UT and durations in seconds.

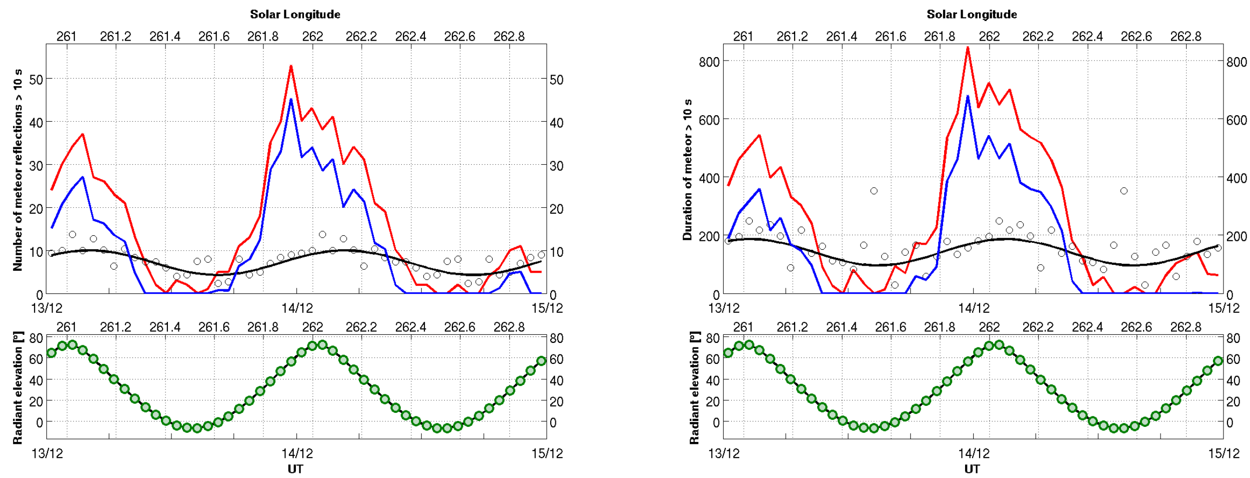

Figure 6 – Estimate of Geminids 2017 activity (BRAMS receiving station: Humain). *Top left:* Hourly number of meteor reflections lasting at least 10 seconds (upper red curve: total observed; black circles and curve: estimation of diurnal variation of sporadic background and its weighted sine fit; lower blue curve: estimated hourly number of Geminid reflections). *Bottom left:* Radiant elevation. *Top right:* Hourly total duration (s) of meteor reflections lasting at least 10 seconds (upper red curve: total observed; black circles and curve: estimation of diurnal variation of sporadic background and its weighted sine fit; lower blue curve: estimated hourly total duration of Geminid reflections). *Bottom right:* Radiant elevation. Times are in UT and durations in seconds.

Solar-Terrestrial Center of Excellence (STCE). The authors thank all volunteers who helped us with the classification of the spectrograms. These volunteers make the success of the Radio Meteor Zoo. We also thank the Zooniverse team, who are hosting the Radio Meteor Zoo and who are always very enthusiastic in supporting us. Last but not least: no observations without volunteers hosting the BRAMS receiving stations. The authors are grateful for their constant support.

References

Calders S., Verbeeck C., Lamy H., and Martínez Picar A. (2016). "The Radio Meteor Zoo: a citizen science project". In Roggemans A. and Roggemans P., editors, *Proceedings of the International Meteor Conference,* Egmond, The Netherlands, 2–5 June 2016. IMO, 46–49.

Calders S., Lamy H., Martínez Picar A., Tétard C., Verbeeck C., and Gamby E. (2017). "The Radio Meteor Zoo: involving citizen scientists in radio meteor research". In Gyssens M., Pavlović D., and Rault J.-L., editors, *Proceedings of the International Meteor Conference,* Petnica, Serbia, 21–24 September 2017. IMO, 13–15.

Lamy H., Anciaux M., Ranvier S., Calders S., Gamby E., Martínez Picar A., and Verbeeck C. (2015). "Recent advances in the BRAMS network". In Rault J.-L. and Roggemans P., editors, *Proceedings of the International Meteor Conference,* Mistelbach, Austria, 27–30 August 2015. IMO, 171–175.

Lintott C. J., Schawinski K., Slosar A., Land K., Bamford S., Thomas D., Raddick M. J., Nichol R. C., Szalay A., Andreescu D., Murray P., and Vandenberg J. (2008). "Galaxy Zoo: Morphologies derived from visual inspection of galaxies from the Sloan Digital Sky Survey". *Monthly Notices of the Royal Astronomical Society*, **389**, 1179–1189.

Molau S., Crivello S., Goncalves R., Saraiva C., Stomeo E., Strunk J., and Kac J. (2018). "Results of the IMO Video Meteor Network — December 2017". *WGN, Journal of the IMO*, **46:5**, 166–172.

Molau S., Crivello S., Goncalves R., Saraiva C., Stomeo E., Strunk J., and Kac J. (2018). "Results of the IMO Video Meteor Network — January 2018". *WGN, Journal of the IMO*, **46:6**, 205–209.

Rendtel J., Veljković K., Weiland T., Verbeeck C., and Knöfel A. (2019). "Perseids 2018 — Analysis of Global Visual Data". *WGN, Journal of the IMO*, **47:X**, XX–XX.

Verbeeck C. (1997). "Calculating the sensitivity of a forward scatter setup for underdense shower meteors". In Knöfel A. and Roggemans P., editors, *Proceedings of the International Meteor Conference,* Apeldoorn, The Netherlands, 19-22 September 1997. IMO, 122–132.

Verbeeck C., Lamy H., Calders S., Tétard C., and Martínez Picar A. (2017). "Overview of major shower observations 2016–2017 by the BRAMS network". In Gyssens M., Pavlović D., and Rault J.-L., editors, *Proceedings of the International Meteor Conference,* Petnica, Serbia, 21–24 September 2017. IMO, 138–144.

EARS Geminids 2017 radio observation

G. T. Tomezzoli[1]

[1] EurAstro Association, Zeppelinstrasse 43, D–81669, Munich, Germany
gt21949@gmx.de

The previous forward–scattering radio observations of the daytime meteor showers 2016 by EARS (EurAstro Radio Station) manifested the necessity of improving the quality of the observations by taking into account various parameters like the sporadic background, the radiant elevation and the observability function which influence the observed underdense and overdense meteor rates. This article shows the EARS observation improvements and the difficult encountered in determining the observability function in the case of the EARS Geminids 2017 radio observation.

1 Introduction

The past EARS (EurAstro Radio Station) meteor radio observations provided matter for several publications.

A first article by Tomezzoli & Verbeeck (2015) described the EARS configuration and the radio observation of the Daytime Sextantids (221 DSX) made in Munich (DE) (48° 07' 51.07" N (48.130852° N), 11° 34' 47.36" E (11.579823 E)) in the recording period 30/09/2014, 07:00 UT - 05/10/2014, 16:00 UT. The conclusion was that the Sextantides radio meteor activity, if present at all, was at a level much lower than that of the sporadic radio meteor activity.

A second article by Tomezzoli & Barbieri (2016) described the combined observations of the daytime Sextantides made by EARS and the Radio Astronomy and Meteor Bologna (RAMBO) in Bologna (IT) (44° 30' 28.9" N, 11° 21' 12.0" E) in the recording periods, respectively, of 27/09/2015, 08:15 UT - 03/10/2015, 07:30 UT and 28/09/2015, 00:00 UT - 04/10/2015, 00:00 UT. The conclusion was that the EARS and RAMBO radio observations were in agreement, confirming that also in 2015 the daytime Sextantides showed no relevant radio meteor activity.

A third article by Tomezzoli (2018) described the EARS radio observations of the 2016 daytime meteor showers listed in the IMO Meteor Shower Calendar 2016 by Rendtel (2015). The conclusion was that the EARS measured rates of said meteor showers manifested a certain agreement with the expected rates listed in said IMO Calendar. The article was presented by Verbeeck at the IMC 2017 in Petnica (Serbia) and his valuable comments and observations concerning the EARS radio observations were inserted in the article.

The Verbeeck's (1997) general recommendation to avoid presentations of raw meteor rates and other data directly derived from the radio observations but rather to present observations taking into account time-dependent parameters that dramatically influence the sensitivity of the radio stations motivated the EARS radio observation of the Geminids 2017 and offered the possibility to test the application of said parameters.

2 Geminids 2017 – raw meteor rates

EARS, based on the forward–scattering principle, adopted the following configuration: emitter – radar GRAVES (Broyes-les-Pesmaes, 47° 20' 51.72" N, 05° 30' 58.68" E), distant about 500 km from EARS, 2m/70cm Diamond Duoband-Groundplane vertical antenna located about 45m high with respect to the ground, receiver ICOM 1500 (USB mode, 143.049 MHz), computer Pavillion dv6 (processor Intel Core Duo T2500) and SpecLab V26 b10 as recording software.

Underdense and overdense raw meteor rates were derived by visually counting the radio echoes on the JPG images recorded every 5 minutes by SpecLab.

The EARS radio observation took place in the recording period 10/12/2017 14:40 UT - 15/12/2017 06:10 UT. It run smoothly, except for an interruption on 13/12/2017 20:10 UT - 14/12/2017 08:25 UT and another interruption on 14/12/2017 10:30 UT - 11:00 UT both caused by storms over Munich which affected the connection between receiver and antenna. Figure 1(1)-(6) shows the recorded raw meteor rates.

The Geminids raw meteor rates (Figure 1(1)-(6)) showed:

1. a raw underdense max. (Figure 1(3)-(4)) within 12/12/2017 20:00 UT - 13/12/2017 05:00 UT with up to 119 underdense/hour,
2. a first raw overdense max (Figure 1(5)) within 14/12/2017 18:00 UT - 14/12/2017 21:00 UT with up to 12 underdense/hour,
3. a second raw overdense max. (Figure 1(5)-(6)) within 14/12/2017 23:00 UT - 15/12/2017 04:00 UT with up to 22 underdense/hour.

3 Geminids 2017 - net meteor rates

The observed underdense and overdense meteor rates on 11/12/2017, preceding said Geminids raw max. rates, were assumed as the sporadic underdense and overdense rates (Tables 1-2) to be subtracted from the observed raw underdense and overdense rates in the recording period for obtaining the Geminids net underdense and overdense rates (Tables 3-6).

Table 1 – Sporadic underdense rates - 11/12/2017

0	1	2	3	4	5	6	7	8	9	10	11	UT
64	62	46	46	44	48	54	54	43	30	25	26	rates
12	13	14	15	16	17	18	19	20	21	22	23	UT
27	24	21	21	23	22	22	35	53	49	74	81	rates

Table 2 – Sporadic overdense rates - 11/12/2017

0	1	2	3	4	5	6	7	8	9	10	11	UT
6	2	1	2	7	7	3	6	4	3	2	0	rates
12	13	14	15	16	17	18	19	20	21	22	23	UT
3	0	1	0	1	1	1	4	2	3	7	2	rates

Table 3 – Geminids 2017 net underdense rates - 12/12/2017

0	1	2	3	4	5	6	7	8	9	10	11	UT
11	0	5	11	15	5	20	2	0	0	0	4	rates
12	13	14	15	16	17	18	19	20	21	22	23	UT
0	3	0	4	0	5	8	12	16	31	15	38	rates

Table 4 – Geminids 2017 net underdense rates - 13/12/2017

0	1	2	3	4	5	6	7	8	9	10	11	UT
64	10	13	25	44	33	22	15	11	5	8	0	rates
12	13	14	15	16	17	18	19	20	21	22	23	UT
0	2	1	0	0	0	29	28	0	0	0	0	rates

Table 5 – Geminids 2017 net overdense rates - 14/12/2017

0	1	2	3	4	5	6	7	8	9	10	11	UT
0	0	0	0	0	0	0	0	0	0	0	3	rates
12	13	14	15	16	17	18	19	20	21	22	23	UT
0	4	0	0	0	0	5	8	8	3	0	20	rates

Table 6 – Geminids 2017 net overdense rates - 15/12/2017

0	1	2	3	4	5	6	7	8	9	10	11	UT
14	6	8	6	1	0	0	0	0	0	0	0	rates
12	13	14	15	16	17	18	19	20	21	22	23	UT
0	0	0	0	0	0	0	0	0	0	0	0	rates

Table 7 – Geminids 2017 net underdense rates - estimated count errors - 12/12/2017

0	1	2	3	4	5	6	7	8	9	10	11	UT
11	0	5	11	15	5	20	2	0	0	0	4	rates
.3		.4	.3	.3	.4	.2	.7				.5	err.
12	13	14	15	16	17	18	19	20	21	22	23	UT
0	3	0	4	0	5	8	12	16	31	15	38	rates
	.6		.5		.4	.4	.3	.3	.2	.3	.2	err.

Table 8 – Geminids 2017 net underdense rates - estimated count errors - 13/12/2017

0	1	2	3	4	5	6	7	8	9	10	11	UT
64	10	13	25	44	33	22	15	11	5	8	0	rates
.1	.3	.3	.2	.2	.2	.2	.3	.3	.4	.4		err.
12	13	14	15	16	17	18	19	20	21	22	23	UT
0	2	1	0	0	0	29	28	0	0	0	0	rates
	.7	1				.2	.2					err.

Table 9 – Geminids 2017 net overdense rates - estimated count errors - 14/12/2017

0	1	2	3	4	5	6	7	8	9	10	11	UT
0	0	0	0	0	0	0	0	0	0	0	3	rates
											.6	err.
12	13	14	15	16	17	18	19	20	21	22	23	UT
0	4	0	0	0	0	5	8	8	3	0	20	rates
	.5					.4	.4	.4	.6		.2	err.

Table 10 – Geminids 2017 net overdense rates - estimated count errors - 15/12/2017

0	1	2	3	4	5	6	7	8	9	10	11	UT
14	6	8	6	1	0	0	0	0	0	0	0	err.
.3	.4	.4	.4	1								err.
12	13	14	15	16	17	18	19	20	21	22	23	UT
0	0	0	0	0	0	0	0	0	0	0	0	rates
												err.

Table 11 – Geminids 2017 net. underdense rates - radiant elevation - 12/12/2017

0	1	2	3	4	5	6	7	8	9	10	11	UT
11	0	5	11	15	5	20	2	0	0	0	4	rates
68	73	72	64	55	45	35	26	17	8	1	-4	Alt.
131	167	211	239	257	270	280	290	300	310	320	331	Az.
12	13	14	15	16	17	18	19	20	21	22	23	UT
0	3	0	4	0	5	8	12	16	31	15	38	rates
-8	-10	-9	-6	-2	5	12	21	31	40	50	60	Alt.
344	357	10	22	34	45	55	65	75	84	96	110	Az.

Table 12 – Geminids 2017 net underdense rates - radiant elevation - 13/12/2017

0	1	2	3	4	5	6	7	8	9	10	11	UT
64	10	13	25	44	33	22	15	11	5	8	0	rates
69	73	72	64	55	45	35	25	16	8	1	-5	Alt.
132	169	213	241	258	251	281	291	300	310	321	333	Az.
12	13	14	15	16	17	18	19	20	21	22	23	UT
0	2	1	0	0	0	29	28	0	0	0	0	rates
-8	-9	-9	-6	-1	5	13	22	31	41	51	52	Alt.
344	358	10	23	35	46	56	66	75	85	97	97	Az.

Table 13 – Geminids 2017 net overdense rates - radiant elevation - 14/12/2017

0	1	2	3	4	5	6	7	8	9	10	11	UT
0	0	0	0	0	0	0	0	0	0	0	3	rates
69	74	71	63	54	44	34	24	15	7.5	0.5	-5	Alt.
134	172	214	242	259	271	281	291	300	310	321	333	Az.
12	13	14	15	16	17	18	19	20	21	22	23	UT
0	4	0	0	0	0	5	8	8	3	0	20	rates
-8	-9	-9	-6	-1	5	13	22	32	41	52	61	Alt.
345	358	11	24	35	46	57	66	76	85	97	112	Az.

Table 14 – Geminids 2017 net overdense rates - radiant elevation - 15/12/2017

0	1	2	3	4	5	6	7	8	9	10	11	UT
14	6	8	6	1	0	0	0	0	0	0	0	err.
70	74	70	63	54	44	33	24	15	7	0	-5	Alt.
136	175	218	244	259	272	282	292	301	311	322	334	Az.
12	13	14	15	16	17	18	19	20	21	22	23	UT
0	0	0	0	0	0	0	0	0	0	0	0	rates
-9	-9	-9	-6	1	6	14	23	32	45	52	62	Alt.
346	359	12	24	36	47	57	66	76	87	98	114	Az.

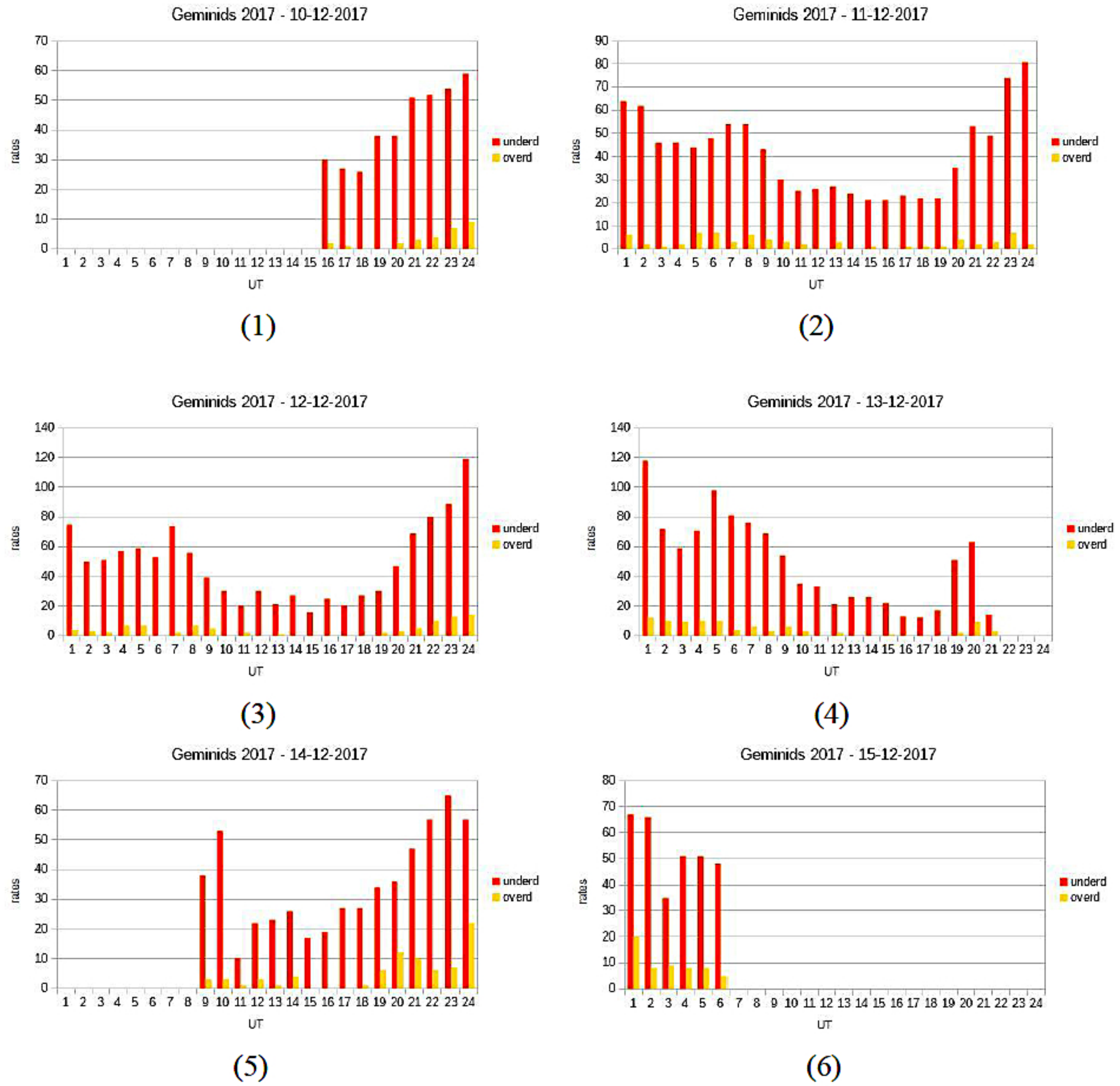

Figure 1 – Geminids 2017 - (1) - (6) EARS recorded raw meteor rates. Here ”overd” and ”underd” stands for overdense and underdense, respectively.

The net meteor rates (Tables 3-6) showed max rates corresponding to the above mentioned raw meteor max. rates:

1. a net underdense max. (Tables 3-4, marked in red) within 12/12/2017 20:00 UT - 13/12/2017 05:00 UT with up to 64 underdense/hour,
2. a net first overdense max (Table 5, marked in yellow) within 14/12/2017 18:00 UT - 14/12/2017 21:00 UT with up to 8 underdense/hour,
3. a net second overdense max. (Tables 5-6, marked in yellow) within 14/12/2017 23:00 UT - 15/12/2017 04:00 UT with up to 20 underdense/hour.

4 Geminids 2017 - error counts

The underdense and overdense rates error counts were estimated as $1/\sqrt{n}$ where n = rate (Tables 7-11).

The error counts (Tables 7-10, marked in light blue) were negligible. Therefore, no correction was applied to the net Geminids net underdense and overdense rates.

5 Geminids 2017 - radiant elevations

The Geminids radiant elevations during the days 14-15/12/2018 was estimated by means of the Javascript calculator Convertalot (Schmitt, 2004). The assumed radiant coordinates were: AR $07^{\mathrm{h}}\ 28^{\mathrm{m}}$, decl. 32°.

The radiant elevation (Tables 11-14, marked in green) was:

1. at the max height of 69°-73° for net underdense max. (Tables 11-12, marked in red),
2. at a height of 22°- 41° for the net first overdense max. (Table 13, marked in yellow),
3. at the height of 61°-70° for the second net overdense max. (Tables 13-14, marked in yellow).

6 Geminids 2017 - observability function

To determine the observability function for radar Graves - EARS system), several publications were considered.

An observability factor F_0 for forward-scattering of underdense trails was proposed by Hines (1955) on the basis of the Fresnel diffraction theory by using prolate spheroids approximated by circular cylinders having the transmitter - receiver line as common axis. The factor calculation assumed emitter - receiver distances in the range 2300 - 1000 km, horizontal polarized component of the electric vector for the transmitting and receiving antennae, five elements Yagis transmitting and receiving antennae of which only the main lobes were considered.

A spatial distribution of observable meteor trails was calculated by Hines & Pugh (1956) on the basis of received signals above a counting level for forward-scattering underdense trails. The distribution calculation considered the possible orientation of the meteor trails, the received signal peak amplitude and the meteor trail position.

An observability function for forward-scattering of five-element horizontal Yagis was proposed by Hines (1958). The function calculation removed the circular cylinder approximation (Hines, 1955) and adopted the full ellipsoidal geometry.

A first FORWARD program for calculating the observability function, having general application and taking into account the meteor radiant coordinates, the azimuth of the transmitter and receiver and antenna parameters, was proposed by Steyaert (1987a) followed by a second FORWARD program again by Steyaert (1987b) for a plurality of observing stations.

An observability function for underdense meteor rates was proposed by Verbeeck (1997) based on the ellipsoidal theory of Hines (1958) taking into account the power of the transmitter and the gain of the transmitting and the receiving antennae, proportional to the number of underdense detected and assuming constant meteor rates.

An observability function was calculated by Zigo (2008) for forward-scattering of Bologna (emitter) - Modra (receiver) system using the ellipsoidal theory of Hines (1958) and was used by Zigo et al. (2009) for correcting the Geminids observation in the period 1996-2007. The system used two identical 4 elements Yagis mounted horizontally, separated by 612 km and a frequency of 42.7 MHz with peak power of 1 Kw. The value of the observability function ranged from 0 when the radiant was below the horizon up to 1 under the optimal conditions for detection of the Geminids showers.

However, all these examples of observability functions are not applicable to radar Graves - EARS system. In fact, radar Graves and EARS have different antennae, both the Graves and EARS antenna diagrams are not well known and the antennae separation (500 km) is lower than those considered in said publications. The first FORWARD program (`metel123.exe`) runs on the EARS computer, however, it is not applicable because radar Graves - EARS system does not use Yagis antennae. Moreover, an anonymous publication (Anonymous, 2019) suggested not to use the observability function when the corrections suggested by FORWARD are too large and that the observability function given by FORWARD is based on many approximations, and thus not totally reliable. Consequently, unfortunately, it was not possible to calculate an observability function for radar Graves - EARS system for correcting the Geminids 2017 net underdense and overdense rates observed.

7 Geminids 2017 - Overdense Mass Index

The sporadic overdense to from subtracted to the Geminids 2017 overdense for calculating the mass index were those of 11/12/2017. The criteria used for subtracting the sporadic overdense from the Geminids 2017 overdense was the following:

- - Geminids overdense having time duration matching the time duration of sporadic overdense were discarded,
- Geminids overdense having time duration not matching the time duration of sporadic overdense were retained,
- sporadic overdense having time duration not matching the time duration of Geminids overdense were discarded.

This criteria caused differences between the Geminids 2017 net overdense rates and the Geminids 2017 rates for mass index calculation.

The Geminids overdense mass index were:

1. 1-s = 1.314 in the period 14/12/2017 18:00 UT - 14/12/2017 21:00 UT corresponding to the net first overdense max.,
2. 1-s = 3.359 in the period 14/12/2017 23:00 UT - 15/12/2017 04:00 UT corresponding to the net second overdense max.

These values are not in agreement with the value of 1.68 ± 0.04 obtained for the Geminids 2015 by Blaauw (2017) using radar, optical and lunar impact data. This may be principally due to the too small number of overdense Geminids detected by EARS.

8 Conclusion

The EARS adopted configuration, revealed itself reliable in providing Geminids 2017 raw meteor rates in the recording period around the expected max. This, in line with the above mentioned comments and general recommendation, allowed a substantial improvement in the quality of the data reduction, although, unfortunately, the observability function for radar Graves - EARS system, up to now, remained to be determined.

Acknowledgement

I am very grateful to C. Verbeeck, IMO President, for his valuable comments and suggestions which motivated me to improve the quality of the EARS radio observation.

References

Anonymous (2019). "Statistical reduction of radio meteor observations". `https://www.imo.net/observations/methods/radio-observation/reduction/`.

Blaauw R. (2017). "The mass index and mass of the Geminid meteoroid stream as determined with radar, optical and lunar impact data". *Planetary and Space Science*, **143**, 83–88.

Hines C. (1955). "Diurnal variations in the number of shower meteors detected by the forward-scattering of radio waves part i: Theory". *Canadian Journal of Physics*, **33**, 493–503.

Hines C. (1958). "Diurnal variations in the number of shower meteors detected by the forward-scattering of radio waves part iii: Ellipsoidal theory". *Canadian Journal of Physics*, **36**, 117–126.

Hines C. and Pugh R. (1956). "The spatial distribution of signal sources in meteoric forward-scattering". *Canadian Journal of Physics*, **34:10**, 1005–1015.

Rendtel J. (2015). "Daytime meteor showers". In *2016 Meteor Shower Calendar, IMO INFO*. pages 2–15.

Schmitt S. R. (2004). `http://www.convertalot.com/celestial_horizon_co-ordinates_calculator.html`.

Steyaert C. (1987a). "FORWARD: a general program for calculating the observability function". *WGN, Journal of the International Meteor Organization*, **15**, 90–93.

Steyaert C. (1987b). "FORWARD: extension for multiple stations". *WGN, Journal of the International Meteor Organization*, **15**, 193–195.

Tomezzoli G. (2018). "Radio Observation of the 2016 dense Geminids detected by EARS. Daytime Meteor Showers". In Gyssens M. and Rault J.-L., editors, *International Meteor Conference, Petnica, Serbia, 22-24 Sep 2017*. pages 291–293.

Tomezzoli G. and Barbieri L. (2016). "No sign of the 2015 Daytime Sextantids through combined radio observations". In Roggemans A. and Roggemans P., editors, *International Meteor Conference Egmond, the Netherlands, 2-5 June 2016*. pages 291–293.

Tomezzoli G. and Verbeeck C. (2015). "No sign of the 2014 Daytime Sextantids and mass indexes determination from radio observations". In Rault J.-L. and Roggemans P., editors, *International Meteor Conference Mistelbach, Austria*. pages 165–170.

Verbeeck C. (1997). "Calculating the sensitivity of a forward scatter setup for underdense shower meteors". In Knöfel A. and Roggemans P., editors, *Proceedings of the International Meteor Conference, Apeldoorn, The Netherlands, 19-22 Sep 1996*. pages 122–132.

Zigo P. (2008). "Observability function of the Bologna-Modra forward scatter system". *Contributions of the Astronomical Observatory Skalnate Pleso*, **38**, 61–69.

Zigo P., Porubčan V., Cevolani G., and Pupillo G. (2009). "Observability function of the Bologna-Modra forward scatter system". *Contributions of the Astronomical Observatory Skalnate Pleso*, **39**, 5–17.

Modelling the Geminid meteor shower activity

Galina O. Ryabova[1]

[1] Research Institute of Applied Mathematics and Mechanics of Tomsk State University, Tomsk, Russian Federation

galina.ryabova@mail.tsu.ru

The Geminid meteor shower is an annual major shower with its maximum activity on December 14. In 2017, asteroid (3200) Phaethon, the recognized parent body of the stream, had a close encounter with the Earth on December 16. When the Earth passes closer to a parent body orbit of a meteoroid stream, an increased activity of the shower is expected. It is hardly the case for the Geminids, because the Geminid stream most probably had no replenishment after the initial catastrophic generation. A model was elaborated to see how the shower activity behaves.

1 Introduction

At European Planetary Science Congress 2017 (EPSC 2017, Riga, Latvia, 17 – 22 September 2017), my colleagues and I were eagerly discussing the soon-coming close encounter of (3200) Phaethon with the Earth. I happened to mention that some increase in activity is expected. Please, note: some increase, not an outburst.

When a live comet approaches the Earth, it is reasonable to expect that meteoroids recently ejected from the comet had insufficient time to spread around the orbit. They are located somewhere near the nucleus and so can produce outburst meteor activity on the Earth. However, the asteroid (3200) Phaethon had never shown any trace of cometary activity since its discovery in 1983.

So I concentrated, did more modelling and invited Jürgen Rendtel to revisit his previous analysis of the visual observations (Rendtel, 2004). The result of our research was published in MNRAS Letters (Ryabova and Rendtel, 2018). I invite the reader, who happens to be interested, to read this publication. My talk at the IMC 2018 follows it completely.

2 Why activity increases

The main factor of the activity increase is the current gradual approach of the Geminids' mean orbit (i.e. the most dense part of the stream) to the Earth (see Ryabova and Rendtel, 2018, Figure 2.) Gravitational perturbations shift the orbits of the Geminid meteoroids and the asteroid in such a way that Phaethon's node should intersect the Earth's orbit in about 2200, and the Geminid stream core some time later. After that the Geminid shower activity should decrease.

3 Concluding remarks

Time has shown that we were right in not expecting any outburst meteor activity in 2017 (Figure 1). It was even a bit lower than in 2016.

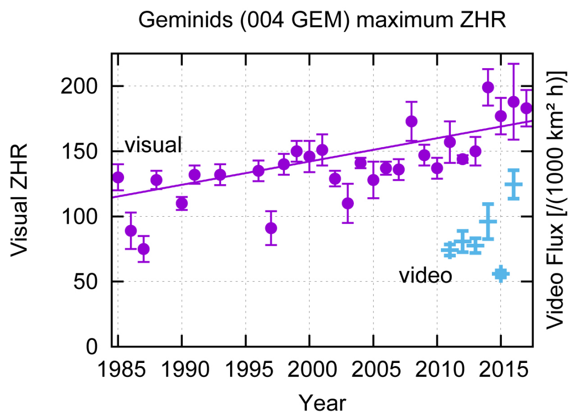

Figure 1 – Activity level of the Geminids in 1985-2017. The figure was modified after the publication (Ryabova and Rendtel, 2018, Figure 3) and reported at the EPSC 2018 (Berlin, Germany, 16–21 September 2018).[1]

Acknowledgement

R.G.O. thanks the IAU for the grant to participate in the XXXth General Assembly of the International Astronomical Union (Vienna, Austria). This grant covered in part my travel expenses, which allowed me to participate also in IMC 2018.

References

Rendtel J. (2004), "Evolution of the Geminids observed over 60 years". *Earth Moon and Planets*, **95**, 27–32. doi = 10.1007/s11038-004-6958-5.

Ryabova G.O., Rendtel J. (2018), "Increasing Geminid meteor shower activity". *Monthly Notices of the Royal Astronomical Society: Letters*, **475**, L77–L80

[1]https://meetingorganizer.copernicus.org/EPSC2018/EPSC2018-397.pdf

Geminid activity over a century

Jürgen Rendtel[1]

[1] **Leibniz-Institut für Astrophysik Potsdam, An der Sternwarte 16, 14482 Potsdam, Germany**
jrendtel@aip.de

The temporal evolution of the Geminids is documented by observational data obtained with various techniques over the last decades. Information of the activity back into the 19th century can be reconstructed from visual reports. This allows us to compare observations with conclusions from theoretical meteoroid stream modelling, particularly to investigate the recently observed rate increase.

1 Introduction

The Geminid shower is one of the annual "big three" and has shown ZHRs well above 120 over some years. Both, the population index profile and the rate profile has been shown to be rather constant over many well-observed returns of the shower (Rendtel, Arlt & Brown, 1993; Arlt & Rendtel, 1994; Rendtel & Arlt, 1997; Arlt & Rendtel, 2006). Recent years showed an increase of the peak activity. Initiated by recent modelling by Galina Ryabova (Ryabova & Rendtel, 2018; Ryabova, 2018) which indicate a further increase of the Geminid activity, we checked the available peak ZHR from visual observations collected in the IMO's VMDB. Additionally, we provide rates and fluxes derived from independent data samples.

Previous models of the stream (Fox, Williams & Hughes, 1983; Williams & Wu, 1993) rather indicated that the highest rates should be observable already now, followed by a subsequent decrease. So the current years provide us with a chance to see high Geminid rates and also offer the possibility to check the validity of stream model calculations.

2 Recent observations

2.1. Visual data

Visual data obtained in the period 1988–2017 have been analysed using the Visual Meteor DataBase (VMDB). For this study, we are mainly interested in the peak activity. Hence a constant $r = 2.40$ was used throughout the period. Due to the varying lunar interference conditions, the data coverage for each of the returns differs. We do not look for short periods of "activity bursts" but for a representative value of the peak ZHR level lasting for at least two hours. Previous analyses of single returns were made for the years 1991 (Rendtel, Arlt & Brown, 1993), for 1993 (Arlt & Rendtel, 1994), for 1996 (Rendtel & Arlt, 1997), and for 2004 (Arlt & Rendtel, 2006). Further, a long-term study revealed only a small increase of the ZHR level (Rendtel, 2004) and a rather stable maximum ZHR profile for at least 20 years. The maximum ZHR for the Geminid returns since 1988 are shown in Figure 1 and confirm a significant increase of the ZHR.

2.2. Video meteor flux

The video meteor flux is derived from the data collected by the IMO Video Meteor Network (Molau & Barentsen, 2014). For the Geminids we obtained the respective data from 2011 onwards (see the data respective points in Figure 1). The flux also shows an increase over the period of nine years, similar to the visual data. It is obvious, that the increase is not a steady process, but it has variations from one return to the next. So the 2015 maximum is lower than the neighbouring values – in both the visual and video data. It is no effect of observational bias as both 2015 samples are comprised of a large sample of well distributed individual reports.

2.3. Radio forward scatter data

This data has the advantage of not being disturbed by daytime and weather effects. However, the data reduction is somewhat limited (Ogawa et al., 2004; Rendtel, Ogawa & Sugimoto, 2017) as it includes some assumptions on the non-shower activity used for calibration. In the case of the Geminids, such effects certainly can be neglected. Sugimoto's "radio ZHR" as well as Ogawa's "Activity index" confirm the increase of Geminid activity within the period 2002–2017. Note, that the two measures discussed here are based on the same raw data sample.

3 Recovery of historic visual data

Systematic meteor observations have been carried out since about middle of 19th century. The main focus has changed over time. For a long time, the determination of radiants was the main purpose (Denning and many other observers at the end of the 19th and in the early 20th centuries) while rates and other data of showers were of rather little interest or have not been well recorded. Further, there are apparent gaps in the documentation of meteor events. One remarkable gap exists between about 1950 and 1970. The process of searching for further data and completing the series is still in progress. Certainly, there will be reports hidden in national or local papers. Here also the MetLib project (see `https://www.imo.net/resources/projects/metlib/`) may help, but also local groups may find such reports.

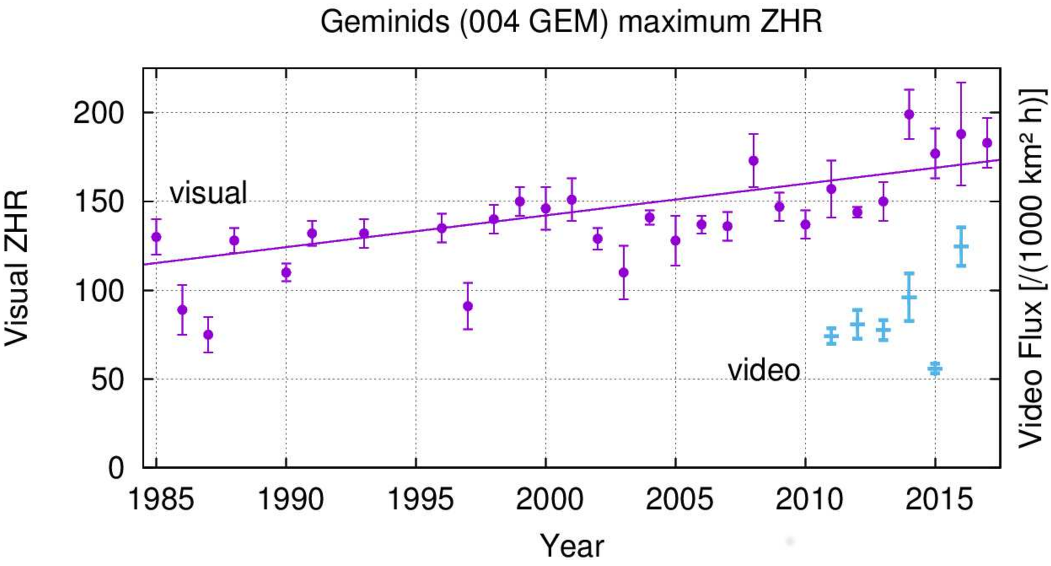

Figure 1 – Geminid activity data obtained from independent data sets expressed as the maximum ZHR or meteoroid flux per return. The visual ZHR (axis on the left) is shown back to 1985, while the meteoroid flux derived from video data (IMO Video Meteor Network) is available from 2011 onwards (axis on the right).

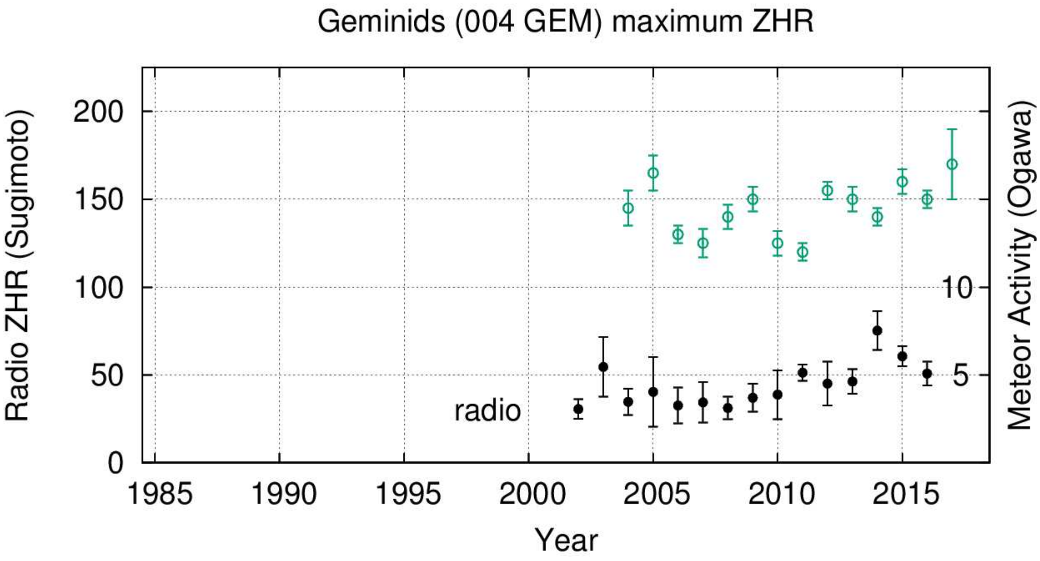

Figure 2 – Geminid activity data obtained from radio forward scatter data expressed as the maximum ZHR (left axis; Sugimoto) or Activity Index A (right axis; Ogawa) per return. The graph shows the same period as Figure 1.

Since the observations were not made primarily for rate determination, we have little or no information about the effective observing time or the conditions. We may guess qualitatively an LM from the descriptions and moonlight conditions. In a few reports, the number of non-Geminids is given so that this can be tentatively used for calibration. Two examples are shown in Figures 3 and 4. It is also necessary to verify the observing location (sometimes the name of the observer is given but not the site).

1896, Dec. 9, 8h 30m–13h (at intervals): 39 meteors (22 Geminids). Dec. 11, 10h–15h: 111 (89). Dec. 12, 14h, 15h–16h 15m: 30 (21); 9 were of the 1st magnitude, and only three left streaks. At midnight on December 11 the horary rates for all meteors and Geminids were 30 and 20 respectively.—H. Corder.

Figure 3 – Geminid report from H. Corder in 1896 giving already interval data and distiguishing between Geminids and non-Geminids (from Besley, 1900).

(1934) 13/14 Dez

The actual numbers of meteors observed are recorded in Table 1. The hourly rates, reduced to six observers, are plotted in Figure 1. (r = 2.4)

TABLE 1

UT	E.S.T.	h	Geminids	hRad	Non-Geminids		LM 5.0	5.5	6.0
0340–0407	10.40-11.07	0.30	11	50°	3		175	114	73
0414–0445	11.14-11.45	0.45	8	56	1		80	51	33
0537–0610	12.37- 1.10	0.50	19	70	2		150	96	62
0709–0741	2.09- 2.41	0.50	(G 15) 12	79	3	haze light clouds sky half clouded	136	88	56
0804–0830	3.04- 3.30	0.40	8	74°	2		77	50	32
0830–0850	3.30- 3.50	0.30	8	70	2		105	68	44
0850–0910	3.50- 4.10	0.30	11	67	4		147	95	61
0910–0930	4.10- 4.30	0.30	2	63	1	clouding	28	18	11
	Totals......		79		18				

Figure 4 – Geminid report from 1934 and rate reconstruction, assuming three different limiting magnitudes and a population index of $r = 2.4$ (table from Millman, 1935).

The currently available few data points are shown in Figure 5. Since we are looking for the maximum ZHR, we have to be aware of large uncertainties whether the available data indeed covers the Geminid maximum.

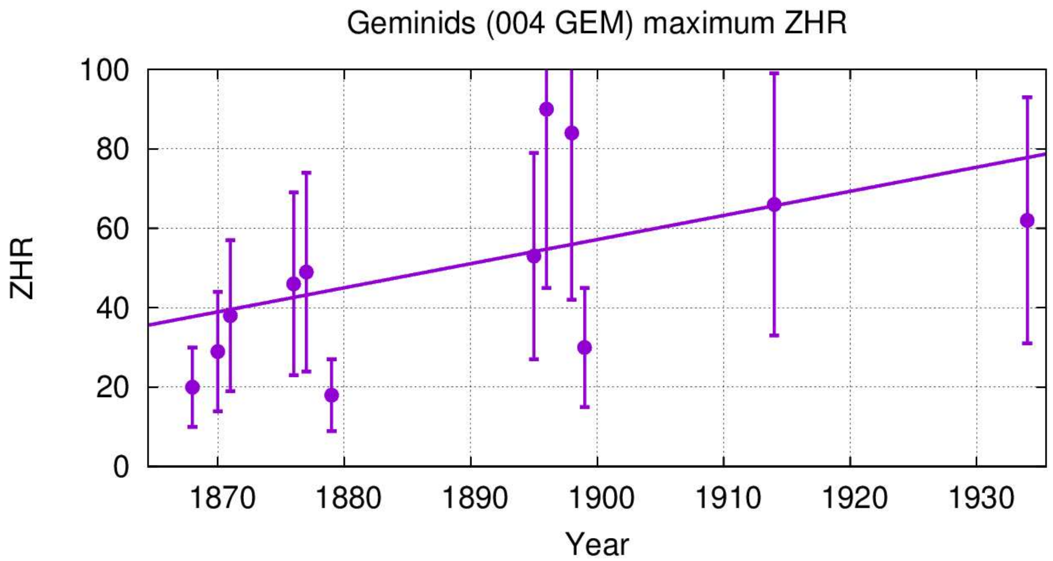

Figure 5 – Currently calculated maximum Geminid ZHRs around 1900 and a first guess of a trend (see the remarks in the text).

For example, the data points shown in Figure 5 for 1879 and 1899 are definitively pre-maximum values (December 9 and 10, respectively). From the few data we currently have in the list, we may deduct a general ZHR level of < 50 before 1900 and roughly > 60 after 1910. Further data was already described in an earlier Geminid study (Rendtel 2006) and covers the 1940ies (Czechoslovak reports) and the period preceding the IMO foundation when standards of reporting were still under discussion but can probably included in the analysis.

4 Conclusions

For the Geminid activity over the past about 20 years, we have three independent data samples at hand: visual ZHR data, video flux calculations from the IMO Video Meteor network, and radio forward scatter data.

The visual ZHR data can be calculated back to 1985 consistently, and further back into the mid-1970ies with comparable accuracy and standards. All data prior to this has very different quality and require manual handling. With some care, the Geminid peak level actvity can be estimated and established over more than a century.

The coming returns will provide us with data which should allow us to check the ZHR trend. So all observational data are welcome. This study also underlines the importance of continuation of visual observations in order to continue a long lasting series until the overlap with data from other techniques is long enough to ensure conclusions.

References

Arlt R., Rendtel J. (1994). "A global analysis of the 1993 Geminids." *WGN, Journal of the IMO*, **22**, 167–172.

Arlt R., Rendtel J. (2006). "The activity of the 2004 Geminid meteor shower from global visual observations." *MNRAS*, **367**, 1721–1726. doi:10.1111/j.1365-2966.2006.10077.x

Besley W.E. (1900). "The Geminid meteor-shower." *The Observatory* **23**, 366–370.

Fox K., Williams I.P., Hughes D.W. (1983). "The rate profile of the Geminid meteor shower." *MNRAS* **205**, 1155–1169.

Millman, P.M. (1935). "Meteor News – Observations of the 1934 Geminids." *Journal of the Royal Astronomical Society of Canada*, **29**, 115–116.

Molau S., Barentsen G. (2014). "Status and history of the IMO Video Meteor Network." In: T.J. Jopek, F.J.M. Rietmeijer, J. Watanabe, I.P. Williams, editors, *Proc. Meteoroids 2013, Poznań, Poland, Aug. 26-30, 2013*, A.M. University Press, 297–305.

Molau S., Rendtel J. (2009). "A comprehensive list of meteor showers obtained from 10 years of observations with the IMO Video Meteor Network." *WGN* **37**, 98–121.

Ogawa H., Toyomasu S., Ohnishi K., Maegawa K., Amikura S., and Miyao K. (2004). "The international project for radio meteor observation 2001–2003." In: Triglav-Čekada M. and Trayner C., editors, *Proc. IMC Bollmannsruh, Germany, 2003*, 107–113.

Rendtel J. (2004). "Evolution of the Geminids observed over 60 years." *Earth, Moon, Planets* **95**, 27–32. doi: 10.1007/s11038-004-6958-5

Rendtel J., Arlt R. (1997). "Activity analysis of the 1996 Geminids." *WGN* **25**, 75–78.

Rendtel J., Arlt R., Brown P. (1993). "The 1991 Geminid meteor shower." *WGN* **21**, 19–28.

Rendtel J., Ogawa H., Sugimoto H. (2017). "Meteor showers 2016: review of predictions and observations." *WGN* **45**, 49–55.

Ryabova G. (2018). "Could the Geminid meteoroid stream be the result of long-term thermal fracture?" *MNRAS* **479**, 1017–1020. doi: 10.1093/mnras/sty1532

Ryabova G., Rendtel J. (2018). Increasing Geminid meteor shower activity. *MNRAS Letters*, **475**, L77–L80. doi: 10.1093/mnrasl/slx205

Williams, I.P., Wu Z. (1993). "The Geminid meteor stream and asteroid 3200 Phaethon." *MNRAS* **262**, 231–248.

September ϵ Perseids observed by the Czech Fireball Network

Lukáš Shrbený[1], Pavel Spurný[1], Jiří Borovička[1]

[1] **Astronomical Institute of the Czech Academy of Sciences, Ondřejov observatory**
shrbeny@asu.cas.cz

We report exceptional high activity of bright photographic fireballs belonging to September epsilon Perseid (SPE, IAU #208) meteor shower in 2013. The center of the fireball outburst in 2013 was found at solar longitude 167.196±0.003° corresponding to 2013 September 9, 22h13m 4m UT. We determined atmospheric trajectories, physical properties, radiants, and heliocentric orbits of 25 SPE fireballs observed from 2013 to 2017. We observed two multi-station persistent trains and grating spectra of two SPE fireballs. The details will be published in a professional journal, and thus we provide only brief and preliminary conclusion.

Conclusion

The results on atmospheric trajectories, orbits, light curves, and physical properties of 12 SPE fireballs recorded by cameras of the Czech Fireball Network during high SPE activity on 9 September 2013 are as follows.

- The maximum fireball activity was observed at 22:13 UT±4 min and corresponds to the maximum of video meteors observed by Rendtel et al. (2014) (single-station video meteors) and the first maximum of Gajdoš et al. (2014) (double-station video meteors).
- Two types of light curves were observed (Figure1): with expressive flare (PE type IIIA) and without expressive flare (PE type II/IIIA).
- On the basis of PE coefficients, dynamic pressures, and initial velocities we can conclude that the material of SPE meteoroids is of cometary origin and is a bit harder than that of Orionids and statistically the same as that of Perseids.
- The mean geocentric radiant for solar longitude 167.2° is 47.7°, 39.5° and can be used for confirmation of future outbursts predicted by Rendtel et al. (2014).
- On the basis of orbits the parent body is long-period comet

The results on atmospheric trajectories, orbits, light curves, and physical properties of SPE fireballs observed from 2015 to 2017 confirm the results of the 2013 SPE fireballs and extend the conclusion as follows.

- Two spectral components were observed in spectra of SPE fireballs. Spectra are similar to spectra of other shower meteors with similar velocity and brightness and does not show any exceptional or rare features.

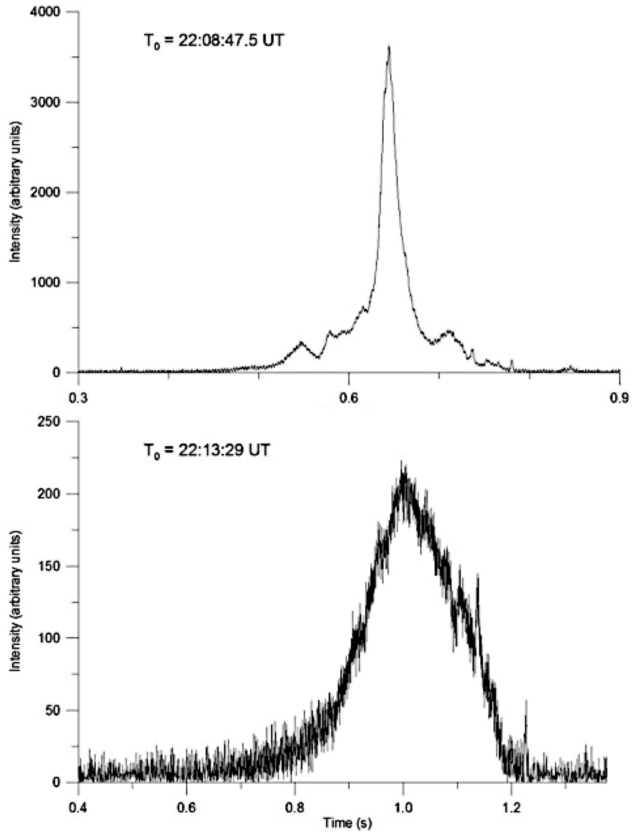

Figure 1 – Comparison of SPE light curve types.

References

Gajdoš Š., Tóth J., Kornoš L., Koukal J., and Piffl R. (2014). “The September epsilon Perseids in 2013”. *WGN, Journal of the International Meteor Organization*, **42:2**, 48–56.

Rendtel J., Lyytinen E., Molau S., and Barentsen G. (2014). “Peculiar activity of the September epsilon-Perseids on 2013 September 9”. *WGN, Journal of the International Meteor Organization*, **42:2**, 40–47.

Analysis of the dynamic relationship between the asteroid (196256) 2003 EH1 and comets C/1490 Y1 & C/1385 U1

Georgy E. Sambarov[1], Tatyana Yu. Galushina [2], and Olga M. Syusina [2]

[1] **Research Institute of Applied Mathematics and Mechanics of Tomsk State University, Tomsk, Russia**
detovelli@gmail.com

[2] **Tomsk State University, Tomsk, Russia**
volna@sibmail.com and kleo77@sibmail.com

The Quadrantids is one of the strongest meteor showers. The core of the Quadrantids is only 200-300 years old and is associated with asteroid (196256) 2003 EH1 while a wide part of stream is connected with comet 96P/Machholz. The asteroid is thought to be the remnant of a past cometary object, tentatively identified with the historical comets C/1490 Y1 and C/1385 U1. In this paper, we use all observations that present on Minor Planet Center (MPC) to extend the observed arc of the asteroid (196256) 2003 EH1 from 10 months to about 11 years, enough to exclude the proposed direct relationship of the asteroid with both of the comets.

1 Introduction

The Quadrantid shower is one of the most intense. It is observed at the beginning of January each year. The name of the shower originates from the Quadrans Muralis constellation. This is now a defunct constellation but it existed when the stream was recognized in 1835 by Quetelet (Fisher, 1930). The core of the Quadrantids is only $200 - 300$ years old and is associated with asteroid (196256)2003EH1 (Abedin et al., 2015) while a wide part of stream is connected with comet 96P/Machholz (Abedin et al., 2018). The age and formation mechanism of the Quadrantids meteoroid stream core and the relationship with the asteroid (196256) 2003 EH1 have been studied previously by several authors (Jenniskens, 2004; Williams et al., 2004; Wiegert & Brown, 2005; Abedin et al., 2015). Current dust production from (196256) 2003 EH1 is too small (Kasuga & Jewitt, 2015) to supply the mass of the Quadrantids on interval $200 - 500$ years ago from now. If 2003 EH1 is the source of the Quadrantids core then mass must be delivered episodically.

There have been numerous suggestions regarding a possible parent for the stream, which are proposed comets C/1490 Y1 (Hasegawa, 1979; Williams & Wu, 1993; Ki-Won et al., 2009) and C/1385 U1 (Micheli et al., 2008) as possible parent bodies. Hasegawa has derived the orbital elements of several historical comets and has concluded that comet C/1490 Y1 might be the parent comet of the Quadrantids (Hasegawa, 1979). Other authors (Williams & Wu, 1993; Micheli et al., 2008) have concluded that another historical comet C/1385U1 is probably identical to comet C/1490 Y1. The main result of their work is the exclusion of the proposed identification of the comets C/1490 Y1 and C/1385 U1 as the historical cometary apparitions of the asteroid (196256)2003 EH1. In this work, we attempt to repeat this experiment with the extended observations' arc of asteroid (196256) 2003EH1 from 10 months to about 11 years.

2 Is the asteroid (196256) 2003 EH1 associate with the comets C/1490 Y1 and C/1385 U1?

This section of paper is an updated analysis of the study relationship of the asteroid (196256)2003 EH1 and the comet C/1490 Y1. In our analysis, we used a method similar to the one applied by many authors (Chernitsov et al., 1998; Williams et al., 2004; Syusina et al., 2012). At first we generated 500 clones and got 12 vertices of the confidence ellipsoid of (196256)2003 EH1. The equations of motion of the asteroid with him clones were integrated using the Everhart (Everhart, 1974) 19th-order procedure with variable step size until 1491 January(or 1385 November). We used the parameter MEGNO (Mean Exponential Growth factor of Nearby Orbit) to study regular and chaotic dynamics of the nominal orbit of the asteroid and vertices of its confidence ellipsoid. The MEGNO chaos indicator is a powerful tool used to identify chaos in dynamical systems. Chaotic orbits are characterized by a large MEGNO value ($Y > 2$) which grows linearly while regular or quasi-periodic orbits are associated with $Y < 2$ (Cincotta et al., 2003).

In the article by Galushina et. al. (Galushina & Sambarov, 2017), the perturbation structure and the orbital evolution of the asteroid (196256) 2003 EH1 were considered in more detail, but part of the study of the relationship with the Quadrantids meteor shower was not considered. At the time of the publication of the paper (Williams et al., 2004), there were large uncertainties in determining the orbital parameters of the orbit of the asteroid (196256) 2003 EH1. These uncertainties were due to the insufficient number of observa-

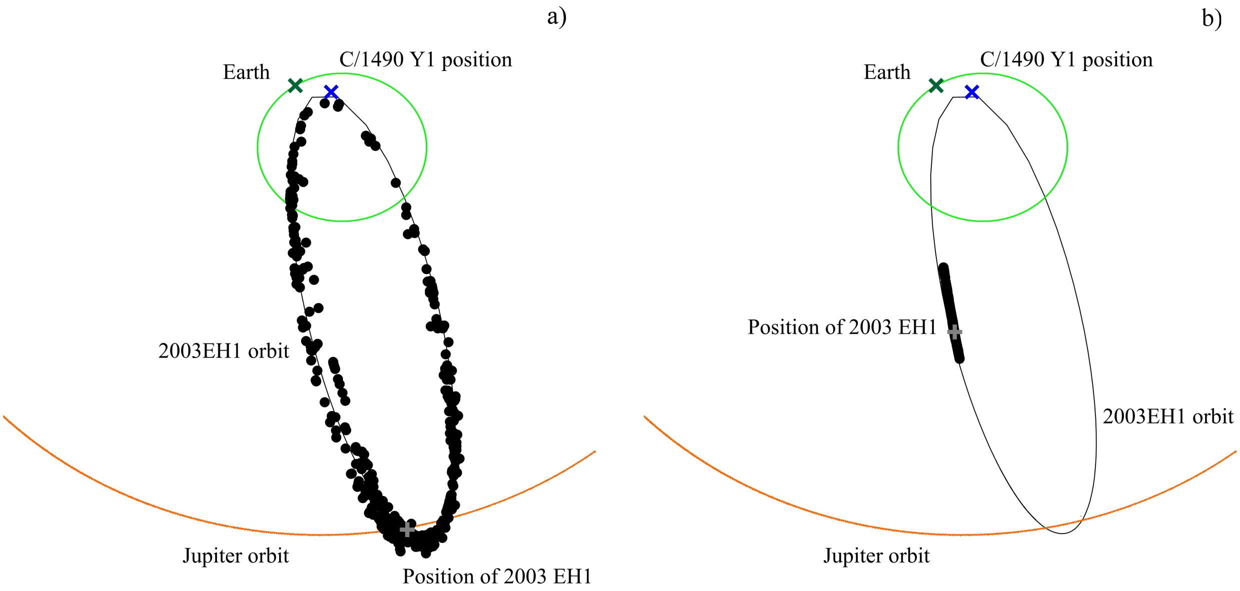

Figure 1 – A projection on to the ecliptic of the nominal orbit of asteroid (196256) 2003 EH1, its actual position (large grey cross) and position of the 500 clones (black dots) on 1491 January 7. Also shown is the orbit of C/1490 Y1 with its position at the relevant date shown by large blue cross, as is the position of the Earth by large green cross. The results on the left are obtained from 44 observations from March 6 to April 23, 2003 on left. The results on the right are obtained from 95 observations from March 6, 2003 to March 23, 2014.

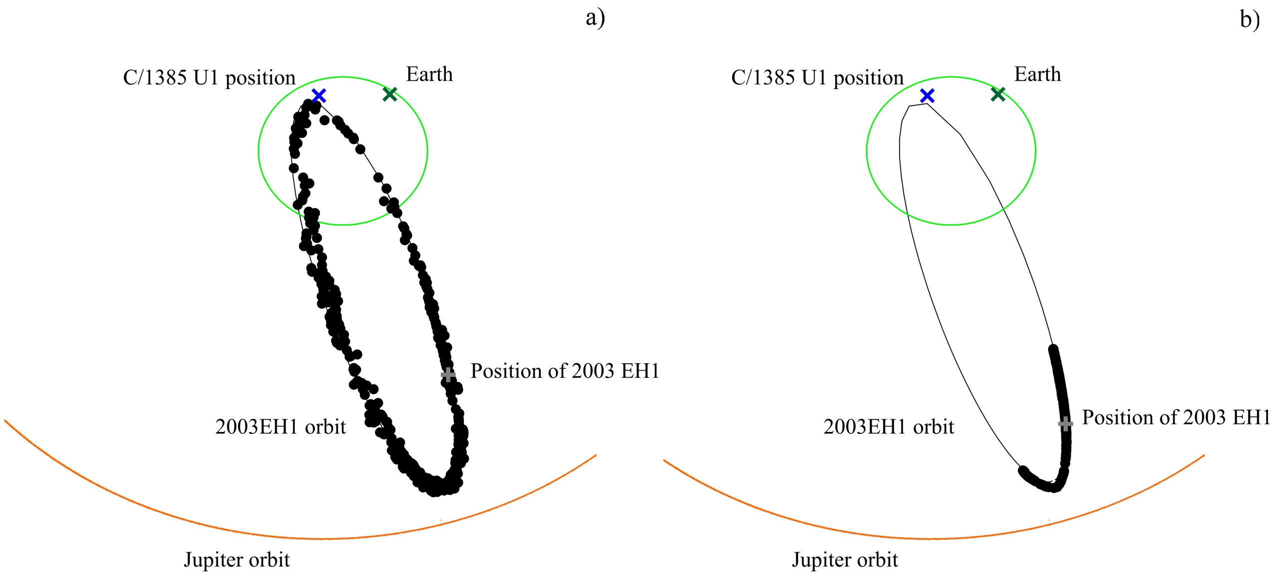

Figure 2 – The same as in Fig. 1 but for comet C/1385 U1 on 1385 November 1.

tions and a small dimensional arc. In their paper, it is also noted that in 1491 the orbital elements of the object under study are surprisingly similar to the orbits of the middle stream of the Quadrantids and are similar to those given by Hasegawa (Hasegawa, 1979) for comet C/1490 Y1. According to historical accounts, the comet was moving like a bright object, visible to the naked eye in the last days of 1490. It was widely noted during the first two months of 1491 by Chinese, Korean and Japanese astronomers, according to Ho (Ho, 1962). Also, various attempts were made to integrate the orbit of the Quadrantids stream in 1491 (Williams & Wu, 1993), with the integrated orbit showing a surprising similarity with the comet. Ki-Won Lee et. al. (Ki-Won et al., 2009) studied annual historical reports compiled in Korea during the Joseon Dynasty, in which there are

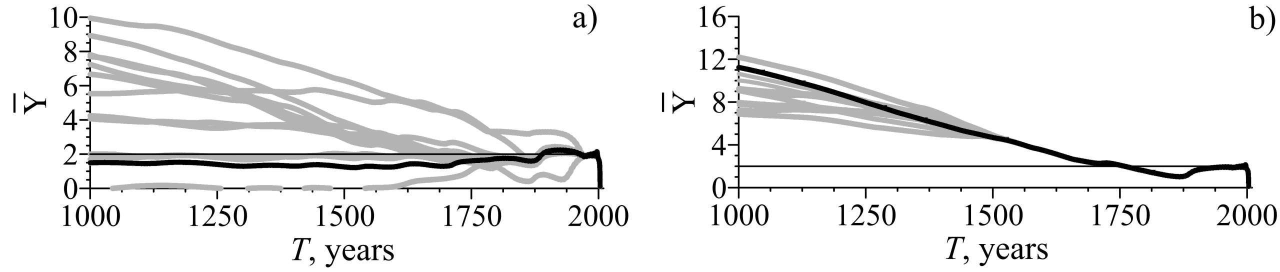

Figure 3 – Evolution of the MEGNO parameter for the asteroid (196256) 2003 EH1 of the nominal particle (black color) and the vertices of the confidence ellipsoid (gray). A sample for 44 observations (from March 6, 2003 to April 23, 2003) (a) and a full sample (b).

various astronomical objects covering the entire period of Korea's history (1392 – 1910). Ki-Won Lee et al. have shown that the asteroid (196256) 2003 EH1 and comet C/1490 Y1 can be connected to each other, and possibly be a single object, like a sleeping comet. Based on these points, we conducted the following study.

In this paper we attempted to repeat the experiment given in article (Williams et al., 2004) for the asteroid (196256) 2003 EH1 in which an attempt was made to integrate the object's orbit to the desired epoch using the observations at that time covering a time period less than 1 year, from March 6, 2003 to April 23, 2003. The authors (Williams et al., 2004) sampled the confidence ellipsoid for the 2003 EH1 with 500 clones whose orbits lie within the uncertainties and integrated them in the 1491 epoch. The main result of their work is that the integral position of the clones has an extreme scatter, but at least one of them has characteristics very close to those of the comet C/1490 Y1, and its path in the sky is also close and corresponds to the observed comet. However, most integrated orbits predicted that the object is located around the aphelion, and not close to the perihelion on which the comet C/1490 Y1 was observed.

Due to the fact that updates are frequently being made on the MPC website, and we do not know exactly which observations were used in this work, we will take only those that fall within the dimensional interval specified in the article (Williams et al., 2004). Next, we expand the observation arc a little, and in the end we compare it with the result that was obtained in the article by Galushina (Galushina & Sambarov, 2017). But a comparison between different orbits makes sense only if they belong to the same epoch, since the effect of various gravitational perturbations is often significant for several centuries. This caution is especially important, since the orbit (196256) 2003 EH1 has an aphelion around Jupiter's orbit, so it often enters a region of space in which strong perturbing effects act. This comparison can only be done by integrating the orbit (196256) 2003 EH1 at the time of the appearance of the historical comets, because the comet orbit is not accurately defined to be integrated into the future.

The results were evaluated according to the article (Williams et al., 2004). The nominal position of the asteroid on its orbit is close to aphelion and thus moving slowly at the relevant time. However, the comet was close to perihelion. Since the orbit is of high inclination, this difference in true anomaly also explains the incorrect position, in declination as well as right ascension, of the nominal asteroid. We also see from Fig. 1a that the clones are spread essentially all around the orbit. About 300 yr clones should be spread all around the orbit. This implies that some of the clones are close to perihelion as can see in Fig. 1.

As expected, the clones lie on the same line of variations that were obtained from observations from March 6, 2003 to April 23, 2003. Comet C/1490 Y1 is close to perihelion, and the nominal position of the asteroid (196256) 2003 EH1 in its orbit is close to the aphelion and, thus, slowly moves at the appropriate time. Fig. 1a also shows that most of the clones are located just as close to the aphelion. This is not surprising. If you look at the confidence region consisting of 500 test points (Fig. 1a), note that they all spread over the entire orbit of the asteroid. For a variant with 95 observations(Fig. 1b), it is seen that the vertices of the confidence ellipsoid are located close to the position of the nominal orbit of the asteroid, which is very different from the position of the orbit from Williams et al. The same scenario can be seen on Fig.2. The clones are spread essentially over the entire orbit of the asteroid, whereas for all observations the clones are concentrated near nominal position of the asteroid.

Not only the nominal orbit for each sample of observations, but also the vertices of the trusted ellipsoid (Fig. 3) were investigated for chaotic motion. As a result, our studies showed that for the first variant (44 observations) the nominal orbit and two vertices can be considered regular on all time intervals. But other vertices are characterized by a large MEGNO value ($Y > 2$) which grows linearly, which indicates the manifestation of chaos in motion. It is interesting to note that for some vertices obtained for the first sample, the regular motion is maintained up to 1600 years ago. The insufficient number of observations and a small dimensional arc can lead to scattering in space. For the second variant (95 observations), a chaotic movement appears after 1760, both for the nominal orbit and for the vertices of the confidence ellipsoid.

3 Conclusions

The results obtained in this paper exclude the proposed identification of comets C/1490 Y1 and C/1385 U1 as the historical cometary phenomena of the asteroid (196256) 2003 EH1. None of the integrated orbits obtained from the full set of observations from 2003 March 6 to 2014 March 23 is consistent with the situation and the movement of objects in 1491 AD and 1385 AD. Although new observations appear to exclude the identification of the asteroid (196256) 2003 EH1 with comets C/1490 Y1 and C/1385 U1, it cannot be ruled out that they are fragments of the same parent body that have long since split.

Acknowledgements

One of the authors (SGE) would like to acknowledge a gratitude to the Organizers of the IMC-2018 conference. This research has made use of data and/or services provided by the International Astronomical Union's Minor Planet Center. This research has made use of NASA's Astrophysics Data System.

References

Abedin A., Spurný P., Wiegert P., Pokorný P., Borovička J., and Brown P. (2015). "On the age and formation mechanism of the core of the Quadrantid meteoroid stream". *Icarus*, **261**, 100–117.

Abedin A., Wiegert P., Janches D., Pokorný P., Brown P., and Hormaechea J. L. (2018). "Formation and past evolution of the showers of 96P/Machholz complex". *Icarus*, **300**, 360–385.

Chernitsov A. M., Baturin A. P., and Tamarov V. A. (1998). "An analysis of some methods for the determination of the probabilistic evolution of motion of the solar system's small bodies". *Solar System Research*, **32**, 405.

Cincotta P. M., Girdano C. M., and Simo C. (2003). "Phase space structure of multi-dimensional systems by means of the mean exponential growth factor of nearby orbits". *Phys. D*, **182**, 151–178.

Everhart E. (1974). "Implicit single-sequence methods for integrating orbits". *Celestial Mechanics*, **10**, 35–55.

Fisher W. J. (1930). "The Quadrantid Meteors - History to 1927". *Harvard College Observatory. Circular*, **346**, 1–11.

Galushina T. Y. and Sambarov G. E. (2017). "The dynamical evolution and the force model for asteroid (196256) 2003 EH1". *Planetary and Space Science*, **142**, 38–47.

Hasegawa I. (1979). "Orbits of ancient and medieval comets". *Publ. Astr. Soc. Japan*, **31**, 257–270.

Ho P. Y. (1962). "Ancient and mediaeval observations of comets and novae in Chinese sources". *Vistas in Astronomy*, **5**, 127–225.

Jenniskens P. (2004). "2003 EH1 is the Quadrantid shower parent comet". *The Astronomical Journal*, **127**, 3018–3022.

Kasuga T. and Jewitt D. (2015). "Physical observations of (196256) 2003 EH1, presumed parent of the Quadrantid meteoroid stream". *The Astronomical Journal*, **150**, 152–162.

Ki-Won L., Hong-Jin Y., and Myeong-Gu P. (2009). "Orbital elements of comet C/1490 Y1 and the Quadrantid shower". *MNRAS*, **400**, 1389–1393.

Micheli M., Bernardi F., and Tholen J. D. (2008). "Updated analysis of the dynamical relation between asteroid 2003 EH1 and comets C/1490 Y1 and C/1385 U1". *MNRAS*, **390**, L6–L8.

Syusina O. M., Chernitsov A. M., and Tamarov V. A. (2012). "Construction of confidence regions in problem on probabilistic study into motion of minor bodies of the solar system". *Solar System Research*, **46**, 195–207.

Wiegert P. and Brown P. (2005). "The Quadrantid meteoroid complex". *Icarus*, **179**, 139–157.

Williams I. P., Ryabova G. O., Baturin A. P., and Chernitsov A. M. (2004). "The parent of the Quadrantid meteoroid stream and asteroid 2003 EH1". *MNRAS*, **355**, 1171–1181.

Williams I. P. and Wu Z. D. (1993). "The Quadrantid meteoroid mtream and comet 1491I". *MNRAS*, **264**, 659–162.

Developing a Cost-Effective Radiometer for Fireball Light Curves

Stuart R. G. Buchan[1], Robert M. Howie[1], Jonathan Paxman[2], and Hadrien A. R. Devillepoix[1]

[1] **School of Earth and Planetary Sciences, Curtin University, Perth, WA 6845, Australia**
stuart.buchan@curtin.edu.au, robert.howie@curtin.edu.au and hadrien.devillepoix@curtin.edu.au

[2] **Department of Mechanical Engineering, Curtin University, Perth, WA 6845, Australia**
j.paxman@curtin.edu.au

Fireball light curves can give insight into the meteor ablation process which can be used to improve fireball trajectory and mass modelling. To this aim, the Desert Fireball Network (DFN) is developing a low cost add-on fireball radiometer to supplement existing observatories. The objective is to collect radiometric data on fireballs across a wide spectral range at 1000 samples per second with sensitivity to a large dynamic range (mV ∈[-4, -20]), whilst maintaining a low cost. Here we discuss the current prototype design and first light results.

1 Introduction

Due to the often very rapid period of ablation in the upper atmosphere, the light intensity of a meteor can be difficult to characterise using solely photographic means. This shows the necessity of a standalone, high-accuracy radiometric device to supplement existing cameras in a fireball network. The implementation of radiometry in the production of meteor light curves provides the unique advantage of a fast sampling rate, unparalleled by photometric equipment, that allows the device to accurately portray rapid changes in brightness. Moreover, through the use of inexpensive silicon photodiodes, the spectral response range can be larger than that of photographic detectors. This means that radiometry possesses sensitivity to wavelengths that could otherwise be neglected by photographic cameras. An example of this can be seen in Figure 1, which demonstrates high sensitivity in the near-IR spectrum. Furthermore, it can be seen that radiometry shows good coverage of the 777 nm oxygen line (Jenniskens et al., 2018). As radiometers can detect fireball events in cloudy conditions, they have been proven to supplement photographic methods to increase throughput of meteor detection (Spurny et al., 2001). Whilst showing high applicability to meteor detection, it is evident that radiometry is not as popular as photometry in fireball networks around the world. In an effort to amend this, it is proposed that inexpensive off-the-shelf circuit components are to be assembled into a low-cost radiometric device suitable for mass implementation in a fireball network.

2 Design

Using the recommendations proposed by Denis Vida in his IMC 2015 paper, design goals for the radiometer were set to have 24-bit resolution, a large dynamic range, and a minimum sampling rate of 1 kHz (Vida et al., 2015).

2.1 Collection Method

As an aim for the radiometer is to collect irradiance data over a wide range of wavelengths, silicon photodiodes sensitive in a broad spectral range are desirable. Furthermore, they are seen to possess a very low dark current and high speed response, showing high applicability to the project. At 50, the Hamamatsu S1337-1010BR silicon photodiode offers an effective photosensitive area of 100 mm^2 with a peak photosensitivity of 0.6 Amps/Watt, as can be seen from Figure 1.

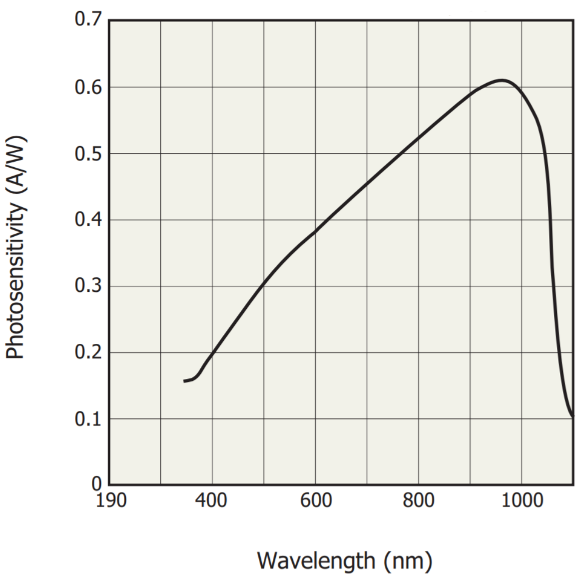

Figure 1 – Hamamatsu S1337-1010BR Spectral Response[1]

The irradiance (in W/m^2) of a fireball as a function of apparent magnitude can be calculated by the following:

$$E = 1100 * 2.512^{-26.7-M_{fb}} \quad (1)$$

[1] https://www.hamamatsu.com/resources/pdf/ssd/s1337_series_kspd1032e.pdf

Where M_{fb} refers to the apparent magnitude of the fireball (Spalding et al., 2017). In an effort to simulate the response of the chosen photodiode to impinging light, a Python script was used to iterate through the dynamic range of interest and calculate the output current using the irradiance derived through Equation 1 with the effective photosensitive area and peak spectral response. The result can be seen in Figure 2.

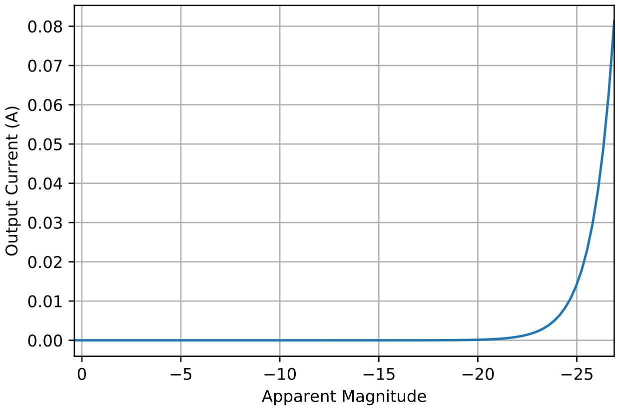

Figure 2 – Theoretical current output over the range mV ∈[0.4, -26.9]

2.2 Amplifier

The purpose of the amplifier is to not only amplify the signal to a recordable level, but to also convert the current signal coming from the photodiode into a voltage that can be sampled. As is evident from Figure 2, the magnitude of the output signal from the photodiode is insignificantly small for the majority of the dynamic range before ramping suddenly towards the higher end of the range. As a design goal is for a high saturation point, it was decided that a fixed amplifier gain would not be suitable as it would lead to premature circuit saturation before reaching the end of the dynamic range desired. Rather, a logarithmic gain showed strong suitability due to its ability to amplify an input current in a logarithmic manner. The selected component, the Analog Devices ADL5304, offers ten decades of input current from 1 pA to 10 mA, showing strong applicability to the project. The chosen circuit configuration gave a slope of 200 mV per decade, and the output was simulated using the currents seen in Figure 2 to produce the response seen in Figure 3.

2.3 Analog to Digital Converter (ADC)

To store the voltage signal produced by the amplifier, it needs to be converted into an integer through the use of an analog to digital converter. The chosen device, the Texas Instruments ADS1255, is a low-noise sigma-delta ADC which offers 24-bit resolution and supports sampling rates up to 30 kS/s. For the current prototype design, the ADC has been programmed to sample at 1 kS/s due to limitations of the circuit readout hindering conversion speed. The chosen package outputs

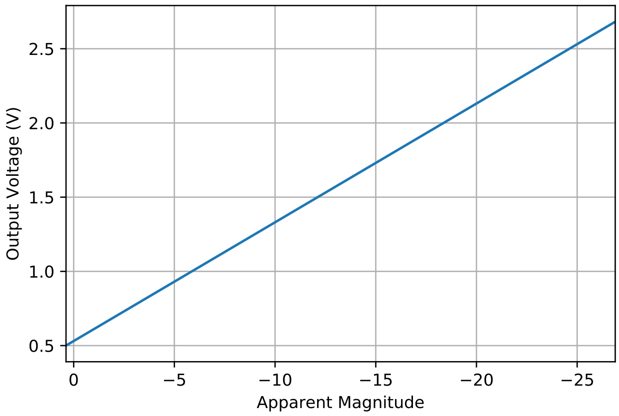

Figure 3 – Theoretical voltage output over the range mV ∈[0.4, -26.9]

the 24 bit sample as three successive bytes via a serial peripheral interface.

2.4 Readout

To remain within the design criteria of low cost and USB accessibility, it was decided that the readout of the radiometer was to be implemented using an inexpensive Arduino Micro microcontroller. The microcontroller communicates with the radiometer through the ADC, and hence needs to conform to the strict timing procedures detailed in the data sheet for the ADS1255. The initialisation and communication protocol was coded using Embedded C. After receiving and converting the two's compliment sample from the ADC, the microcontroller then outputs the radiometric data over USB serial. To log the data, a Python script was written utilising the PySerial library to access the system serial ports. The script when executed waits until the top of the UTC minute, and then starts receiving samples when they are available on the serial buffer. In the current prototype design, the script time-stamps each sample using the system clock, however future revisions will see the implementation of GNSS timing. After storing these values in memory until thirty seconds has elapsed, the script then writes the values to the disk. At the time of the IMC conference, this was done in csv format. However, this has since been updated to logging using FITS tables.

3 Implementation

The assembled prototype can be seen in Figure 5. The completed radiometer is sensitive to a wide spectral range (ultraviolet to near infrared) for under 100. Due to the large collection area and amplification method, it is able to reliably sample light signals within the range mV ∈[0.4, -26.9], exceeding the desired initial range. The unit can be powered off a voltage source within the range of 6-36 V, consuming less than 3 W. Future revisions will see the radiometer functioning through a single USB cable for both data logging and power.

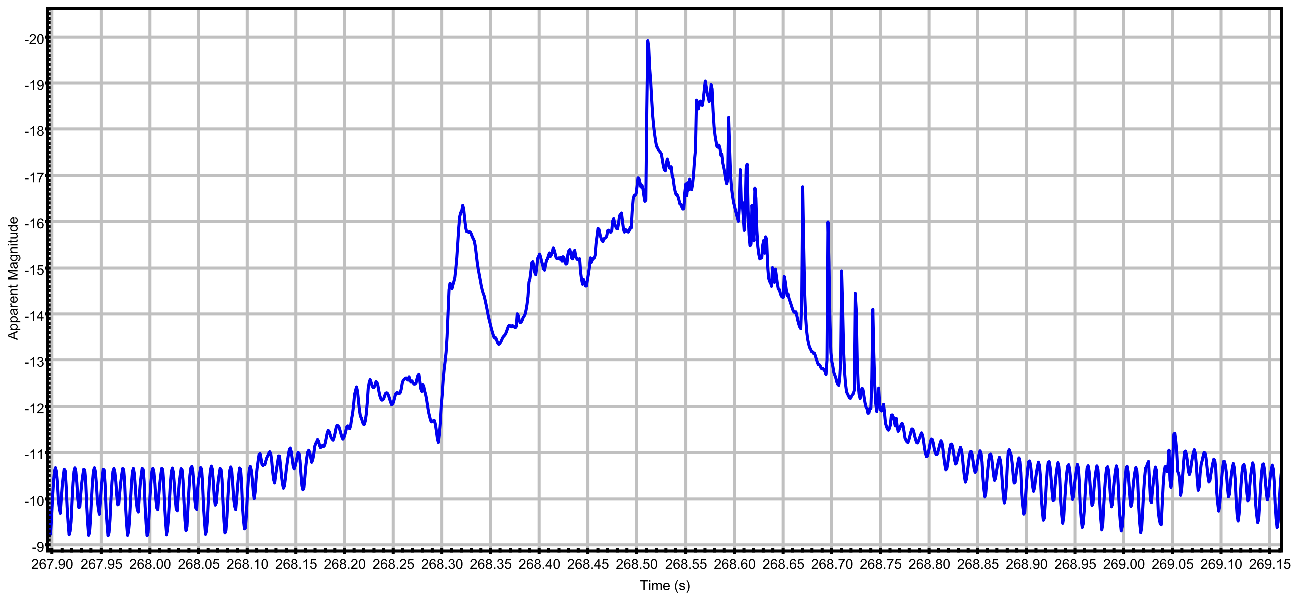

Figure 4 – Light curve of a lightning strike. Plotted against seconds from starting time of 2018-09-01T20:53:00.0 UTC

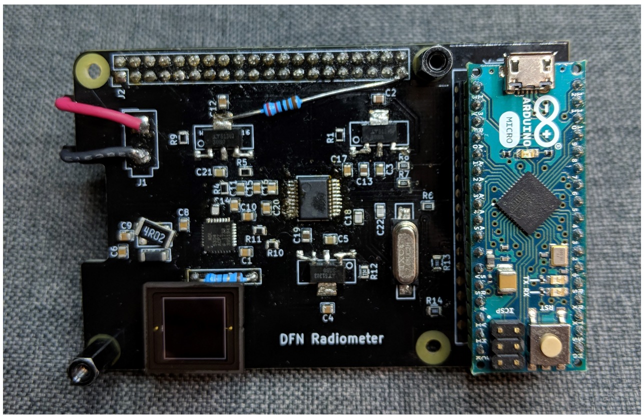

Figure 5 – Assembled radiometer prototype

4 Calibration

The unit was calibrated initially by mathematically deriving the relationship between photodiode current and output sample by using the ideal equations given in the data sheet for the circuit components. This however showed an inconsistent error of around three percent, and hence further calibration was done using celestial bodies. Firstly, the radiometer was exposed to the sun with an incidence angle of 90 degrees. Following this, the radiometer was exposed to the moon with an incidence angle of 90 degrees. The apparent magnitudes recorded for the bodies were -24.5 and -11.2 respectively. These apparent magnitudes were cross referenced with the HORIZONS web interface[2], showing the true values of -26.72 and -11.52 respectively. As the errors were not unanimous, a simple scale was not appropriate, and hence a new model was derived using a linear two point approximation of the sources. This approach is different to photomultiplier tube based radiometers which require external photographic measurements to calibrate for each event, whereas this unit can be absolutely calibrated independently.

[2]`https://ssd.jpl.nasa.gov/horizons.cgi#results`

5 Results

On the night of the first of September 2018, the last night of the IMC, Pezinok was struck with a thunderstorm. Taking advantage of this event, the radiometer was placed facing out of a window at the sky to capture light curves of the lightning taking place. An example of the light curves collected can be seen in Figure 4. The light curve has been calibrated into apparent magnitude using the model discussed in Section 4. The data is plotted in seconds from the start of the recording session at 20:53:00. The oscillation seen in the data is due to the 50 Hz electrical mains frequency emanating from a streetlamp at an approximate apparent magnitude of -10. It is evident that the peak of the strike occurs just below an apparent magnitude of -20, showing unsaturated recordings over ten magnitudes. As can be seen from Figure 4, the event begins at 268.10 seconds, and ends at 269.0 seconds, spanning a total length of 0.9 seconds. Due to this length, it is expected that the light curve shows the illumination from multiple strikes happening in succession.

6 Conclusions and Future Work

The proposed design criteria for the project were met to produce a working radiometer for under 100. Using the prototype design, it was possible to produce apparent magnitude calibrated light curves to a satisfactory standard. The next revision of the radiometer will see implementation of GNSS timing for better resolution time stamping. Furthermore, the single photodiode will be replaced by an array with a similar integrated collection area, allowing for an increase in frequency response. Future revisions will also see the addition of narrow-band filters around selected spectral lines. It is therefore deemed that the initial prototype design was a success, and with some improvements would make a valuable addition to any fireball observatory.

References

Jenniskens P., Albers J., Tillier C. E., Edgington S. F., Longenbaugh R. S., Goodman S. J., Rudlosky S. D., Hildebrand A. R., Hanton L., Ciceri F., Nowell R., Lyytinen E., Hladiuk D., Free D., Moskovitz N., Bright L., Johnston C. O., and Stern E. (2018). "Detection of meteoroid impacts by the geostationary lightning mapper on the goes-16 satellite". *Meteoritics & Planetary Science*, **53**, 2445-2469.

Spalding R., Tencer J., Sweatt W., Conley B., Hogan R., Boslough M., Gonzales G., and Spurn P. (2017). "Photoacoustic sounds from meteors". *Scientific Reports*, **7**, srep41251.

Spurny P., Spalding R. E., and Jacobs C. (2001). "Common ground-based optical and radiometric detections within Czech fireball network". In Warmbein B., editor, *Meteoroids 2001 Conference*, volume 495 of *ESA Special Publication*, pages 135–140.

Vida D., Turcinov R., Segon D., and Siladi E. (2016). "Low-cost meteor radiometer". In Rault J.-L. and Roggemans P., editors, *Proceedings IMC Mistelbach, Austria, 27-30 August 2015*. IMO, pages 180–184.

MT: Software for calculating Meteor Trajectories and orbits from multiple-stations observations

František Ďuriš[1], Leonard Kornoš[1], and Juraj Tóth[1],

[1] **Faculty of Mathematics, Physics and Informatics, Comenius University in Bratislava, Slovakia**
fduris@dcs.fmph.uniba.sk

We designed and developed a GUI tool for calculating and visualizing trajectories of meteors in Earth's atmosphere and Solar system from multiple-station observations. The current version of the program includes calculation of 1) atmospheric trajectory and velocity, 2) Solar system trajectory, 3) photometric mass, 4) dark flight and impact, 5) Monte Carlo simulation of errors. The program is written in Lazarus/Object Pascal and can be run under Windows as well as Linux systems. Numerical simulations and graphical outputs are produced in R.

1 Introduction

The Slovak Video Meteor Network based on four stations from October 2013 (double station from 2009) (Tóth et al., 2011; Tóth et al., 2015a), two cameras on Canary Islands (Tóth et al., 2015b) from March 2015 and two cameras in Chile from March 2016 have recorded several tens of thousands meteors by the end of 2016. Naturally, only a part (about 20% - 40%) was observed simultaneously. Using precise all-sky astrometry (Borovička et al., 1995) and our own trajectory and orbit program (Tóth et al., 2015a; Kornoš et al., 2017) based on (Ceplecha, 1987), we gained the high quality video meteors database for further meteor studies.

In this paper, we present details of some parts of our software MT, and we introduce our software for all-sky astrometric reduction called RS.

2 RS – A tool for astrometric reduction

The tool is based on Borovička Fortran code (Borovička et al., 1995) for astrometric reduction (Figure 1). However, we added a few improvements to better suit our needs. The software roughly comprises of the following steps:

- Initial star identification (exact analytic formulae for Azimuth, Zenit $\rightarrow$ X,Y transformation),
- Computation of reduction constants (three iterations with the removal of outlying stars),
- Iterative change of scale.

The change of scale is directed to improve the quality of reduction constants (computed and ascertained by Borovička Fortran procedure), but we select the final constants based on all iterations through the program run (Table 1).

Currently, we are working on calibration of meteor magnitude based on the linear fit of logarithm of brightness and catalogue magnitude of the identified stars. The saturated objects were calibrated using Moon and planets (Figure 2).

	Init. Iter. 1	**Init. Iter. 2**	**Init. Iter. 3**	**Scale iter. 1**
A0	-0.05496	-0.05533	-0.05536	-0.05519
X0	0.003959	0.001482	0.002604	0.004808
Y0	0.002279	0.003547	0.001767	-0.00323
V	0.576411	0.575852	0.574763	0.575284
S	-0.18599	-0.18415	-0.18064	-0.18175
D	0.25	0.25	0.25	0.25
EPS	0.004856	0.004348	0.005294	0.008230
E	4.907745	4.579636	4.703682	4.833792
A	0.003638	0.003646	0.003574	0.003884
F	0.912314	0.765284	0.705125	0.541376
P	0.00045	0.00045	0.00045	0.00045
Q	0.366	0.366	0.366	0.366
C	1	1	1	1
Sigma	0.07453	0.03814	0.03529	0.03326
sca.X	0.004946	0.004946	0.004946	0.004946
sca.Y	0.004994	0.004994	0.004994	0.004989

Table 1 – Excerpt from the RS iteration table. Observe the change of sigma during the iterations. Also, during the scale iterations, the scale Y is systematically changed until sigma is below 0.05. In this case, this was already the case, so only one iteration was performed, which still improved the constants.

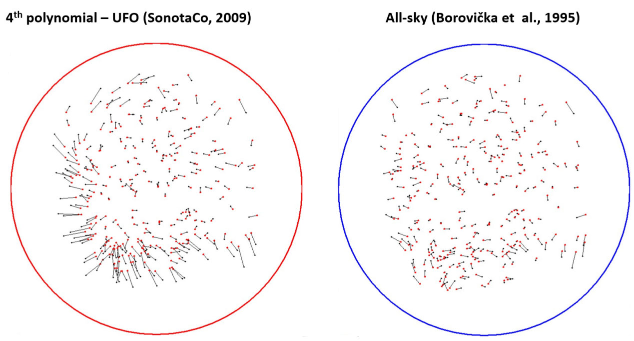

Figure 1 – The comparison of UFO and RS astrometric reduction. Bars represent differences O-C.

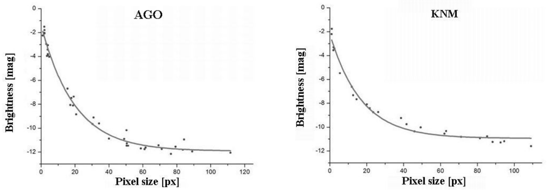

Figure 2 – Brightness calibration curves from stations AGO and KNM, where pixel size of the Moon, Venus, Jupiter and Mars and its brightness (Zsilinszká, 2018).

3 MT – A tool for meteor trajectories and more

The software MT was already introduced on previous IMC (Kornoš et al., 2015; Kornoš et al., 2017). Briefly, it is a GUI tool for calculating and visualizing trajectories and orbits of meteors in Earth's atmosphere and Solar system from multiple-station observations. The current version of the program includes calculation of:

1. Atmospheric trajectory and velocity,
2. Solar system orbit,
3. Photometric mass,
4. Dark flight and impact,
5. Monte Carlo simulation of errors.

The program is written in Lazarus/Object Pascal and can be run under Windows as well as Linux systems. Numerical simulations and graphical outputs are produced in R.

Current version has been modified to run on Linux machines. Additionally, we are working on improving the precision of the photometric mass by calibrating meteor magnitude based on the background stars (see RS).

4 MT – Photometric mass

We implemented the complete equation (1) in computing the photometric mass (usually, the deceleration part is omitted). The equation is solved iteratively, with the first iteration omitting the second, deceleration part. Subsequent iterations are based on the approximation of the photometric mass from the previous one. We observed that the iterations converge to a stable value within 10 iterations (Figure 3).

$$I = \tau \frac{v^2}{2} dt \frac{dm}{dt} - \omega m v \frac{dv}{dt} \qquad (1)$$

5 Acknowledgement

This work was supported by grant APVV-16-0148 and VEGA 1/0596/18.

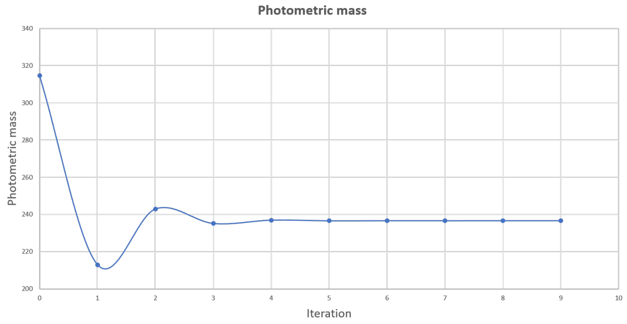

Figure 3 – Convergence of photometric mass during ten iterations.

References

Borovička J., Spurný P., and Keclíková J. (1995). "A new positional astrometric method for all-sky cameras.". *Astronomy and Astrophysics Supplement Series*, **112**, 173.

Ceplecha Z. (1987). "Geometric, dynamic, orbital and photometric data on meteoroids from photographic fireball networks". *Bulletin of the Astronomical Institutes of Czechoslovakia*, **38**, 222–234.

Kornoš L., Ďuriš F., and Tóth J. (2015). "Astrometric precision and orbit determination by AMOS". In *Proceedings of the International Meteor Conference, Mistelbach, Austria.* pages 27–30.

Kornoš L., Ďuriš F., and Tóth J. (2017). "AMOS orbit software and EDMOND database". In *Proceedings of the International Meteor Conference, Petnica, Serbia.*

SonotaCo A. (2009). "Meteor shower catalog based on video observations in 2007–2008". *WGN J. Int. Meteor Org.*, **37**, 55–62.

Tóth J., Kornoš L., Vereš P., Šilha J., Kalmančok D., Zigo P., and Világi J. (2011). "All-sky video orbits of Lyrids 2009". *Publications of the Astronomical Society of Japan*, **63:2**, 331–334.

Tóth J., Kornoš L., Zigo P., Gajdoš Š., Kalmančok D., Világi J., Šimon J., Vereš P., Šilha J., Buček M., et al. (2015a). "All-sky Meteor Orbit System AMOS and preliminary analysis of three unusual meteor showers". *Planetary and Space Science*, **118**, 102–106.

Tóth J., Zigo P., Kalmančok D., Šimon J., Kornoš L., Világi J., Rudawska R., Serra-Ricart M., Perez J. C., and Licandro J. (2015b). "5 months of AMOS on the Canary Islands". In *International Meteor Conference Mistelbach, Austria.* pages 63–65.

Zsilinszká L. (2018). "Photometric calibration of AMOS system". *Diploma thesis, FMFI UK.*

AMOS cameras status

Juraj Tóth, Leonard Kornoš, Pavol Zigo, Dušan Kalmančok, Jozef Világi, Jaroslav Šimon, Jiří Šilha, Pavol Matlovič, Peter Vereš

Dept. of Astronomy, Physics of the Earth and Meteorology, Faculty of Mathematics, Physics and Informatics, Comenius University in Bratislava, Slovak Republic

toth@fmph.uniba.sk

We describe the status of AMOS installations and future plans in the aim of building a global network of meteor cameras.

1 Introduction

AMOS (All-sky Meteor Orbit System) is an intensified all-sky meteor video system originally developed for the Slovak Video Meteor Network in 2007 at the Astronomical and Geophysical Observatory (AGO) Modra, Comenius University (Tóth et al., 2011; Zigo et al., 2013). Currently, four stations are operated in Slovakia, two cameras were installed on the Canary Islands in March 2015 (Tóth et al., 2015). A pair of AMOS cameras were installed in Chile in March 2016 (Tóth and Kaniansky, 2016) for the permanent meteor activity monitoring of the southern sky. AMOS cameras were continuously updated from the first prototype of the optical part in 2007 equipped by analog cameras with a plastic outer shell. Currently, digital cameras DMK with resolution 1600 $\times$ 1200 pixels and 20 fps are used, which corresponds to a field of view 180 $^\circ$ $\times$ 140 $^\circ$ and limiting sensitivity comparable to human eye (+5.5 mag. for stellar objects, +4 mag. for meteors and other moving targets). Also the aluminum outer shell was updated with light, rain, temperature and humidity sensors to operate cameras fully autonomously at distant locations.

2 Meteor observations

AMOS cameras are operated continuously through the whole year to monitor meteor activity even during the full moon phase. A single AMOS station usually detects 10 000 – 20 000 meteors per year. Depending on weather conditions and distance between stations (Slovakia average 90 km, Canary Islands 147 km, Chile 83 km), simultaneous detections are on the level of 30-40%. We are working on new detection software and meteor trajectory and orbits (Ceplecha, 1987; Borovicka et al., 1995; Kornoš et al., 2017) program. Also, each site of the network is equipped with a spectral camera.

3 Future plans

Currently, we are developing AMOS stations on the Hawaii islands and plan to find a suitable place and collaborators in Australia and Namibia (Figure 1, blue crosses). The aim is to develop a global network for 24 hour continuous monitoring of the influx of relatively faint meteors and characterization of weak meteor showers (Rudawska et al., 2015).

Acknowledgement

This work was supported by grant APVV-16-0148 and VEGA 1/0596/18 and by operation of AMOS cameras by colleagues from AGO Modra and students work. Many thanks to Alain Maury in SpaceObs and to Silvia Lisoni in Paniri Caur Chile. https://fmph.uniba.sk/daa

References

Borovicka J., Spurny P., Keclikova J. (1995), "A new positional astrometric method for all-sky cameras". *Astronomy and Astrophysics Suppl. Ser.*, **112**, 173

Ceplecha Z. (1987), "Geometric, dynamic, orbital and photometric data on meteoroids from photographic fireball networks". *Bulletin of the Astronomical Institutes of Czechoslovakia*, **38**, 222–234

Kornoš L., Ďuriš F., Tóth J. (2018), "AMOS orbit software, EDMOND database". *M. Gyssens, J.-L. Rault (eds.): Proc. Int. Meteor Conference, Petnica, Serbia, 21-24 September 2017*, IMO, 46–49.

Rudawska R., Matlovič P., Tóth J., Kornoš L. (2015), "Independent identification of meteor showers in EDMOND database". *Planetary and Space Science*, **118**, 38–47.

Tóth J., Kaniansky S. (2016), "Expedition Atacama-project AMOS in Chile". *A. Roggemans, P. Roggemans (eds.): Proc. Int. Meteor Conference Egmond, the Netherlands, 2-5 June 2016*, IMO, 295–296.

Tóth J., Kornoš L., Vereš P., Šilha J., Kalmancok D., Zigo P., Világi J. (2011), "All-sky video orbits of Lyrids 2009". *Publications of the Astronomical Society of Japan*, **63**, 331–334.

Tóth J., Zigo P., Kalmancok D., Simon J., Kornos L., Világi J., Rudawska R., Serra-Ricart M., Perez J.C., Licandro J. (2015), *J.-L. Rault, P. Roggemans (eds.): Proc. Int. Meteor Conference, Mistelbach, Austria*, IMO, 63–65.

Zigo P., Tóth J., Kalmančok D. (2013), "All-Sky Meteor Orbit System (AMOS)". *M. Gyssens, P. Roggemans (eds.): Proc. Int. Meteor Conference, La Palma, Canary Islands, Spain, 2012*, IMO, 18–20.

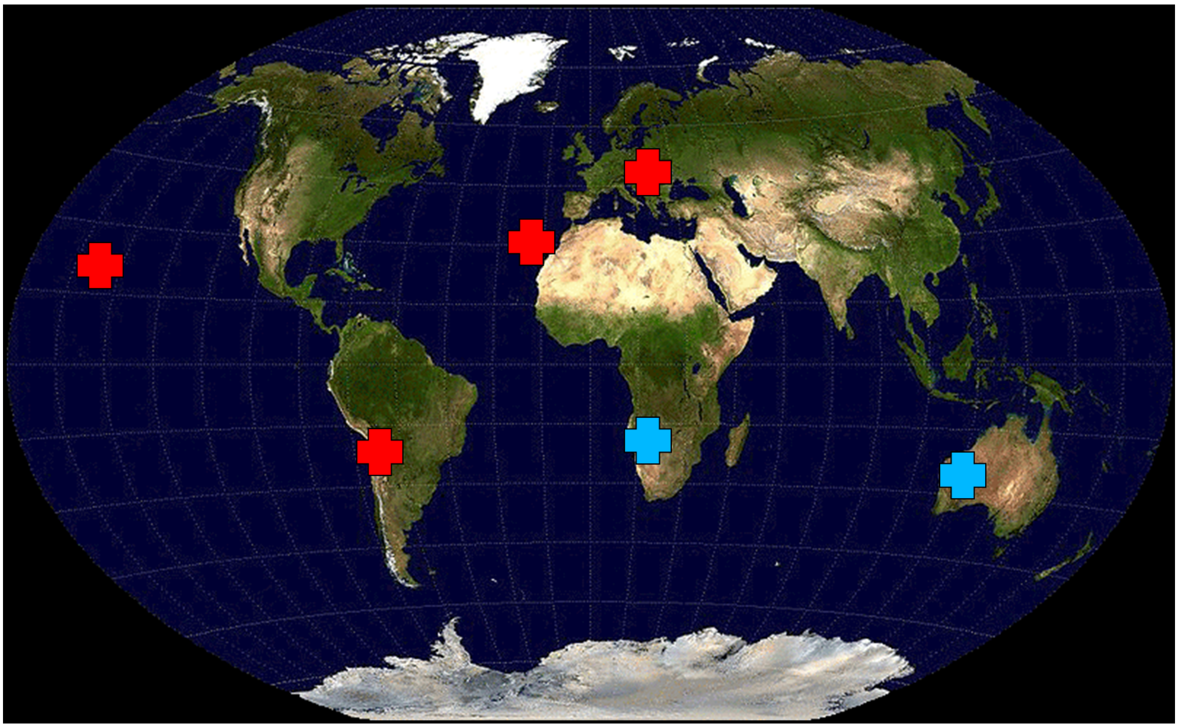

Figure 1 – Current state of the AMOS system global network. In red, operating stations in Slovakia (4 stations), Canary Islands (2 stations), Chile (2 stations) and Hawaii (2 stations). In blue, planned expansion of the network in Australia and Namibia.

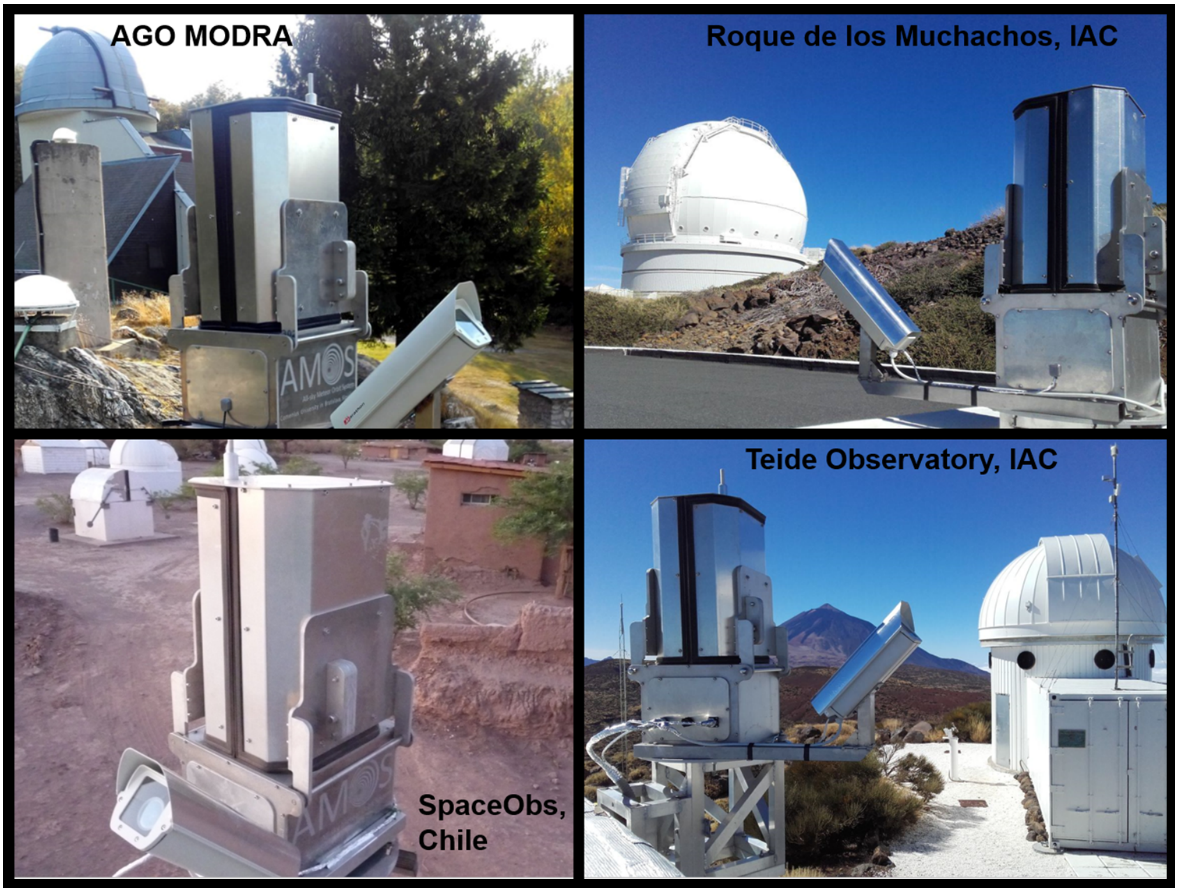

Figure 2 – Examples of AMOS system installations with spectral cameras at AGO Modra, Roque de los Muchachos and Teide Observatrory, IAC at Canary Islands and San Pedro de Atacama, Chile.

Towards an autonomous BRAMS network

S. Calders[1], H. Lamy[1], M. Anciaux[1], S. Ranvier[1], A. Martinez-Picar[2], C. Verbeeck[2]

[1] **Royal Belgian Institute for Space Aeronomy, Brussels, Belgium**
`Stijn.Calders@aeronomie.be`

[2] **Royal Observatory of Belgium, Brussels, Belgium**

The BRAMS (Belgian Radio Meteor Stations, `http://brams.aeronomie.be`) network consists of one transmitter in the south of Belgium (Dourbes) and about 25 receiving stations spread all over the country. At the start of the project in 2010, the observations were sent once per month on a USB stick to the Royal Belgian Institute for Space Aeronomy (BIRA-IASB, `http://www.aeronomie.be`). Nowadays the observations of most receiving stations are copied automatically to BIRA-IASB's FTP server. The BRAMS researchers and station owners use the data availability tool that shows a color-coded timeline per station, where the color indicates the (un)availability of observations.
In this paper we will investigate how we can further improve the BRAMS network management, with the ultimate goal to construct an autonomous BRAMS network: a network that runs with minimal human intervention. We want to go to a (semi-)automatic system to transfer, archive, access, assess the reliability and quality of the data and process observations.
Firstly we will investigate which parameters (e.g. the noise level or the intensity of the calibrator and the direct beacon signal) are relevant as a health status of a receiving station. Then we will analyze the evolution of those parameters, either by looking at time series for a single station (temporal evolution) or by comparing the measurements with nearby stations. Finally if a diminution of a station's performance is detected, action can be taken: either by sending an automated email to the BRAMS team, or (after sufficient testing) by automatically adjusting a receiver's settings. Our last idea will however require the replacement of the current analog receivers by SDR (software defined radio) receivers.

1 Introduction

The BRAMS (Belgian RAdio Meteor Stations, `http://brams.aeronomie.be`) network consists of about 25 receiving stations spread all over the Belgian territory (as shown in Figure 1) and a single radio transmitter installed at the Geophysical Centre of the Royal Meteorological Institute (RMI) in Dourbes (Calders & Lamy, 2014; Lamy et al., 2015). This radio transmitter emits a sine wave with circular polarization at a frequency of 49.97 MHz and with a constant power of 150 W. At each receiving station, the signal is sampled with a frequency of 5512 Hz, providing a bandwidth of 2.5 kHz. Data are saved as WAV (sound) files every 5 minutes.

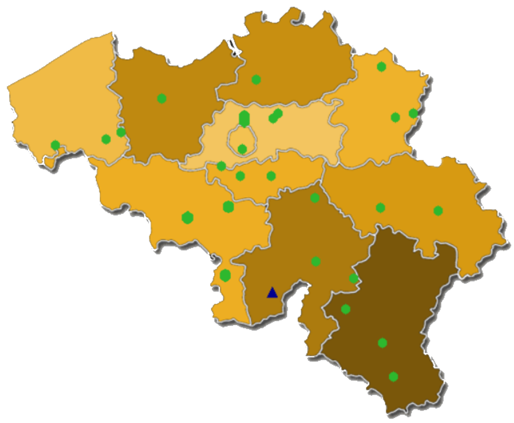

Figure 1 – The blue triangle in the south of Belgium is the radio beacon situated in Dourbes. The green dots spread along the country are the receiving stations.

Monitoring manually the health status of each BRAMS receiving station is very labor intensive. Therefore we investigated how we can improve the BRAMS network management, with the ultimate goal to construct an autonomous BRAMS network: a network that runs with minimal human intervention. We want to go to a (semi-) automatic system to transfer, archive, access, assess the reliability and quality of the data and process observations.

2 Method

Since 2015 all receiving stations are equipped with a calibrator (Lamy et al., 2015). The goal is twofold: monitor the gain and frequency offset/drift of each station, and identify sudden jumps or anomalous behavior. This is achieved by feeding a signal of a known frequency (49.97050 MHz) and amplitude (<-130dBm or 10-16 W) into the front end. Figure 2 is a schematic of the receiving chain of a BRAMS station while Figure 3 shows the calibrator and how it is inserted in the reception chain.

The internal frequency reference using a Temperature Controlled Crystal Oscillator (TCXO) ensures a much better frequency stability (a few Hz) than the local oscillator (LO) in the receiver. Since the signals of the BRAMS calibrator and from the antenna are combined in front of the receiver, the frequency drift of the LO affects both signals in the same way.

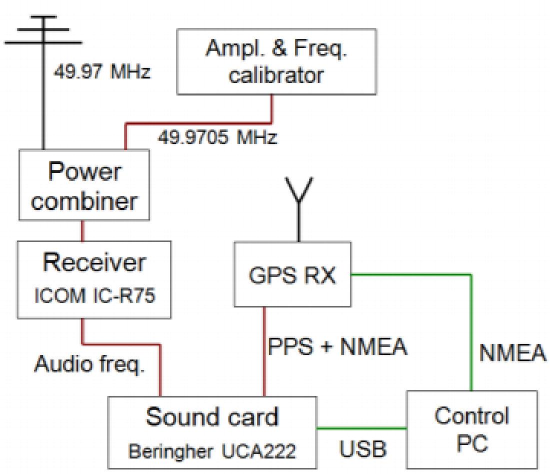

Figure 2 – Schematic of the reception chain of a BRAMS station including the calibrator

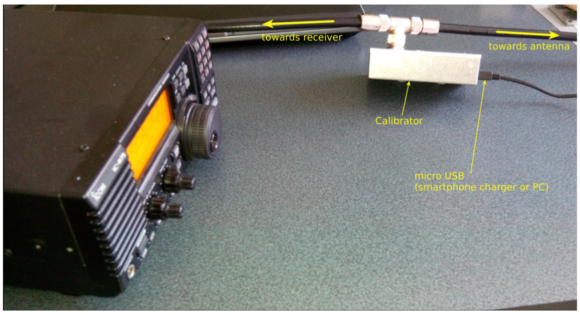

Figure 3 – The calibrator injects a very stable signal close to the receiver. This allows us to monitor the receiver's performance through time

This setup allows us to monitor the quality of the receiver and the soundcard in a very simple and objective way by following the temporal evolution of the calibrator's power and frequency. A major drawback of this method is that the status of the antenna and the coax cable is not monitored.

All other methods that we have considered, e.g. monitoring the variations in the beacon power and frequency, have been proven far more complicated and were thus discarded.

3 Results

We first look at the calibrator's frequency, as recorded by the PC (i.e. after the down sampling to an audible signal by the receiver and the digitalization by the soundcard).

Most of the stations are basic receiving systems consisting of a single 3-element Yagi antenna, a single receiver (ICOM IC-R75), an amplitude and frequency calibrator (developed at BISA), a GPS clock, a sound card and a PC. However in Humain an interferometer has been built (Lamy et al., 2017). It comprises five 3-elements Yagi type (standard BRAMS) antennas which allow applying interferometric techniques over the data recorded by the receivers connected to each antenna. In order to accurately measuring phase differences between the signals, these receivers are connected to a common GPS-controlled 10 MHz reference oscillator. Therefore the frequency drift of this interferometer is very small (<1 Hz) compared to any other station (e.g. the one in Uccle) as shown in Figure 4.

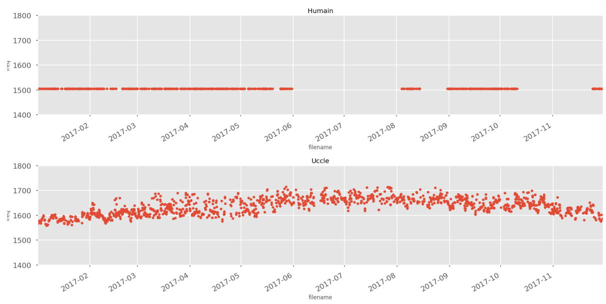

Figure 4 – The frequency drift of the interferometer station in Humain is small compared to any other receiving station (in this example Uccle).

The main cause for the frequency drift of the Uccle station are the temperature variations (see Figure 5).The Pearson correlation coefficient between the temperature and the frequency drift for this receiving station is 0,88.

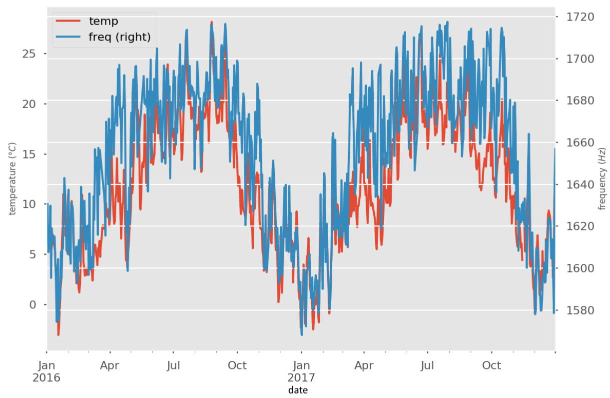

Figure 5 – There is a strong correlation between the temperature and the frequency drift for the BRAMS receiving station in Uccle (ρ =0,88).

We have also looked at the power of the calibrator as recorded by the receiving station in Ottignies in 2016-2017. It shows that it is constantly decreasing. On 16 September 2017 the receiver broke and has been replaced. After replacement, the calibrator power returned to its original level. It teaches us that monitoring the power output of the calibrator (as measured by the sound card) is probably a good indication for the receiver's status.

The remaining outliers after replacing the receiver are due to discrete jumps in the frequency of the calibrator. The frequency jumps of the calibrator at the stations is a direct effect of the temperature compensation on the TCXO (temperature compensated crystal oscillator).

4 Conclusions and further work

The ultimate goal is to construct an autonomous BRAMS network: a network that runs with minimal human in-

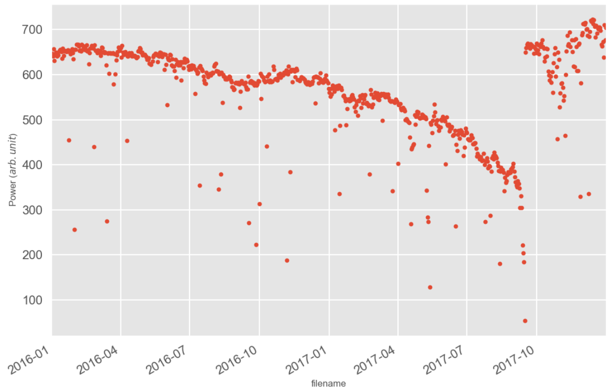

Figure 6 – The power of the calibrator as recorded for the BRAMS station in Ottignies. On 16 September 2017 the receiver broke and has been replaced.

tervention. This requires an automated way to monitor the health status of all BRAMS receiving stations.

We have investigated different methods and parameters. Following the variations of the calibrator's frequency and power has proved to be a powerful yet easy way to monitor the health status of the receiver and the soundcard. However one should bear in mind that this does not cover potential issues with the antenna or the coax cable.

In the results section of this paper, it has been shown that there is a strong correlation (ρ =0,88) between the frequency drift and the temperature for simple BRAMS receiving stations. This is due to a well-known temperature dependency of the LO in the ICOM IC-R75 receiver. The receivers of the interferometer in Humain are connected to a common GPS controlled 10 MHz reference oscillator, and are thus much less sensitive to temperature variations.

The ICOM IC-R75 receiver in Ottignies failed on 16 September 2017 and was replaced subsequently. It has been demonstrated that the received power from the calibrator was already decreasing since April 2016. Since the power of the calibrator is very stable, this is an indication that the receiver (or the soundcard) was deteriorating and it could have been replaced during a preventive maintenance.

In the future, the whole chain from the calibrator to the PC could be calibrated with an accurate signal generator to be able to measure precisely the absolute power of an incoming signal. One could consider to assess also the antenna and the coax cable by monitoring the number of echoes received by a given station over time. On long term this should be rather constant. One can also compare the number of echoes recorded between stations.

Finally automatic actions could be taken based on the frequency and power measurements of the calibrator: either by sending an automated email to the BRAMS team, or (after sufficient testing) by automatically adjusting a receiver's settings.

Acknowledgement

The BRAMS network is a project from the Royal Belgian Institute for Space Aeronomy and partially funded by the Solar-Terrestrial Center of Excellence (STCE). Last but not least: no observations without volunteers hosting the BRAMS receiving stations. The authors are grateful for their constant support.

References

Calders S. and Lamy H. (2014). "Automatic detection of meteors in the BRAMS data". In *Proceedings of the International Meteor Conference, Giron, France,* 18–21.

Lamy H., Anciaux M., Ranvier S., Calders S., Gamby E., Martinez Picar A., and Verbeeck C. (2015). "Recent advances in the BRAMS network". In *Proceedings of the International Meteor Conference Mistelbach, Austria,* 171–175.

Lamy H., Tetard C., Anciaux M., Ranvier S., Martinez Picar A., Calders S., and Verbeeck C. (2017). "Observations of the Geminids 2016 with the BRAMS radio interferometer". In *Proceedings of the International Meteor Conference, Petnica, Serbia, 21-24 September 2017,* 132-137.

Martínez Picar A., Marqué C., Verbeeck C., Calders S., Ranvier S., Gamby E., Anciaux M., Tetard C., and Lamy H. (2016). "Numerical simulation of the BRAMS interferometer in Humain". In *Proceedings of the International Meteor Conference Egmond, the Netherlands, 2-5 June 2016,* 175–178.

The first confirmed lunar impact flash observed from Brazil

David Duarte[2], Lauriston Trinidade[1], Marcelo Zurita[1,3], Romualdo Caldas[1,2], Marcelo Domingues[1]

[1] **BRAMON – Brazilian Meteor Observation Network**

[2] **CEAAL – Centro de Estudos Astronômicos de Alagoas**

[3] **Associação Paraibana de Astronomia**

david.duarte.br@gmail.com and lauriston.lauriston@gmail.com and marcelozurita@gmail.com and romualdoarthur@gmail.com and ayatola@gmail.com

During the Geminids meteor shower in 2017, a campaign organized by BRAMON (Brazilian Meteor Observation Network) called on Brazilian amateur astronomers to monitor the Moon during the shower's peak night. Several people across the country set up their observation points and two teams, one in Araruna in Paraíba and another in Maceió in Alagoas, managed to register at 07:13:46 (UTC) on December 14, 2017, at the selenographic coordinates of 9.9° N and 45.4° E. This was the first impact lunar flash confirmed on video by Brazilian observers.

1 Introduction

Planet Earth is bombarded daily by dozens of tons of debris from space that enter its atmosphere and can be seen in the form of meteors (Murad and Williams, 2002). It is no different on the Moon. Space rocks may strike it at any moment, but since it has no atmosphere, the impact on its surface is direct, generating flashes that are commonly called TLP, or Transient Lunar Phenomena (Kim et al., 2015).

During a meteor shower, the likelihood of observing a TLP increases considerably (Rembold and Ryan, 2015), and it was during one such shower, the 2017 Geminids, that the National Lunar Impact Observing Campaign was launched in Brazil in order to monitor the Moon's surface on the day of the shower's peak and to detect possible meteoroid impacts on its surface.

The campaign was conceived when members of BRAMON (Brazilian Meteor Observation Network) realized that the Moon's altitude and phase during the shower's peak would place it in a privileged position for impact observation, according with Figure 1.

2 Organizing the Campaign

Once it was established that the window of opportunity would be on December 14th 2017, the campaign's organization got started and Brazilian amateur astronomers were called upon to take part in the event.

Live broadcasts were held to address technical aspects and communicate the event, explanatory texts about the campaign were shared on social media to gather the highest number of participants, and supporting material was put together for those who were interested in participating.

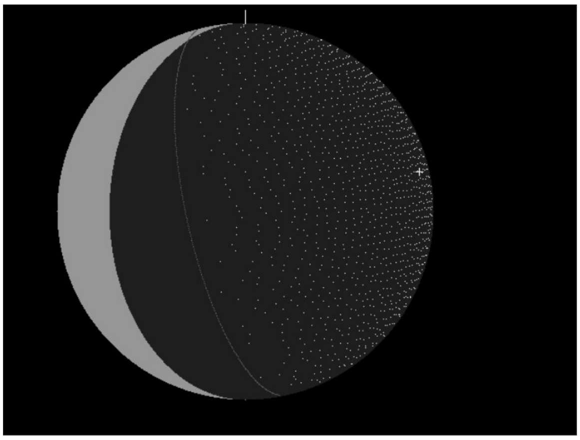

Figure 1 – Prediction of impact geometry for December 14, 2017 – generated by LunarScan 2.00

3 Methodology

To determine whether a lunar impact has actually occurred, the same phenomenon must be watched by two independent observers placed at different locations far from each other. This will eliminate the possibility of it not having occurred on the satellite's surface, but being otherwise caused by cosmic rays, satellite flares, meteors and other phenomena.

In order to confirm that the phenomenon seen by two different observers is really a TLP, a few criteria have to be met:

- Both events must have occurred at the same moment, which requires time synchronization between the computers used to perform the observations.
- Both events must have occurred on the same region of the lunar surface.
- Both events must have similar duration and magnitude when observed under the same conditions,

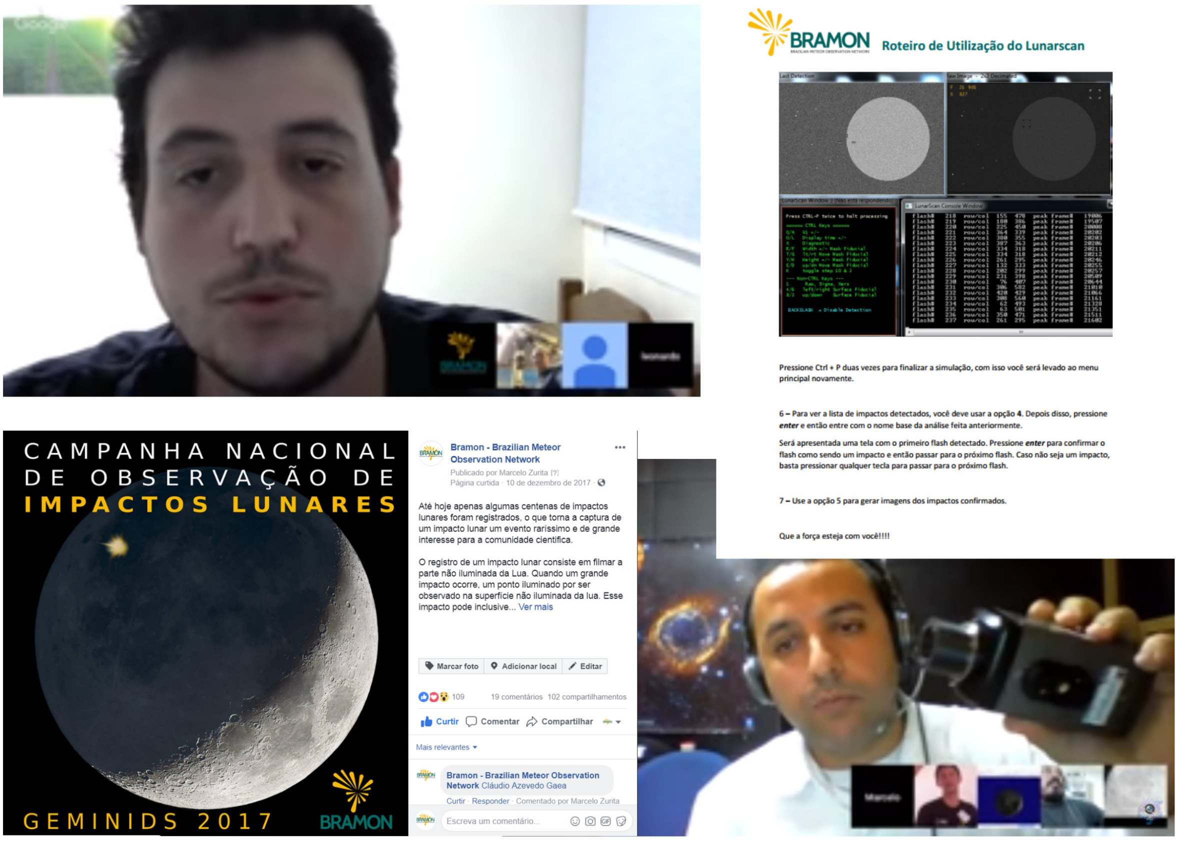

Figure 2 – Live broadcasts, call to amateurs in social media and LunarScan Tutorial in Portuguese

or after calibration when under different conditions.

The minimum equipment required to collect data is:

- A video camera or astronomical CCD with a frame rate of at least 24 frames per second.
- A minimum resolution of 640 × 480 pixels.
- A telescope equipped with automatic sidereal tracking.
- A computer with a fair amount of disk space.

Software used to capture and compress data:

- SharpCap (or equivalent) – Imaging.
- NTP (Network Time Protocol) – Time synchronization.
- LunarScan – Automated TLP search.

4 Results

Despite the unfavorable weather conditions, some observers managed to implement the TLP search with footage of the Moon recorded during much of the stipulated period. Among the observers, Marcelo Zurita (APA/BRAMON) as well as Romualdo Caldas (CEAAL/BRAMON) and David Duarte (CEAAL) succeeded in capturing a flash on the Moon's surface at 07:13:46 UT on Dec 14, 2017, caused by an impact at the selenographic coordinates of 9.9° N and 45.4° E.

David Duarte and Romualdo Caldas, from the city of Maceió, in the state of Alagoas, Brazil, at the geographical coordinates of 9°37'14.1" S and 35°43'12" W, at a height of 45 m had recorded the flash using a 200mm F/10 Schmidt-Cassegrain Telescope (MEADE LX90-SC 8-inch) with the computerized mount NexStar 8SE and ZWO ASI 1600MM-Cool camera, which is monochrome and cooled, bearing a 4/3" CMOS sensor working at 5 frames per second in 1320 × 1320 resolution.

Marcelo Zurita, from the city of Ararura, in the state of Paraíba, Brazil, at the geographical coordinates of

Figure 3 – Setups used in Moon footage. Left: Skywatcher 130mm F5 + Samsung SCB 2000 camera. Right: Meade LX80 8" + ASI 1600 CCD

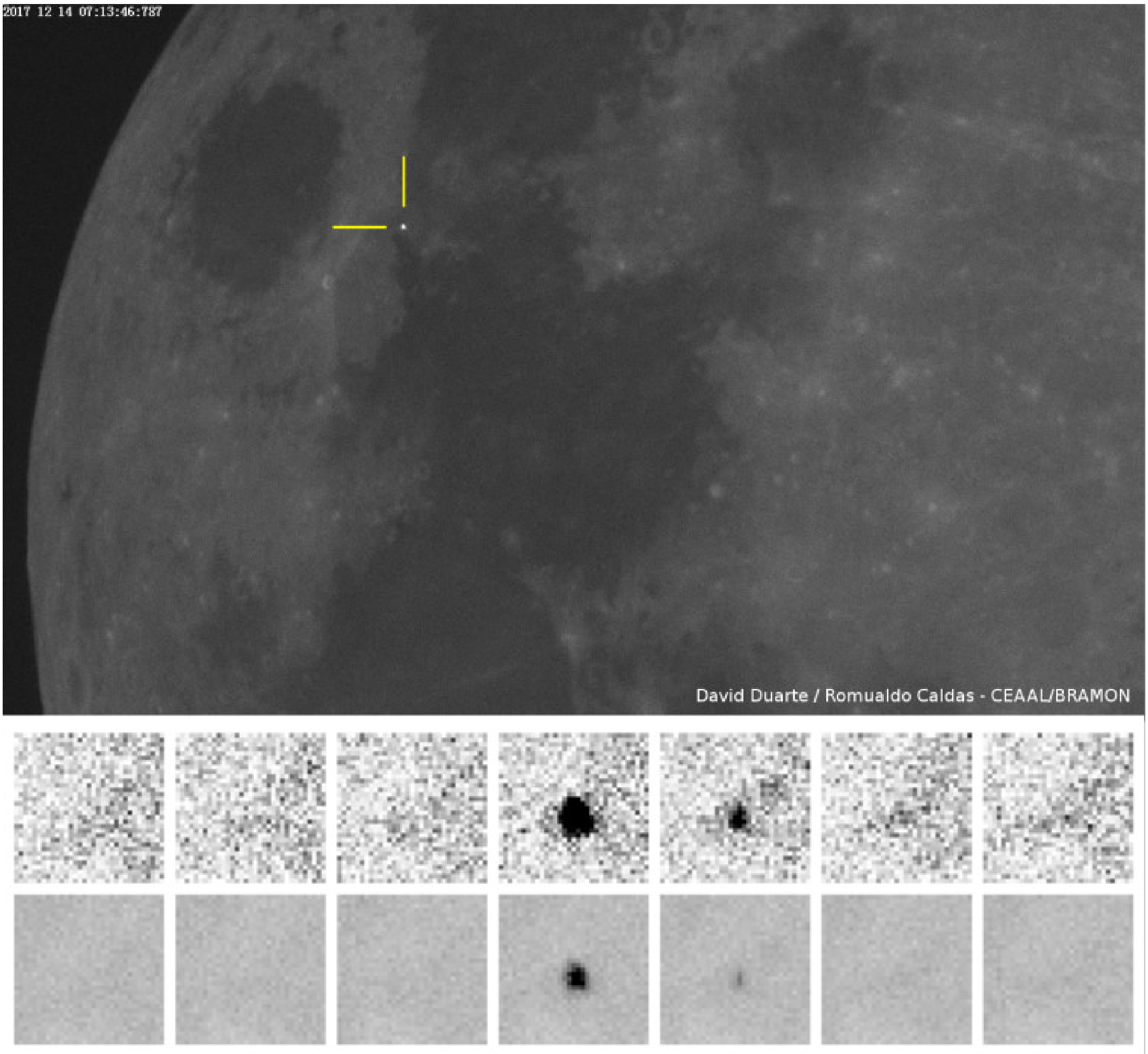

Figure 4 – Observer A: David Duarte (CEAAL) & Romualdo Caldas (CEAAL/BRAMON). Observer's Site: Maceio, AL, Brazil / Lat: -9.6205, Long: -35.7200. Instruments: Schmidt Cassegrain MEADE 8" + ASI 1600 Mono Cooled Camera.

6°27'8.28" S and 35°40'23.52" W, at a height of 185 m had recorded the flash using a 130 mm F/5 Newtonian Telescope (Skywatcher 130) with the motorrized mount Orion EQ3-2 and a modified Samsung SCB 2000 security camera (without IR filter), bearing a 1/3" CCD sensor working at 30 frames per second in 720 × 480 resolution.

A detailed analysis of impact location was made by amateur astronomer Avani Soares. The high resolution images of LRO (Lunar Reconnaissance Orbiter) available in NASA website[1] was superposed with flash image recorded by David Duarte and Romualdo Caldas resulting in location pointed in Figure 6:

Both videos was analyzed to extract light curve based in three reference stars recorded during moon monitoring session. The resulting brightness of flash was calculated to 7.1 magnitude and the light curve is shown in Figure 7.

[1]https://lunar.gsfc.nasa.gov/

5 Next Steps

All the data collected are being analyzed to obtain more detailed information about this first recorded impact. A request was sent to NASA to get new images on impact area through LRO. From these images it will be possible to search for a probable new small crater originating from this event.

Based on the success of the first campaign, another 3 efforts were scheduled for 2018, for Lyrids on April 21 and 22, Perseids on August 13 and 14 and for the Geminids on December 14. Thus comes enhancing the technique, gathering more observers and encouraging lunar observation and TLP searching.

Figure 5 – Observer B: Marcelo Zurita (APA/ BRAMON). Observer's Site: Araruna, PB, Brazil / Lat: -6.4523°; Long: -35.6732°. Instruments: 130mm f/5 newtonian + SCB 2000 Camera.

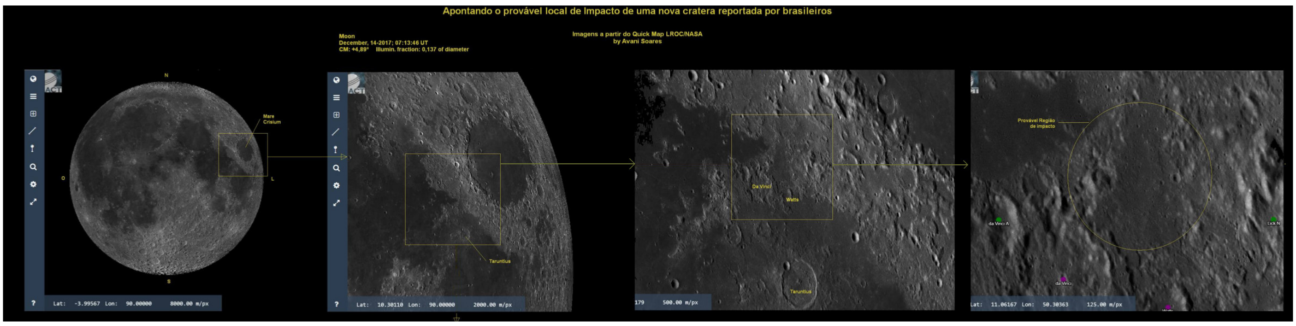

Figure 6 – Pointing the probable impact location Produced by Avani Soares, a Brazilian amateur astronomer from LRO images

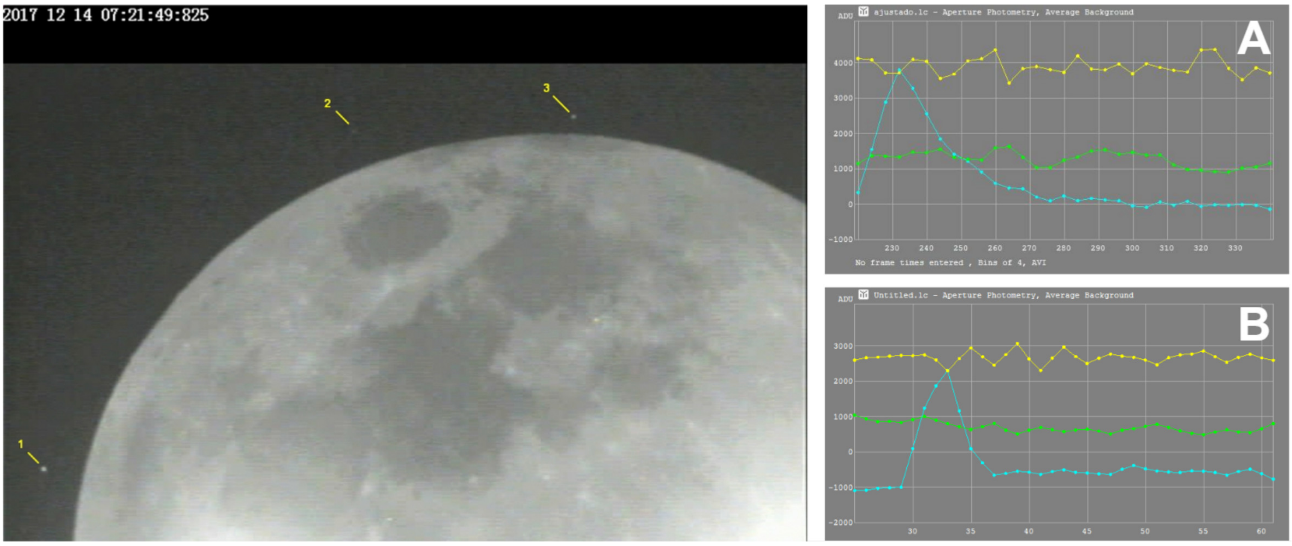

Figure 7 – Left: Reference Stars used to determination of impact flash magnitude. Right: Photometric analysis showing typical light curve of a lunar impact for both observers (A: David Duarte & Romualdo Caldas; B: Marcelo Zurita)

References

Kim E., Kim Y.H., Hong I-S., Yu J., Lee E., Kim K. (2015), "Detection of an impact flash candidate on the Moon with an educational telescope system". *Journal of Astronomy and Space Sciences*, **32**, 121–125.

Murad E., Williams I.P. (2002), "Meteors in the Earth's Atmosphere: Meteoroids and Cosmic Dust and Their Interactions with the Earth's Upper Atmosphere". *Cambridge University Press*.

Rembold J.J., Ryan E.V. (2015), "Characterization and analysis of near-earth objects via lunar impact observations". *Planetary and Space Science*, **117**, 119–126

Automation of a video meteor network

Vladimir Nikolić[1]

[1] **Petnica Meteor Group, Petnica, 14104 Valjevo, Srbija**
vladimir.nik94@gmail.com

In an effort to automate the Petnica Meteor Group video network, we have implemented a system in which stations periodically send various data to the central server for convenient monitoring and automatically turn cameras on at night and off in the morning. The system is still in an alpha stage, and is right now a proof of concept. This paper describes only the software aspect of the system.

1 Introduction

As a meteor observing network grows, there is a need for a scalable solution for maintaining the stations. If something on a station goes wrong, it is helpful to have a way to know that without inspecting the station manually. Moreover, having a complete overview of the whole network with information for each station helps maintainers keep everything in check. This is the goal we aim to achieve, and this paper presents what we have so far.

2 How it works

There are three main components of the system:

- Central server
- Station computer
- Camera microcontroller and power supply

2.1 Central server

The central server hosts a web interface for the stations and a database with all the gathered information. When stations start their code, they automatically register at the server and wait for approval of registration at the central server. After that, the server continually listens for status reports from the stations and updates the information accordingly. Right now, the status information transmitted includes:

- Disk usage and capacity
- Humidity and temperature of the camera compartment
- Whether the power supply is on and voltage on the camera

The server stores the history of this information in the database and displays plots on the web interface. In case a station fails to send a status message within a given time frame, the server shows a message on the web interface to alert the maintainers.

2.2 Station computer

Station computers in our networks use UFO Capture[1] to record meteors. Alongside UFO Capture, we run our code that handles data transmission to the server and communication with the microcontroller that manages the camera and power supply.

Upon starting, the station code user is asked for basic station information, such as station name, coordinates, and maintainer's contact information. After that, the code periodically does the following:

- Queries the microcontroller for sensor data
- Checks whether it is night or day, and accordingly opens the shutter and turns the camera on, or closes the shutter and turns the camera off, respectively
- Tries to upload gathered data to the server

If any error occurs, the error message is transmitted to the server and the code restarts itself. It is also capable of updating itself with the latest version available on the server, as new features are introduced.

2.3 Camera microcontroller and power supply

The microcontroller that manages the camera and the power supply is connected via USB to the station computer and continuously listens for instructions. Right now, it is capable of:

- Controlling a servo that opens or closes the camera shutter
- Turning the camera on or off
- Measuring humidity and temperature in the camera compartment
- Measuring voltage on the camera

The microcontroller does not do any of these by itself, but instead upon a request from the station computer, which handles the logic of when to perform each action.

[1] http://sonotaco.com/

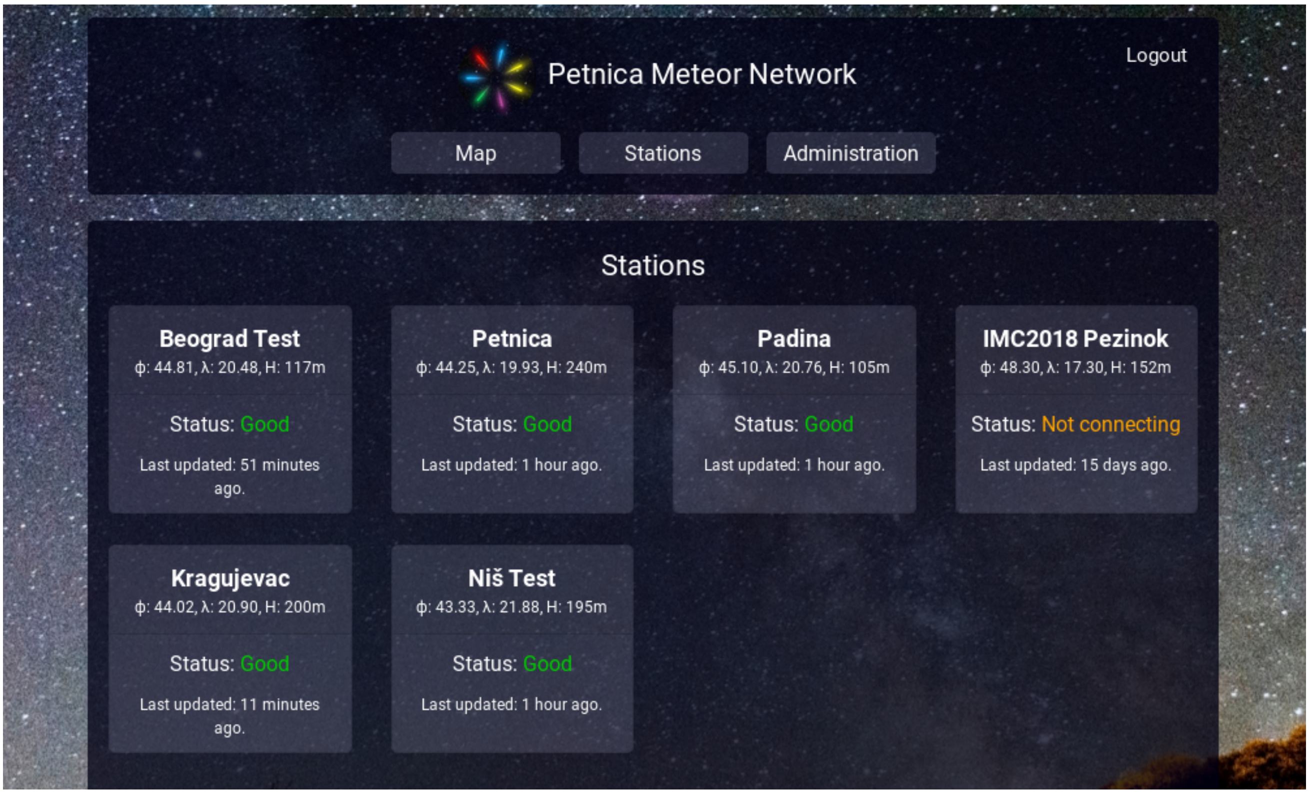

Figure 1 – Web interface showing a list of stations we used for testing.

Figure 2 – Introduction message upon starting station code.

3 Conclusions

This paper introduces our attempt of automating maintenance of meteor observing stations. It is in its early stages and serves to present our goals in making a robust system for observation. Some of the planned features that we want to implement in the future include:

- Filtering actual meteor data from spurious sightings, such as birds and planes
- Automatic upload of filtered data to the central server
- Email notifications to station maintainers for station problems or potential fireball sightings

Acknowledgements

This work has been done in close collaboration with Stevan Golubović from Petnica Meteor Group. Stevan has provided his hardware expertise to make a station prototype on which the code is running. His work is presented in another poster and paper from IMC 2018 and gives more context to the work presented here.

Starcounters - A Citizen Science Project for registering the meteor showers

Raquel Cedazo[1], Miguel R. Alarcon[2], Esteban Gonzalez[1], Miquel Serra-Ricart[3] and Samuel Lemes[3]

[1] **High School of Technical Industrial and Design Engineering. Universidad Politecnica de Madrid, C/ Ronda de Valencia, 3, 28012 Madrid, Spain**
raquel.cedazo@upm.es and egonzalez@ciclope.info

[2] **Universidad de la Laguna, C/ Padre Herrera, s/n, 38200, San Cristobal de La Laguna, Santa Cruz de Tenerife, Spain**
miguelrguez.alarcon@gmail.com

[3] **Instituto Astrofisico de Canarias, Calle Via Lactea, s/n, 38205 San Cristobal de La Laguna, Santa Cruz de Tenerife, Spain**
mserra@iac.es and SamuelLemesPerera@gmail.com

Starcounters, in Spanish *Contadores de Estrellas*, is a citizen science project that started in June 2018 with the aim to involve the general public on meteor counting. This paper explains the different ways for citizens, thanks to the use of the technologies, to be direct participants in the research led by professional astronomers, monitoring and helping to record the meteors in a simple, attractive and rigorous way.

1 Introduction

The observation of meteor showers is a very important work to answer key questions that still exist about the minor bodies of our Solar System. The majority of meteor showers have been studied and analyzed for years by professional astronomers, but even today, new showers continue to be discovered and predictions of existing ones are improved.

This project aims to develop a mobile application that will allow citizens not only to watch the meteor showers live, but also to be direct participants in the research carried out in this regard, helping to record information about the meteors in a rigorous but simple and attractive manner. Taking advantage of the importance of mobile technology in today's society and its degree of integration in our daily lives, this project wants to make meteor research a simple, global and interactive task, eliminating the barriers between the scientific process of quality and the general public.

Citizen science is a powerful tool to involve the general public in scientific tasks (Bonney et al., 2009). The most important indicator of a successful project is to build a community around it (Reeves et al., 2017).

In the field of Meteor Science, there is already a community of professional and amateur astronomers dedicated to the study of meteors using visual observations, radio detection or video detection.

Regarding visual observations, one of the main projects is the **IMO Visual Observations** where users report observations of meteors and fireballs. Data is visualized openly in Live ZHR Graphs from its website[1] and can be downloaded by registered users.

[1]Website: https://www.imo.net/members/imo_live_shower

NASA Meteor Counter[2] is another example of citizen science applied to the meteor domain. With an iPhone app, users will be able to report meteors with an intuitive interface. There are three levels of users based on their expertise.

These last two projects are focused in the acquisition of data reported by volunteers through visual observations. On the other hand, **Radio Meteor Zoo**[3] is a project where citizens can analyze images provided by the Belgian RAdio Meteor Stations (BRAMS).

One variant of visual observation is the detection of meteors using video cameras such as the IMO Video Meteor Network (Molau & Barentsen, 2014). This network combines algorithms and human validation to detect them. In our case, this detection will be carry out by the community.

But, in meteor detection, visual observations are not the only techniques used. Radio detection is also applied to detect meteors such as VVS (Steyaert, 2006), BRAMS[4], HRO (Maegawa, 1999) or another based on GRAVES radar.

In the next section it is explained how Starcounters deal with these different approaches.

2 Technical description

The project proposes four possible ways for citizens to participate, as it is represented in the Figure 1:

[2]Website: https://science.nasa.gov/science-news/science-at-nasa/2011/13dec_meteorcounter/
[3]Website: https://www.zooniverse.org/projects/zooniverse/radio-meteor-zoo
[4]Website: http://brams.aeronomie.be/

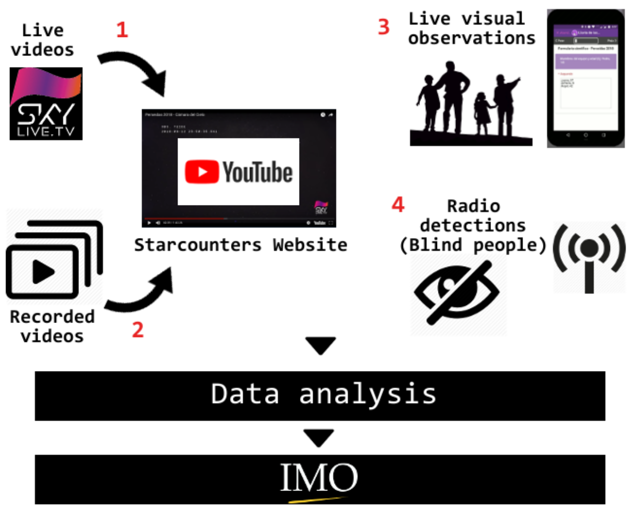

Figure 1 – Different ways to participate in Starcounters. The process shows how, after collecting the data, they will be analyzed and sent to the IMO.

1. Live videos.
2. Recorded videos.
3. Live visual observations.
4. Meteor radio detection.

2.1 Live videos

Visual observation is not always possible due to the calendar or weather conditions, so this project aims to solve these problems thanks to the existing technology. Citizens will even be able to follow live broadcasts and, also, click a button every time they watch a meteor.

The authors already have the sky-live.tv portal to make live broadcasts, which works over YouTube, and has a large set of followers in each astronomical event.

2.2 Recorded videos

Citizens will have at their disposal a large number of videos of previously recorded meteor showers. Furthermore, metainformation will be offered to the user to understand the different parameters that affect the calculation of the activity rate and that are necessary to take into account in the visual observation method (i.e.: time, location, radiant position, limiting magnitude...). From a web browser, the user can mark over the video itself the moments in which a meteor appears, draw its trajectory, as well as other interesting parameters to study these phenomena such as color, thickness and speed.

2.3 Live visual observations

The authors pretend to demonstrate that thanks to the collaboration of the general public it is possible to obtain the same results as with experienced amateurs and professional astronomers who report their visual observations to the International Meteor Organization (IMO), organism who makes global analyses of observations received world-wide, among one of their objectives.

The goal is, on the one hand, the automation of the data collection during an observation session through a smartphone, so that an inexperienced user could be guided through the procedure to be able to report the results. On the other hand, gamification techniques will be applied to make the meteor showers an event to participate with friends and family, being able to compete in an internal ranking and even win some prizes.

To achieve this, the designed app will integrate all the necessary procedures to complete a report, making an effort to use or design environments that facilitate the capture of data:

- **Detection times and location**. These data are easy to take with most current smartphones, so the user should not worry about it. Count distribution can be set automatically according to the characteristics of the meteor shower.
- **Radiant position, Limiting Magnitude and meteor shower**. We think that Google Sky Map technology is the best way for users to get used to night sky orientation. For this, we will use the free app Loss Of The Night that integrates the functions of location and stellar mapping and, in addition, allows us to estimate the Limiting Magnitude of the observer through the search of several stars in the sky. This technique has been tested during the Perseids 2018 campaign and its conclusions are presented in the next section.
- **Magnitude distribution**. This is one of the great impediments of the application because it is not easy for inexperienced users to accurately estimate the magnitude of the meteors. However, an attempt will be made to make the user familiar with the night sky, identifying several stars of different magnitudes so that they can learn how to estimate it. Several short tutorials will be visible when they start using the app and at each step of the reporting procedure.

Until the new app is designed and to be able to test different methods in data collection, the EpiCollect5 app is being used. Both apps, EpiCollect5 and Loss of the Night, are shown in Figure 2.

2.4 First results: Perseids 2018

The results of the Perseids 2018 visual observation campaign are shown in Figure 3, which represents the Zenital Hourly Rate calculated from the data reported by volunteer observers, filling out the EpicCollect5 form

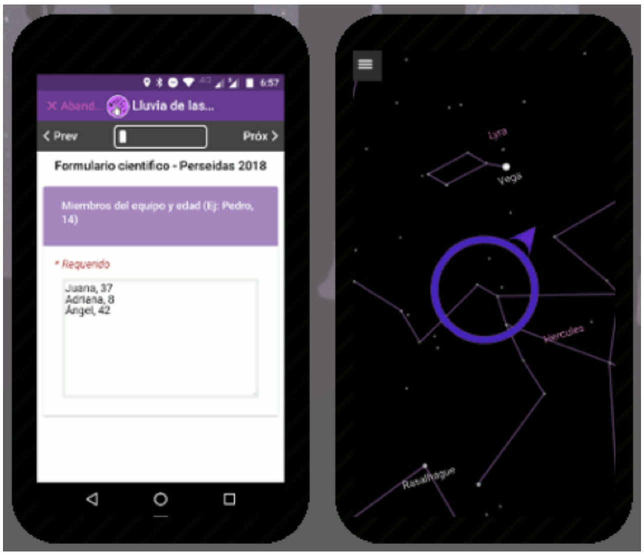

Figure 2 – Some screenshots of the apps used during the didactic activity, EpiCollect5 (left) and Loss of the Night (right).

as was explained before and compared with the results presented by IMO[5].

2.5 Meteor radio detections

Within the project Starcounters is planned to develop an app for meteor radio detection. There are many groups of amateur astronomers and professionals who use radio detection for tracking meteor showers. The novelty would be, in this case, the use of a smartphone as receiver, simplifying the procedure and encouraging collaborative science. In addition, radio detection makes it possible for people who are blind or visually impaired to follow the meteor showers.

For this, it is first necessary to have a national network of observatories that collaborate by sharing data received from the same transmitting source. Due to the Spanish geography and to make sure that regions such as the Canary Islands or North Africa can also participate, a 50 W, 49.990 MHz continuous carrier wave transmitter is expected to be placed in the south of Extremadura (Spain). This is one of the most interesting actions, since the transmitter can be tuned to any amateur radio receiver. It will be studied, on the one hand, the possibility of designing a low cost receiver that can be used by students, amateurs or professionals, thus increasing the radio detection network. On the other hand, all data will be gathered in a web server, so they are accessible to whoever would be interested.

3 Conclusions

From the dissemination point of view, this project aims for society to understand the importance of studying these phenomena and the need to involve them in this scientific task.

In the case of the live visual observations and the first results presented, more observations are needed to test the reliability of the method, especially of the Limiting Magnitude estimation made using the app Loss of the Night, which seems to be the easiest way to calculate it for volunteers not familiarized with night sky orientation. However, further research will be made to try to simplify observation report forms and to improve the accuracy of Limiting Magnitude estimation and classification of meteors into different active showers (or sporadic) at the time. Magnitude distribution is also needed to be able to fill the IMO online report.

Other novel approaches have been implemented to promote the interest of the general public, such as the possibility of participating in the counts from live and previously recorded videos embedded into a web browser. Furthermore, it has been taken into account to reach a special audience, such as people with some type of visual disability. Part of this project is focused on offering a tool with which they can be part of these events.

In addition to this, a clear research approach is pursued to process the information registered by citizens and contribute to the official data managed by the IMO.

Acknowledgements

The authors wish to thank to **The Spanish Foundation for Science and Technology** (FECYT) - Ministry of Economy, Industry and Competitiveness by funding the Starcounters Project (FCT-17-12520)[6].

References

Asher D. (2010). "International Meteor Conference 2010, September 16–19, Armagh, UK". *WGN, Journal of the IMO*, **38**, 4–5.

Bonney R., Cooper C. B., Dickinson J., Kelling S., Phillips T., Rosenberg K. V., and Shirk J. (2009). "Citizen science: A developing tool for expanding science knowledge and scientific literacy". *BioScience*, **59**, 977–984.

Egorova L. A. (2012). "Effect of 'terminal explosion'". In Gyssens M. and Roggemans P., editors, *Proceedings of the International Meteor Conference,* Sibiu, 15–18 September 2011. IMO, pages 19–21.

Maegawa K. (1999). "HRO: A new forward-scatter observation method using a ham-band beacon". *WGN, Journal of the IMO*, **27**, 64–72.

Molau S. and Barentsen G. (2014). "Status and history of the IMO Video Meteor Network". In Jopek T., Rietmeijer F., Watanabe J., and Williams I., editors, *Meteoroids 2013, Proceedings of the Astronomical Conference.* A.M. University, Poznań,

[5]Website: `http://www.imo.net/members/imo_live_shower?shower=PER&year=2018`

[6]Website: `http://www.contadoresdeestrellas.ciclope.info/`

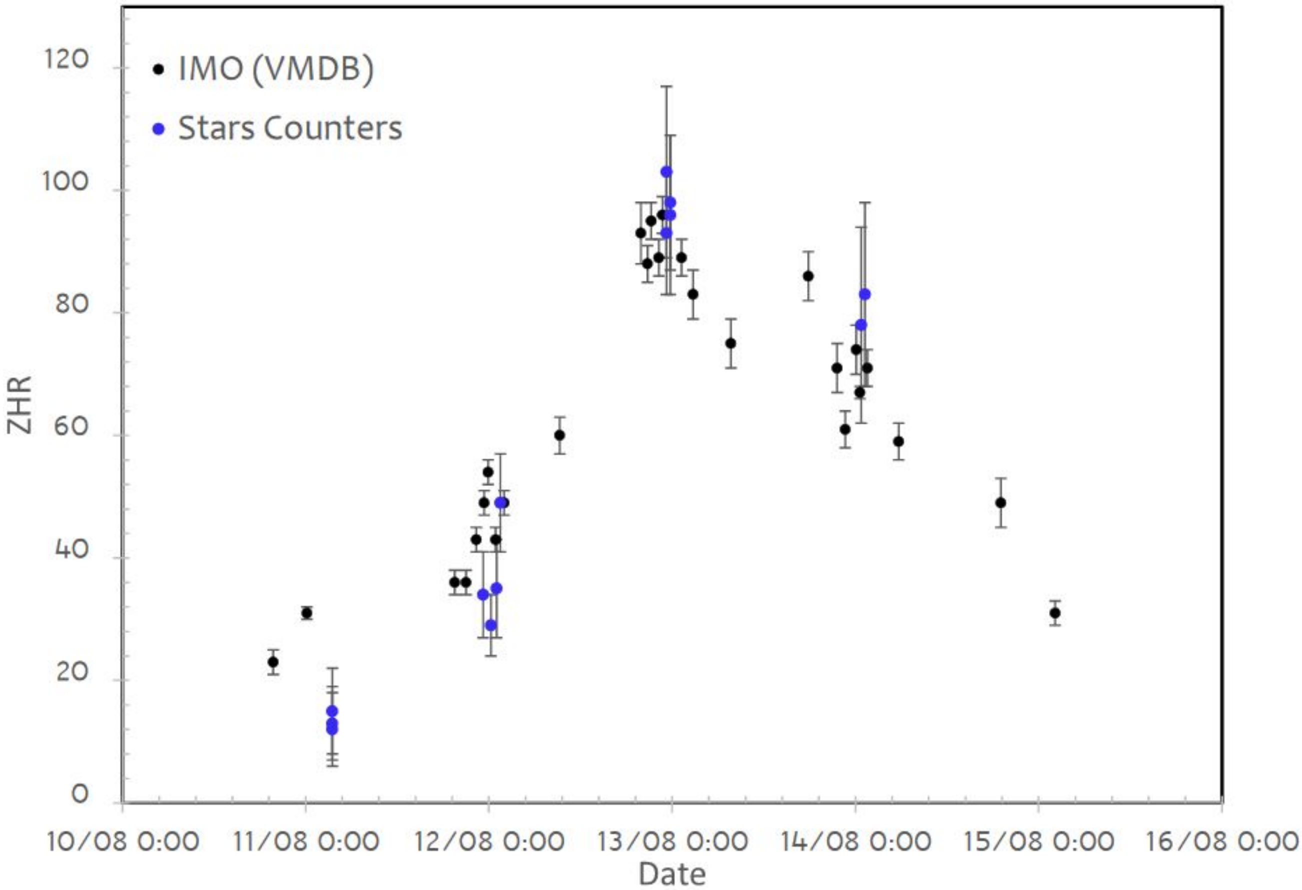

Figure 3 – Results of the Perseids 2018 campaign based on visual observations reported by volunteer observers through Star Counters didactic activity (blue) and IMO online form (black).

Poland, Aug. 26-30, 2013. University Press in Poznan, pages 297–305.

Reeves N., Tinati R., Zerr S., Van Kleek M. G., and Simperl E. (2017). “From crowd to community: A survey of online community features in citizen science projects”. In *Proceedings of the 2017 ACM Conference on Computer Supported Cooperative Work and Social Computing*, CSCW ’17, New York, NY, USA. ACM, pages 2137–2152.

Rendtel J. and Arlt R., editors (2011). *Handbook for Meteor Observers*. Third edition. IMO.

Steyaert C. (2006). “The VVS meteor beacon”. In Bastiaens L., Verbert J., Wislez J.-M., and Verbeeck C., editors, *Proceedings of the International Meteor Conference* Oostmalle, Belgium, 15-18 September, 2005. IMO, pages 25–33.

Vaubaillon J. (2005). “2005 Leonid forecastings”. `http://www.imcce.fr/langues/en/ephemerides/phenomenes/meteor/DATABASE/Leonids/2005` . IMCCE webpage.

CAMS update on hardware interfaces and software enhancements

Peter S. Gural[1]

[1] **Gural Software and Analysis LLC, Sterling VA, USA**
pgural@gmail.com

The Cameras for All-sky Meteor Surveillance (CAMS) system software has recently incorporated additional camera options that are associated with the new digital video formats as well as new processing modules for trajectory and astrometry. These imagery types include GigE live feed, digital video files compressed using H.264 and stored in an MP4 container, and the ZWO line of digital cameras. The processing upgrades include reconciliation of the orbital estimation code, trajectory robustness improvements, and various all-sky astrometric fitting options.

1 Introduction

CAMS has been operational for 8 years and thus a number of papers and reports have been published (Gural, 2011; Jenniskens et al., 2018, 2011, 2016). In the past two years, the end-to-end software processing chain has been undergoing changes to be more modular, handle newer digital cameras, process larger frame sizes, perform both wide field and all-sky astrometry, along with ongoing improvements in detection processing. This paper is a summary of the significant changes in the categories of camera interfaces, astrometry, detection, and trajectory estimation with a listing of the available software interfaces and modules for potential use and application on other systems.

2 Camera Interfaces for Analog and Digital

Until recently, CAMS has operated with analog cameras generating either NTSC or PAL type video signals. The associated video signal capture interface has involved using either a digitizing USB 2.0 dongle like EZcap or Diamond VC500 for each independent video stream, or a Sensoray multi-channel frame-grabber/PCI-board. A software interface module wrapped around a third-party code base called VideoInput, has been used when employing frame grabber dongles and remains available for general use, but is becoming a bit dated. For CAMS systems that employ one of the Sensoray multi-channel capture devices, the CAMS video capture applications make direct C calls using the Sensoray SDKs, so a generic interface code in those cases does not exist due to different SDK interface calls for each Sensoray model. With the recent announcement by SONY to discontinue manufacture of the recommended sensor chip for CAMS (e.g. the Exview HAD II sensor embedded in a Watec 902H2 Ultimate camera), it has been necessary to begin migration to newer digital cameras. Table 1 provides a breakdown of the cameras interfaced to CAMS that various groups have been focusing on from low cost digital board cameras, the ZWO line of megapixel cameras, and GigE compliant cameras with standardized communications protocols. An example is the Basler GigE camera employed by FRIPON. In each case, an interface module is available as a C header file of functions, that permit ingestion of video frames from either saved files (H.264 board camera) or via direct streaming to CPU memory (ZWO and GigE).

Table 1 – CAMS Camera Interfaces in the Migration from Analog to Digital.

Software Module	Recent Upgrades	"C" Code
TrajectorySolutionB	Particle swarm optimization for non-linear minimization Inserted site motion into measurement rays Weighted cost function based on individual measurement errors Added gravitational term to trajectory model Improved V_∞ and time offset initial guesses User adjustable particle swarm parameters *TBD: Measurement based velocity model* *TBD: Forward/Back propagation for zenith attraction*	Available
OrbitSolutionC	Moved Earth rotation to trajectory code Added full VSOP87 heliocentric for Keplerian orbit products Reconciled orbit parameter generation with the UWO	Available
Common theme header files		
TimeFunctions	UT from PC clock; Julian ↔ Calendar; $\lambda_\odot$, LST, Twilight, $\theta_\odot$	Available
CoordinateFunctions	Vector math; α,δ ↔ azel; α,δ ↔ std; α,δ ↔ xyz; LLA ↔ ECEF; $\lvert\angle\rvert_{sph}$	
UtilityFunctions	Text embedding in an image; Heap sort for integers and doubles	
SystemFileFunctions	Windows and Linux file interfacing	
DynamicArrayAllocation	Allocation of 2D arrays in C	
VSOP87	Full set of coefs for Earth position in heliocentric or barycentric	
ImageProcessing	Unique versions for EMCCD, HCAMS, ANDES-FIRE	
I/O Functions	Unique versions for CAMS, HCAMS, ANDES-FIRE	

Various new considerations must be addressed with some of these digital cameras. One is the use of USB 2.0 or 3.0 for raw video signal transfer which limits the allowable cable length from camera to PC. For example, USB 3.0 can only run up to 3 meters or when using an active extender cable, up to at most 10 meters. On the other hand GigE allows up to 100 meter CAT6 cable lengths. Some of the lower cost digital cameras also employ rolling shutters, but this can now be adjusted for either temporally or spatially (Kukic et.al, 2018). It should be noted that some digital cameras such as the ZWO ASI 174 has a large 1" format sensor chip size. So lens costs are also a consideration when choosing a digital video sensor chip as larger formats require more glass and expense for lenses. Fortunately, most board cameras seem to fall in the 1/3" size format which are supported by very low cost Chinese manufactured lenses. The processing load on detection software also goes up dramatically as we transition from one third mega-pixel analog cameras to 2 megapixel HD formats or larger, resulting in at least a six-fold increase in pixel count. This has been addressed in CAMS by switching to a fast clustering technique for meteor detection.

3 Using Astrometry from Narrow Field to All-sky

CAMS has traditionally been comprised of camera systems with moderate 20 to 40 degrees field of view (FOV) to obtain a roughly 3 arcminute per pixel angular resolution. This was selected to provide better quality orbits than contemporary all-sky systems. To perform astrometry for these moderate FOV systems, it has been adequate to use a third order cubic polynomial to represent the lens distortion and map the image positions to equatorial coordinates. However just recently, the need has arisen to support wide (∼80 degree FOV) and all-sky digital systems in which a cubic is not adequate to account for radial and barrel distortion in the lens. See Figure 1 for a processing flow diagram comparing the two basic FOV size configurations given in red.

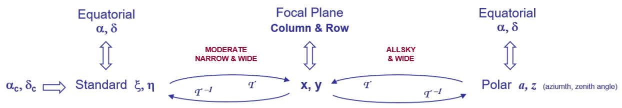

Figure 2: Processing Flow of Parameters for Narrow/Moderate and Wide/All-sky Astrometry.

A new set of C functions has been developed for wider FOVs than traditionally found in CAMS systems. This has been based on several published papers on all-sky astrometry (Borovicka, 1992; Borovicka et al., 1995; Howell, 2018). These C callable functions can also be easily interfaced into other processing pipelines. This current implementation is unique in that a single function is designed around a general formulation with an extended vector of unknown coefficients, that when combined, actually represent all the fitting algorithms published. Note that both the forward T and inverse T^{-1} mapping transformations have been implemented. Table 2 shows the various FOV astrometry options available at this time.

Table 2 – Astrometry Code Modules Supporting Narrow to All-sky Astrometry..

Field of View	System	Formulation	Solver	"C" Code Module
Narrow to Moderate < 60°	CAMS	Linear or Cubic	LMS + Iterative α_o,δ_o	Embedded in Manual, Auto, Nudger
Wide > 60°	Allsky6 CAMS TBD	Linear, Quadratic Cubic, Quintic Cubic + Radial **New allsky option**	LMS + Iterative α_o,δ_o	Functions Available
All-sky	ANDES-FIRE	Borovicka 1992 Borovicka 1995 Bannister 2013 Howell 2018	Non-Linear Fit via Particle Swarm	Functions Available

4 Meteor Detection Processing

CAMS applications versioned as 1.x were originally wrapped around the MeteorScan detection module that employed a localized pixel pair Hough transform to detect propagating streaks. Since the release of version 2.x in January 2017, the detection module within CAMS has changed to a fast clustering and tracking algorithm that runs forty times faster with the same detection performance (Gural, 2016). The new detection module is also completely modular and available as C functions. They are now used in the EMCCD system at the University of Western Ontario, the ANDES-FIRE all-sky GigE one-megapixel system, and Mike Hankey's "Allsky6" camera system. See Table 3 for details of the processing approaches evolution over time for various systems.

Table 3 – Meteor Detection Software Work Flow and Module Availability.

System	Front End Threshold "T"	Detection Algorithm	Post-Detection Processing (False Alarm Mitigation)	"C" Code Module
CAMS 1.x 2010 - 2016	Frame Difference T > k σ	Local Pixel Pairing Hough Transform	Matched Filter Max Likelihood Estimate	Embedded **"MeteorScan"**
AIM-IT "Mirror Steering"	Running Mean Sigma T > <X> + k σ	Fast Clustering Single αβ Tracker	None	Embedded **"AIM-IT"**
CAMSS Spectral	Running Mean Sigma T > <X> + k σ	Σ Columns vs Time Matched Filter	Spatial-Temporal CAMS Coincidence	Embedded **"CAMSS"**
CAMS 2.x Allsky6	CAMS Compression T = Maxpixel	Fast Clustering Multiple αβ Trackers	Linear Track Constraints	Functions Available
EMCCD at the UWO	1x, 2x Decimation CAMS Compression T = Maxpixel	Fast Clustering Multiple αβ Trackers	Matched Filter MLE Track Refinement	Functions Available
ANDES-FIRE	CAMS Compression T = Maxpixel	Fast Clustering Multiple αβ Trackers	Track and ω (FOV) Constraints	Functions Available

5 Trajectories, Orbits, and Utility Software Modules

Supporting the processing of meteor tracks and post-detection calculation of orbits are a number of utility functions for time, coordinate transforms, system file handling, dynamic array allocation, Earth position, image processing, and input/output functions for various camera systems that have been recently modularized into C header files. Included in this list as shown in Table 4, are also the trajectory and orbit estimation modules used in CAMS.

Specifically, the trajectory module was upgraded with the particle swarm optimization module for non-linear multi-parameter fitting, site motion added to the measurement rays, weighting of the measurements based on each measurements accuracy, and inclusion of gravitational attraction in the motion model. To be done in the near future are to incorporate a measurement-based model for velocity as well as forward/backward propagation to replace the simplified zenith attraction correction. The final orbit calculations given the meteor state vector in geocentric coordinates have been compared to the University of Western Ontario's processing codes with agreement to 5 significant figures in the output.

Note that all software files and modules described herein are available from the author via the provided email address.

Table 4 – Trajectory, orbit and utility functions.

Software Module	Recent Upgrades	"C" Code
TrajectorySolutionB	Particle swarm optimization for non-linear minimization Inserted site motion into measurement rays Weighted cost function based on individual measurement errors Added gravitational term to trajectory model Improved V_∞ and time offset initial guesses User adjustable particle swarm parameters *TBD: Measurement based velocity model* *TBD: Forward/Back propagation for zenith attraction*	Available
OrbitSolutionC	Moved Earth rotation to trajectory code Added full VSOP87 heliocentric for Keplerian orbit products Reconciled orbit parameter generation with the UWO	Available
Common theme header files		
TimeFunctions	UT from PC clock; Julian ↔ Calendar; $\lambda_\odot$, LST, Twilight, $\theta_\odot$	Available
CoordinateFunctions	Vector math; α,δ ↔ azel; α,δ ↔ std; α,δ ↔ xyz; LLA ↔ ECEF; $\lvert\angle\rvert_{sph}$	
UtilityFunctions	Text embedding in an image; Heap sort for integers and doubles	
SystemFileFunctions	Windows and Linux file interfacing	
DynamicArrayAllocation	Allocation of 2D arrays in C	
VSOP87	Full set of coefs for Earth position in heliocentric or barycentric	
ImageProcessing	Unique versions for EMCCD, HCAMS, ANDES-FIRE	
I/O Functions	Unique versions for CAMS, HCAMS, ANDES-FIRE	

References

Bannister S., Boucheron L. E., and Voelz D. G. (2013). "A numerical analysis of a frame calibration method for video-based all-sky camera systems". *Publications of the Astronomical Society of the Pacific*, **125:931**, 1108.

Borovicka J. (1992). "Astrometry with all-sky cameras.". *Publications of the Astronomical Institute of the Czechoslovak Academy of Sciences*, **79**.

Borovicka J., Spurny P., and Keclikova J. (1995). "A new positional astrometric method for all-sky cameras.". *Astronomy and Astrophysics Supplement Series*, **112**, 173.

Gural P. (2011). "The california all-sky meteor surveillance (cams) system". In *Proceedings of the International Meteor Conference, 29th IMC, Armagh, Northern Ireland, 2010.* pages 28–31.

Gural P. (2016). "A fast meteor detection algorithm". In *International Meteor Conference Egmond, the Netherlands, 2-5 June 2016.* pages 96–104.

Howell A. (2018). Private communication.

Jenniskens P., Baggaley J., Crumpton I., Aldous P., Pokorny P., Janches D., Gural P., Samuels D., Albers J., Howell A., and others (2018). "A survey of southern hemisphere meteor showers". *Planetary and Space Science*, **154**, 21–29.

Jenniskens P., Gural P., Dynneson L., Grigsby B., Newman K., Borden M., Koop M., and Holman D. (2011). "Cams: Cameras for allsky meteor surveillance to establish minor meteor showers". *Icarus*, **216:1**, 40–61.

Jenniskens P., Nénon Q., Gural P., Albers J., Haberman B., Johnson B., Morales R., Grigsby B., Samuels D., and Johannink C. (2016). "Cams newly detected meteor showers and the sporadic background". *Icarus*, **266**, 384–409.

Kukic P., Gural P., Vida D., Segon D., and Merlak A. (2018). "Correction for meteor centroids observed using rolling shutter cameras". *WGN, Journal of the International Meteor Organization*, **46**, 154–165.

Determination of the properties of meteor particles

V. V. Efremov[1], O. P. Popova[1], D. O. Glazachev[1] and A. P. Kartashova[2]

[1] **Institute of Geosphere Dynamics, Russian Academy of Sciences, Moscow, Russia**
efremov.vv@phystech.edu

[2] **Institute of Astronomy, Russian Academy of Sciences, Moscow, Russia**

The two most used models describing the interaction of small meteoroids with the Earth's atmosphere were applied to estimate meteor parameters from observational data. Meteoroid parameters (size and density) were estimated. Also, the parameters of the models used were refined in an attempt to find the best fit to observational data. The results of different models were compared with each other and with independent estimates, in those cases where they exist.

1 Introduction

Meteoroids hold information about the structure and composition of the matter at the initial stages of the Solar system's formation. Large parts of meteor particles do not reach the Earth's surface, and their properties could be determined indirectly based on observational data. Properties of meteor particles are important for understanding the small bodies distribution in the Solar system, the origin and the evolution of the meteoroid streams, the risk assessment for space exploration, etc. The energy deposition due to an interaction of the meteor particle with the Earth's atmosphere determines the light and the ionization curves, which are observed by different observational techniques. The energy deposition depends on the ablation rate and the deceleration of the meteor particles, which are determined by the particle size and density, as well as the entry angle and velocity.

To determine the parameters (size, density) of the meteor particle different models could be applied to the observational data. Currently, the precision of meteor particles parameters estimates is low. Meteor mass estimates, obtained by different authors, vary by orders of magnitude (Campbell-Brown et al., 2012). An attempt to apply two different ablation models to the same meteor observational data and to compare obtained results is presented in this paper.

2 Observational data

Institute of Astronomy RAS (INASAN) carries out systematic optical meteor observations from the Zvenigorod observatory INASAN (ZO) and "Istra" station (Kartashova et al., 2016) Simultaneous meteor observations are organized by IDG RAS at the Geophysical observatory Mikhnevo (GPhO Mikhnevo). The meteor camera in ZO INASAN are oriented at the zenith, the other cameras supported it for double – station observations. The distance between stations are 20 and 104 km. The meteor systems are equipped by cameras Watec 902H Ultimate with the lens Computar 6/0.8. The limiting meteor magnitude of the system is +4.0. The observations from ZO INASAN and GPhO Mikhnevo were used for investigations presented in this paper.

To increase the set of observational data and to be able to compare the results with an independent approach, a number of meteors observed by a Canadian observational system were considered.

Observations in Canada were made at the Canadian Automated Meteor Observatory (CAMO) (Stokan and Campbell-Brown, 2014). The distance between two stations is 45 km. The limiting magnitude is +5 (for meteors). In total, 11 meteors were considered, which were registered in 2010 and 2016.

3 Descriptions of models

Light curves are usually reproduced with the help of two most commonly used ablation models (**?**). The first model (will be named below model A) assumes that the entire incoming energy flux is consumed for the ablation. Corresponding mass loss equation is as follows:

$$L\frac{\mathrm{d}M}{\mathrm{d}t} = -\frac{1}{2}c_h\rho_a V^3 S, \tag{1}$$

where M, V are mass and velocity of the meteoroid; S is its cross-section area; ρ_a is the atmospheric density at the flight altitude; L is the heat of ablation and c_h is the heat transfer coefficient (Bronshten, 1983).

The second model (model B) suggests that the incoming energy is expended on re-radiation, ablation and heating of the meteoroid. The heat flux equation is:

$$\frac{1}{2}c_h\rho_a V^3 = 4\xi\sigma(T^4 - T_0^4) - \frac{L}{S}\frac{\mathrm{d}M}{\mathrm{d}t} + \frac{4}{3}R\rho c\frac{\mathrm{d}T}{\mathrm{d}t}. \tag{2}$$

The mass loss is determined by the saturated vapor pressure:

$$\frac{\mathrm{d}M}{\mathrm{d}t} = -4\pi R p_v(T)\sqrt{\frac{\mu}{2\pi kT}}, \tag{3}$$

where T is the body temperature; p_v is the saturated vapor pressure; μ is the atomic mass of the meteoroid substance; ρ is the density of the meteoroid; R is the radius of the body; ξ is the emissivity; c is the heat capacity (Lebedinets, 1980).

In both models, the heat flux equation is complemented by the equations of motion:

$$M\frac{\mathrm{d}V}{\mathrm{d}t} = -\frac{1}{2}c_d\rho_a V^3 S + Mg\sin\gamma, \tag{4}$$

$$MV\frac{\mathrm{d}\gamma}{\mathrm{d}t} = Mg\cos\gamma - \frac{MV^3}{R_p}\cos\gamma, \tag{5}$$

$$\frac{\mathrm{d}H}{\mathrm{d}t} = -V\sin\gamma, \tag{6}$$

where H is the height above the surface of the planet; γ is the entry angle (to the horizon); g is the gravitational acceleration; R_p is the radius of the planet; c_d is the drag coefficient (Bronsthen, 1983).

The radiation intensity is a fraction of kinetic energy loss:

$$I = -\tau\frac{\mathrm{d}E_k}{\mathrm{d}t}, \tag{7}$$

where I is the radiation intensity; τ is the luminous efficiency; E_k is the kinetic energy (**?**).

The coefficients, included in model equations (2-6) (the drag, the heat transfer coefficient and the luminous efficiency i.e. the model coefficients), should be determined based on assumptions about the realized flow regime. The model coefficients, used by different authors, vary which introduces uncertainty into the obtained meteoroid properties. For example, the luminous efficiency is often assumed to be constant along the trajectory and used values demonstrate large scatter in the range from 0.7% to 5%. In fact, the luminous efficiency may depend on the substance of the meteoroid, the meteoroid velocity and the altitude of the flight. The same is valid for the heat transfer coefficient. In addition, a large uncertainty is introduced by the mass loss estimate through saturated vapor pressure. The saturated vapor pressure is determined experimentally or modeled The scatter in suggested pressure values at the same temperature for similar meteoroid substances exceeds an order of magnitude.

The fit to the observed light curves was found by searching the meteor parameters (the size, the density) as well as the model coefficients (the luminous efficiency, the heat transfer coefficient). The solution was searched using a genetic algorithm. The discrepancy was used as the quality of a fit criterion. The discrepancy was calculated by the equation:

$$\frac{\sum_{i=1}^{n}\left|\frac{I_i^H - I_i^P}{I_i^H}\right|}{n}, \tag{8}$$

where I_i^H is the observed intensity, I_i^P is the model intensity, and n is the number of points on the light curve.

With the help of genetic algorithms and discrepancy, the best solution was found. But the found solution may be a local minimum (not global), which may lead to incorrect estimates of parameters. To find the global minimum, independent parameters (the body size and the luminous efficiency) were chosen. Based on these parameters, the grid was built. There was a minimum in each grid cell and it was analyzed. It allows the true solution to be found.

4 Simulation results

Each meteor was considered in the frame of both models (A and B), mentioned above. Two different dependencies for saturated vapor pressure were used in model B. The solutions were found by the method of differential evolution.

The comparison of the model fit with observational data is shown on Figure 1 for one selected meteor. For this particular case both models are able to find reasonable fit to observational data and to determine corresponding meteoroid parameters.

Some meteors are satisfactorily described by only one of the models, the others could be described by both models. Model A fits the observed data in 3 cases out of 11 (27%). Model B provides better fit in 9 cases (82%), so it looks that model B is better suited for modeling of the interaction of small meteor particles with the atmosphere.

There are other common ways to estimate the mass of a meteor. Different estimates based on maximal meteor brightness and semi-empirical dependencies are often applied (Jenniskens, 2006).

5 Model parameters

The obtained values of luminous efficiency are within the range of the literature data (Figure 2). The relationship between the evaluation of the efficiency and the model used is not traced.

The coefficient of heat transfer does not demonstrate the dependence on the speed (Figure 3). It varies in the range 0.3-0.9, and basically does not reach the value of c_h= 1, which is most often used in modeling. Thus, when modeling small meteors, one can not use the approximation of free molecular flow.

6 Conclusion

Both models allow finding of meteor particles parameters based on observational data. Model B is supposed to be better for modeling of the interaction of small meteor particles with the atmosphere.

The obtained estimates of the sizes of meteor particles are consistent with each other and with independent estimates with an accuracy of about 2 times. Differences between mass estimates for different models are 1–4

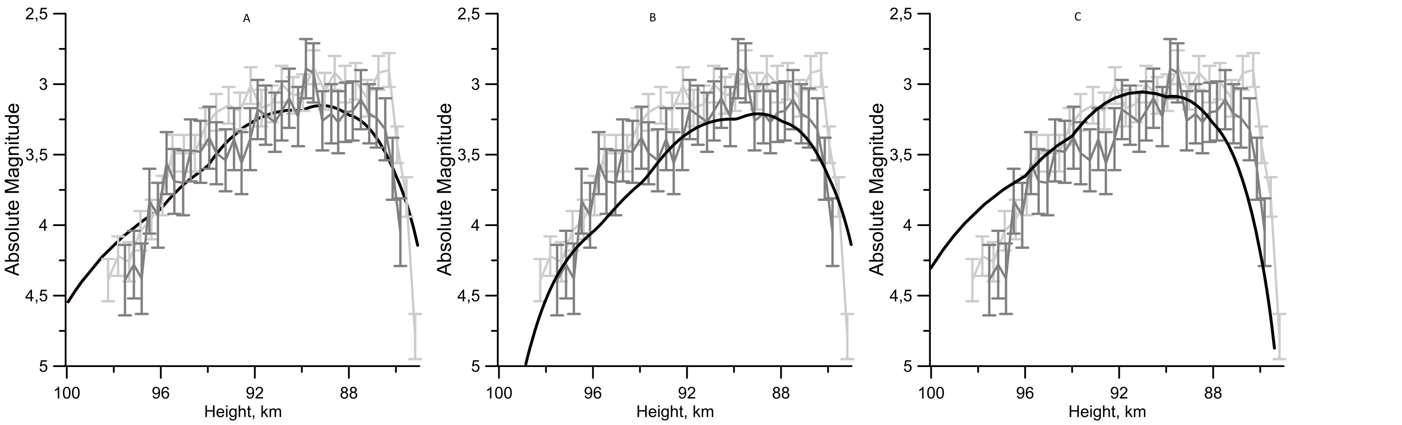

Figure 1 – Comparison of the observed and model light curves for a meteor 20101020_100214 (entry velocity 41.1 km/s, entry angle 390). Model curve: (A) is obtained in the frame of model A (R= 0,0012 m; ρ= 1288 kg/m^3; c_h = 0,49; L = 3,98·10^6 J/kg; τ= 0,97%); (B) is obtained in a frame of model B with saturated vapor pressure from (Moses, 1992) (R= 0,0011 m; ρ= 845 kg/m^3; c_h = 0,59; L= 3,8·10^6 J/kg; τ= 1,46%); (C) is the result of independent modeling in the frame of model A (Stokan and Campbell-Brown, 2014) (R= 0,00052 m; ρ= 2400 kg/m^3; c_h= 1; L= 6,3·10^6 J/kg; τ= 5%).

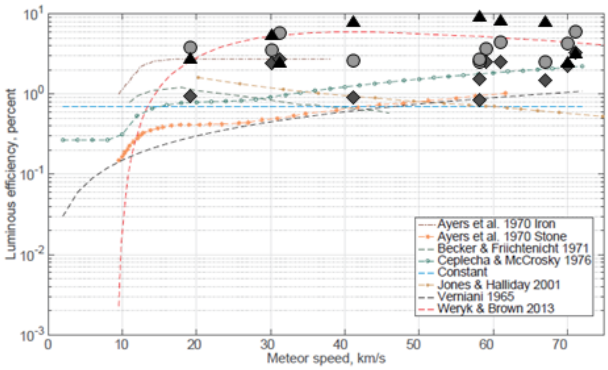

Figure 2 – Dependence of the luminous efficiency on velocity (from Subasinghe et al., 2017). Rhombus points show the luminous efficiencies obtained in the frame of the model A, circle – in the frame of the model B (vapor pressure from Campbell-Brown and Koschny, 2004), triangle correspond to the model B with vapor pressure from (Moses, 1992).

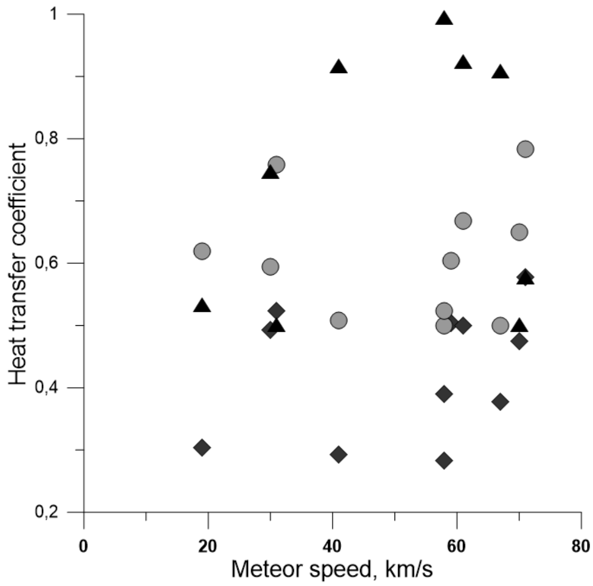

Figure 3 – Dependence of the heat transfer coefficient, obtained in the modeling, on velocity. Rhombus show the heat transfer coefficient obtained in the frame of the model A, circle – in the frame of the model B (vapor pressure from Campbell-Brown and Koschny, 2004), triangle correspond to the model B with vapor pressure from (Moses, 1992).

times. Comparison with independent modeling demonstrates the average difference is 3–4 times, the comparison with the simple estimates shows much larger scatter – the spread exceeds two orders of magnitude.

7 Summary and further work

The modeling should be continued, the dynamical data should be included in the simulation as well. It is necessary to evaluate the effect of the parameters, which still were not varied (drag coefficient etc.), to apply the existing dependencies for c_h and c_d; to apply the developed methods to a larger set of observational data.

Acknowledgement

This work was done under Government contract (No. 0146-2017-0003). AK acknowledges partial support from the Program No. 28 of the fundamental research of the Presidium of RAS.

References

Bronshten V.A. (1983), “Physics of Meteoric Phenomena”. *Reidel Publishing Co., Dordrecht*

Campbell-Brown M.D., Koschny D. (2004), “Model of the ablation of faint meteors”. *Astronomy & Astrophysics*, **418**, 751–758.

Campbell-Brown M.D., Kero J., Szasz C., Pellinen-Wannberg A., Weryk R.J. (2012), “Photometric and ionization masses of meteors with simultaneous EISCAT UHF radar and intensified video observations”. *Journal of Geophysical Research: Space Physics*, **117**, nr. A9.

Jenniskens P. (2006), “Meteor showers and their parent comets”. *Cambridge University Press*

Kartashova A., Bolgova G., Rybnov Y., Popova O., Glazachev D. (2016), "The multi technique meteor observations in 2014". *Proc. International Meteor Conference, Egmond, the Netherlands, 2–5 June 2016, Eds. A. Roggemans and P. Roggemans*, IMO, 120–122.

Lebedinets V.N. (1980), "Dust in the upper atmosphere and in space. Meteors". *Leningrad: Gidrometeoizdat*, **248**.

Moses J.I. (1992), "Meteoroid ablation in Neptune's atmosphere'. *Icarus*, **99**, 368–383.

Popova O. (2004), "Meteoroid ablation models". *Earth, Moon, and Planets*, **95**, 303–319.

Stokan E., Campbell-Brown M.D. (2014), "A particle-based model for ablation and wake formation in faint meteors". *MNRAS*, **447**, 1580–1597.

Subasinghe D., Campbell-Brown M., Stokan E. (2017), "Luminous efficiency estimates of meteors-I. Uncertainty analysis". *Planetary and Space Science*, **143**, 71–77.

The Italian bolide of May 2017: trajectory, orbit and preliminary fall data

Albino Carbognani[1], Dario Barghini[2,3] Daniele Gardiol[2], Mario Di Martino[2], Giovanni B. Valsecchi[4], Paolo Trivero[5], Alberto Buzzoni[6], Stefania Rasetti[2], Danilo Selvestrel[7], Cristina Knapic[8], Elisa Londero[8], Sonia Zorba[8], Cosimo A. Volpicelli[2], Matteo Di Carlo[9], Jeremie Vaubaillon[10], Chiara Marmo[11], Francois Colas[10], Diego Valeri[12], Ferruccio Zanotti[12], Maurizio Morini[12], Paolo Demaria[12], Umberto Repetti[13], Brigitte Zanda[14], Sylvain Bouley[11], Pierre Vernazza[15], Jrme Gattacceca[16], Jean-Louis Rault[17], Lucie Maquet[10], Mirel Birlan[10]

[1] **Osservatorio Astronomico della Regione Autonoma Valle d'Aosta (OAVdA), Italy**
`albino.carbognani@inaf.it`

[2] **INAF – Osservatorio Astrofisico di Torino, Italy**
`dario.barghini@edu.inaf.it` and `daniele.gardiol@inaf.it` and `dimartino@oato.inaf.it` and `stefania.rasetti@inaf.it` and `cosimo.volpicelli@inaf.it`

[3] **Dipartimento di Fisica, Universit degli studi di Torino, Italy**
`dario.barghini@edu.unito.it`

[4] **IAPS-INAF Roma; IFAC-CNR Sesto Fiorentino, Italy,**
`giovanni@iaps.inaf.it`

[5] **Dip. Di Scienze e Innovazione Tecnologica, Universit del Piemonte Orientale, Italy**
`paolo.trivero@uniupo.it`

[6] **INAF – Osservatorio di Astrofisica e Scienza dello Spazio di Bologna, Italy**
`alberto.buzzoni@oabo.inaf.it`

[7] **INAF – Osservatorio Astronomico di Padova, Italy**
`danilo.selvestrel@inaf.it`

[8] **INAF – Osservatorio Astronomico di Trieste, Italy**
`cristina.knapic@inaf.it` and `elisa.londero@inaf.it` and `sonia.zorba@inaf.it`

[9] **INAF – Osservatorio Astronomico dAbruzzo, Italy**
`matteo@oa-teramo.inaf.it`

[10] **IMCCE, Observatoire de Paris, PSL Research University, CNRS, Sorbonne Universits, UPMC, France**
`Jeremie.Vaubaillon@obspm.fr` and `Francois.Colas@imcce.fr` and `Lucie.Maquet@obspm.fr` and `Mirel.Birlan@imcce.fr`

[11] **GEOPS, Univ. Paris-Sud, CNRS, Univ. Paris-Saclay, Orsay, France**
`chiara.marmo@u-psud.fr` and `sylvain.bouley@u-psud.fr`

[12] **Italian Meteor and TLE Network (IMTN), Italy**
`dvaler@alice.it` and `esploriamoluniverso@gmail.com` and `morinmau@gmail.com` and `paolomclaren@libero.it`

[13] **Associazione Meteoriti Italia, Feltre (BL), Italy**
`minfluomet@yahoo.it`

[14] **IMPMC, Musum National dHistoire Naturelle, Paris, France**
`zanda@mnhn.fr`

[15] **LAM, Institut Pytheas, Marseille, France**
`pierre.vernazza@lam.fr`

[16] **CEREGE, Institut Pytheas, Marseille, France**
`gattacceca@cerege.fr`

[17] **FRIPON, Collaborative Team, Paris, France**
`f6agr@orange.fr`

On May 30th, 2017 at about 21^h 09^m 17^s UTC a green bright fireball, that we named IT20170530, crossed the sky of north-eastern Italy. The fireball path was observed starting from a mean altitude of 80.9 ± 0.7 km (Lat. 44.372° N; Long. 11.859° E) and extinct at 23.7 ± 0.2 km (Lat. 45.248° N; Long. 12.050° E), between the Italian cities of Venice and Padua. The meteoroid pre-atmospheric velocity was 17.3 ± 0.1 km/s with an estimated starting mass/section ratio of 507 ± 20 kg/m^2, a mean drag coefficient of 0.58 and an ablation coefficient of 0.0140 ± 0.0006 s^2/km^2, a value compatible with a typical type I chondritic meteoroid. On the basis of the data collected from PRISMA, IMTN and CMN sky-networks, we have computed the best fireball atmospheric trajectory, modeled the meteoroid atmospheric dynamics, modeled the dark flight phase of the residual meteoroid and computed the best heliocentric orbit of the progenitor body. Searches for meteorites on the ground have not produced any results so far.

1 Introduction

One of the most interesting astronomical phenomena that can be seen in the sky is a fireball, namely a very bright meteor caused by the fall of a big meteoroid into the atmosphere. Unfortunately, as the events are sporadic and unpredictable, it is not possible to know when you will see the next fireball so you need constant monitoring of the whole sky in order to observe one. The analysis of a fireball event can be divided into four distinct phases:

1. Triangulation between different stations on the ground for the reconstruction of the average fireball trajectory in the atmosphere.
2. Estimation of pre-atmospheric velocity, mean drag coefficient, ablation coefficient and mass-section ratio.
3. Starting from the terminal point of the luminous path, modeling of the dark flight phase to estimate the area on the ground where to look for possible meteorites (strewn field).
4. Compute the heliocentric velocity from the meteoroid true geocentric velocity and, knowing the position vector of the Earth at the fireball time, compute the meteoroid heliocentric orbit.

This is the logical path we will follow in this preliminary work applied to the Italian fireball of May 30, 2017 (IT20170530).

2 PRISMA, FRIPON, IMTN and CMN networks

PRISMA network was born in 2016 (Gardiol et al., 2016). PRISMA means "Prima Rete Italiana per la Sorveglianza sistematica di Meteore e Atmosfera", i.e. First Italian Network for Meteor and Atmosphere systematic Surveillance. The PRISMA project is an international European collaboration with the French project FRIPON (Fireball Recovery and InterPlanetary Observation Network), started in 2014 long before PRISMA and managed by Observatorire de Paris, Muséum National d'Histoire Naturelle, Université Paris-Sud, Université Aix Marseille and CNRS (Colas et al., 2015). The IMTN (Italian Meteor and TLE Network) is a national surveillance network both for the study of meteors and high-atmosphere phenomena or TLE, Transient Luminous Events. The network is managed by volunteers. The CMN (Croatian Meteor Network) consists of 30 surveillance cameras that monitor most of the night sky over Croatia.

3 The fireball atmospheric trajectory

We did not use the FRIPON astrometric pipeline. Rather, for the PRISMA team the observation of IT2017 0530 was a good opportunity to start developing an autonomous pipeline. The triangulation of the fireball trajectory was performed with the data from PRISMA-Rovigo station crossed with the data from the IMTN/CMN stations (see Figure 2). From PRISMA-Navacchio and PRISMA-Piacenza stations the fireball was too low above the horizon to produce good astrometry from the images. The atmospheric trajectory of the fireball was computed as geometric intersection of the best planes containing the two stations and the unit vectors of the fireball's observed points (Ceplecha, 1987). A tool to perform triangulation using observations from $N > 2$ PRISMA stations simultaneously using the Borovička

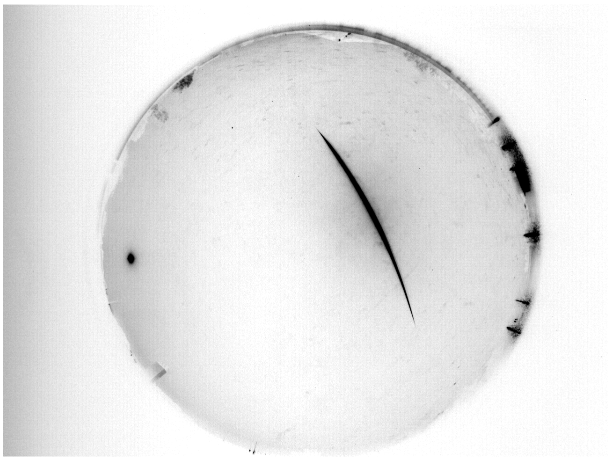

Figure 1 – A negative image showing the full path of IT20170530 from PRISMA-Rovigo station. North is down, south is up. The bright object on the left is the Moon near the western horizon. The fireball moved from top-left to bottom-right. The total duration of the fireball was about 9.51 s. From this image no significant fragmentation of the meteoroid appears.

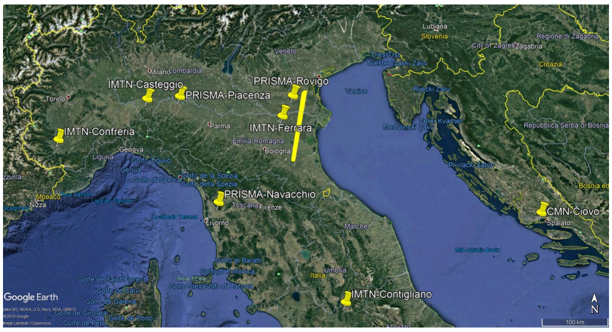

Figure 2 – A Google Earth map showing the position of the stations and the fireball trajectory projected on the ground.

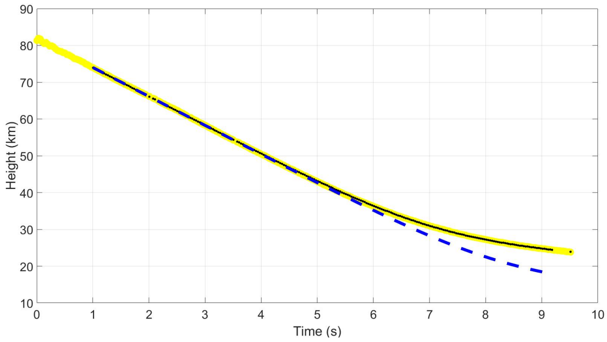

Figure 3 – The fireball height vs. time from PRISMA-Rovigo as a result of the triangulation from PRISMA-Rovigo with IMTN Contigliano. Yellow dots = observed values; dotted blue line = model with starting guess values; black line = best fit model.

method was also developed (Borovicka, 1990) for future fireballs. However, in this specific case with heterogeneous observations (from PRISMA and IMTN stations), we preferred the triangulation from two stations at a time, to have a better control on results.

4 The dynamic model of the meteoroid

In order to estimate the fireball main physical parameters, i.e. drag and ablation coefficients, pre-atmospheric velocity, mass/section ratio and to compute the best height, velocity and acceleration in the terminal point of the luminous path, we have implemented a single body dynamical model numerically integrating the differential equations describing the motion and the ablation of the meteoroid. In this classical model ablation begins when the surface of the meteoroid reaches the boiling temperature. At this point the temperature is assumed to remain constant and the light emission negligible with respect to the kinetic energy of the meteoroid (Kalenichenko, 2006). With the dynamical model results, assuming a mean density of about 3500 kg/m^3, we can estimate a mass of about 19 kg and a dimension of about 0.2 m for the progenitor meteoroid.

5 The dark flight phase and the strewn field

In order to model the dark flight phase it is important, even if not strictly necessary, to know the profile of the

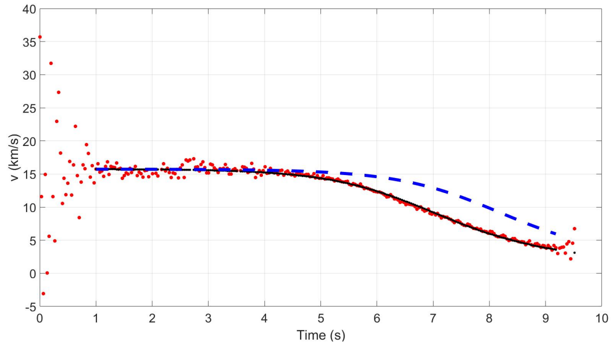

Figure 4 – The fireball velocity vs. time from PRISMA-Rovigo as a result of the triangulation from PRISMA-Rovigo with IMTN-Contigliano. Red dots = observed values; dotted blue line = model with starting guess values; black line = best fit model.

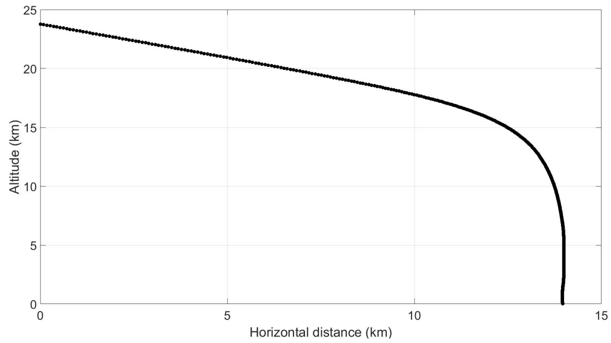

Figure 5 – Parallel view of the residual meteoroid height vs. horizontal distance starting from the terminal point. Notice the small deformations at the end of the vertical section of the trajectory, due to the wind.

atmosphere at the moment closest to the meteoroid fall because the trajectory, after the end of the luminous path, is heavily influenced by the atmospheric conditions. The data about wind velocity, wind direction, density, pressure and temperature vs. the height above Earth's surface can be obtained from weather balloons up to an altitude of about 30–40 km. The motion of the residual meteoroid, starting from the observed terminal point of the luminous path, can be described using Newton's Resistance law (Ceplecha, 1987), because the meteoroid motion takes place in a turbulent regime, i.e. a motion characterized by high Reynolds number. According to the mass/cross-section values, the distance of the impact point from the projection on the ground of the terminal point varies from 13.8 to 14.1 km with a difference of about 0.4 km. The strewn field dimension is about 1×0.6 km, around the geographical coordinates +45.3721° N and 12.0786° E and we estimate a mass of about 2 kg and a dimension of about 0.1 m for the meteorite.

6 The meteoroid heliocentric orbit

Knowing the heliocentric velocity vector of the progenitor meteoroid and the Earth's vector position at the time of the meteoroid fall, it is possible to compute the heliocentric orbital elements (Ceplecha, 1987). The computed orbital elements indicate that the meteoroid was an Apollo-type object, with an aphelion

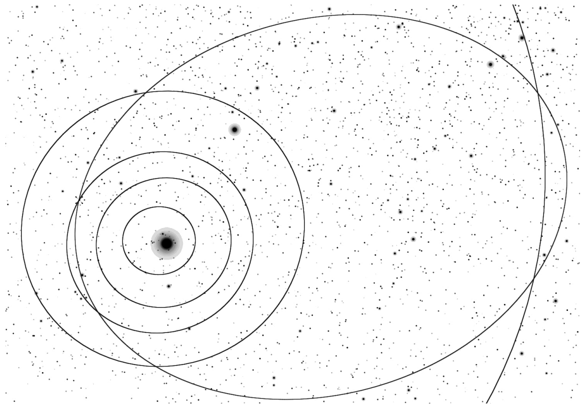

Figure 6 – The nominal heliocentric orbit for the progenitor meteoroid of the fireball IT20170530 as seen from the ecliptic north pole. The error bars of the aphelion (±0.3 UA) and perihelion distance (±0.001 UA) are not indicated.

near Jupiter's orbit and with low inclination above the ecliptic plane. The orbital period is about half the one of Jupiter, so the progenitor meteoroid was very close to 2:1 mean motion resonance with Jupiter. No NEAs among those known appear to be good candidates as progenitor bodies. What we know for sure is that the object was in a very chaotic orbital region as it is very close to the 2:1 resonance with Jupiter.

7 Conclusion

We have presented the provisional results obtained about the fireball observed by PRISMA, IMTN and CMN stations on May 30th, 2017 at about 21^h 09^m 17^s UTC. This fireball was very interesting, the data collected allowed us to draw an identikit of the phenomenon but much work remains to be done. We do not rule out the possibility of finding a meteorite in the near future with more thorough searches.

Acknowledgement

The authors wish to thank all the owners and managers of the PRISMA stations that with their support make possible the study of fireballs and the search for meteorites. The complete list of people, associations and institutions (both public and private) is available on the PRISMA website: `http://www.prisma.inaf.it.PRISMA` is a collaborative project proposed and coordinated by the italian National Institute for Astrophysics (INAF). PRISMA was partially funded by a 2016 "Research and Education" grant from Fondazione CRT. The initial FRIPON hardware and software has been developed by the FRIPON-France core team under a French ANR grant (2014-2018). Many thanks to J. Belas and D. Šegon of the Croatian Meteor Network for giving us their data about IT20170530. The Astronomical Observatory of the Autonomous Region of the Aosta Valley (OAVdA) is managed by the Fondazione Clément Fillietroz-ONLUS, which is supported by the Regional Government of the Aosta Valley, the Town Municipality of Nus and the "Unité des Communes valdôtaines Mont-émilius". The research was partially funded by a 2017 "Research and Education" grant from Fondazione CRT.

References

Borovicka J. (1990). "The comparison of two methods of determining meteor trajectories from photographs". *Bulletin of the Astronomical Institutes of Czechoslovakia*, **41**, 391–396.

Ceplecha Z. (1987). "Geometric, dynamic, orbital and photometric data on meteoroids from photographic fireball networks". *Bulletin of the Astronomical Institutes of Czechoslovakia*, **38**, 222–234.

Colas F., Zanda B., Bouley S., Vaubaillon J., Marmo C., Audureau Y., Kwon M., Rault J., Caminade S., Vernazza P., et al. (2015). "Fripon, the french fireball network". In *European Planetary Science Congress*, volume 10.

Gardiol D., Cellino A., and Di Martino M. (2016). "Prisma, italian network for meteors and atmospheric studies". In *International Meteor Conference Egmond, the Netherlands, 2-5 June 2016*. pages 76–79.

Kalenichenko V. (2006). "The pecina-ceplecha functional as a tool to evaluate physical parameters of fireball bodies from observational data". *Astronomy & Astrophysics*, **448:3**, 1185–1190.

Impact effects calculator: scaling relations for shock wave and radiation effects applied to Chelyabinsk and Tunguska events

Glazachev, D. O.[1], Podobnaya, E.D.[1], Popova, O.P.[1], Kartashova, A.P.[2], Artemieva, N.A.[1], Shuvalov, V.V.[1] and Svetsov, V.V.[1]

[1] **Institute for Dynamics of Geospheres Russian Academy of Sciences (IDG RAS), Moscow, Russia**
GlazachevD@gmail.com

[2] **Institute of Astronomy of the Russian Academy of Science (INASAN), Moscow, Russia**

Thermal radiation and shock wave effects are the main hazardous factors in impact scenarios, which could result in fire ignition over large areas, damage and collapse of buildings, and injuries. The impact of cosmic objects cannot be reproduced in full-scale in a laboratory, so the main approach is numerical modeling. The comprehensive full description of an impact and its consequences is complicated and time-consuming. On the other hand, scaling relations are quick and much easier to perform. The main purpose of this work is to develop an easy-to-use using tool (for scaling relations), which will give a good quick estimate for all hazardous effects from large meteoroids impacts. The airburst events at Chelyabinsk and Tunguska in Russia are the best-documented cosmic object impacts, so we compared our scaling relations predictions with observed effects of these impacts.

1 Introduction

Asteroid impact risk models require an understanding of how asteroid impacts can injure people and damage property (Mathias et al., 2017; Nemchinov et al., 2008). Thermal radiation and shock wave effects are the main hazardous factors in impact scenarios, which could result in fire ignition over large areas, damage and collapse of buildings, and injuries. The shockwave can be lethal due to overpressure and strong winds. Overpressure can cause unconsciousness, concussion, lung damage, eardrum rupture, and shock. Winds can cause people to be hit by solid objects (glass, rocks, trees) or to be thrown into objects. Winds can also cause exposure to dangerous chemicals and other materials brought into the environment by the shockwave. UV and thermal radiation can cause injuries by direct burns (flash burns) of different degrees, sunburn from UV light, retinal and conjunctiva damage and blinding (Gelfand & Silnikov, 2002; Glasstone & Dolan, 1977). All these effects occur when corresponding physical values, i.e. overpressure, thermal exposure etc, exceeds some boundary. To predict the consequences one needs to know the spatial distributions of thermal energy and flux, shock wave overpressure, and wind. The cosmic objects of cometary and asteroidal origin with sizes 20-150 meters, which result in airbusts during the entry, are considered.

2 Numerical simulations and scaling relations

Modeling

The disruption and deceleration of a meteoroid in the atmosphere, subsequent propagation of the shock wave to long distances and determination of the radiative field were calculated using a two-step model described in (Shuvalov et al., 2013). Firstly, the motion of a meteoroid in the atmosphere was simulated with allowance for its deformation, deceleration, destruction, and evaporation. The simulation involved the model, equations, and numerical scheme described in (Shuvalov et al., 2017a; Shuvalov & Trubetskaya, 2007).

The model is applied when the meteoroid moves at heights where aerodynamic loads considerably exceed its strength; so it is supposed that the meteoroid is already disrupted and can be described in the hydrodynamic approximation. The problem was solved in

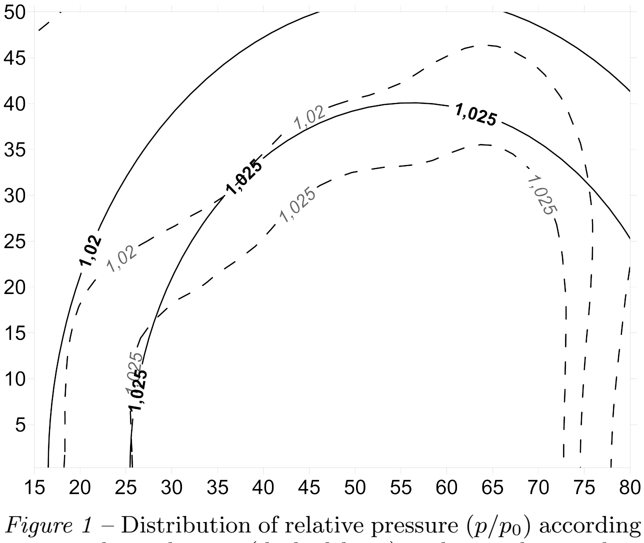

Figure 1 – Distribution of relative pressure (p/p_0) according numerical simulations (dashed lines) and according scaling relations (solid lines) for cometary body with diameter 30 m, entry angle 30° and velocity 30 km/s. Relative pressure values are marked on corresponding levels.

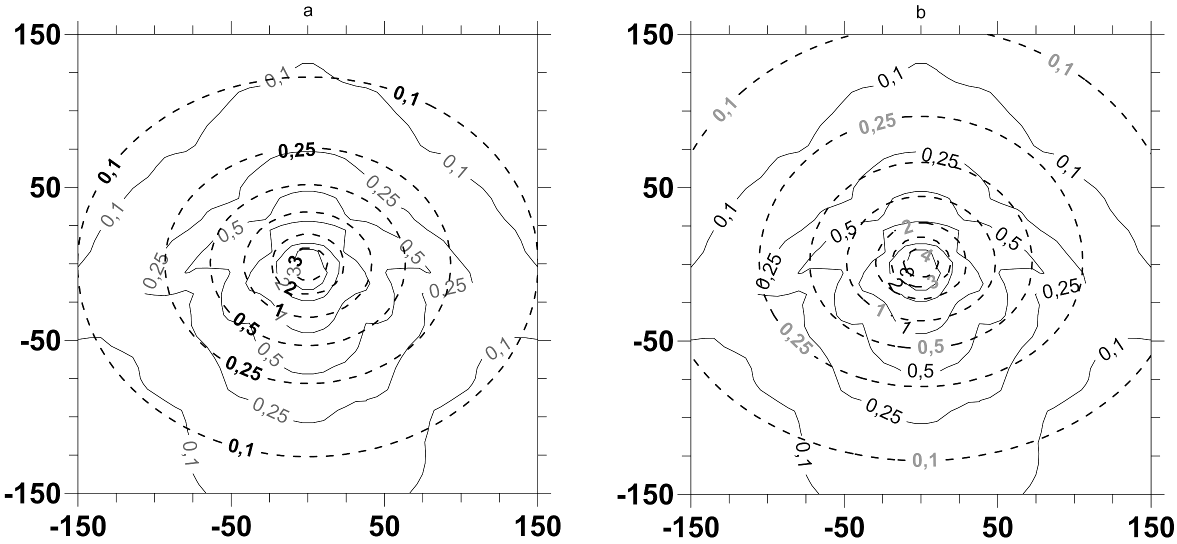

Figure 2 – Distribution of radiative exposure (exposure values are given on contour lines in J/cm^2) on the surface for a 30 m cometary body that entered the atmosphere with velocity 20 km/s and entry angle 450. Solid lines represent corresponding numerical simulations; dashed lines demonstrate application of simplified approximations, taking into account the heterogeneity of the radiation field (a) and without it (i.e. point source approximation) (b). The axes correspond to distance in km, the trajectory is directed from top to the bottom, maximum luminosity point is in the point of origin of coordinates.

a coordinate system associated with the falling body, which was blown by air, whose density varied according to the atmosphere stratification and the flow velocity was equal to the velocity of the body. The calculations terminated when the meteoroid was disrupted and almost completely decelerated (its velocity in the coordinate system associated with the Earth decreased by about five times, i.e., when its further fall had no effect on the determined effective height of the energy deposition) or reached the Earth's surface. The distributions of gas-dynamic and thermodynamic parameters in the atmosphere were used as initial data for the second step of calculations. At that step, the propagation of a shock wave to great distances was simulated in a coordinate system associated with the Earth's surface. Both calculation steps were implemented using the SOVA numerical method (Shuvalov, 1999).

The temperature and density distributions obtained during the simulation of the fall in the atmosphere allow determination of the radiation fluxes on the Earth's surface. For these calculations, a computational grid on the ground was set and geometric rays that emerge from the grid nodes at different angles to the surface and cross the heated volume of a fireball were produced. The equation of radiative transfer was solved along the rays (Svetsov & Shuvalov, 2017).

Analyses of simulation results permit to suggest scaling relations, which allow estimation of irradiated energy, overpressure and to approximate these fields on the surface based only on impactor properties.

Scaling relations of the air blast

Based on the results of numerical simulations it is possible to suggest the following scaling relation for relative pressure (pressure ratio at location (x, y) to atmospheric pressure), which takes into account the spatial heterogeneity:

$$\frac{p}{p_0} = 1 + a\left(\frac{E_k^{2/3}}{H_{eff}^2 + (x - x_0)^2 + el \cdot y^2}\right)^{0.66} \qquad (1)$$

Here p is a pressure at location (x,y) and p_0 is undisturbed atmospheric pressure at the surface level; el is an ellipticity parameter, which allows inclusion of spatial heterogeneity; a is a normalizing constant; x, y are the coordinates (point of origin is the point where the trajectory (without deceleration) crosses the Earth surface); x_0 is corresponding shift of the maximum pressure point from the origin point; E_k is a kinetic energy of impactor in kt TNT. H_{ref} is an effective altitude for point source, and it is a height of the equivalent explosion point generating the same shock wave (in zero-order approximation and circular symmetry) as the fall of a cosmic body with the given parameters. It roughly corresponds to the altitude where the cosmic body loses most of its energy and decelerates (Shuvalov et al., 2016). Effective altitude H_{ref} is determined by entry angle, the size and the density of impactor. Small values of overpressure are determined in numerical simulations with uncertainty, reliable values were considered to exceed about 1-2 kPa, which corresponds to p/p_0=1.01-1.02.

All parameters included into the relation (1) are determined based on the properties of the impactor. A shift of maximal pressure point x_0 was determined as a dependence of the entry angle and the effective altitude. Both model coefficient a and el-ellipticity parameter depend on the kinetic energy of the impactor and on the effective altitude, the ellipticity parameter depends also on the entry angle. Suggested scaling relations are dependent only on the properties of the entering object (size, density, velocity and entry angle). The important quantities to determine are the peak overpressure,

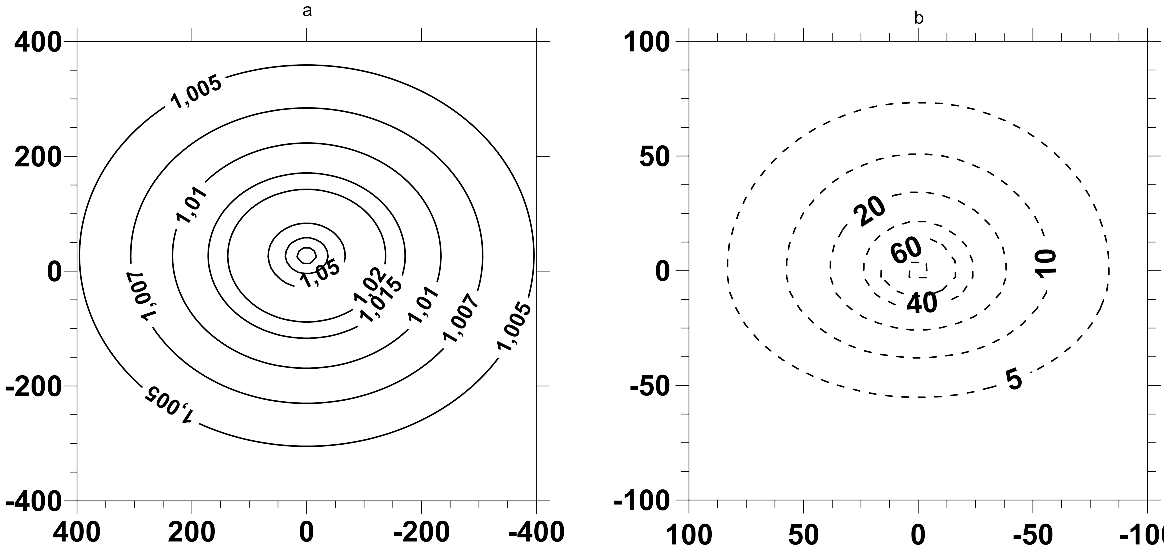

Figure 3 – Scaling relations results for Tunguska body with density 1000 kg/m^3, entry angle 30°, diameter 84 m, velocity 20 km/s and kinetic energy 15 Mt TNT (a) Distribution of relative pressure (p/p_0). (b) Distribution of thermal exposure (J/cm^2).

that is, the maximum pressure in excess of the ambient atmospheric pressure, and the ensuing maximum wind speed. Scaling relation for the peak overpressure does not depend on the density of the cosmic body, but depends on kinetic energy, velocity, diameter of impactor and effective altitude. Maximal wind velocity behind the front depends only on kinetic energy of impactor and its effective altitude. Areas, at which chosen levels of overpressure is exceeded, depend not only on the kinetic energy and the effective altitude, but also on the entry angle.

Scaling relations allow determination of a surface distribution of the overpressure and speed of wind (Figure 1). Besides they allow estimation of an area, at which chosen levels of overpressure is exceeded. As there is a connection between the level of overpressure and the speed of wind behind the front, it is possible to obtain the wind velocity distribution from the overpressure distribution (Glasstone & Dolan, 1977).

These scaling relations can be considered a first approximation, which takes into account the main features of the overpressure distribution with one maximum. They do not take into account the more complex character of the overpressure distribution, which can be created by the destruction and deceleration of the cosmic body, in which local maxima could be observed. In addition, levels of small excess pressures of less than p/p_0=1.01-1.02, outside the central area, also require separate consideration. Value of relative pressure $p/p_0 \sim 1.02$ exceeds the threshold of glass damage (1.005-1.01) (Gi et al., 2018) and is smaller than the threshold of minor damage to house structures (1.048) (Glasstone & Dolan, 1977).

Scaling relations of the thermal field

Results of numerical simulations were used also to construct scaling relations for radiative effects, which allows estimation of irradiated energy and approximation of other important parameters.

Thermal field Q (in J/cm^2) can be approximated as following

$$Q\left(x,y\right) = \frac{\eta \cdot E_k}{H_{rad}^2 + el \cdot x^2 + y^2} \qquad (2)$$

Here E_k is the kinetic energy of impactor (kt TNT); η is an integral luminous efficiency (in %) which is determined as the ratio of the integral of the thermal exposure on the whole surface to the kinetic energy of the body; x and y are spatial coordinates (in this relation point of origin is under the point of maximal effect), el is an ellipticity parameter (it differs from the ellipticity in pressure distribution). The distributions for radiative flux were also approximated.

In relation (2), there are two unknown parameters for impactor, i.e. an effective radiative altitude H_{rad} and an integral luminous efficiency. The efficiency of radiation varies from several percent to 10-20%, and is dependent on kinetic energy, entry angle and density of the impactor.

The effective radiative altitude is the analogue of the effective altitude mentioned above but obtained for the thermal field. It should be noted that the point of maximal thermal exposure and point of maximal pressure are different; the radiative altitude is larger than effective altitude. Scaling relation for effective radiative altitude depends on impactor density and effective altitude. The maximal thermal exposure, maximal radiative flux and the duration of radiative pulse were also approximated.

Applied scaling relations are shown in Figure 2 for a 30 m comet entering the atmosphere with a 20 km/s velocity at an entry angle of 450 in comparison with the result of numerical modeling for two cases. The scaling relation with spatial heterogeneity is shown in Figure 2a, whereas the distribution on Figure 2b demonstrates scaling under assumption of the point source.

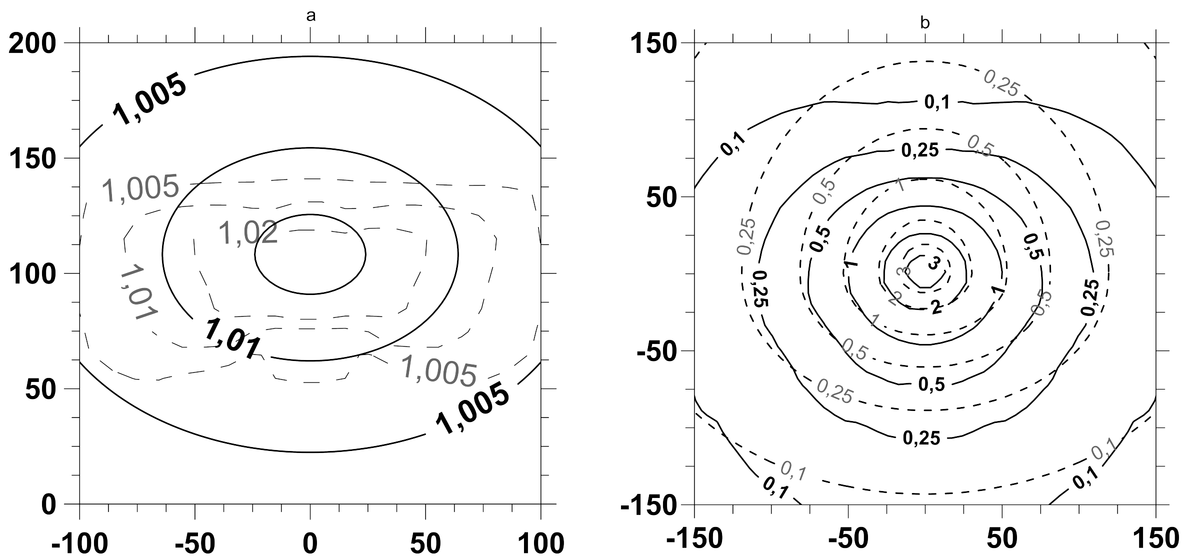

Figure 4 – Modeling results for Chelyabinsk body with density 3320 kg/m^3, entry angle 18°, diameter 19 m, velocity 19 km/s and kinetic energy 514 kt TNT (a) Distribution of relative pressure (p/p_0). (b) Distribution of thermal exposure (J/cm^2) Solid lines are numerical simulations; dashed lines are scaling relations results.

The inclusion of heterogeneity of the radiation field allows to obtain better agreement.

Small values of thermal radiation are determined in numerical simulations with uncertainty, reliable values were considered to be about 3-5 J/cm^2. These values are close to second degree burn (4-25 J/cm^2) and far less than newspaper ignition (15-40 J/cm^2).

3 Application for Chelyabinsk and Tunguska cosmic bodies

Suggested scaling relations were applied for the two most famous cosmic body entries, i.e. Chelyabinsk and Tunguska (Figure 3, 4). Scaling relations show a good approximation quality over results of numerical simulations and observational data.

For the case of the Tunguska cosmic body many different variants of meteoroid parameters were considered (i.e. kinetic energy from 10 to 15 Mt TNT; meteoroid density 1000 and 3320 kg/m3; entry angle 20-45° and velocity 15-40 km/s). Comparison of scaling relation results with data on glass damage and fallen trees (for overpressure and wind) and with burn area and eyewitness accounts (for thermal exposure) demonstrates satisfactory agreement (Jenniskens et al., 2018). One possible solution for the Tunguska meteoroid is shown on Figure 3a (relative pressure) and Figure 3b (thermal exposure).

Chelyabinsk numerical simulations for liquid-like approximation (Shuvalov et al., 2017b) demonstrated good agreement with observational data (Kartashova et al., 2018; Shuvalov et al., 2017c). The comparison of numerical simulation results with scaling relations estimates is given on Figure 4. The thermal exposure distribution demonstrates good agreement over the whole considered area, the relative pressure distribution shows satisfactory agreement in the half-plane and the current ellipticity underestimates the spatial heterogeneity in the other half-plane. It should be noted here that the relative overpressure values in this case are low and not very certain (as it was noted above).

Thermal exposure distributions (Figure 3, 4) shows that the maximal value of irradiated energy is about 4 J/cm^2 for Chelyabinsk and 100 J/cm^2 for Tunguska. Maximal overpressure is 0.025 bar for Chelyabinsk and 0.3 bar for Tunguska.

4 Conclusion

An easy-to-use tool (scaling relations), which gives a good quick estimate for hazardous effects from large meteoroids impacts are suggested. These scaling relations were tested on data and different modelling efforts for Tunguska and Chelyabinsk events and allowed satisfactory description of the observed/modelled overpressures, wind and thermal radiation.

Impact risk assessment motivates the need for simplified approaches and creation of fast damage calculators, which may use the suggested scaling relations. The Impact effect Calculator will be available in the nearest year. The test mode is available at the link: `http://www.AsteroidHazard.pro`. Currently, the thermal radiation effects (including thermal energy distribution on the surface), air blast overpressure, wind speed distributions, acoustic gravitational waves and seismic effect are incorporated into the developing Impact Calculator version. Other effects (crater size, ejecta) will be included in future.

Acknowledgement

This work was supported by Russian Science Foundation, project no. 16-17-00107.

References

Gelfand B. and Silnikov M. (2002). “High-explosive effects of explosion”. *Poligon, St. Petersburg.*

Gi N., Brown P., and Aftosmis M. (2018). “The frequency of window damage caused by bolide airbursts: A quarter century case study”. *Meteoritics & Planetary Science*, pages 1413–1431.

Glasstone S. and Dolan P. (1977). *The Effects of Nuclear Weapons.* Third edition edition. United States Department of Defense and Department of Energy, Washington.

Jenniskens P., Popova P., Glazachev D., Podobnaya E., and Kartashova A. (2018). “Tunguska eyewitness accounts, injuries, and casualties”. *Icarus (submitted).*

Kartashova A., Popova O., Glazachev D., Jenniskens P., Emelyanenko V., Podobnaya ., and Skripnik A. Y. (2018). “Study of injuries from the chelyabinsk airburst event”. *Planetary and Space Science*, **160**, 107–114.

Mathias D. L., Wheeler L. F., and Dotson J. L. (2017). “A probabilistic asteroid impact risk model: assessment of sub-300 m impacts”. *Icarus*, **289**, 106–119.

Nemchinov I., Shuvalov V., and Svetsov V. (2008). “Main factors of hazards due to comets and asteroids”. In *Catastrophic Events Caused by Cosmic Objects*, pages 1–89. Springer.

Shuvalov V. (1999). “Multi-dimensional hydrodynamic code sova for interfacial flows: Application to the thermal layer effect”. *Shock waves*, **9:6**, 381–390.

Shuvalov V., Popova O., Svettsov V., Trubetskaya I., and Glazachev D. (2016). “Determination of the height of the meteoric explosion”. *Solar system research*, **50:1**, 1–12.

Shuvalov V., Svetsov V., Popova O., and Glazachev D. (2017a). “Numerical model of the Chelyabinsk meteoroid as a strengthless object”. *Planetary and Space Science*, **147**, 38–47.

Shuvalov V., Svetsov V., Popova O., and Glazachev D. (2017b). “Numerical model of the chelyabinsk meteoroid as a strengthless object”. *Planetary and Space Science*, **147**, 38–47.

Shuvalov V., Svettsov V., Artemeva N., Trubetskaya I., Popova O., and Glazachev D. (2017c). “Asteroid apophis: Evaluating the impact hazards of such bodies”. *Solar System Research*, **51:1**, 44–58.

Shuvalov V., Svettsov V., and Trubetskaya I. (2013). “An estimate for the size of the area of damage on the earths surface after impacts of 10–300-m asteroids”. *Solar System Research*, **47:4**, 260–267.

Shuvalov V. and Trubetskaya I. (2007). “Aerial bursts in the terrestrial atmosphere”. *Solar System Research*, **41:3**, 220–230.

Svetsov V. and Shuvalov V. (2017). “Thermal radiation from large bolides and impact plumes”. In *European Planetary Science Congress*, volume 11.

Photography and poster contest

The tradition initiated at the International Meteor Conference 2016 in Egmond, the Netherlands, has been continued into 2018 with two competitions. During the IMC, participants had numerous occasions to look at the posters as well as the photographs which had been submitted before the IMC. While the posters automatically enter the "best poster competition", images related to meteors have to be submitted separately.

In the announcement of this competition it is emphasized that observations of meteors can often become a crossover between science and art, involving inspirational landscapes or innovative means of data visualisation. The competition is open to all participants of an IMC and requires that a submitted image needs to be your own work.

Poster award

Two of the three posters rated highest by the participants had a tie for the number of votes – hence there were two "winners". All three posters are found in the Proceedings:

> **Most votes have been cast for** "AMOS cameras status", by *J. Tóth, L. Kornoš, P. Zigo, J. Vilagi, J. Simon, D. Kalmancok, J. Silha, P. Matlovič* (on page 129)
>
> and with the **same number of votes** "The first confirmed lunar impact flash observed from Brazil", by *D. Duarte C. Pinto, L. Trindade, M.L. do P. Villarroel Zurita, R.A.A. Caldas and M. Domingues* (on page 134).
>
> '**Third in this contest is the poster** "Initial design and results of a fireball network add-on radiometer to collect meteor light curves", by *S.R.G. Buchan, R.M. Howie, J. Paxman, H. Devillepoix* (on page 123).

Photography award

Last but not least, there are three images of the photo competition at the IMC 2018.

The winning photo was taken by H. Aziz Kayihan on 2017 July 29 during the 21st edition of the National Star Festival, organised by the National Observatory. It is an event where amateurs and enthusiasts gather with professionals and have a chance the learn the basics of astronomy, gaze through telescopes, and visit the National Observatory. As we were taking the photos of the northern sky in Saklıkent (also with the aim of showing the light pollution caused by the marble quarries around which is visible over the small hill to the right of the meteor), we spotted the meteor in the sky at 02^h06^m local time (UTC +3 hours) with the naked eye as well. This image received the most votes and is shown on the inside back cover of these Proceedings.

2nd in the contest is the image submitted by Marcelo Domingues, called "meteor reflected by the lake". It was taken on 2018 June 17. Marcelo added: A green meteor reflected by the lake near the *Chapada dos Veadeiros* National Park in Brazil. The meteor appeared during a 30 second exposure, using a Canon EOS5D Mark II with an $f = 16$ mm Tamron lens.

The third place went to Ivica Ćiković from Croatia. He wrote: We have a long tradition of observing meteors in our country. This meteor reminded me on my beginnings of meteor observations thirty years ago when I was only a small innocent child who was fascinated by the beauties of the night sky. The way this long meteor scratched the celestial dome, reminded me how our lifetime also passes by, from our emergence to our end. A human lifetime may be more than 70 years, while duration of this meteor was less than a second, but comparing it to the age of the Universe our lifetimes seem insignificant. The photo shows a Perseid meteor which was taken on 2018 August 12/13 from Platak mountain near Rijeka, Croatia.

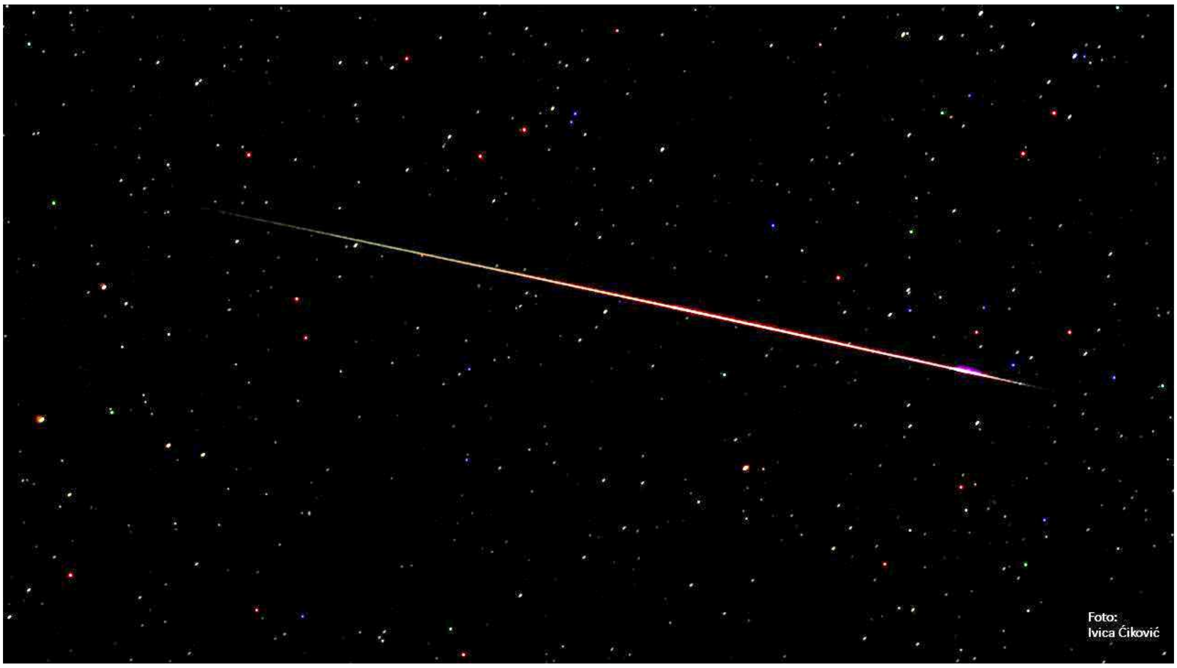

Perseid from Platak mountain, by Ivica Ćiković, Croatia.

Meteor reflected by the lake, by Marcelo Domingues from Brazil.

Meteor during the 21st edition of the National Star Festival in Saklıkent,
by H. Aziz Kayihan, Turkey.